



KATHOLIEKE UNIVERSITEIT LEUVEN
FACULTEIT INGENIEURSWETENSCHAPPEN
DEPARTEMENT ELEKTROTECHNIEK (ESAT)
AFDELING PSI
Kasteelpark Arenberg 10, B-3001 Leuven-Heverlee (Belgium)

KATHOLIEKE UNIVERSITEIT LEUVEN
FACULTEIT GENEESKUNDE
DEPT. MEDISCH DIAGNOSTISCHE WETENSCHAPPEN
AFDELING NUCLEAIRE GENEESKUNDE
Herestraat 49, B-3000 Leuven (Belgium)

Emission Tomography Techniques for Non-Invasive Presurgical Evaluation of Patients with Refractory Partial Epilepsy

Promotoren:

Prof. dr. ir. P. Suetens
Prof. dr. W. Van Paesschen

Proefschrift voorgedragen tot
het behalen van het doctoraat
in de ingenieurswetenschappen
door

Kristof BAETE



KATHOLIEKE UNIVERSITEIT LEUVEN
FACULTEIT INGENIEURSWETENSCHAPPEN
DEPARTEMENT ELEKTROTECHNIEK (ESAT)
AFDELING PSI
Kasteelpark Arenberg 10, B-3001 Leuven-Heverlee (Belgium)

KATHOLIEKE UNIVERSITEIT LEUVEN
FACULTEIT GENEESKUNDE
DEPT. MEDISCH DIAGNOSTISCHE WETENSCHAPPEN
AFDELING NUCLEAIRE GENEESKUNDE
Herestraat 49, B-3000 Leuven (Belgium)

Emission Tomography Techniques for Non-Invasive Presurgical Evaluation of Patients with Refractory Partial Epilepsy

Leden van de jury:

Prof. dr. ir. Y. Willems (voorzitter)
Prof. dr. ir. P. Suetens (promotor)
Prof. dr. W. Van Paesschen (promotor)
Prof. dr. sc. P. Dupont (assessor)
Prof. dr. ir. J. Nuyts (assessor)
Prof. dr. ir. D. Vandermeulen (assessor)
Prof. dr. ir. S. Van Huffel (assessor)
Prof. dr. ir. H. Herzog (Forschungszentrum Jülich)
Prof. dr. sc. M. Defrise (Vrije Universiteit Brussel)

Proefschrift voorgelegd tot
het behalen van het doctoraat
in de ingenieurswetenschappen
door

Kristof BAETE

U.D.C. 681.3*I4

22-6-2006

© Katholieke Universiteit Leuven – Faculteit Ingenieurswetenschappen
Arenbergkasteel, B-3001 Heverlee (Belgium)

Alle rechten voorbehouden. Niets uit deze uitgave mag worden vermenigvuldigd en/of openbaar gemaakt worden door middel van druk, fotokopie, microfilm, elektronisch of op welke andere wijze ook, zonder voorafgaande schriftelijke toestemming van de uitgever.

All rights reserved. No part of this publication may be reproduced in any form by print, photoprint, microfilm or any other means without written permission from the publisher.

ISBN 90-5682-704-9
D/2006/7515/38

Acknowledgements

In 2000, I was given the opportunity to do research in the exciting and challenging field of medical imaging. Doing research was not really what I had in mind, at that time. But, I was prepared to give it a try. Now, after these fascinating years, this work nears its completion and has resulted into this document. And I am glad that I took that step. Let me assure you, what lies before you is not the work of one person. Along the way, many people have contributed, shown their generous support, and helped me to make it all possible. To them, I owe many thanks.

First of all, I would like to thank all members of the jury, for the interest they have shown in this work, and for all comments and valuable discussions that helped to shape this document in its current form.

In particular, I would like to thank my promotores, Prof. Paul Suetens and Prof. Wim Van Paesschen for giving me the possibility to perform research. During these years, they have not only shown great confidence in me, but they have also given me freedom and support in this project. I am enormously grateful to them.

This work would not have been possible without the guidance and the advice of Prof. Patrick Dupont and Prof. Johan Nuyts. Their enthusiasm and experience have been of inspiration to me on numerous occasions. I thank Patrick for the many hours we have spent together thinking about how to solve this or that. His feeling that something was on its track, was always right and encouraging. I thank him for sharing with me his large experience in the understanding of the human brain. I thank Johan for his quick insight in complex ideas and situations. His large experience in emission and transmission tomography was a driving force. I am grateful for his talent in finding a cure for some of my *ill*-posed questions and problems. I am grateful that both of them were there when I was in need for support.

I thank Prof. Dirk Vandermeulen and Prof. Sabine Van Huffel for their effort in attending research meetings and seminars, and for reading and improving the manuscript. The questions and remarks were of great value to me and to this work. I am deeply honored by the presence of Prof. Michel Defrise of the Vrije Universiteit Brussel and Prof. Hans Herzog of the Forschungszentrum Jülich as members of the jury.

I thank Prof. Luc Mortelmans, head of the department of Nuclear Medicine, for giving me the opportunity to perform research at the department, and for using the equipment for some of the experiments. I also thank Prof. Koen Van Laere for his interest in my

research, and I thank Prof. Sigrid Stroobants and dr. Sarah Ceyssens for their expertise and cooperation, and for the nice chats we had from time to time. I thank chief technologist Ludo Verhaegen for the nice collaboration. I thank him also for his support, his concern, and his guidance in many issues. I express my thanks to Stefaan Vleugels for solving various computer related and other practical problems that I encountered during these years. I want to express my special appreciation for the work of our secretaries Francine Reniers, Christel Van Meerbeeck, and Annitta De Messemaker, who have been indispensable at many occasions.

A special acknowledgement goes to my former colleague Dirk Bequé. We started doing research around the same time at the department. I really miss our vivid discussions about our research, our open thoughts about the famous *coffee room* problems, and not to mention those about economy. I enjoyed the annual IEEE conferences we attended together with Johan.

I would like to thank Siddharth Srivastava for the contributions he made in magnetic resonance imaging, which were useful for my research as well. I enjoyed the many interdisciplinary research meetings we had. I would also like to express my gratitude to Prof. André Palmini from Porto Alegre in Brazil, for sharing his knowledge and expertise in the diagnosis and treatment of epilepsy. I thank Guido Van Driel for his involvement in the project. His precision and care for the patients is of great importance. I would also like to thank Shivani Ghoorun from South-Africa for her regular visits to Leuven. During all those years, we have co-authored some nice abstracts, posters, and papers.

I would like to thank all members of the department of Nuclear Medicine, the Laboratory for Radiopharmacy, and the Laboratory for Medical Image Computing. During all those years, I have met a lot of new friends for which I am very happy. I also thank the Katholieke Universiteit Leuven for its financial support by means of grants IDO-99/005 and OT-00/32. I should also thank the Nationale Maatschappij der Belgische Spoorwegen, because a considerable part of this document was written on the train between Brugge and Leuven.

Ook buiten het werk hebben familie, studiegenoten, vrienden, en kennissen bijgedragen aan het tot stand komen van dit proefschrift. Bedankt voor de steun die ik van jullie mocht ontvangen.

Ma, Pa, het ís zover, jullie zoon is (eindelijk) afgestudeerd! Voor zoveel dingen ben ik jullie dankbaar. Wat ik tot nu toe bereikt heb, is mede door jullie mogelijk gemaakt. Dank vanuit het diepste van mijn hart voor de kansen die jullie mij gegeven hebben.

Tot slot, maar niet in het minst, wil ik mijn vrouw Iris bedanken. Bedankt voor je liefde, je geduld, en je vertrouwen. Dank om mij Ruben, een pracht van een zoon, te schenken. Ik ben trots, niet alleen omwille van het voltooien van dit werk, maar meer nog omwille van ons gezinnetje waarin ik gelukkig ben. Ik hou van jullie.

Kristof
22 juni 2006

Abstract

Emission Tomography Techniques for Non-Invasive Presurgical Evaluation of Patients with Refractory Partial Epilepsy

Emission tomography of cerebral blood flow and glucose metabolism are useful for non-invasive presurgical evaluation of patients with refractory partial epilepsy. This work provides techniques to reduce the influence of image degrading effects on the detection of epileptogenic regions. We developed an anatomy based maximum-a-posteriori (A-MAP) reconstruction method for partial volume correction of the gray matter activity. The method uses segmented magnetic resonance imaging data and knowledge of the pathology. A-MAP yields excellent results and has been applied successfully in practice. We also studied the influence of the reconstruction and noise suppression technique on the characterization of clustered voxels in subtraction SPECT. The results indicate that the application of A-MAP on SPECT data improves the presurgical localization accuracy of epileptogenic regions.

Emissie Tomografie Technieken voor Niet-Invasieve Preoperatieve Evaluatie van Patiënten met Refractaire Partiële Epilepsie

Emissie tomografie van de cerebrale doorbloeding en glucose metabolisme is nuttig voor de niet-invasieve preoperatieve evaluatie van patiënten met moeilijk te behandelen partiële epilepsie. Dit werk verschafft technieken die de invloed van beeld degradatie effecten op de detectie van epileptische regio's reduceren. Een op anatomie gebaseerd maximum-a-posteriori (A-MAP) algoritme voor partieel volume correctie van de activiteit in de grijze stof werd ontwikkeld. De methode gebruikt gesegmenteerde kern-spin tomografie data en kennis van de pathologie. A-MAP levert excellente resultaten en is met succes in de praktijk toegepast. Daarnaast hebben we de invloed van de reconstructie methode en de techniek voor ruisonderdrukking onderzocht voor het karakteriseren van gegroepeerde voxels bij subtractie SPECT. De resultaten tonen aan dat A-MAP toegepast op SPECT data de nauwkeurigheid bij de preoperatieve lokalisatie van epileptische regio's verbetert.

Samenvatting

Inleiding

Epilepsie verwijst naar een verzameling van chronisch neurologische condities die gekarakteriseerd zijn door het zich herhaald manifesteren van *epileptische aanvallen*. Deze aanvallen zijn de klinische manifestaties van plotse, abnormale, en gesynchroniseerde elektrische ontladingen van cellen in de grijze stof van de hersenschors. De aard van een epileptische aanval hangt voornamelijk af van waar de elektrische ontladingen beginnen, hoever die zich doorheen de hersenen verspreiden, en hoelang die duren. Epileptische aanvallen kunnen gepaard gaan met het verlies van bewustzijn, en het verstoren van sensorische, motorische, en mentale functies. De duur en de ernst van de aanvallen, alsook de gemiddelde tijd tussen opeenvolgende aanvallen, kunnen van patiënt tot patiënt sterk variëren.

Omdat er verschillende soorten epileptische aanvallen bestaan, werd een classificatie systeem uitgewerkt. De voornaamste onderverdeling daarin is dat van *partiële* versus *gegeneraliseerde* aanvallen. Partiële aanvallen starten vanuit een bepaalde zone in de hersenen, de zogenaamde *epileptische focus*, terwijl beide hersenhelften van bij het begin betrokken zijn bij het type gegeneraliseerde aanvallen. Dit onderzoek spitst zich toe op partiële aanvallen, met als voornaamste doel het zo nauwkeurig mogelijk omschrijven van de epileptische focus.

De Wereld Gezondheid Organisatie (WHO) schat dat ongeveer 0.82 % van de wereldbevolking een vorm van epilepsie heeft die een medische behandeling vereist. Bij een derde van deze patiënten zal blijken dat het huidig aanbod aan geneesmiddelen niet helpt. Voor deze groep patiënten met zogenaamde refractaire of moeilijk te behandelen epilepsie is het aangewezen zich te laten evalueren in een gespecialiseerd epilepsie referentie centrum. Deze centra, die door de overheid erkend worden, beschikken over het diagnostisch materiaal en de gespecialiseerde zorgen voor een zo optimaal mogelijke behandeling. Bij een deel van de patiënten met moeilijk te behandelen partiële epilepsie zal, mits een uitgebreide preoperatieve evaluatie, een curatieve chirurgische behandeling voorgesteld kunnen worden.

Preoperatieve Evaluatie van Refractaire Partiële Epilepsie

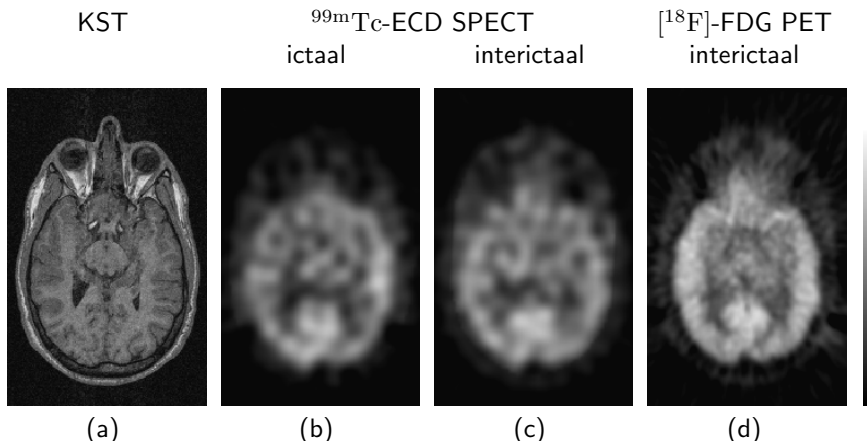
De preoperatieve evaluatie van patiënten met moeilijk te behandelen partiële epilepsie heeft meestal tot doel te achterhalen of één of meerdere letsels aanleiding geven tot epileptische aanvallen. Het is eveneens de bedoeling de letsels zo accuraat mogelijk te lokaliseren. Indien het een letsel betreft dat niet in een delicaat of onmisbaar stuk van de hersenen ligt, dan kan de patiënt een chirurgische behandeling van de aandoening voorgesteld worden. Deze procedure omvat het wegnemen van het epileptisch letsel. Omdat een dergelijke behandeling niet zonder risico is, zullen meerdere klinische onderzoeken uitgevoerd worden om een zo nauwkeurig mogelijk beeld te krijgen van het letsel dat de epileptische aanvallen genereert.

De preoperatieve evaluatie start met het gedetailleerd beschrijven van de aanvallen, het uitvoeren van neurologische onderzoeken, en electro-encefalografie (EEG). Hoge-resolutie kern-spin tomografie (KST) wordt gebruikt om een mogelijk anatomisch letsel op te sporen. Al in dit stadium van de evaluatie kunnen de resultaten aantonen of een chirurgische behandeling voor de patiënt voordelen zal kunnen bieden. Indien dit het geval is, wordt de patiënt uitgenodigd voor verdere onderzoeken.

De voortgezette preoperatieve evaluatie omvat video-EEG observatie gedurende een week. Indien er zich tijdens die week een aanval voordoet, dan zal de patiënt zo snel mogelijk na de eerste symptomen van een epileptische aanval geïnjecteerd worden met de radioactief gemerkte stof ^{99m}Tc -ECD, die de doorbloeding van de hersenen in beeld kan brengen. Deze procedure, die ictale SPECT wordt genoemd, toont meestal een verhoogde doorbloeding ter hoogte van het begin van de aanval. Op een later moment, wanneer de patiënt vrij is van aanvallen, kan een interictale SPECT opname gebeuren. Interictale SPECT toont meestal een verlaagde doorbloeding ter hoogte van het epileptisch letsel. Indien het interictale van het ictale SPECT beeld afgetrokken wordt en het verschil met KST geregistreerd wordt, dan kan een vrij nauwkeurige lokalisatie van het begin van de aanval in beeld gebracht worden. Men verwijst naar deze procedure met de naam SISCOM. Wanneer de patiënt vrij is van aanvallen, kan men op een ander tijdstip met PET ook het glucose verbruik meten. Men gebruik daarvoor de radioactief gemerkte stof $[^{18}\text{F}]$ -FDG. Gebieden met een verlaagd glucose verbruik op interictale PET omvatten gewoonlijk het epileptisch letsel.

Wanneer verdachte epileptische zones zich dicht bij delicate gebieden van de hersenen zouden bevinden, dan kan de arts aansturen op functionele KST, zodat een mogelijk risico bij het weghalen van deze gebieden ingeschat kan worden. Indien de niet-invasieve preoperatieve evaluatie onvoldoende zou blijken, dan kan men een beroep doen op meer invasieve diagnostische methoden, zoals bijvoorbeeld het meten van het EEG binnenin de schedel gedurende een langere periode. Deze methode kan helpen bij het beter lokaliseren van het begin van een aanval.

De resultaten die uit de preoperatieve evaluatie voortvloeien worden telkens besproken in een multidisciplinaire vergadering van experten. Indien de resultaten van de verschillende onderzoeken concordant zijn, er slechts één enkel epileptisch letsel gevonden werd, en de kans op slagen voldoende groot wordt geacht, dan stelt men de patiënt een curatieve chirurgische behandeling voor.



Figuur 1: De preoperatieve evaluatie van patiënten met refractaire partiële epilepsie omvat o.m. (a) hoge-resolutie kern-spin tomografie (KST) die de anatomie van de hersenen in beeld brengt, (b) ictale en (c) interictale SPECT waar men de cerebrale doorbloeding tijdens en tussen aanvallen mee meet, en (d) interictale PET die het glucose verbruik van de hersenen tussen aanvallen toont.

Doel van dit Werk

Dit werk heeft tot doel een bijdrage te leveren tot de emissie tomografie technieken die gebruikt worden voor de preoperatieve evaluatie van patiënten met moeilijk te behandelen partiële epilepsie. Het objectief van dit onderzoek is het zo accuraat mogelijk en niet-invasief lokaliseren van epileptische letsels door nieuwe beeldvormings- en beeldverwerkingstechnieken te optimaliseren en te implementeren. De technieken waar men in de klinische praktijk gebruik van maakt zijn FDG-PET van het cerebraal glucose verbruik en ECD-SPECT van de cerebrale doorbloeding. Deze technieken spelen een belangrijke rol bij het detecteren en lokaliseren van verdachte epileptische zones. De kwaliteit en de kwantitatieve betrouwbaarheid van de beelden kunnen het detecteren van epileptische letsels echter sterk beïnvloeden (Fig. 1).

Emissie tomografie meet op een indirecte en niet-invasieve manier de ruimtelijke verdeling van een radioactief gemerkte stof. Deze modaliteit uit de nucleaire geneeskunde maakt het mogelijk om fysiologische processen te meten in levende organismen. De radioactieve stof die aan het subject toegediend wordt, is zo gemaakt dat het zal participeren, in interactie, of in competitie treden met een bepaald fysiologisch proces. De radioactieve eigenschap van de stof maakt het mogelijk om de ruimtelijke verdeling ervan in het organisme op een niet-invasieve manier van buitenaf te meten. Na de meting moet de data echter eerst gereconstrueerd worden vooraleer men de twee- of driedimensionale beelden kan analyseren. Helaas kunnen ongunstige effecten vanaf het meten tot en met het afbeelden van de data de kwaliteit van de beeldvorming beïnvloeden. In dit werk proberen we de invloed van enkele van deze effecten te reduceren.

De resolutie van het systeem en de bemonstering van het signaal zijn twee belangrijke eigenschappen van elk systeem dat dient voor medische beeldvorming. De resolutie van emissie tomografie is in het algemeen veel slechter dan dat van andere modaliteiten. De beperkte resolutie zorgt ervoor dat de intensiteit van de ontvangen signalen, gewogen met de puntspreidingsfunctie van het systeem, uitgesmeerd worden. Dit effect, in combinatie met het discreet bemonsteren van het signaal, leidt tot een verlies van informatie, en is beter bekend als het *partieel volume effect* (PVE). Dit effect is het meest opvallend voor objecten met afmetingen die relatief klein zijn in vergelijking met het ruimtelijk interval van de bemonstering en de resolutie van het systeem. De gemiddelde dikte van de hersenschors komt jammer genoeg in aanmerking voor dit effect. Als gevolg van het PVE zal de intensiteit in sommige gebieden van de hersenen artificieel verlaagd zijn. Bij interictale FDG-PET data kan dit effect het detecteren van epileptische letsels, die zich normaal gezien als zones met een verlaagd metabolisme laten tonen, bemoeilijken. In dit werk ontwikkelen we een reconstructie algoritme dat voor het PVE corrigeert. Dit moet de arts toelaten om beter te kunnen differentiëren tussen regio's met een echte, en regio's met een artificieel verlaagde intensiteit.

Bij emissie tomografie zal Poisson ruis de meting van fotonen, en dus de kwaliteit van het gereconstrueerd beeld, beïnvloeden. Bij de subtractie analyse van iciale en interictale SPECT beelden (SISCOM) kan de invloed van ruis in het beeld tot artificiële verschillen in de cerebrale doorbloeding leiden. Bovendien kunnen deze door ruis geïnduceerde verschillen de visuele analyse van SISCOM data bemoeilijken. Dit werk heeft eveneens tot doel de arts te helpen bij het analyseren van deze data door meer informatie te verschaffen over de significantie van de verschillen in een subtractie analyse van SPECT data.

Partieel Volume Effect

Bij emissie tomografie komt het te meten signaal vanuit de patiënt. De meting van het signaal is van buitenaf niet zo makkelijk te controleren als bij een CT of een KST toestel. De hoeveelheid activiteit die men aan de patiënt kan toedienen, alsook de duur van de meting, is beperkt. Ook al zou langer meten een betere beeldkwaliteit kunnen opleveren, het zou de kans dat de patiënt beweegt te zeer verhogen. De winst van het langer meten zou op die manier teniet worden gedaan. Voorts beïnvloeden een aantal fysische effecten de beeldkwaliteit zonder meer ongunstig. Voorbeelden van dergelijke effecten zijn het verwakken en verstrooien van fotonen, de dracht van het positron, en random coïncidentie detectie.

Emissie tomografie leidt in het algemeen tot gemeten data met een vrij lage signaal-ruis verhouding. Daarom worden de gereconstrueerde beelden voor een kwalitatieve beoordeling vaak met een laag-doorlaat filter bewerkt. Hoewel de beelden dan beter ogen, zal het filteren de kwantitatieve betrouwbaarheid van de data reduceren. De beeldkwaliteit van emissie tomografie mag dan misschien wel minder goed lijken dan dat van CT of KST, toch bevatten de gegevens meestal genoeg informatie voor het maken van klinische beslissingen.

Alle systemen voor beeldvorming waarin signalen digitaal bemonsterd worden zijn onderhevig aan het PVE. Het onderscheid tussen het bemonsteren van het signaal enerzijds, en de ruimtelijke resolutie van het systeem anderzijds, is belangrijk bij emissie tomografie. Het discreet bemonsteren van het signaal leidt tot een benadering van de werkelijke ruimtelijke verdeling van de radioactieve stof, en dus tot een zeker verlies van informatie. De ruimtelijke resolutie van het systeem, bepaald door zowel de detector als het reconstructie algoritme, leidt tot het uitsmeren van de intensiteit van het signaal en tot het verspreiden van informatie naar naburige gebieden. Bij andere modaliteiten voor beeldvorming, bv. bij KST, is het ruimtelijk interval voor het bemonsteren van het signaal gewoonlijk groter dan de ruimtelijke resolutie van het systeem. In dat geval is het onderscheid tussen de twee minder belangrijk. In emissie tomografie zijn de dimensies van een detector element vaak kleiner dan de resolutie van die detector. Het onderscheid tussen de bemonstering en de resolutie is in dat geval wel belangrijk.

De kwantitatieve betrouwbaarheid van emissie tomografie is belangrijk bij de functionele beeldvorming van hersenen. Het PVE zal de analyse van kleine structuren in de hersenen bemoeilijken en tot onder- en overschattingen leiden van de lokale stapeling van de radioactieve stof. Hersenen hebben immers een vrij complexe morfologie, en de ruimtelijke afmetingen van meerdere structuren in de hersenen zijn relatief klein in vergelijking met de voxel grootte en de ruimtelijke resolutie van het systeem. Door het PVE is het soms onduidelijk of wijzigingen in de intensiteit van de reconstructie het gevolg zijn van variaties in de opname van de radioactieve stof, of van variaties in de ruimtelijke afmetingen van de overeenkomstige structuren (bv. atrofie). Bij de preoperatieve evaluatie van patiënten met epilepsie kan het PVE tot een verhoogd aantal vals-positieve epileptische regio's leiden. Indien de resolutie van het systeem niet in rekening gebracht wordt, kan de uitgebreidheid van epileptische regio's verkeerd geïnterpreteerd worden.

Partieel Volume Correctie in Emissie Tomografie

Om de invloed van het PVE te reduceren werden reeds een aantal partieel volume correctie (PVC) technieken ontwikkeld. Deze technieken zijn voornamelijk gebaseerd op de volgende gedachtegang. Indien een PVC techniek de invloed van het PVE wil reduceren, dan heeft die techniek daar aanvullende gegevens voor nodig. De emissie data bevat daar immers zelf niet genoeg informatie voor. De meeste PVC technieken maken gebruik van anatomische informatie uit geregistreerde en in verschillende weefsels gesegmenteerde KST data. Sommige PVC technieken houden eveneens rekening met de resolutie van het systeem voor emissie tomografie. Op die manier kan de bijdrage van elk type weefsel aan de overeenkomstige voxels in het emissie beeld berekend worden. Als men bovendien de resolutie van het systeem kent, dan kan er gecorrigeerd worden voor het uitsmeren van de activiteit in het gereconstrueerd beeld.

In het algemeen zijn er twee methodologische benaderingen voor het uitvoeren van PVC in emissie tomografie. Bij de eerste benadering maakt men gebruik van

anatomische informatie na de reconstructie van de emissie data. Daarvoor gebruikt men vaak analytische reconstructie methoden die weinig of niet compenseren voor de ongunstige effecten die we eerder aanhaalden. Bij de tweede benadering maakt men daarentegen gebruik van anatomische informatie tijdens het reconstructie proces. Voor deze benadering gebruikt men meestal statistische reconstructie technieken, die in vele gevallen wel toelaten om te compenseren voor ongunstige effecten.

Anatomie Gebaseerde Reconstructie

In dit werk stellen we een maximum-a-posteriori (MAP) reconstructie algoritme voor dat ontwikkeld werd om tijdens het reconstrueren van emissie data met behulp van anatomische informatie te corrigeren voor het PVE. We noemen dit nieuwe algoritme dan ook een anatomie gebaseerde MAP reconstructie, of kortweg A-MAP. De drie voornaamste soorten weefsel in de hersenen, i.e. de grijze en witte stof, en het cerebrospinaal vocht, kunnen door het segmenteren van hoge-resolutie KST bepaald worden. De meeste segmentatie algoritmen kennen aan elke voxel in het KST beeld een bepaalde waarschijnlijkheid voor het type weefsel toe. We nemen aan dat deze waarschijnlijkheid de partiële bijdrage van elk type weefsel in de voxels van de emissie tomografie beelden weerspiegelt.

Elke voxel die de ruimtelijke verdeling van de radioactieve stof in de hersenen weergeeft, kan gezien worden als een aparte bron van straling. Deze bron bevat een hoeveelheid activiteit die gelijk is aan de som van de fractionele activiteiten van elk weefsel. Dit concept noemt men het weefsel compositie model. De gemeten emissie data bevat echter maar voldoende informatie om voor elke voxel de som van alle fractionele activiteiten te bepalen. Er is niet genoeg informatie om het reconstructie probleem voor elke parameter van het compositie model op te lossen. We zijn dus genoodzaakt om voor A-MAP extra informatie onder de vorm van assumpties in te voeren. De doorbloeding en het metabolisme van de witte stof bij epilepsie is lager en uniformer dan dat van de grijze stof. We nemen daarom aan dat de activiteit die de witte stof zal bijdragen op een uniforme verdeling is gebaseerd. We nemen ook aan dat de activiteit niet in het cerebrospinaal vocht zal stapelen.

A-MAP is ontworpen om PVC uit te voeren in één bepaald type weefsel. Voor de preoperatieve evaluatie van epilepsie, en vermoedelijk ook voor een aantal andere toepassingen die in dit werk niet onderzocht werden, is dit type weefsel de grijze stof. Om voor het PVE te corrigeren is er in een aantal weefsels een regularisatie methode geïntroduceerd. Omdat sommige voxels meer dan één type weefsel bevatten werd een techniek ontwikkeld om de regularisatie tot één enkel type weefsel te beperken.

De voxel ruimte wordt, op basis van de anatomische informatie in de KST segmentatie beelden, opgedeeld in een aantal deelverzamelingen van voxels. In de verzameling van grijze stof voxels maken we een vereenvoudiging van het weefsel compositie model. Daarin vervangen we de bijdrage van de witte stof en het cerebrospinaal vocht door de gemiddelde waarde berekend aan de hand van de voxels in de respectievelijke deelverzamelingen. Vervolgens introduceren we een nieuwe verzameling van variabelen, bestaande uit de activiteit die de grijze stof bijdraagt

in de verzameling van grijze stof voxels, en de activiteit van de andere weefsels in het complement van de verzameling van grijze stof voxels. Deze nieuwe verzameling van variabelen kan aanzien worden als een parameter transformatie van de originele variabelen. Deze parameter transformatie laat ons toe om enkel de bijdrage van de grijze stof te bepalen, zelfs in voxels die een mengeling van grijze stof en andere weefsels bevatten. De meest waarschijnlijke verdeling van de activiteit voor deze nieuwe parameters wordt dan bepaald door een statistisch reconstructie algoritme.

Het algoritme bevat nog twee bijkomende randvoorwaarden. Ten eerste, de assumpties voor de verdeling van de activiteit van de witte stof en het cerebrospinaal vocht worden als a priori kennis tijdens het statistisch reconstructie proces gebruikt. Ten tweede, ruis die tijdens het reconstructie proces van de gemeten data naar de grijze stof voxels zou kunnen propageren wordt tegengewerkt door een Gibbs-Markov prior die de relatieve verschillen tussen naburige voxels zal penaliseren.

Evaluatie van het A-MAP Algoritme

Het A-MAP reconstructie algoritme werd aan een uitvoerige evaluatie onderworpen. Eerst werd het gebruik van perfecte en niet-perfecte anatomische informatie onderzocht. A-MAP met gebruik van perfecte anatomische informatie stelt ons in staat om het algoritme onder optimale omstandigheden te evalueren. Deze situatie werd vergeleken met het gebruik van niet-perfecte anatomische informatie. Daarmee evalueren we A-MAP met data die segmentatie technieken in de praktijk produceren. We maakten gebruik van computer simulaties op basis van een realistisch 2-D software fantoom dat het glucose metabolisme van de hersenen weerspiegelt. De ene helft van de data werd met een normaal metabolisme gesimuleerd. In de andere helft van de data werd de activiteit in enkele grijze stof regio's kunstmatig verlaagd. Daardoor kunnen we op een objectieve manier bepalen welk algoritme betere resultaten geeft voor het detecteren van gebieden met een verlaagd metabolisme. Voor de evaluatie keken we naar de afwijking en spreiding van de gereconstrueerde intensiteit, en de signaal-ruis verhouding van de beelden. In vergelijking met andere statistische reconstructie methoden, die geen anatomische informatie gebruiken, geeft A-MAP goede resultaten voor het gebruik van perfecte anatomische informatie. Het gebruik van niet-perfecte anatomische informatie leidt tot een afname van de signaal-ruis verhouding bij A-MAP.

Bij het A-MAP algoritme nemen we aan dat variaties van het metabolisme enkel in de grijze stof plaatsvinden. In deze regio onderdrukt het algoritme ruis met behulp van een Gibbs-Markov prior. We onderzochten de invloed van deze prior op het detecteren van gebieden met een verlaagd metabolisme (cfr. supra). We vergeleken de resultaten met reconstructie algoritmen die een andere techniek voor het onderdrukken van ruis gebruiken. De gereconstrueerde intensiteit van A-MAP wijkt minder af van de oorspronkelijke waarde en heeft een kleinere spreiding dan de methoden waarmee vergeleken werd. We onderzochten eveneens de invloed van kleine fouten bij de ruimtelijke registratie van de anatomische informatie en van lokale fouten in de segmentatie data.

Om het detecteren van gebieden met een verlaagde intensiteit bij verschillende reconstructie algoritmen te vergelijken, werd een studie met menselijke waarnemers opgezet. Aan enkele artsen werd gevraagd om verborgen regio's met een verlaagde metabolisme in 2-D gesimuleerde FDG-PET beelden van de hersenen aan te duiden. Het A-MAP reconstructie algoritme toonde een significant verbetering van de detectie van de verborgen zones dan het standaard maximum-likelihood (ML) reconstructie algoritme. Tenslotte werd de FDG-PET data van een patiënt met moeilijk te behandelen partiële epilepsie gereconstrueerd met A-MAP. De toepasbaarheid van A-MAP in de klinische praktijk werd daarmee aangetoond.

Cluster Hoogte en Grootte in Subtractie SPECT

SPECT van de cerebrale doorbloeding is nuttig bij de preoperatieve evaluatie van patiënten met moeilijk te behandelen partiële epilepsie. Tijdens een aanval is er een toename van de doorbloeding in epileptische regio's, en bij ongeveer de helft van de patiënten is de doorbloeding afgenomen tussen de aanvallen. Door iciale en interictale SPECT beelden naast elkaar te bekijken is het mogelijk om verdachte epileptische gebieden op te sporen. Deze techniek is echter subjectief en weinig sensitief voor subtielere veranderingen.

De subtractie van iciale en interictale SPECT beelden is een techniek die betere resultaten geeft voor het detecteren van epileptische regio's. Na het registreren van de SPECT beelden met KST data is het mogelijk om functionele en anatomische correlaties in detail te bestuderen. Deze techniek, afgekort tot SISCOM, weerhoudt enkel de grootste verschillen van de cerebrale doorbloeding en toont die bovenop het KST beeld. Jammer genoeg kan Poisson ruis in de gemeten projectie data eveneens tot verschillen in de doorbloeding leiden.

Een kwantitatieve analyse van subtractie SPECT data kan de diagnostische waarde van de techniek voor de klinische praktijk verhogen. Dit kan door een probabilistisch onderscheid te maken tussen verschillen die het gevolg zijn van ruis, en verschillen van fysiologische of pathologische aard. Gelijkaardige technieken, zoals Statistical Parametric Mapping (SPM), worden gebruikt bij functionele beeldvorming voor fundamenteel neurofysiologisch onderzoek. Bij SISCOM is het aantal beelden per studie echter te klein waardoor bestaande technieken, zoals SPM, tot conservatieve conclusies zal leiden en een verhoogd aantal vals-positieve predicties. Bovendien houden deze technieken meestal geen rekening met de invloed die de meting, het reconstructie algoritme, of de verdere verwerking van beelden op de significantie van de gevonden verschillen kan hebben.

In dit werk bestuderen we een methode voor het karakteriseren van verschillen in de subtractie analyse van SPECT data. We bestuderen, net zoals bij SPM, de significantie van de verschillen op voxel en op cluster niveau. Een cluster is gedefinieerd als een groep samenhangende voxels met een intensiteit boven een vooraf bepaalde drempelwaarde. Voor iedere cluster bepalen we twee cluster parameters: (a) de cluster hoogte, en (b) de cluster grootte. De hoogte is gedefinieerd als het grootste verschil binnen de cluster, en de grootte is het aantal voxels in de clus-

ter. Met behulp van een empirische methode kennen we aan iedere cluster een waarschijnlijkheid toe voor, enerzijds de cluster hoogte, en anderzijds de cluster grootte, en onder de hypothese dat er geen verschillen zijn in de doorbloeding van de hersenen.

In eerste instantie werd de reproduceerbaarheid van de empirische methode onderzocht met gesimuleerde SPECT projectie data. De experimenten tonen aan dat ruis in staat is om vrij grote en hoge clusters te induceren. Daarna werd de methode gebruikt om te bepalen of de cluster grootte een even belangrijke parameter is als de cluster hoogte voor het karakteriseren van significante verschillen in subtractie SPECT. Deze hypothese werd getest met simulaties op basis van een realistisch 3-D software fantoom van de doorbloeding van de hersenen. De experimenten tonen aan dat het detecteren van verschillen op basis van de parameter cluster grootte betere resultaten geeft dan voor de parameter cluster hoogte. Bij eenzelfde significantie niveau levert de cluster grootte veel minder vals-positieve resultaten dan de cluster hoogte.

Ruisonderdrukking en PVC in Subtractie SPECT

Bij de subtractie analyse van SPECT data onderzochten we de invloed van het reconstructie algoritme, en de daarbij gebruikte techniek voor het onderdrukken van ruis, op de hoogte en grootte van clusters. De reconstructie algoritmen die gebruikt werden, zijn de gefilterde terugprojectie (FBP), het maximum-likelihood (ML) algoritme, en A-MAP. Het onderdrukken van ruis gebeurde bij FBP en ML door middel van convolutie met een Gaussische functie. Bij A-MAP werd het gewicht van de Gibbs-Markov prior in de grijze stof gevareerd.

Op basis van een realistisch 3-D software fantoom van de doorbloeding van de hersenen werden Poisson ruis realisaties van SPECT projectie data gesimuleerd. De projectie data werden met een aantal methoden gereconstrueerd, en voor elke methode werd de verdeling van de hoogte en grootte van clusters in de subtractie analyse van de SPECT data onderzocht. Het gedrag van de clusters parameters onder invloed van ruis werd vervolgens gebruikt om voor elke methode het detecteren van een gebied met een kunstmatig verhoogde doorbloeding te bepalen.

Het gebruik van veel ruisonderdrukking leidt tot een beter detectie vermogen van gebieden met een verhoogde doorbloeding bij het FBP en ML reconstructie algoritme. Wanneer er echter anatomische informatie vorhanden is, dan kan een reconstructie met A-MAP tot dezelfde resultaten leiden. A-MAP reconstructies hebben bovendien minder last van de nadelige effecten van ruisonderdrukking bij FBP en ML, zoals een slechter lokaliserend vermogen.

Bijdrage van dit Werk

Dit werk levert een bijdrage tot het verbeteren van emissie tomografie technieken voor de preoperatieve evaluatie van patiënten met moeilijk te behandelen partiële

epilepsie. De invloed van sommige effecten die nadelig zijn voor het detecteren van epileptische letsets in ECD-SPECT en FDG-PET data werden onderzocht. Dit werk reikt technieken aan voor het reduceren van de gevolgen van deze effecten. We spitsten het onderzoek toe op, enerzijds de correctie voor het partieel volume effect in PET en SPECT, en anderzijds de invloed van het reconstructie algoritme en de techniek voor ruisonderdrukking op de subtractie analyse van SPECT data.

De oorzaken en invloed van het partieel volume effect werden onderzocht in PET en SPECT, en de consequenties voor de klinische besluitvorming werden bestudeerd. Er werd een nieuwe partieel volume correctie methode ontwikkeld die de naam A-MAP toegewezen kreeg. In tegenstelling tot de reeds bestaande PVC methodes, is A-MAP ontworpen om te corrigeren voor het PVE in de grijze stof gedurende het statistisch reconstrueren van de projectie data. Het algoritme maakt daarvoor gebruik van gesegmenteerde KST data en bevat specifieke aannames betreffende de pathologie. Daardoor laat het algoritme toe om meer voorkennis te gebruiken tijdens het reconstructie proces, in tegenstelling tot bestaande PVC methodes. De aannames waarop A-MAP gebaseerd is, alsook de wiskundige afleiding van het iteratief algoritme, werden gepresenteerd. De PVC eigenschappen van het algoritme werden gedemonstreerd en het algoritme werd aan een uitgebreide evaluatie onderworpen.

We onderzochten de invloed van ruis op de subtractie analyse van ictale en interictale ECD-SPECT data. We stelden een statistische methode op om clusters te karakteriseren op basis van de cluster hoogte en grootte. Het gedrag van deze parameters onder invloed van ruis in de projectie data werd gebruikt om aan clusters een waarschijnlijkheid toe te kennen. De reproduceerbaarheid van de methode werd aangetoond, alsook het belang van de parameter cluster extent voor het detecteren van significante clusters. Tot slot onderzochten we de invloed van het reconstructie algoritme en de techniek voor het onderdrukken van ruis op het karakteriseren van clusters in de subtractie analyse van SPECT data.

Suggesties voor Verder Onderzoek

Omdat de exacte verdeling van de radioactieve stof in het lichaam niet te achterhalen is, werd voor het evalueren van de ontwikkelde technieken hoofdzakelijk met computer simulaties op basis van realistische data gewerkt. Het is de bedoeling om deze technieken in de toekomst verder te evalueren met klinische data. Er is echter nood aan concrete richtlijnen betreffende het evalueren van nieuwe reconstructie technieken voor PET en SPECT.

Een interessante eigenschap van het A-MAP algoritme is het reconstrueren van de fractionele activiteit van de grijze stof voor voxels die slechts gedeeltelijk grijze stof bevatten. Het nut van deze informatie werd in dit werk niet onderzocht. We verwachten wel dat deze informatie kan helpen bij het analyseren van gebieden die zowel grijze als witte stof bevatten. A-MAP is gebaseerd op een aantal veronderstellingen, waaronder de verdeling van activiteit in de witte stof bij epilepsie. Verder onderzoek zal moeten aantonen wat de implicaties zijn indien deze nieuwe

reconstructie techniek gebruikt wordt voor andere neurologische aandoeningen.

Tijdens dit onderzoek werd door andere groepen vooruitgang geboekt op het vlak van de beeldverwerking van KST en de signaalverwerking van EEG data bij epilepsie. Er werd een verbeterd KST segmentatie algoritme ontwikkeld die het verkeerd classificeren van weefsels tot een minimum beperkt. We verwachten dat verdere verbeteringen van het segmentatie algoritme een gunstig effect zullen hebben op de resultaten van A-MAP. Er werd eveneens een techniek ontwikkeld voor het verwijderen van artefacten uit het EEG signaal. Het combineren en integreren van de resultaten van deze nieuwe technieken kan helpen bij het onderzoek naar de oorzaak van epileptische aanvallen.

A-MAP kan ook toegepast worden op data die gemeten werd met een dynamisch acquisitie protocol. Een dergelijk protocol wordt meestal gebruikt voor het kwantificeren van het kinetisch gedrag van een radioactief gemerkte stof *in vivo*. De emissie data bevat meestal veel ruis en is onderhevig aan het PVE. Corrigeren voor het PVE kan zowel voor als na het kinetisch modelleren van de data gebeuren. Zoals eerder aangehaald, zijn we van mening dat de data beter eerst gecorrigerd wordt voor het PVE. In dat geval is het A-MAP algoritme de door ons geprefereerde methode.

De laatste jaren levert de beeldvorming van kleine proefdieren met behulp van gespecialiseerde emissie tomografie apparatuur, zoals micro-PET en micro-SPECT, een waardevolle bijdrage aan fundamenteel biomedisch onderzoek. Dit nieuw onderzoeksgebied, dat moleculaire beeldvorming wordt genoemd, houdt zich voornamelijk bezig met de preklinische analyse van nieuwe medicijnen, enzymes, receptoren, en het in beeld brengen van gen expressie *in vivo*. We voorzien dat A-MAP kan helpen om de beeldkwaliteit en de kwantitatieve betrouwbaarheid van micro-PET en micro-SPECT data te verbeteren.

Voor een aantal klinische toepassingen is het vorhanden zijn van zowel anatomische (KST, CT) als functionele (PET, SPECT) beeldvorming een minimum vereiste. Vaak komt het ruimtelijk registreren van de data de visuele inspectie ten goede. In de klinische oncologie, bijvoorbeeld, kan een simultane analyse van PET en CT beelden tot een betere diagnose leiden. Algoritmen voor het automatisch registreren van PET en CT beelden maken deze analyse mogelijk. Het recent gebruik van hybride PET/CT scanners maakt dit proces al een stuk eenvoudiger. De anatomie en functie worden in PET/CT echter niet simultaan, maar vlak na elkaar gemeten. De registratie is dus niet steeds perfect. Een gelijkaardige technologische vernieuwing vindt ondertussen plaats tussen KST en PET. Onderzoekers hebben met succes de compatibiliteit van PET acquisitie hardware in het sterke magneetveld van een KST toestel onderzocht. We verwachten dat binnen enkele jaren hybride KST/PET beeldvorming mogelijk zal zijn. Waarschijnlijk zullen binnenkort de eerste toepassingen voor deze nieuwe modaliteit verschijnen. Het A-MAP algoritme komt hier al voor in aanmerking.

De SPECT subtractie methode die in dit werk ontwikkeld werd levert voor iedere cluster in een SISCOM analyse informatie over de grootte, hoogte, en voor elk van deze parameters de cluster probabiliteit. Deze informatie kan nuttig zijn bij het analyseren van SISCOM data. Met behulp van een drempelwaarde kan men enkel de

meest significante clusters weerhouden. Deze aanpak zou bij voorkeur geëvalueerd moeten worden met een groot aantal ECD-SPECT studies. De subtractie methode kan eveneens gebruikt worden om SPECT beelden van eenzelfde patiënt onder twee condities met elkaar te vergelijken. Het meten van de doorbloeding van de hersenen met en zonder toediening van acetazolamide is een bekende methode om de vasculaire reserve te meten bij patiënten met een beroerte, transiënte ischemie, of arterioveneuze malformaties.

Het normaliseren van emissie tomografie beelden bij het uitvoeren van een subtractie analyse is cruciaal omdat de globale activiteit in de hersenen tijdens het meten van de data niet noodzakelijk gelijk hoeft te zijn. Hoe deze normalisatie procedure precies dient te gebeuren, is momenteel onderwerp van verder onderzoek. De huidige methoden zijn moeilijk te valideren, en de onderliggende pathologie is grotendeels onbekend en onvoorspelbaar. In dit werk werd een heuristische methode gebruikt voor het bepalen van een referentie regio die nodig is om de beelden te normaliseren. Anatomische informatie onder de vorm van gesegmenteerde KST data zou kunnen helpen om bijvoorbeeld de reconstrueerde beelden te normaliseren op basis van de activiteit in de witte stof. Dit alles zou gecombineerd kunnen worden met een A-MAP reconstructie van de PET of SPECT data.

List of acronyms

<i>n</i> -D	<i>n</i> -dimensional
A-MAP	anatomy based maximum-a-posteriori
AUC	area under the ROC-curve
CBF	cerebral blood flow
CDF	cumulative distribution function
CSF	cerebrospinal fluid
ECD	99m Tc-ethyl-cysteinate-dimer
EEG	electroencephalography
EM	expectation-maximization
FBP	filtered back-projection
FDG	2-[18 F]fluoro-2-deoxy-D-glucose
FOV	field-of-view
FPF	false positive fraction
FWHM	full-width at half-maximum
GM	gray matter
GTM	geometric transfer matrix
IBE	International Bureau for Epilepsy
ILAE	International League Against Epilepsy
LEUHR	low-energy ultra-high resolution
LOR	line-of-response
MAP	maximum-a-posteriori
ML	maximum-likelihood
MIRIT	..	multi-modal image registration by maximization of mutual information
MPRAGE	magnetization prepared rapid gradient echo
MRF	Markov random field
MRI	magnetic resonance imaging
OS	ordered subsets
PDF	probability density function
PET	positron emission tomography
PSF	point spread function
PVC	partial volume correction
PVE	partial volume effect
RC	retrieved cluster

ROC	receiver operating characteristic
ROI	region-of-interest
SISCOM	subtraction ictal SPECT co-registered to MRI
SNR	signal-to-noise ratio
SPECT	single photon emission computed tomography
SPM	statistical parametric mapping
TPF	true positive fraction
WM	white matter

Symbols

\otimes	convolution
\triangleq	is by definition equal to
\propto	is proportional to
$\#_R$	number of non-zero elements in R
λ_j	activity in voxel j
Λ	reconstruction image
I	total number of detector elements
i	detector element i
J	total number of image voxels
j	voxel j
δ	Dirac impulse function
q_i	number of (co)incidences measured by detector (pair) i
c_{ij}	detection sensitivity of detector i for activity in voxel j
μ	linear attenuation coefficient [cm^{-1}]
L	logarithm of the likelihood
M	logarithm of the prior
$p(\cdot)$	probability
$p(\cdot \cdot)$	conditional probability
\mathbb{G}	set of gray matter voxels
\mathbb{W}	set of white matter voxels
\mathbb{C}	set of cerebrospinal fluid voxels
\mathbb{B}	set of brain voxels
f	tissue fraction
N_j	neighborhood of j
\mathcal{P}	projection operator
\mathcal{B}	back-projection operator
\mathcal{R}	Radon transformation
\mathcal{F}	Fourier transformation
\mathcal{F}^{-1}	inverse Fourier transformation

Contents

Acknowledgements	i
Abstract	iii
Samenvatting	v
Acronyms	xvii
Symbols	xix
1 General introduction	1
1.1 Epilepsy and Seizures	1
1.2 Presurgical Evaluation of Refractory Partial Epilepsy	3
1.3 Purpose of this Work	6
1.4 Organization of this Thesis	7
2 Emission Tomography	9
2.1 Introduction	9
2.2 Radionuclides and Tracers	10
2.2.1 Statistical Description of Radioactive Decay	10
2.2.2 Radioactive Decay Modes	11
2.2.3 Tracer Distribution	12
2.3 Data Acquisition	12
2.3.1 Gamma Ray Detection	12
2.3.2 Resolution and Sensitivity	13
2.3.3 Attenuation and Scatter	17
2.4 Image Reconstruction	18
2.4.1 Analytical Reconstruction	18

2.4.2	Digital Image Representation and System Modeling	23
2.4.3	Statistical Reconstruction	27
2.5	Conclusion	33
3	Partial Volume Correction in Emission Tomography	35
3.1	Image Degrading Effects	35
3.2	Partial Volume and Spill-Over Effect	36
3.2.1	Origin of the Effects	36
3.2.2	Consequences for Clinical Decision Making	38
3.3	Partial Volume Correction	39
3.3.1	Rationale	39
3.3.2	Post-Processing Methods	40
3.3.3	Statistical Techniques	43
3.3.4	Discussion	50
3.4	Anatomy Based MAP Reconstruction	51
3.4.1	Assumptions	51
3.4.2	Derivation of A-MAP	52
3.4.3	Proof-of-Principle: A-MAP and PVC	58
3.5	Discussion	60
3.6	Conclusion	63
4	Evaluation of the A-MAP Reconstruction Algorithm	65
4.1	Introduction	65
4.2	Materials and Methods	66
4.2.1	2-D Phantom Simulation Experiments	66
4.2.1.1	Use of Perfect and Imperfect Anatomical Information	67
4.2.1.2	Evaluation measures	68
4.2.2	3-D Phantom Simulation Experiments	69
4.2.2.1	Influence of Anatomical Prior Weight	70
4.2.2.2	Effect of Small Misalignments	70
4.2.2.3	Effect of Segmentation Errors	70
4.2.2.4	Evaluation Measures	71
4.2.3	Human Observer Study	72
4.2.4	Patient Study	74
4.3	Results	75
4.3.1	2-D Phantom Simulation Experiments	75
4.3.1.1	Perfect Anatomical Information	75
4.3.1.2	Imperfect Anatomical Information	76
4.3.2	3-D Phantom Simulation Experiments	80
4.3.2.1	Influence of Anatomical Prior Weight	80

4.3.2.2 Effect of Small Misalignments	82
4.3.2.3 Effect of Segmentation Errors	83
4.3.3 Human Observer Study	85
4.3.4 Patient Study	87
4.4 Discussion	87
4.4.1 2-D Phantom Simulation Experiments	87
4.4.2 3-D Phantom Simulation Experiments	88
4.4.3 Registration and Segmentation Errors	90
4.4.4 Detection of Hypometabolic Regions	90
4.4.5 Clinical Application	93
4.5 Conclusion	93
5 Excess Height and Cluster Extent in Subtraction SPECT	95
5.1 Introduction	95
5.2 Materials and Methods	97
5.2.1 Distribution of Cluster Extent and Excess Height	97
5.2.2 Simulation Experiments	100
5.3 Results	101
5.3.1 Cumulative Distribution Functions	101
5.3.2 Simulation Experiments	102
5.4 Discussion	103
5.5 Conclusion	106
6 Noise Suppression and PVC in Subtraction SPECT	107
6.1 Introduction	107
6.2 Materials and Methods	107
6.2.1 Simulation Experiments	108
6.2.2 Subtraction and Cluster Analysis	110
6.3 Results	111
6.3.1 Cumulative Distribution Functions	111
6.3.2 Cluster Analysis	111
6.4 Discussion	112
6.5 Conclusion	118
7 General Conclusion	119
7.1 Main Contributions	119
7.2 Suggestions for Future Research	121
A Appendix	125
A.1 Proof of Concavity	125
A.2 Implementation of the A-MAP Reconstruction Algorithm	128

References	131
Publications	141
Curriculum Vitae	145

General introduction

If the patient's fits are local, frequently recur, and are always similarly localized, it is surely a necessary inference that there is some local disease in his nervous system . . . Local symptoms must of necessity depend on local lesions."

JOHN HUGHLINGS JACKSON
(1835–1911)
[Jackson, 1931]

1.1 Epilepsy and Seizures

Epilepsy refers to a class of disorders which can be defined as chronic neurological conditions that are characterized by recurrent manifestations of epileptic seizures [Engel, 1995]. Epilepsy is diagnosed, by convention, when a person experienced at least two unprovoked seizures [Brodie *et al.*, 2003a]. *Epileptic seizures* are the clinical manifestations of sudden, abnormal, excessive, and synchronized electrical discharges of a population of neurons in one or more locations of the cortical gray matter (GM) [Westbrook, 2000]. The clinical manifestations may vary and depend on the location where the electrical discharges originate, how far they spread, and how long they last. A whole variety of symptoms may occur, such as the loss of consciousness, disturbances of movement, sensation, including vision, hearing and taste, mood, or mental function. The duration and severity of seizures may also vary from very brief lapses of attention or muscle jerks, to severe and prolonged convulsions. They may also vary in frequency, from less than one a year, up to several seizures per day. In recent years, progress has been made in the diagnosis and treatment of seizure disorders. However, a thorough understanding of the

cellular and molecular mechanisms by which seizures may or may not develop is still far from being complete [Chang and Lowenstein, 2003].

Many different types of epileptic seizures have been observed. Therefore, the International League Against Epilepsy (ILAE) introduced the International Classification of Epileptic Seizures (ICES), which considers both the clinical semiology as well as electroencephalography (EEG) findings of the seizures [ILAE, 1981].

The main distinction between seizure types is that of *partial* versus *generalized* seizures. Partial seizures, on the one hand, start in a circumscribed set of neurons, i.e. the *epileptic focus*, in one hemisphere of the brain, and spread from there. Generalized seizures, on the other hand, involve both sides of the brain from the seizure onset. However, this subdivision does not completely represent all the different conditions and states that constitute epileptic seizures. Therefore, further distinctions are made on the basis of the signs or symptoms associated with the seizure. Another distinguishing feature is whether or not the seizure is associated with impairment of consciousness. Partial seizures, for example, are further subdivided into *simple partial seizures*, in which consciousness is not impaired, *complex partial* seizures, in which there is impairment of consciousness, often combined with automatisms, and *secondarily generalized partial* seizures, e.g. generalized tonic-clonic seizures. Seizures may be isolated events, or they may occur in series. Repeated seizures, where one seizure cannot be separated from the next episode, or where consciousness is not regained between two consecutive seizures, are called *status epilepticus*. This condition may be life-threatening.

The classification of seizure types does not completely represent all different conditions and states that constitute epilepsy. Therefore, many different *epileptic syndromes*, which are a cluster of signs and symptoms that occur together, have been described. Some epileptic syndromes share a common cause, and may be grouped together as distinct *epilepsies*. These epileptic syndromes have been classified to guide treatment and determine the prognosis of the patient [ILAE, 1989].

The main distinction between epileptic syndromes, which is similar to that of epileptic seizures, is that of *generalized* versus *location-related* epilepsies. Generalized epilepsies are characterized by seizures originating in both hemispheres. In location-related epilepsies, all seizures have a focal onset. The location of the focus strongly influences the clinical appearance of the patient. A second subdivision is that of *symptomatic* versus *idiopathic* epilepsies. Symptomatic epilepsies are due to a recognizable insult to the brain, e.g. a malformation, trauma, or tumor. In idiopathic epilepsies, which are commonly caused by a genetic defect, the epilepsy itself is the primary disorder [Berkovic and Scheffer, 2001]. When a symptomatic cause is suspected, but cannot be demonstrated, the conditions are referred to as *cryptogenic* epilepsies. There is also a subdivision into *active* and *inactive* epilepsy, with active epilepsy being defined as two or more epileptic seizures in the last five years that have been unprovoked by any immediate identified cause.

An ILAE Task Force on classification and terminology was appointed to recommend revision of the classification [Engel, 1998]. Currently, the Task Force considers the development of specific classifications as a continuing work in progress and has the intention to report on a periodic basis.

During the last few decades, epilepsy has been given an increased amount of attention. In 1997, the ILAE, the International Bureau for Epilepsy (IBE), and the World Health Organization (WHO) joined forces and established a *Global Campaign Against Epilepsy*. The initiative aims at improving prevention, treatment, care, and services for people with epilepsy, and raise public awareness about the disorder. In 1998, the *European Concerted Action and Research in Epilepsy* was founded and has become a joint initiative of the ILAE and IBE. Both initiatives have stimulated ongoing research in the diagnosis and treatment of epilepsy.

Epilepsy and epileptic seizures can be traced back as far as medical records exist, in all civilizations, without any racial, geographical, or social boundaries. Epilepsy is known to occur in men and women, and can begin at any age. However, it is most frequently diagnosed in infancy, childhood, adolescence, and in elderly people. Anyone can be affected by epileptic seizures. In fact, up to 5% of the world's population may have a single seizure at some time in life.

The need for medical attention and the diagnosis of epilepsy is primarily reserved for those who have recurring seizures. It has been estimated that the mean prevalence of epilepsy patients who need medical treatment is approximately 8.2 per 1000 people of the general population [WHO, 2005]. It is likely that around 50 million people in the world have epilepsy at any one time. After the first seizure, about 80 % of these patients experience another seizure within the first three years following the first seizure. For about 70 % of these patients, epilepsy will disappear spontaneously after some time. Flanders counts about 6 million habitants. About 30 000 people have active epilepsy, and about 3000 will develop epilepsy each year. Of these 3000 new epilepsy patients, about 900 will not respond to any of the currently available drug treatment programs.

When seizures are considered to be intractable, the evaluation and further medical treatment of the patient should be supervised by a neurologist in a specialized epilepsy reference center. A number of these epilepsy reference centers have been recognized by the government and can offer the required diagnostic equipment and specialized services for treatment. The options of treatment which are left for these patients are the inclusion in clinical trials for the evaluation of new anti-epileptic drugs, implantation of a nervus vagus stimulator, a ketogenic diet, or epilepsy surgery [Brodie *et al.*, 2003b]. About one third of the patients with refractory epilepsy would eventually be admitted for neurosurgical treatment after successful completion of an extensive presurgical evaluation procedure. However, currently only one third of that number of patients are actually treated. Surgical treatment of refractory epilepsy has shown to be cost-effective [Platt and Sperling, 2002]. Long-term expenses associated with epilepsy surgery compare favorably with those generated by medical drug treatment.

1.2 Presurgical Evaluation of Refractory Partial Epilepsy

The presurgical evaluation of patients with refractory partial epilepsy has the aim to determine whether the patient has a single epileptogenic focus which gives rise to

partial seizures, and to provide an accurate localization of the epileptogenic focus inside the brain. If the epileptogenic focus is not located in the eloquent cortex, i.e. that region of the cortex that is indispensable for defined cortical functions, the epileptogenic focus may be outlined as a candidate for surgical resection without causing unacceptable neurological deficits [Rosenow and Lüders, 2001]. Because brain surgery is a delicate procedure, multiple examinations are conducted in order to delineate the *epileptogenic zone* as accurately as possible. By definition, the total removal or disconnection of the epileptogenic zone is a necessary requirement in order to render the patient seizure free. Actually, the prognosis of curative epilepsy surgery is largely determined by the resection of a lesion which proves to be pathological after surgery, the nature of the epileptic lesion, and the completeness of the resection. Moreover, surgical therapy has shown to be a cost-effective treatment [Platt and Sperling, 2002]. Surgery renders between 70 to 80 % of the treated refractory partial epilepsy patients seizure free. Epilepsy surgery is not only the best therapy for many patients, it is also the cheapest one for society. Long-term expenses associated with the surgical treatment compare favorably with those incurred by medical treatment.

The first stage of the presurgical evaluation procedure starts by obtaining detailed descriptions of typical seizures. Clinical and physical neurological examinations are conducted by a neurologist, and routine scalp electroencephalography (EEG) measurements are performed. Furthermore, high-resolution magnetic resonance imaging (MRI) of the brain is used to assess the possibility of structural abnormalities. It has been shown that a high sensitivity and specificity for the detection of epileptogenic lesion is reached when MRI protocols make use of T1-weighted thin-slice volumetric, T2-weighted FLAIR (fluid attenuation inversion recovery), and T2-weighted spin echo sequences [Duncan, 1997, 2002; Knowlton, 2004]. The results obtained by all these examinations can show at this stage whether epilepsy surgery will give benefit to the condition of the patient. If so, the patient is invited for an extension of the presurgical evaluation procedure.

The second stage of presurgical evaluation involves video-EEG monitoring of the patient over a longer period. The goal is to record a number of typical seizure events. Video-EEG monitoring allows adequate observation, not only of seizures, but also of the simultaneous EEG recordings. Thereby, it may be possible to draw some conclusions regarding the lateralization and localization of the ictal onset zone [Siegel, 2004]. The condition of the patient during a seizure is referred to as the *ictal* state, in between seizures the condition is referred to as the *interictal* state. The clinical manifestation of a seizure as seen on the video capturing is also of important localizing value. For example, a patient with temporal lobe epilepsy may show to have an epigastric aura, followed by a quiet period of unresponsiveness, with staring, picking at sheets or clothes, presenting manual automatisms, contralateral dystonic posturing, and postictal confusion. If the seizure originates from the dominant brain hemisphere, there is usually delayed recovery of language, often combined with transient aphasia.

Video-EEG can be easily performed in combination with ictal single photon emission computed tomography (SPECT) of the cerebral blood flow (CBF). Ictal

SPECT has the potential to localize the ictal-onset zone accurately in a noninvasive manner. SPECT usually reveals a region of ictal hyper-perfusion at the site of seizure onset. Tracers that are commonly used are ^{99m}Tc -hexamethylpropylene-amine oxime (HMPAO) and ^{99m}Tc -ethyl cysteinate dimer (ECD). These neutral and lipophilic compounds cross the blood-brain barrier and are subsequently hydrolyzed and therefore trapped in the cell. The accumulation of the tracer molecules in the cell depends on the amount of blood supply, thereby reflecting the local CBF. SPECT can then show the distribution of the radioactive labeled tracer molecules. The success of the imaging technique, however, depends for a large part on the timing of tracer injection. Early ictal SPECT injections minimize the problem of seizure propagation and of non-localization due to an early switch from ictal hyper-perfusion to postictal hypo-perfusion during brief seizures [Van Paesschen, 2004]. Seizure propagation may occur when there is sufficient activation to recruit surrounding neurons, leading to a loss of surround inhibition and spread of the seizure activity. For that reason, the radioactive tracer should be available in the patient room, and the injection system should allow for fast ictal injections, based on signs or symptoms shown by the video-EEG.

At another moment in between seizures, the patient is invited for interictal SPECT imaging of the CBF. Interictal SPECT, which may show epileptogenic regions as having reduced CBF, is less useful for the localization of the epileptogenic region [Duncan, 1997]. However, in combination with the ictal SPECT data, it allows to perform subtraction of the ictal and interictal SPECT images, and spatially align the obtained differences to MRI data. This technique, which is called *subtraction ictal SPECT co-registered to MRI* (SISCOM), allows for the localization of the seizure-onset and propagation zone [Cascino, 2001; O'Brien *et al.*, 1998a, 2000, 1998b, 1999].

Also in between seizures, one can measure the regional cerebral glucose metabolism using positron emission tomography (PET). For that purpose, the radiopharmaceutical 2-[^{18}F]fluoro-2-deoxy-D-glucose (FDG) is used. FDG, an analogue of glucose in which a hydroxyl-group is replaced by a positron emitting fluor atom, is picked up by the cell by facilitated diffusion through the glucose transporters. In the cell, FDG is metabolized by hexokinase into FDG-6-phosphate, which is not further metabolized. FDG-6-phosphate cannot leave the cell by diffusion and it is very slowly hydrolyzed. Hence, the intracellular concentration of FDG-6-phosphate will be proportional to the intensity of the glucose transport and the activity of hexokinase. The concentration of FDG-6-phosphate, i.e. proportional to the ^{18}F concentration, reflects the regional glucose metabolism. Interictal FDG-PET may reveal areas of reduced glucose metabolism [Casse *et al.*, 2002; Kuhl *et al.*, 1980]. These areas usually include the epileptogenic region, however that may not always be the case [Duncan, 1997; Engel *et al.*, 1990; Henry, 1996; Salmenpera and Duncan, 2005]. The use of the statistical parametric mapping (SPM) technique, on the other hand, has shown to improve the diagnostic yield of interictal FDG-PET [Lee *et al.*, 2001; Signorini *et al.*, 1999; Van Bogaert *et al.*, 2000].

When suspected epileptogenic foci are found close to some *eloquent* cortical regions, physicians may choose to perform functional MRI in order to assess the

potential risk of removing these lesions. Functional MRI can detect focal changes in blood flow and oxygenation levels that occur when an area of the brain is activated. It allows for mapping of motor, sensory, and language functions in a noninvasive manner. Once the information is gathered, a better understanding of the cortical functions can guide the further presurgical evaluation.

If noninvasive presurgical evaluation procedures have failed, or if they have found to be inadequate to define the epileptogenic zone reliably, one might try to use more invasive diagnostic procedures. Two of such methods are *depth electrodes* and *subdural electrodes*. Both techniques measure the intracranial EEG over a longer period [Zumsteg and Wieser, 2000]. Depth electrodes are thin cables with cylindrical contacts that are surgically inserted into the brain. This technique can help to distinguish, for example, medial from lateral seizure onset, or rapid seizure propagation. Subdural electrodes, on the other hand, are used to record from the cortical surface of the brain and consist of multiple electrodes placed in grids or strips on a thin sheet of plastic. The electrodes can be used to record the area of seizure onset, as well as allow for electrical stimulation of some important cortical functions in the neighborhood of suspected epileptogenic regions.

The results which have been obtained after all presurgical examinations are systematically discussed in a joint session of supervising neurologists, and all involved experts, such as neuropsychologists, nuclear medicine physicians, radiologists, neurosurgeons, ... The patient is then offered the possibility for curative surgical treatment only when the results are concordant and suggest a single focal epileptogenic lesion that is amenable for surgical resection.

In a number of patients, the epileptogenic zone cannot be identified, or it may be located in a precarious part of the brain. Patients who are unsuitable candidates for curative surgery, or who have experienced insufficient benefit from such treatment, might be helped with vagal nerve stimulation. This technique involves electrical stimulation of the left vagal nerve in the neck which is used to reduce the frequency and severity of the seizures [Henry, 2002]. The technique is based on animal experiments in which EEG de-synchronization has been shown when the vagal nerve was electrically stimulated [Bailey and Bremer, 1938].

1.3 Purpose of this Work

The main goal of this work was to contribute to the improvement of emission tomography techniques that are used for the presurgical evaluation of patients with refractory partial epilepsy. Actually, this work is only one aspect of a much larger research project which has the aim to construct a multidisciplinary epilepsy surgery unit by optimizing and implementing new imaging and image processing techniques (EEG, MRI, PET, and SPECT) for the accurate and non-invasive delineation of epileptogenic lesions and zones in patients with refractory partial epilepsy.

In the current clinical settings, the applied nuclear medicine imaging modalities are FDG-PET of the cerebral glucose metabolism, and ECD-SPECT of the cerebral blood flow. The techniques play an important role in the detection and localization

of suspected epileptogenic regions. However, the quality and quantitative accuracy of these images may have an influence on the detection performance.

Emission tomography can measure the spatial distribution of a radioactive labeled substance *in vivo*, for which it makes use of specialized radiation detection equipment. After the acquisition step, the measured data have to be reconstructed in order to be presentable to the observer. In each of the steps involved in the image formation process, i.e. from the acquisition to the displaying of images, the quality of the data may be affected. In this work, we aim primarily at reducing the influence of image degrading effects that may be produced during the reconstruction of the acquired emission data.

The spatial sampling and the resolving power are two important characteristic features of any imaging system. The spatial resolution achieved by emission tomography is, in general, much worse than that of other medical imaging modalities, such as e.g. high-resolution MRI. The limited resolution of the system spreads out the intensity of the signal and leads to a signal averaging described by the (local) point spread function. This effect in combination with the digital sampling of the signal, which leads to a certain loss of information, is referred to as the *partial volume effect* [Hoffman *et al.*, 1979]. This effect is most prominent for structures having dimensions that are relatively small in comparison to the resolution and spatial sampling frequency of emission tomography imaging systems. Unfortunately, this is the case for the cortical thickness of the human brain [Fischl and Dale, 2000]. As consequence of the partial volume effect, the intensity of the signal in these areas of the brain will be decreased. For the presurgical evaluation of epilepsy patients, this effect can pose problems for the detection of epileptogenic regions which are normally shown as, for example, hypometabolic regions on interictal FDG-PET. The purpose of this work is to develop a partial volume correction technique which helps differentiating between true and false hypo-intensity regions.

The influence of Poisson noise is an unavoidable component of uncertainty during the measurement of radiation in emission tomography. Unfortunately, the noise contained by the measurement can have a considerable effect on the final image quality. The problem occurs when, during image reconstruction, a significant amount of noise is transferred from the measurement to the reconstructed images. In the subtraction analysis of ictal and interictal SPECT, which forms the basis of the SISCOM technique, the influence of noise may lead to spurious differences that may look similar to those obtained by pathological or normal physiological changes. Furthermore, noise induced differences can make the visual assessment of SISCOM data more difficult. The purpose of this work is to aid the physician and provide more information about the significance of the differences on SISCOM.

1.4 Organization of this Thesis

In this chapter, we situated the purpose of this work into the broader context of medical imaging, and more specific into the field of presurgical evaluation of patients with refractory partial epilepsy in emission tomography.

An overview of the different steps that are needed for performing emission tomography are given in Chapter 2. The purpose of that chapter is to explain the terminology used in the following chapters. We describe the role of radionuclides and tracer molecules for measuring physiological processes in living organisms. Next, we explain the data acquisition procedure for SPECT and PET, including some aspects which may have an influence on image quality and quantitative accuracy in these modalities. Thereafter, we discuss the reconstruction of the acquired emission data. In the first place, we present the analytical reconstruction approach. A transition is made towards statistical reconstruction techniques after an intermediate section which discusses some aspects of digital image representation and system modeling.

In Chapter 3, we discuss the influence of a number of image degrading effects. We focus on the partial volume and spill-over effect as two problems of special importance for emission tomography of the human brain. The origin of these effects is discussed, as well as the consequences for the clinical decision making. A number of partial volume correction techniques that have been developed and published in literature are presented and discussed. A new statistical reconstruction algorithm, in which anatomical information is used to correct for the partial volume effect, is proposed and the mathematical derivation of the algorithm is given. We illustrate the partial volume correction properties of the new reconstruction method using a proof-of-principle experiment. In Chapter 4, we present a thorough evaluation and validation analysis of the proposed method using 2-D and 3-D computer simulation experiments. A human observer study is performed and the new algorithm is applied to clinical FDG-PET data of a patient with known refractory temporal lobe epilepsy.

The effect of noise on the subtraction analysis of simulated ictal and interictal SPECT data is studied in Chapter 5. We propose a method which allows for the characterization of supra-threshold clusters in subtraction SPECT images by means of two parameters. The behavior of these two parameters is assessed under the influence of noise, and this information is used to define significance levels for each parameter. The observer may then choose to retain only those differences that are found to be significant for that parameter. It is expected that this method will help physicians during the inspection of SISCOM data. We also compare the performance of each parameter to the other for the detection of induced clusters. The reconstruction method and noise suppression settings are fixed during this investigation.

In Chapter 6, we investigate the influence of the reconstruction method and noise suppression technique on the behavior of the cluster parameters in the subtraction analysis of simulated ictal and interictal SPECT data. Three reconstruction methods are compared, including the new reconstruction algorithm in which anatomical information is used to correct for the partial volume effect. We also assess the influence of the strength of the noise suppression technique in each reconstruction method. In that way, all techniques which have been developed in previous chapters of this work are combined and evaluated. A general conclusion of this work is given in Chapter 7.

Chapter 2

Emission Tomography

2.1 Introduction

Emission tomography is a non-invasive nuclear medicine imaging modality which provides cross-sectional images of the spatial distribution of a radioactive labeled substance that has been administered to the subject.

The World Health Organization has defined *nuclear medicine* as *that speciality which embraces all applications of radioactive materials in the diagnosis, treatment, or in medical research, with the exception of the use of sealed radiation sources in radiotherapy* [WHO, TRS-492]. The success of nuclear medicine depends largely on its multidisciplinary nature, bringing together the skills of physicians, nurses, technologists, pharmacists, engineers, and physicists. The complementary role of these various specialist groups has led to the successful introduction and routine clinical use of a broad range of nuclear medicine imaging and measurement techniques.

The aim of emission tomography is to measure physiological processes in living organisms. The techniques that are used differ from traditional radiology procedures, where radiation is applied from an external source. Here, a radioactive substance is administered to the subject. Usually this is done by means of an intravenous injection. The radioactive substance is chosen such that it interacts, participates, or competes in some way with the physiological process that has to be investigated, while the radioactive property of the substance makes it possible to measure the spatial distribution of the molecule *in vivo*. The administered substance is often referred to as the *tracer molecule*, or for short, *tracer*.

In the following sections, we will look deeper into the properties of the radionuclides and tracers, the data acquisition procedure, and finally, the image formation in emission tomography.

2.2 Radionuclides and Tracers

Radioactive nuclides or *radionuclides* are atoms of which the nuclear configuration is energetically unfavorable to remain stable. As a result, the radionuclide is committed to change its configuration. It will do that by means of a *disintegration process*. All kinds of disintegrations are characterized by an amount of energy that is released during the process, the speed of the process, and the type of particles or energy quanta that are emitted. The disintegration process is usually referred to as the *decay* of the radionuclide. The parameter that is most often used for the speed of decay is the *half-life*, which is denoted $T_{1/2}$, and defined as the expected time it takes to decay half of the members of a large sample of radionuclides of a given kind.

2.2.1 Statistical Description of Radioactive Decay

Decay is a statistical one-shot process. When one particular nucleus has decayed, it cannot repeat the same process again. As long as the nucleus has not decayed, the probability for it doing so during the next time interval dt remains constant for each radionuclide. The probability is defined as the *decay constant* α [h^{-1}]. This constant is related to the physical half-life of the radionuclide $T_{1/2} = \ln 2/\alpha$. The number of atoms dn that are expected to have been decayed over dt is

$$\frac{dn}{dt} = -\alpha n. \quad (2.1)$$

It follows that the amount decreases exponentially over time. Given n_0 radionuclides at $t = 0$, the expected amount after a time interval Δt is

$$n = n_0 e^{-\alpha \Delta t}. \quad (2.2)$$

The number of disintegrations per second dn/dt is the *activity*, the units are expressed in Becquerel [Bq]. Due to the statistical nature of decay, the observation of it is subject to statistical uncertainty. If the count rate of observed events $r = \bar{n}/\Delta t$ remains constant during the observation period Δt , then, the probability to observe n events is given by the Poisson probability

$$P_n = \frac{\bar{n}^n}{n!} e^{-\bar{n}}, \quad (2.3)$$

where \bar{n} represents the mean number of events. The first moment $\sum_n n P_n$ of the Poisson distribution gives the expected value, i.e. the mean number of events \bar{n} . The variance of the distribution $\sigma^2 = \sum_n (n - \bar{n})^2 P_n$ is also \bar{n} , which means that the standard deviation of the distribution $\sigma = \sqrt{\bar{n}}$. The Poisson probability is only valid for observations that are relatively short compared to the half-life of the radionuclide. For a changing count rate during the observation, i.e. $r(t)$, one should replace \bar{n} by the mean count rate \bar{r} times the observation time Δt .

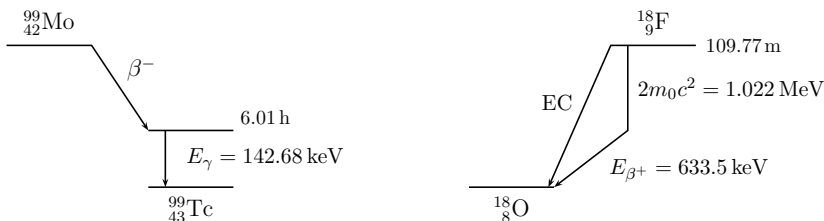


Figure 2.1: The left figure shows the decay scheme of $^{99m}_{43}\text{Tc}$ by means of isomeric transition. The right figure shows the decay scheme of $^{18}_{9}\text{F}$ which disintegrates by electron capture and by β^+ decay. Source: [Ekström and Firestone \[2004\]](#).

2.2.2 Radioactive Decay Modes

There are a variety of ways in which radionuclides can emit their excess of energy. In general, the different ways are subdivided into: (a) the emission of neutral, positive, or negative charged particles, and (b) the emission of electromagnetic radiation. For diagnostic imaging in nuclear medicine, electromagnetic radiation emitting radionuclides are preferred for a number of reasons. First of all, the electromagnetic radiation is used to find out the location of the radioactive labeled tracer molecule in the subject. Electromagnetic radiation of a sufficient high energy is expected to leave the subject, as opposed to particle emitting radionuclides. Secondly, particles give much larger energy depositions which in turn leads to an increased radiation dose that is attributed to the subject. The nuclear decay modes that are relevant for the remainder of this dissertation are summarized hereafter.

- β^- decay: a neutron is transformed into a proton and an electron, or β^- particle, and an anti-neutrino is created.
- electron capture (EC): an orbital electron is captured, combined with a proton, and transformed into a neutron and a neutrino. The electron vacancy can be filled up by other electrons, thereby emitting characteristic X-rays.
- β^+ decay: a proton is transformed into a neutron, a positron, and a neutrino. When a positron is slowed down in matter, it will eventually pair with an electron. The system exists for a short while as a *positronium* and subsequently de-excites itself by the emission of two photons, each of 511 keV. An example of a radionuclide which disintegrates by both EC (3.27 %) and β^+ decay (96.73 %) is ^{18}F . The decay scheme of ^{18}F is shown in Fig. 2.1.
- Very often β^- , β^+ decay or EC leaves the daughter nucleus in an excited state, in which case electromagnetic de-excitation of the nucleus brings a more stable configuration. The excess energy is released as one or more gamma ray photons. The daughter nucleus may be in a more stable, i.e. *metastable* or *isomeric* state, characterized by a longer half-life. ^{99m}Tc is an example of this decay mode, and probably the most important radionuclide used in nuclear medicine. The decay scheme of ^{99m}Tc is shown in Fig. 2.1.

2.2.3 Tracer Distribution

The spatial distribution of tracer molecules inside the body is continuously influenced over time by blood flow, physiology, metabolism, ..., and this immediately after the individual has been injected with the radioactive labeled substance. Let $\vec{x}_k(t)$ be the position of tracer molecule k at time t , when a number of tracer molecules have been administered to a subject at the time of injection t_0 . Then, the locations of the individual tracer molecules at any time post-injection $t > t_0$ are independent random variables, identically distributed according to a common probability density function (PDF) $p_t(\vec{x})$. This PDF is determined by the characteristic properties of both the individual (e.g. blood flow, physiology, ...) as well as that of the tracer molecule (e.g. chemical properties). What is being measured by the imaging equipment, is actually a sample from the probability distribution. Moreover, the ultimate goal of emission tomography is not to know the exact location of all tracer atoms at all times post-injection, which is an impossible task, but rather to obtain the PDF of the tracer molecules over time. Unfortunately, we cannot observe the PDF. We can only observe tracer atoms when they disintegrate, and even then, we observe only a fraction of all events, since most are not recorded.

2.3 Data Acquisition

2.3.1 Gamma Ray Detection

The preferred and most efficient way to detect photons is through photo-electric absorption. Although there are different types of gamma ray detectors, the current standard that is used in nuclear medicine is the *scintillation detector*. This type of detector consists of a *scintillation crystal* onto which a *photomultiplier tube* (PMT) is attached. The scintillation crystal is designed such that the energy of an incoming gamma ray photon is absorbed by the material in the form of kinetic energy of one or more electrons, depending on the type and number of interactions. These electrons are able to excite other electrons to the conduction band of the crystal lattice. These excited electrons can be captured by an impurity, i.e. the activator, and cause subsequent de-excitations leading to the emission of visible light, i.e. photons of a few electronvolt (eV). These photons are guided towards the PMT through optical coupling, converted to electrons by means of a photocathode, and the electrons subsequently amplified through a series of dynodes. The final PMT output is an electrical current which is proportional to the energy of the incoming gamma ray photon.

For planar imaging and tomography, it is required to measure the spatial location of detection events on the detector surface. For that purpose, the scintillation detector has been extended to two dimensions. In general, there are two 2-D scintillation detector extensions. These configurations form the basis of two emission tomography sub-modalities, that are (a) *single photon emission computed tomography* or *SPECT*, and (b) *positron emission tomography* or *PET*. The main difference

between both techniques is that PET is designed to measure positron-electron annihilation photons by means of coincidence detection, while SPECT is designed to measure single events.

- The first extension of the scintillation detector consists of a single large planar crystal of which one side is covered by many PMT's. The position of an event is expected to be the barycenter of the light output seen by all PMT's over the scintillation duration. The energy of the event is related to the integral output of all PMT's. This design is known as the *single crystal detector* and it is mostly used for the construction of a SPECT camera. This camera consists of a detector head that contains a planar scintillation detector. The head is held by the gantry which is able to perform a rotation around the object, and retract or bring the head closer to the object. For reasons of efficiency, systems have been designed that contain two or three heads.
- The second extension consists of a (small) crystal with a few PMT's. The position of a detection event is that of the scintillating crystal unit and the energy is proportional to the integral output of all contributing PMT's. This design is known as the *multi-crystal* or *block detector* and it is mostly used for the construction of a PET camera. The camera consists of many block detectors, which are positioned side by side in a circular ring. A number of rings are usually stacked next to each other such that a reasonable axial field of view is achieved.

The scintillation detector configuration is the first step towards medical imaging in emission tomography. It makes it possible to detect gamma ray photons. However, it's not the only step. The object that is being imaged also needs to be resolved properly. For that purpose, the detector configuration needs to be adjusted such that it becomes possible to resolve the object that is being imaged.

2.3.2 Resolution and Sensitivity

A single or multi-crystal detector has a finite *intrinsic spatial resolution* for the detection of incoming photons which depends on a number of parameters, like e.g. the crystal composition, thickness and geometry. The intrinsic spatial resolution is often approximated by a Gaussian point spread function (PSF) and represented by the variance $\sigma_{\text{intr.}}^2$. However, suppose that the spatial location and energy of a detection event could be measured with an infinite precision, that does not mean that the detector has the ability to bring the object, from which the radiation is coming, *into focus*. For that purpose, knowledge about the trajectory of the incoming radiation is required. Fortunately, there are a few techniques that can retrieve this kind of information. In practice, however, none of the following techniques are perfect in their performance.

- A *collimator* is put in front of the scintillation detector such that radiation with a specific direction is allowed to enter the detector, while gamma ray photons along other directions are absorbed by the collimator material. The collimator actually narrows down the trajectories of the incoming gamma

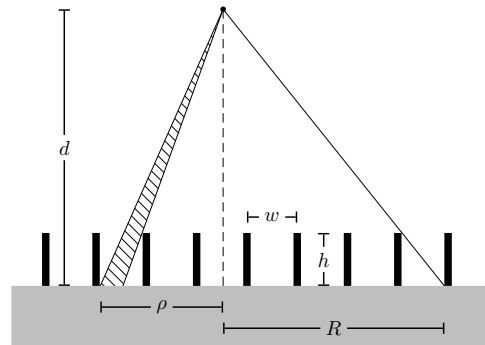


Figure 2.2: A schematic drawing of a parallel hole collimator is shown. The gray frame represents the scintillation crystal. In real parallel hole collimators, the height of the septa h are larger than the space w in between them, or $h \gg w$. All other variables are explained in the text.

ray photons. Unfortunately, this method has the disadvantage to reduce the sensitivity of the detector significantly. Moreover, no information about the origin of the radiation is gained. This technique is used in planar imaging and SPECT.

- An attractive property of positron-electron annihilation is the creation of two photons which are emitted in almost opposite directions. If two events are detected almost simultaneously in two detectors at opposing sides of an object, one can reasonably assume that the annihilation has occurred somewhere along the line that connects both detectors. This technique is used in PET.
- For radiation originating from a point source with a well known spatial location, the direction of the detection events is obvious. The detected events provide information about the total attenuation along the trajectory. This principle is used in transmission tomography, and it is the only technique that provides reasonably accurate information about the attenuation along a line through an object.

Before looking into more detail to the spatial resolution properties of SPECT and PET, we should mention that the temporal resolution of emission tomography is in general very poor. As shown in §2.2.3, if the PDF $p_t(\vec{x})$ describes the distribution of the tracer molecules at any time t post-injection, then, due to the temporal resolution properties of the detection system, one does not really observe samples of $p_t(\vec{x})$, but rather $\int_{\Delta t} p_t(\vec{x}) dt$, where Δt is the usually long duration of a single acquisition procedure. Moreover, if the tracer molecule distribution should change during the acquisition sequence, this will lead to an unavoidable loss of resolution. Ultimately, even if all hardware and software would perform under optimal conditions, patient movement could destroy much of the effort.

SPECT

Consider the use of a *parallel hole collimator* which is the most frequently used type of collimator for performing SPECT. A schematic drawing of such collimator is shown in Fig. 2.2. The finite spacing w and height $h \gg w$ of the septa influence the collimator resolution at a distance. We illustrate this property in 1-D using a simplified detector model. A point source is located at a distance $d \gg h$ from the

Collimator type	Resolution at 10 cm	Sensitivity cps/MBq
LEHR	8.2 mm	110
LEUHR	7.0 mm	70

Table 2.1: Specifications of two parallel hole collimators that are used in daily clinical practice: LEHR = Low-energy high resolution, and LEUHR = Low-energy ultra-high resolution. Sensitivity is expressed in counts per second per mega-becquerel (cps/MBq). Source: user manual of the Triad XLT scanner, Trionix, Twinsburg, Ohio, USA.

detector. The projection of this point perpendicular on the detector is the origin of a distance measure along the detector ρ . Assume that the septa are infinitely thin, the collimator material is totally absorbing photons, and the influence of scatter and noise are neglected. Then, the fraction of the detector between two neighboring septa, i.e. between ρ and $\rho - w$, exposed to the point source, is equal to

$$f(\rho) = 1 - \frac{\rho h}{wd}. \quad (2.4)$$

This expression holds for $0 < \rho < R$, where $R = wd/h$ is the position at which the shadow of the septa cover the detector completely. Because $\rho \ll d$, the *point spread function* (PSF) of the collimated detector, can be approximated by

$$\text{PSF}(\rho) = \frac{f(\rho)}{4\pi d^2}. \quad (2.5)$$

Consequently, the PSF has a triangular profile and the resolution of the collimator can be expressed by the *full-width at half-maximum* of the PSF, which is $\text{FWHM}(d) = wd/h$. This means that, for optimal resolution performance, the distance between the detector and the object should be kept as small as possible. Smaller spacing between septa will improve the resolution, however they will also decrease the sensitivity of the collimator. The ideal collimator should have both high resolution and high sensitivity. Thus, for each imaging protocol, a collimator should be chosen that gives a good trade-off between resolution and sensitivity (Table 2.1).

The total spatial resolution of the detector, i.e. the combination of collimator, crystal and PMT's, is given by the combination of the intrinsic and collimator resolution. If the spatial resolution of the detector is approximated by a Gaussian PSF, the variance is given by

$$\sigma^2(d) = \sigma_{\text{intr}}^2 + \sigma_{\text{collim}}^2 \quad (2.6)$$

$$= \sigma_{\text{intr}}^2 + \frac{1}{8 \ln 2} \left(\frac{wd}{h} \right)^2, \quad (2.7)$$

in which σ_{intr} is the standard deviation of the intrinsic PSF.

PET

If two photons, created by positron-electron annihilation, are detected within a very small time interval, it is reasonable to assume that the annihilation process occurred somewhere between both detectors. Consequently, there is no need to collimate the photons, since the trajectory is known. As a result, PET can acquire more photons per second than SPECT for the same amount of activity in the field of view. However, there are some issues that impose limitations to the spatial resolution of simultaneous or *coincidence* detection of gamma ray pairs.

Physical limitation to the spatial resolution is set by the kinetic energy of the positron, which it has acquired during disintegration. The positron gradually dissipates kinetic energy through elastic collisions, by which the probability for annihilation with a neighboring electron increases. Thereby, the positron moves away from the disintegration site and reduces the spatial resolution of the annihilation event. A positron created by the disintegration of ^{18}F acquires a kinetic energy of 633 keV, which allows it to travel over a mean path length of 0.6 mm and a maximum path length of 2.4 mm. Moreover, if the positron finally annihilates, its kinetic energy is probably not zero. Since momentum is preserved, the annihilation photons will not be emitted in exactly opposite directions. A small deviation angle, for example 0.3 degrees, gives an offset of about 2.8 mm over a distance of 1 m, again reducing the spatial resolution. Because gamma ray photons travel at the speed of light, it is required to use very fast electronic equipment.

The finite detector size imposes further limitations to the spatial resolution of coincidence detection [Hoffman *et al.*, 1980]. It follows that the PSF of the coincidence detector has a triangular profile in the center field, a rectangular profile close to the detectors, and a trapezoidal profile in between. Hence, the FWHM of the PSF due to the finite detector size is in reality position dependent. However, the importance of the position dependency of the spatial resolution in PET should not be exaggerated. When using a 3-D acquisition mode, which is mostly used for brain imaging, the axial spatial resolution remains almost constant, and the FWHM of the trans-axial spatial resolution varies between 5 and 6 mm for radial distances below 10 cm [Adam *et al.*, 1997]. If a human brain, of which the brain width or length is usually smaller than 20 cm, is positioned properly in the center of the field-of-view (FOV), the FWHM of the PSF is not changing that much as it does in SPECT. Hence, we can reasonably assume that the spatial resolution remains constant within the object.

PET scanners are usually equipped with many rings of multi-crystal detectors. Although more detector pairs enhance the detection capabilities of the system, it also results in an increased amount of processing which is required by the coincidence electronics. This approach makes it more difficult to separate true from false events. True events are those coincidences created by photons originating from the same positron-electron annihilation. False events are the opposite and can be subdivided into scattered, single, and random events. In some PET scanners, collimating septa can be placed in between the rings to reduce the additional detection problems. In that case, the term 2-D PET is used, because the object inside the FOV is measured

by means of a stack of detector rings that measure 2-D slices. When the septa are retracted, the term 3-D PET is used. For brain imaging, 3-D PET is preferred, mainly because of the increase in sensitivity of the system.

2.3.3 Attenuation and Scatter

Thus far, we have been assuming that the gamma ray energy remains constant between emission and detection. However, it is very likely that an amount of the emitted radiation will interact in some way with the surrounding.

A narrow collimated beam of photons will interact with matter in such way that for each interaction a photon will be removed from the collimated beam. The interaction probability per unit length is defined as the *linear attenuation coefficient* μ [cm^{-1}]. The number of photons that is expected to be eliminated over the distance ds is $dN = -\mu(s)Nd\mathbf{s}$. It follows that the beam intensity decreases exponentially. If a beam of $N(a)$ photons are emitted in point $s = a$ towards $s = b$, the expected amount of photons arriving in b , coming directly from a , is given by

$$N(b) = N(a)e^{-\int_a^b \mu(s)ds}. \quad (2.8)$$

The predominant interactions that are relevant for the gamma ray energies that are used in nuclear medicine imaging, are (a) the *photo-electric effect*, and (b) the *Compton effect*. The attenuation effect is measurable by means of a *transmission measurement*. The amount of scattered gamma rays can only be measured indirectly. Scattered gamma rays deviate from their original trajectory and propagate with a reduced energy. Consequently, there is a high probability that photons with a lower energy at the moment of detection have reached the detector through one or more Compton interactions. Unfortunately, the energy resolution of a scintillation detector is relatively poor. Photons that change their trajectory over small angles will lose only small amounts of energy, and may be indistinguishable from non-scattered events. It appears that the energy resolution of the scintillator influences the spatial resolution of the detector.

[Ichihara et al. \[1993\]](#) introduced a technique to estimate the contribution of scattered events in the primary energy window. The technique consists of using two additional energy windows that are placed at both sides of the primary energy window. By means of these *scatter windows*, a first order estimate of the scatter contribution in the primary window is derived. Let q_m , q_l , and q_u be the number of photons detected in the primary (main) window, the lower, and the upper scatter window, respectively. Let E_m , E_l , and E_u be the width of the primary, lower, and upper energy window, respectively. Then, the first order scatter correction for the number of photons in the primary energy window, is given by

$$q_{\text{corr}} = q_m - \left(\frac{q_l}{E_l} + \frac{q_u}{E_u} \right) \frac{E_m}{2} \quad (2.9)$$

This scatter correction approach is called the *triple energy window* (TEW) scatter correction method, and it is often applied in SPECT.

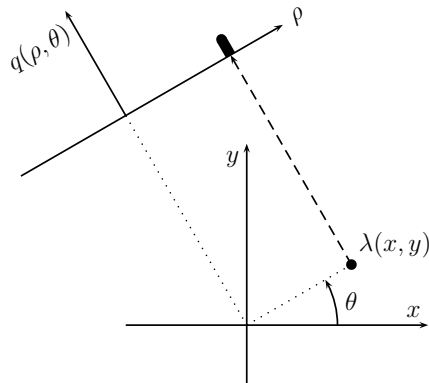


Figure 2.3: Illustration of the Radon transformation. The projection of $\lambda(x, y)$ is the line integral along the projection line (dashed line).

In 3-D PET, several detection events may occur of which the nature of an event could be true, scattered, single, or random. Because of that, 3-D PET will benefit from the use of scatter correction techniques. Actually, one could use equation (2.9). However, because of the poor energy resolution of some PET scintillation detectors, complex scatter correction techniques have been devised [Watson, 2000].

2.4 Image Reconstruction

Imaging by means of emission tomography is based on *indirect measurements* of the spatial distribution of a radioactive tracer molecule inside the imaged object. The obvious next step is to present the acquired information in a readable fashion to the observer by means of a 2-D digital image or a 3-D digital volume. This means that the image information needs to be derived or *reconstructed* from the measurements.

Emission tomography reconstruction can be done in different ways. The two most important approaches are: (a) using an *analytical description* of the acquisition procedure which is then solved by *algebraic techniques*, or (b) using a *statistical description* of the acquisition procedure which is solved by *optimization techniques*. Both approaches have their benefits and their disadvantages, and are being used in current clinical emission tomography, as well as in research. We will now look into the details of these two methods.

2.4.1 Analytical Reconstruction

We explain analytical based reconstruction techniques by means of the Radon transformation and the filtered back-projection (FBP) method in 2-D. This approach is conceptually well suited for SPECT using parallel hole collimators and 2-D PET. These modalities are essentially a set of stacked 2-D slices that make up the 3-D volume.

Consider a continuous 2-D distribution $\lambda(x, y)$ in an orthogonal coordinate system $\perp(x, y)$ (Fig. 2.3). The *Radon transformation* of $\lambda(x, y)$ is found by taking line

integrals along slanted lines,

$$(\mathcal{R}\lambda)(\rho, \theta) = \iint_{-\infty}^{+\infty} \lambda(x, y) \delta(\rho - x \cos \theta - y \sin \theta) dx dy, \quad (2.10)$$

where $\rho = x \cos \theta + y \sin \theta$ is the equation of the slanted line, θ is the angular orientation of the line w.r.t. the coordinate system, and $\delta(\cdot)$ is the Dirac delta-function. If $\lambda(x, y)$ represents the spatial distribution of a radioactive tracer, then the Radon transformation is the mathematical equivalent of a simplified emission tomography acquisition procedure, where attenuation, scatter, resolution, and all other effects are ignored. The Radon transformation is often called the *projection operator* of the tracer distribution,

$$q(\rho, \theta) = (\mathcal{R}\lambda)(\rho, \theta). \quad (2.11)$$

The main purpose of image reconstruction is to retrieve $\lambda(x, y)$ from the measured projection data $q(\rho, \theta)$. For that purpose, we need to invert the Radon transformation. One solution is based on the Fourier Slice Theorem. From Fourier theory, we know that

$$\lambda(x, y) = \iint_{-\infty}^{+\infty} (\mathcal{F}_2 \lambda)(\nu_x, \nu_y) e^{i2\pi(x\nu_x + y\nu_y)} d\nu_x d\nu_y, \quad (2.12)$$

where $(\mathcal{F}_2 \lambda)(\nu_x, \nu_y)$ is the 2-D Fourier transformation of $\lambda(x, y)$, and where $i = \sqrt{-1}$. Introducing polar frequency parameters

$$\begin{pmatrix} \nu_x \\ \nu_y \end{pmatrix} = \nu \begin{pmatrix} \cos \theta \\ \sin \theta \end{pmatrix} \quad (2.13)$$

into equation (2.12) produces

$$\lambda(x, y) = \int_0^\pi \int_{-\infty}^{+\infty} |\nu| (\mathcal{F}_2 \lambda)(\nu \cos \theta, \nu \sin \theta) e^{i2\pi\nu\rho} d\nu d\theta. \quad (2.14)$$

Subsequently, from the Fourier Slice Theorem, we know that

$$(\mathcal{F}_2 \lambda)(\nu \cos \theta, \nu \sin \theta) = \int_{-\infty}^{+\infty} q(\rho, \theta) e^{-i2\pi\rho\nu} d\rho = (\mathcal{F}_1 q)(\nu, \theta), \quad (2.15)$$

where \mathcal{F}_1 is the 1-D Fourier transformation. Then, equation (2.14) becomes

$$\lambda(x, y) = \int_0^\pi \int_{-\infty}^{+\infty} |\nu| \left[(\mathcal{F}_1 q)(\nu, \theta) \right] e^{i2\pi\nu\rho} d\nu d\theta \quad (2.16)$$

$$= \int_0^\pi \left[(\mathcal{F}_1^{-1} \Phi_{|\nu|} \mathcal{F}_1 q)(\nu, \theta) \right] d\theta \quad (2.17)$$

$$= (\mathcal{B} \mathcal{F}_1^{-1} \Phi_{|\nu|} \mathcal{F}_1 q)(\rho, \theta), \quad (2.18)$$

where \mathcal{F}_1^{-1} is the 1-D inverse Fourier transformation, where $\Phi_{|\nu|}$ is the operator that performs multiplication with $|\nu|$ in the frequency domain, which is also called the *ramp* filter, and where \mathcal{B} is the back-projection operator, defined as

$$(\mathcal{B}q)(x, y) = \int_0^\pi q(\rho, \theta) \delta(\rho - x \cos \theta - y \sin \theta) d\theta. \quad (2.19)$$

Then, the operator sequence $(\mathcal{B}\mathcal{F}_1^{-1}\Phi_{|\nu|}\mathcal{F}_1)$ is called the *filtered back-projection* (FBP) of the measured projection data $q(\rho, \theta)$.

The conventional FBP method is based on a mathematical idealization of emission tomography [Fessler, 1994; Radon, 1917]. Nevertheless, the method is widely used for a number of reasons. First of all, it can be easily implemented using existing Fourier techniques, like e.g. *fast Fourier transformation* (FFT). It is a straightforward algorithm that uses relatively little processing equipment. In the early 1970's, when tomography was introduced in radiology and nuclear medicine departments, computers were considerably slower than the equipment which is used nowadays. Being able to produce images using analytical techniques was then a major step forward. Later on, the method was extended to 3-D imaging. Secondly, the algorithm is based on an analytical function, which makes it very attractive for further theoretical research. If the FBP algorithm is combined with an accurate attenuation correction method, it shows less bias than many iterative reconstruction techniques. For some quantitative applications, like e.g. tracer kinetic modeling, it is better to have a reconstruction method that gives less bias to the quantitative data than having a reconstruction method that gives visual good quality images.

However, there are also a number of drawbacks to the FBP method. First of all, the measured emission data are subject to statistical variation. In clinically realistic circumstances, emission data can contain statistical variations that are relatively large compared to the measured values. This *uncertainty* of the measurement is often referred to as *noise*. A considerable drawback of the FBP algorithm is the lack of a statistical framework that can deal with this noise. As a result, the variations in the measurements will produce high frequencies in the Fourier domain that subsequently will be amplified by the ramp filter and propagate to the reconstruction. This noise propagation can be suppressed by apodizing the ramp filter with a low pass filter. However, applying a low pass filter will also degrade the spatial resolution and contrast inside the reconstructed image. Examples of apodizing filters that are frequently used, are

- the Gaussian filter kernel $\Psi_\sigma(\nu) = e^{-2(\pi\sigma\nu)^2}$. The Fourier transformation of a Gaussian kernel is again Gaussian. Hence, the filter can also be applied to the projection space. Then,

$$\Upsilon_\sigma(\rho) = \mathcal{F}^{-1}\Psi_\sigma(\nu) = \frac{1}{\sigma\sqrt{2\pi}} e^{-\frac{\rho^2}{2\sigma^2}} \quad (2.20)$$

is the 1-D convolution kernel that has to be applied to the ramp-filtered projection data. The full-width at half-maximum (FWHM) of the Gaussian convolution kernel which characterizes the smoothing performance of the kernel, is $2\sigma\sqrt{2\ln 2}$.

- the Butterworth filter, which is given by

$$\Psi_{\nu_0, n}(\nu) = \frac{1}{\sqrt{1 + \left(\frac{\nu}{\nu_0}\right)^{2n}}} \quad (2.21)$$

and where ν_0 is the cut-off frequency and n the order of the filter.

In (2.18), $\Phi_{|\nu|}$ is then multiplied in frequency space by the low pass filter $\Psi(\nu)$. Alternatively, the FBP reconstruction could be post-processed with the appropriate apodizing kernel. For that purpose, the Gaussian kernel is often used.

The measured emission data are sampled over a discrete number of detector units and only a finite number of projection angles are measured. For a small number of projection angles, and when using noiseless data, the discrete implementation of the back-projection in (2.18) leads to *star-shaped streaks* around high intensity regions in the reconstructed image [Bruyant *et al.*, 2000]. For noiseless measurements, these streaks would normally disappear with an increasing angular sampling. However, noise in the projection data will pronounce these streaks. In fact, the FBP algorithm can be seen as providing an *un-weighted least-squares* solution to the minimization problem

$$\hat{\lambda}(x, y) = \arg \min_{\lambda} \|q(\rho, \theta) - \mathcal{R}\lambda(\rho, \theta)\|^2, \quad (2.22)$$

where $\hat{\lambda}(x, y)$ is the image estimate after optimization. The FBP algorithm treats all rays equally. This means that noise in $q(\rho, \theta)$ is treated as if it was produced by means of a Gaussian distribution. However, as we saw in equation (2.3), the measured data are samples from a Poisson distribution. For that reason, the reconstructed image will contain a residual amount of structural or correlated noise which is seen by these *streak artifacts*.

Filtered back-projection is based on the assumption that the projection data $q(\rho, \theta)$ truly represent line integrals. Unfortunately, that assumption is not always valid for applications in emission tomography. Both in PET and SPECT, the measured projection data $q(\rho, \theta)$ are overestimated by the Radon transformation of the tracer distribution. This effect is caused by the presence of radiation attenuating tissue. In general, the overestimation will be inconsistent for different projection angles. Before attenuation correction can be performed, one has to obtain an image of the attenuation coefficients. After that, the data may be corrected for the attenuation effect.

In SPECT, the detected photons provide no depth information, and therefore no information about the attenuation along the photon trajectories. For that reason, some types of SPECT scanners have been equipped with external radioactive sources that are used to emit radiation through the object. With this technique, which is called *transmission tomography*, one can measure the attenuation along specific trajectories through the object. This technique is essentially similar to the concept of *computed tomography* or CT.

Recently, state-of-the-art PET-CT and SPECT-CT scanners have been made available and provide high-quality transmission images. These images can be transformed into attenuation coefficients at energies that are comparable with those of the radiation emitted by the tracer, which can be useful for the attenuation correction of the emission data. However, attenuation correction based on transmission tomography can give additional problems. For example, the patient may move in between the measurements of the transmission and the emission data. Moreover, the noise or perhaps artifacts that are contained by the transmission data may influence the quality of the emission data reconstruction.

Suppose that transmission measurements were not acquired. Then, a reasonable substitute might be to derive the contours of the object from the projection data, or extract the contours from a reconstruction without attenuation correction. An artificial attenuation image can then be constructed by using water equivalent attenuation coefficients inside the object and zero coefficients outside. This approximation may be useful as an alternative solution when transmission data are not available.

In SPECT, if an image of attenuation coefficients has been obtained, the method of Chang provides an attenuation correction procedure [Chang, 1978]. For all points (x_0, y_0) inside an object, one can compute the first order correction factor, which is given by

$$c_1(x_0, y_0) = \left(\frac{1}{2\pi} \int_0^{2\pi} e^{-\int_{L_\theta} \mu(x, y) dx dy} d\theta \right)^{-1}, \quad (2.23)$$

where \int_{L_θ} represents the line integral from (x_0, y_0) to the border of the object along projection angle θ , and $\mu(x, y)$ are the linear attenuation coefficients. If $\lambda(x, y)$ represents the FBP reconstruction of $q(\rho, \theta)$, then $\lambda(x, y)c_1(x, y)$ is called the *first order corrected Chang FBP reconstruction*. A second order correction term $c_2(x, y)$ can be found by projecting the first order corrected reconstruction $\lambda(x, y)c_1(x, y)$. Thereafter, the measured projection data $q(\rho, \theta)$ are subtracted, and the result is reconstructed using FBP. The second order correction term is then given by

$$c_2(x, y) = \text{FBP} \left[\mathcal{R} \lambda c_1(\rho, \theta) - q(\rho, \theta) \right]. \quad (2.24)$$

The second order corrected Chang FBP reconstruction is then $\lambda(x, y)c_1(x, y) + c_2(x, y)$.

In PET, true coincidence detection guarantees a line-of-response (LOR) through the object. Hence, the depth information is not required because the attenuation depends on the complete LOR through the object, not on the origin along the LOR. Using an additional transmission measurement, the attenuation along the LOR can be calculated, and attenuation correction can be performed before the reconstruction algorithm is applied to the emission data. In some PET scanners, external point or line sources emitting positrons are placed inside the gantry with the freedom of rotating around the inner FOV, and thus around the object.

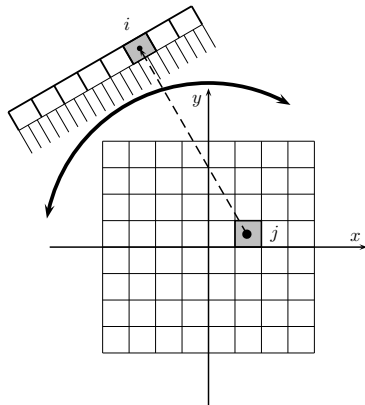


Figure 2.4: Schematic drawing of the digital image representation and system modeling in SPECT. In this example, discrete detector element i measures collimated photons emitted by voxel j . See §2.4.2 for further explanation.

2.4.2 Digital Image Representation and System Modeling

In reality, it is not possible to measure the emitted radiation with an infinite precision. The projection data are sampled and digitized by the acquisition system, and the true measurements are represented by $q(\rho_r, \theta_t)$, where $r = \{0, 1, \dots, R-1\}$ enumerates the discrete detector units, and $t = \{0, 1, \dots, T-1\}$ the discrete projection angles. For economy of writing, we define $i = Rt + r$ to be the enumerator of the *detector bins*, $i = \{0, 1, \dots, I-1\}$, and $I = RT$. This enumeration includes both the detector units as well as the projection angles. Hence, the true measurement of the projection data $q(\rho, \theta)$ can be written as

$$\sum_{i=0}^{I-1} q_i \psi_i(\rho, \theta), \quad (2.25)$$

where ψ_i are the support functions of the projection space, defined as

$$\psi_i(\rho, \theta) = \begin{cases} 1 & \iff (\rho, \theta) \text{ define the projection line through} \\ & \text{the } i^{\text{th}} \text{ detector,} \\ 0 & \iff \text{otherwise,} \end{cases} \quad (2.26)$$

and $q_i = q(\rho_r, \theta_t)$. The true image representation of the spatial tracer distribution is in a similar way approximated by the digitized $\lambda(x_m, y_n)$, where $m = \{0, 1, \dots, M-1\}$ and $n = \{0, 1, \dots, N-1\}$ enumerate the sampling in the x and y direction, respectively. For notational convenience, we define $j = Mn + m$ to be the enumerator of the discrete *image elements*, $j = \{0, 1, \dots, J-1\}$, and $J = MN$. The spatial tracer distribution is approximated by a finite series expansion,

$$\lambda(x, y) \approx \sum_{j=0}^{J-1} \lambda_j \varphi_j(x, y), \quad (2.27)$$

in which φ_j are the support functions of the image space, often defined as *pixels* (2-D), or *voxels* (3-D),

$$\varphi_j(x, y) = \begin{cases} 1 & \iff (x, y) \text{ inside } j^{\text{th}} \text{ pixel/voxel,} \\ 0 & \iff \text{otherwise,} \end{cases} \quad (2.28)$$

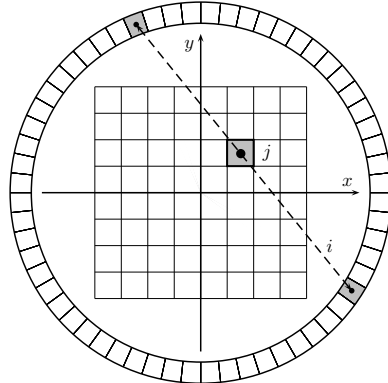


Figure 2.5: Schematic drawing of the digital image representation and system modeling in PET. In this example, discrete coincidence detector pair i measures gamma rays emitted by voxel j . See §2.4.2 for further explanation.

and where $\lambda_j = \lambda(x_m, y_n)$ are the digital approximations of the continuous tracer distribution $\lambda(x, y)$. The digital version of the Radon transformation (2.11) becomes

$$\sum_{i=0}^{I-1} q_i \psi_i(\rho, \theta) = \sum_{j=0}^{J-1} \lambda_j \mathcal{R}\varphi_j(\rho, \theta). \quad (2.29)$$

The Radon transformation of the support functions in image space can then be rewritten as a linear combination of the support functions in projection space, or $\mathcal{R}\varphi_j(x, y) = \sum_i c_{ij} \psi_i(\rho, \theta)$. Equation (2.29) then simplifies to

$$q_i = \sum_{j=0}^{J-1} c_{ij} \lambda_j, \quad (2.30)$$

where c_{ij} are the projection elements for the transformation. The matrix of projection elements $\mathbf{C} = \{c_{ij} \mid i = 0, 1, \dots, I-1 \text{ and } j = 0, 1, \dots, J-1\}$ is called the *system matrix*. It is the mathematical model which describes the relationship between the digitized image and the sampled projection space. The matrix elements describe the details of the acquisition procedure.

The digital Radon transformation is the mathematical equivalent of an idealized acquisition procedure. See Fig. 2.4 and Fig. 2.5 for a schematic drawing of the digital acquisition and image representation and system modeling in SPECT and PET, respectively. Both the attenuation and the detector resolution effect are ignored. However, a more accurate description of the acquisition procedure can improve the qualitative performance of the reconstruction algorithm.

Photons may be attenuated in between their emission and detection. This happens due to the presence of matter. An appropriate correction for the attenuation effect should be applied at the same instance where it occurs. Therefore, equation (2.8) is incorporated into the system model. The elements of the system matrix should then be replaced by

$$c_{ij} \longrightarrow a_{ij} c_{ij}, \quad \text{with} \quad a_{ij} = \exp \left(- \sum_k \Delta_{ij}^k \mu_k \right), \quad (2.31)$$

where Δ_{ij}^k represent the effective intersection length of the projection beam from detector element i to voxel j with the volume represented by voxel k , and where μ_k is the linear attenuation coefficient at voxel k . For PET, equation (2.31) simplifies to

$$c_{ij} \longrightarrow a_i c_{ij}, \quad \text{with} \quad a_i = \exp\left(-\sum_k \Delta_i^k \mu_k\right), \quad (2.32)$$

where Δ_i^k represent the effective intersection length of the projection beam through detector pair i with the volume represented by voxel k . In PET, the attenuation correction can be separated from the projection operation.

Modeling of the detector and collimator spatial resolution is more complex. For PET, however, the position dependent spatial resolution properties of the detector can be approximated by a uniform PSF for objects in the central part of the FOV (cfr. §2.3.2). In that region, the FWHM of the PSF is not changing that much with the distance to the detector, as it does in SPECT [Adam *et al.*, 1997]. The detector spatial response function is then modeled by means of a convolution of the projection with a Gaussian kernel that has a fixed FWHM. Then, the elements of the system matrix are given by

$$c_{ij} \longrightarrow \sum_t a_t c_{tj} h_{it}, \quad (2.33)$$

where the Gaussian kernel is given by

$$h_{it} = \frac{1}{\mathcal{H}} \exp\left(-\frac{d_{it}^2}{2\sigma^2}\right) \quad \text{with} \quad \sigma = \frac{\text{FWHM}}{\sqrt{8 \ln 2}}, \quad (2.34)$$

where \mathcal{H} is a normalization constant, and where d_{it} is the distance on the detector surface between detector elements i and t .

This straightforward approach cannot be used for modeling of the distance dependent resolution effect in SPECT. If we ignore the effect of attenuation, then, for a parallel hole collimator, we can rewrite equation (2.30) as a plane-by-plane projection operation, in which all planes v are parallel to the detector surface at detector element i . For that purpose, we use a plane selection parameter ξ_{ij}^v , which is defined as

$$\xi_{ij}^v = \begin{cases} 1 & \iff \text{voxel } j \text{ lies within plane } v, \text{ i.e. parallel to the} \\ & \text{detector surface, and } j \text{ projects perpendicular} \\ & \text{onto detector element } i, \\ 0 & \iff \text{otherwise.} \end{cases} \quad (2.35)$$

Furthermore, we define that the plane for which $v = 0$ is located at the opposite side of the detector surface, and that the plane onto the detector surface has $v = v_{\max}$. In equation (2.7), we showed that the spatial resolution of the detector can be approximated by a Gaussian kernel of which the variance depends on the distance of

the source to the collimator. Then, the projection operation, with the incorporation of the distance dependent resolution effect, can be written as

$$q_i = \sum_{v=1}^{v_{\max}} \sum_l g_{il}^v \left(\sum_j \lambda_j \xi_{ij}^v \right), \quad (2.36)$$

in which the PSF of the detector in plane v is given by

$$g_{il}^v = \frac{1}{\mathcal{G}} \exp \left(-\frac{d_{il}^2}{2\sigma_v^2} \right), \quad (2.37)$$

where \mathcal{G} is a normalization constant, d_{il} is the Euclidean distance between voxel i and voxel l in plane v , and σ_v^2 is the variance of the PSF in plane v . Unfortunately, the use of equation (2.37) introduces a significant computational burden for statistical reconstruction (§2.4.3). The Gaussian diffusion method, proposed by McCarthy and Miller [1991], can reduce this computational burden. The method exploits the fact that the variances ς^2 of Gaussian functions G add in convolution,

$$G(\varsigma_1^2) \otimes G(\varsigma_2^2) \triangleq G(\varsigma_1^2 + \varsigma_2^2). \quad (2.38)$$

Hence, instead of smoothing with the PSF for each plane v separately, the Gaussian diffusion method applies the resolution effect by means of incremental smoothing with variances ς_v^2 , satisfying

$$\sigma_v^2 = \sum_{u=v}^{v_{\max}} \varsigma_u^2. \quad (2.39)$$

The projection operation described in (2.30), but with the incorporation of the attenuation and distance dependent resolution effect, is then written as a *recursive* plane-by-plane projection, smoothing, and attenuation operation,

$$p_i^v = \begin{cases} e^{-\frac{\Delta}{2} \sum_j [\mu_j \xi_{ij}^0 + \mu_j \xi_{ij}^1]} \sum_l G_{il}^v \left(\sum_j \lambda_j \xi_{ij}^v \right) & \iff v = 0 \\ e^{-\frac{\Delta}{2} \sum_j [\mu_j \xi_{ij}^v + \mu_j \xi_{ij}^{v+1}]} \sum_l G_{il}^v \left(p_i^{v-1} + \sum_j \lambda_j \xi_{ij}^v \right) & \iff v = 1, \dots, v_{\max} \end{cases} \quad (2.40)$$

with $q_i = p_i^{v_{\max}}$, in which Δ is the trans-axial thickness of a voxel, μ_j is the attenuation coefficient, and

$$G_{il}^v = \frac{1}{\mathcal{G}} \exp \left(-\frac{d_{il}^2}{2\varsigma_v^2} \right), \quad (2.41)$$

is the Gaussian smoothing kernel for plane v with variance $\varsigma_v^2 = \sigma_v^2 - \sigma_{v+1}^2$.

2.4.3 Statistical Reconstruction

The statistical framework that has been developed for the reconstruction of emission tomography data is very extensive. Many contributions to the theory have led to a wide variety of iterative algorithms. For the derivation of a certain reconstruction algorithm, the approach in general is based on the following five steps: (1) image parametrization, (2) system modeling, (3) statistical modeling of the measurements, (4) construction of a cost function, and (5) optimization of the cost function using an iterative algorithm [Fessler, 2004]. The first two steps have been described in §2.4.2. For the last three steps, different approaches exist. In the next sections, we describe the Bayesian approach for the restoration of emission tomography data.

Bayesian Approach

Consider an object that contains an unknown spatial distribution of a certain radioactive tracer molecule. The object is located inside the FOV of an emission tomograph. The emission data of the object have been acquired over a certain time and the measurement is given by $Q = \{q_i \mid i = 0, \dots, I - 1\}$. Suppose that, by some procedure, we were able to reconstruct the underlying tracer distribution from the measured data, and we can write the digitized *image reconstruction* of the radioactive tracer distribution as $\Lambda = \{\lambda_j \mid j = 0, \dots, J - 1\}$. Using the conditional and marginal probabilities for the measurement and reconstruction, we can write down the *rule of Bayes*, which states that

$$p(\Lambda|Q) = \frac{p(Q|\Lambda)p(\Lambda)}{p(Q)}. \quad (2.42)$$

The probability for the image without taking into account the measurement is the *prior* $p(\Lambda)$. The probability for obtaining the measurement assuming that the tracer distribution is equal to Λ is the *likelihood* $p(Q|\Lambda)$. The probability for the image Λ , given the measurement Q , is the *posterior* $p(\Lambda|Q)$. Obviously, the probability for obtaining the measurement $p(Q)$ remains constant during the reconstruction procedure. It is the aim of statistical image reconstruction methods to seek for that image Λ for which the posterior probability $p(\Lambda|Q)$ is maximal. This is called the *maximum-a-posteriori* (MAP) approach.

As a first approach to this problem, we can assume that all solutions have equal probability. This means that for all Λ , we assume the prior probability $p(\Lambda)$ to be constant. Then, maximizing $p(\Lambda|Q)$ is equal to maximizing $p(Q|\Lambda)$. This is called the *maximum-likelihood* (ML) approach.

Maximum-Likelihood Estimation

Assume that the acquisition procedure for an emission tomograph has been characterized and that a system matrix (cfr. §2.4.2) was derived. When the tracer distribution in the field of view is equal to Λ , the acquisition procedure is expected

to measure

$$r_i = \sum_{j=0}^{J-1} c_{ij} \lambda_j, \quad (2.43)$$

for all $i = 0, \dots, I - 1$. The c_{ij} describe the detection sensitivity of detector i for activity in voxel j . The next step in the ML approach is to choose a proper statistical model that describes the relationship between the expected and the measured data. As pointed out in §2.2.1, we assume that the observed data are samples from an ordinary Poisson distribution, as shown in equation (2.3). Hence, the conditional probability of measuring q_i while r_i is expected, is given by

$$p(q_i|r_i) = \frac{e^{-r_i} r_i^{q_i}}{q_i!}. \quad (2.44)$$

Because individual observations are assumed to be independent, the likelihood of measuring Q given Λ , is

$$p(Q|\Lambda) = \prod_{i=0}^{I-1} \frac{e^{-r_i} r_i^{q_i}}{q_i!}. \quad (2.45)$$

The natural logarithm is a monotonic function. Hence, maximizing equation (2.45) is equivalent to maximizing its logarithm. The log-likelihood function is

$$L(Q|\Lambda) = \sum_{i=0}^{I-1} q_i \ln(r_i) - r_i - \ln(q_i!) \quad (2.46)$$

$$= \sum_{i=0}^{I-1} \left[q_i \ln \left(\sum_{j=0}^{J-1} c_{ij} \lambda_j \right) - \sum_{j=0}^{J-1} c_{ij} \lambda_j - \ln(q_i!) \right]. \quad (2.47)$$

The most probable tracer distribution estimate $\hat{\Lambda}$, given the measured data, is then given by the maximum-likelihood estimator (MLE), which is defined as

$$\hat{\Lambda} = \arg \max_{\Lambda \geq 0} L(Q|\Lambda). \quad (2.48)$$

A straightforward approach for solving (2.48) is to compute its first derivative,

$$\frac{\partial L}{\partial \lambda_j} = \sum_{i=0}^{I-1} c_{ij} \left(\frac{q_i}{\sum_{j'=0}^{J-1} c_{ij'} \lambda_{j'}} - 1 \right), \quad (2.49)$$

and set it to zero. However, this approach is computationally very impractical. As an alternative, there are iterative estimation techniques that are much easier to implement. One of these techniques is the *expectation-maximization* (EM) algorithm, which was proposed by [Dempster *et al.*, 1977].

Expectation-Maximization

The EM algorithm for maximum-likelihood reconstruction in emission tomography was developed independently by Shepp and Vardi [1982] and Lange and Carson [1984]. We give a description of the algorithm that was proposed by Lange and Carson [1984].

The emission data measured by the detector are *incomplete*. The measurement does not provide information about the origin of measured events. However, one can introduce a set of *complete data* $X = \{x_{ij}\}$, such that

$$\sum_{j=0}^{J-1} x_{ij} = q_i. \quad (2.50)$$

The x_{ij} are the unknown number of photons that have been emitted in voxel j and detected in i . The set of complete data, which cannot be observed, describes the full relationship between the emission and the detection of each event. The expected value of x_{ij} , under the assumption of Λ , is equal to $\bar{x}_{ij} = c_{ij}\lambda_j$. Since the complete data obey Poisson statistics, just like the measured data, one can derive the log-likelihood of the complete data, which is

$$L(X|\Lambda) = \sum_{i=0}^{I-1} \sum_{j=0}^{J-1} x_{ij} \ln \bar{x}_{ij} - \bar{x}_{ij} - \ln(x_{ij}!). \quad (2.51)$$

$$= \sum_{i=0}^{I-1} \sum_{j=0}^{J-1} x_{ij} \ln(c_{ij}\lambda_j) - c_{ij}\lambda_j - \ln(x_{ij}!). \quad (2.52)$$

Because the complete data cannot be observed directly, we need an estimate. Let $\{a_1, \dots, a_n\}$ be a set of independent Poisson variables. The expected value of a_1 , under the assumption that the sum $S = \sum_{j=1}^n a_j$ is known, is given by

$$E(a_1|S) = S \frac{E(a_1)}{\sum_{j=1}^n E(a_j)}. \quad (2.53)$$

Hence, the expected projection data, given the measurement Q and the estimate Λ , and using (2.50), is given by

$$E(x_{ij}|Q, \Lambda) = q_i \frac{c_{ij}\lambda_j}{\sum_{j'=0}^{J-1} c_{ij'}\lambda_{j'}} \triangleq n_{ij}. \quad (2.54)$$

The complete data in (2.52) can then be replaced by the expected value, such that

$$E(L(X|\Lambda)|Q, \Lambda) = \sum_{i=0}^{I-1} \sum_{j=0}^{J-1} n_{ij} \ln(c_{ij}\lambda_j) - c_{ij}\lambda_j - \ln n_{ij}! \quad (2.55)$$

This step is called the *expectation* or *E-step*. In the subsequent *maximization* or *M-step*, the conditional expectation of (2.55) is maximized with respect to λ_j . The

derivative of (2.55), given by

$$\frac{\partial}{\partial \lambda_j} E(L(X|\Lambda)|Q, \Lambda^k) = \sum_{i=0}^{I-1} \left(\frac{n_{ij}}{\lambda_j} - c_{ij} \right), \quad (2.56)$$

is set to zero, which gives the maximum-likelihood estimate

$$\hat{\lambda}_j = \frac{\sum_{i=0}^{I-1} n_{ij}}{\sum_{i=0}^{I-1} c_{ij}}, \quad (2.57)$$

from which the *maximum-likelihood expectation-maximization* (ML-EM) algorithm can be derived,

$$\lambda_j^{k+1} = \frac{\lambda_j^k}{\sum_{i=0}^{I-1} c_{ij}} \sum_{i=0}^{I-1} \frac{c_{ij} q_i}{\sum_{j'=0}^{J-1} c_{ij'} \lambda_{j'}^k}, \quad (2.58)$$

and where Λ^{k+1} is the reconstruction after one iteration when starting from Λ^k . From (2.49) and (2.58), one can show that the ML-EM algorithm is a gradient ascent method

$$\lambda_j^{k+1} = \lambda_j^k + \frac{\lambda_j^k}{\sum_{i=0}^{I-1} c_{ij}} \left. \frac{\partial L}{\partial \lambda_j} \right|_{\Lambda^k}. \quad (2.59)$$

For reasons of computational stability, the latter form is used to implement the ML-EM algorithm.

Ordered Subsets

Although the ML-EM algorithm is guaranteed to converge, its actual convergence rate can be very slow. Fortunately, the ordered subsets (OS) technique, proposed by [Hudson and Larkin \[1994\]](#), can speed up this rate. For this technique, smaller subsets of the projection data are used for reconstruction, thereby speeding up the estimation procedure. Let the projection data be subdivided into T subsets, such that each detector lies in a subset, $i \in S_t$ and $t \in \{1, \dots, T\}$. Then

$$\lambda_j^{(k,t+1)} = \frac{\lambda_j^{(k,t)}}{\sum_{i \in S_t} c_{ij}} \sum_{i \in S_t} \frac{c_{ij} q_i}{\sum_{j'=0}^{J-1} c_{ij'} \lambda_{j'}^{(k,t)}} \quad (2.60)$$

is the t -th subiteration of the OS algorithm. If all subsets have been used,

$$\lambda_j^{k+1} = \lambda_j^{(k,T+1)} \quad (2.61)$$

is the reconstruction after one full iteration, based on many subiterations. Applying this method to the ML-EM algorithm gives rise to the ML-OS-EM reconstruction algorithm.

Unfortunately, the OS technique can prevent that convergence is reached. Except for the reconstruction of noise-free data, ML-OS-EM will converge to a non-maximum likelihood solution. This method will always lead to a cyclic convergence behavior. However, even at this level, ML-OS-EM can produce good results. In order to find a reasonable compromise between convergence guarantee and convergence rate, one could use the ML-OS-EM method with an iteration scheme with a decreasing number of subsets. This approach is used in all experiments that follow.

Maximum-a-Posteriori and Regularization

For the derivation of the ML algorithm, we assumed that all solutions have equal probability. As a result, a solution of (2.48) will fit the data using the statistical model. But, it will also try to explain for some part the statistical fluctuations that are present in the data, i.e. the *noise content*. It should be clear by now that there is plenty of noise in the measurements. The ML reconstruction method cannot prevent the propagation of noise from the measurement into the ML estimate. Moreover, there is no unique solution because the continuous medium that has been measured has to be retrieved using a finite number of measurements. The image restoration problem is said to be *ill-posed*.

Fortunately, a number of solutions exist. One can initialize the ML algorithm with a smooth image estimate $\Lambda^{(0)}$ and terminate it after a few iterations. The transfer of noise is then prevented by stopping the algorithm. A serious disadvantage is that this solutions prevents from coming near the point of convergence, particularly for small structures with high contrast-to-background ratios. A frequently used noise suppression technique is post-smoothing of the reconstruction after many iterations using a low-pass post-smoothing kernel, such as the Gaussian kernel. A different approach consists of using smooth basis functions, called *blobs*, instead of voxels (2.28) for the support functions of the image space [Lewitt, 1983; Matej and Lewitt, 1992]. An alternative regularization approach was proposed by Snyder *et al.* [1987] and is called the method of *sieves*. In both approaches, the image estimate is then smooth by definition.

The most popular approach comes with the use of the prior function $p(\Lambda)$, which was mentioned in §2.4.3. For that approach, the most probable tracer distribution $\hat{\Lambda}$, given the measured data and the additional constraints imposed by the prior function, is given by the MAP estimator, which is defined as

$$\hat{\Lambda} = \arg \max_{\Lambda \geq 0} \left(L(Q|\Lambda) + M(\Lambda) \right), \quad (2.62)$$

and for which the log-prior is defined as $M(\Lambda) \triangleq \ln p(\Lambda)$. Straightforward optimization of (2.62) using the expectation-maximization technique is difficult since the M -step is coupled. However, some solutions have been provided. Hebert and Leahy [1989] proposed a generalized EM method which is a coordinate gradient descent method. An alternative method, developed by Green [1990], has been named the *one-step late* (OSL) algorithm because it makes use of gradients of the previous

iteration step,

$$\lambda_j^{n+1} = \frac{\lambda_j^n}{\sum_i c_{ij} + \beta \left. \frac{\partial M}{\partial \lambda_j} \right|_{\Lambda^n}} \sum_j \frac{c_{ij} q_i}{\sum_{j'} c_{ij'} \lambda_j^n}. \quad (2.63)$$

For large β , the denominator in (2.63) may become very small, or even negative, and thereby cause numerical problems. To avoid this, a different optimization strategy can be used for (2.62). As shown in (2.59), the ML-EM algorithm can be written as a preconditioned gradient ascent algorithm. Then, the prior can be included by adding its gradient to that of the likelihood, and by adapting the preconditioner such that convergence is controlled when the prior dominates. The optimization algorithm is then given by

$$\lambda_j^{n+1} = \lambda_j^n + \lambda_j^n \frac{\left. \frac{\partial L}{\partial \lambda_j} \right|_{\Lambda^n} + \left. \frac{\partial M}{\partial \lambda_j} \right|_{\Lambda^n}}{\sum_i c_{ij} + \lambda_j^n \left. \frac{\partial^2 M}{\partial \lambda_j^2} \right|_{\Lambda^n}}. \quad (2.64)$$

This expression reduces to (2.59) if the likelihood dominates, and to an approximation of Newton's method if the prior dominates. In absence of the prior, (2.64) is guaranteed to be non-negative. However, the preconditioner of the prior does not guarantee non-negativity. For that purpose, negative values are to be replaced with zeros during iterations.

When performing MAP reconstruction, a certain prior function should be used and a proportional weight should be given to it. The choice which prior to use depends on the application. In many cases, the aim is to obtain an image featuring

- local smoothness, perhaps in combination with a tolerance for edges,
- global smoothness.

In an image, local smoothness can be obtained by using a Gibbs-Markov prior [Geman and Geman, 1984]. The a priori probability for the tracer distribution is based on the Gibbs distribution,

$$p(\Lambda) \propto \exp(-\beta U(\Lambda)), \quad (2.65)$$

where $U(\Lambda)$ is the Gibbs energy function, given by

$$U(\Lambda) = \sum_j \sum_{k \in \mathcal{N}_j} \frac{1}{d_{jk}} \Phi(\lambda_j, \lambda_k), \quad (2.66)$$

where $\Phi(x, y)$ is the potential function, d_{jk} the Euclidean distance between voxel j and voxel k , \mathcal{N}_j the neighborhood of voxel j , and β the Gibbs prior weight. There are a number of potential (or penalty) functions that can be used. Popular choices are the quadratic, the Huber, the Median root, and the Geman-McClure function [Alenius *et al.*, 1998; Geman and McClure, 1985; Mumcuoglu *et al.*, 1996, 1994]. Recently, a potential function was derived, which penalizes relative differences rather

than absolute differences, and which becomes tolerant for relatively large differences between neighboring voxels [Nuyts *et al.*, 2002].

If on the other hand a uniform activity distribution is pursued, global smoothness can be obtained by using a Gaussian prior. This approach becomes useful for tissues having a known uniform tracer uptake (cfr. infra). The a priori probability for the tracer distribution is based on Gaussian distributions, and the log-prior is defined as

$$M(\Lambda) = -\beta \sum_j \frac{(\lambda_j - \mu_j)^2}{2\sigma_j^2}, \quad (2.67)$$

in which μ_j are the mean and σ_j the standard deviation of the assumed underlying Gaussian tracer distribution, and β the Gaussian prior weight. In particular, multi-modal Gaussian distributions can be assumed [Nuyts *et al.*, 1999a]. This extension is extremely well suited for the MAP reconstruction of PET transmission data.

2.5 Conclusion

In this chapter, we described the different steps that are required for performing emission tomography. Each of these steps, from the injection of the tracer molecule to the formation of the image, has an influence on the final image quality. We also showed that the digital image representation and system modeling can influence the spatial resolution of the reconstruction. Finally, different image reconstruction techniques were discussed. In the next chapter, we discuss in detail the origin and occurrence of some image degrading effects and we provide some solutions.

Chapter 3

Partial Volume Correction in Emission Tomography

“All models are wrong — but some are useful.”

GEORGE EDWARD PELHAM BOX
(b. 1919)

This chapter is mainly based on K. Baete *et al.*, “Anatomical based FDG-PET reconstruction for the detection of hypo-metabolic regions in epilepsy,” *IEEE Transactions on Medical Imaging*, Vol. 23, No. 4, pp. 510-519, Apr. 2004.

The quality and quantitative accuracy of emission tomography image reconstructions are determined by a variety of issues. Among these, the acquisition and reconstruction parameter settings are crucial. For optimal imaging performance, these acquisition and reconstruction settings will need some adjustment. It is important to study the effect of these settings on the final image quantification. For that reason, we look into the details of some of these effects.

3.1 Image Degrading Effects

Data acquisition procedures in emission tomography are very different from that of other imaging modalities, like e.g. CT or MRI. The main difference is that the pursued signal is coming from inside the patient and cannot that easily be controlled from the outside. The acquisition procedure aims at acquiring an amount of gamma-rays within a certain energy window such that images of a reasonable quality can be produced. The amount of activity administered to the patient should not be

increased beyond limits, even if this would be beneficial to the image quality. Dose levels should be kept reasonably low, while being able to perform good medical practice.

If the dose has to be kept low, one could think of increasing the acquisition time. However, the time that the patient has to spend lying on a table cannot be increased too much. Standard SPECT procedures require up to around 30 minutes. For a lot of patients, this is experienced as a very long period of which the last few minutes tend to be very uncomfortable. Moreover, the patient is required to lay perfectly still during the whole acquisition period. If the duration of the acquisition is long, there is a chance that the patient will move. Patient movement can make the spatial resolution worse, which in the end will destroy the positive effect of longer acquisition times.

A number of physical effects cannot be controlled for, but do influence image quality. These are e.g. scattered radiation, positron range, non-co-linearity of the annihilation process, random coincidence detection, ... Furthermore, it is important to perform quality inspection of all contributing systems on a regular basis. Energy settings, camera uniformity, linearity, center-of-rotation, PET normalization, dose calibrator, ... All of these systems and settings should be monitored closely by technologists and medical physicists such that an optimal imaging performance can be achieved.

In general, emission tomography leads to low count statistics, which is often said to give noisy images. Actually, the signal-to-noise ratio of emission tomography is rather low. For qualitative inspection, the images are therefore often post-processed using a variety of low-pass filters. While these smoothed images look nicer, a lot of the quantitative information has been removed. The quality of emission tomography imaging is poor compared to, for example, MRI or CT. However, the emission data contain enough information to make a tomographic reconstruction that is more than appropriate for clinical decision making.

3.2 Partial Volume and Spill-Over Effect

Suppose that a considerable amount of photons were acquired with an optimal detection efficiency. Even then, we encounter partial volume and spill-over effects.

3.2.1 Origin of the Effects

All imaging systems in which signal intensities are digitally sampled are inherently influenced by the *partial volume effect* (PVE). The importance of this effect for quantitative imaging depends on the spatial dimensions of the sampling interval and the spatial dimensions of the received signal. Any change of the intensity of the signal in between the discrete sampling intervals will lead to a signal averaging which is weighted by the sampling dimensions. Furthermore, if the imaging system has a limited spatial resolution, the signal intensity will be spread out and lead

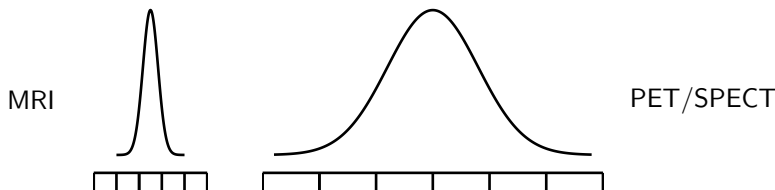


Figure 3.1: This drawing illustrates the differences between high-resolution MRI and emission tomography concerning spatial resolution and sampling properties. On the left, the dimension of a typical sampling in high-resolution MRI, using a voxel size of 1 mm, is usually equal or somewhat larger than the spatial resolution of the detector system, which is shown by the Gaussian curve. On the right, a typical detector sampling in emission tomography of the brain, using a detector size of 2.54 mm, is usually smaller than the spatial resolution of the detector, i.e. several millimeter. The average cortical thickness of the human brain is about 3 mm.

to a signal averaging which is weighted by the point spread function (PSF) of the system. Therefore, if the imaged object is only partially occupied by the sampling volume of the imaging system, the produced effect is named *partial volume* effect. On the other hand, if the PSF of the system exceeds the voxel dimensions, the signal intensity of the object in one voxel will be spilled-over to neighboring voxels. Hence, the effect is named *spill-over* effect. These image degrading effects were pointed out in the first publication of a series of papers by Hoffman *et al.* [1979].

It is important to consider the difference between the *data sampling* and the *spatial resolution* characteristics of a digital imaging system. For each emission tomography imaging protocol, a certain acquisition program is used, which includes settings for the detector sampling frequency. Sampling is defined by the size of the individual detector elements or *detector bins*. In general, the voxel size in the axial direction of the image space is set identical to the size of the detector bins. Hence, the detector sampling leads to a corresponding sampling in the image space. Emission data that has been sampled will lead to an approximation of the true tracer distribution (§2.4.2) and therefore to an inevitable loss of information. Attempting to correct for this effect will require at least some additional knowledge. This information could be measured by other medical imaging modalities.

On the other hand, the imaging system has a finite spatial resolution which is defined by the ability to resolve an infinitely small point source. The PSF of the point source in the reconstruction represents the spatial resolution of the imaging system, which is the result of both the detector spatial resolution, as well as the resolution determined by the reconstruction algorithm (e.g. post-smoothing). The limited spatial resolution of the system, due to the acquisition and reconstruction, will lead to *blurring* of the signal. This effect causes the *spill-over* of information to neighboring regions. The reason why the spill-over effect is often referred to as contributing to the partial volume effect is due to its signal averaging characteristics. Attempting to correct for this effect requires knowledge about the spatial resolution characteristics of the imaging system, which can be measured.

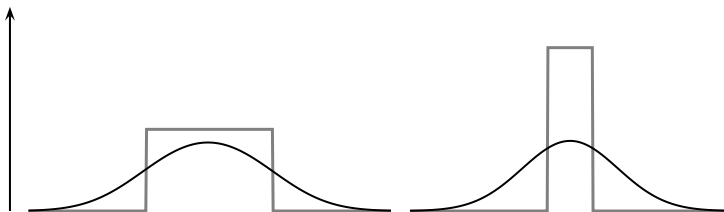


Figure 3.2: This drawing illustrates the influence of the spill-over effect on brain imaging using emission tomography. Let the rectangular functions represent a cross-section of the tracer activity in two cortical regions. On the left, a thicker cortex is shown with lower tracer uptake, on the right, a thinner cortex is shown with higher uptake. The influence of the spill-over effect is demonstrated by convolution of both curves with an identical Gaussian resolution kernel. It appears that the smoothed activity curves have the same maximum intensity and are almost indistinguishable.

In other imaging modalities, like e.g. high-resolution MRI, the sampling dimensions are usually equal or larger than the dimensions of the spatial resolution of the detector system (Fig. 3.1). Then, differences between sampling and resolution become less important and both parameters are often used as synonyms for each other. In emission tomography, the dimensions of the detector sampling are typically much smaller than the dimensions of the spatial resolution of the detector. The reason for this is that one wants to prevent that the acquisition procedure suffers from further loss of resolution.

3.2.2 Consequences for Clinical Decision Making

The loss of quantitative information for small objects can be a significant source of error in studies of the human brain using emission tomography [Hoffman *et al.*, 1979]. The combination of partial volume and spill-over effects limit the ability to accurately resolve structures having small spatial dimensions, and can lead to local under and over estimations of the radioactive tracer distribution [Fazio and Perani, 2000]. This is an important issue when imaging the human brain, since that organ exhibits a rather complex anatomical structure. The thickness and shape of many brain tissues and structures, like e.g. the cortical gray matter (GM), can change over short distances. The average cortical thickness is about 3 mm [Fischl and Dale, 2000]. This means that the spatial dimensions of brain tissues and structures are relatively small compared to the voxel size, which is typically about 2.5 mm, and the spatial resolution of the imaging system, which is about 5 mm in PET. Thereby, it becomes unclear whether certain intensity changes in regions of the reconstructed image are caused by the corresponding variations in the tracer uptake within these regions, or if these changes are due to the varying spatial dimensions of the corresponding structures compared to the resolution of the imaging system.

For physicians, it is difficult and sometimes impossible to determine whether changes observed in PET measurements in normal aging or dementia are due to changes in brain metabolism and physiology, or if these changes are the effect of

structural changes (e.g. atrophy). Perhaps it could be a combination of both [Herscovitch *et al.*, 1986]. PET and SPECT measurements of the cerebral blood flow (CBF) and metabolism may be artificially lowered in cases of normal aging and dementia, since both are associated with a significant probability for the developing of atrophy. Without correction for the PVE one cannot determine the true nature of the signal change. This effect is illustrated in Fig. 3.2.

In the presurgical evaluation of epilepsy patients, the PVE can lead to spurious hypometabolic or hypoperfusion regions, which in turn can yield an increased amount of false positive predicted epileptogenic regions. Moreover, if the finite spatial resolution of the imaging system is not accounted for, spill over of activity to neighboring regions can occur, which in turn can yield a possible misinterpretation of the extent of hypometabolic or hypoperfusion regions. Thereby, the delineation of these regions becomes more difficult and less accurate.

3.3 Partial Volume Correction

In order to reduce the influence of the PVE in emission tomography, a number of *partial volume correction* (PVC) techniques were developed. These techniques have been based on the following rationale.

3.3.1 Rationale

In §3.2, we showed that, if a method aims at reducing the influence of the PVE, it will need additional information. The reason is that the measurement does not provide enough information to correct for the PVE itself. Over the years, PVC techniques have been designed for emission tomography in which anatomical information and, in some cases, spatial resolution properties of the imaging system were included. In general, the anatomical information is measured during a separate acquisition procedure for which magnetic resonance imaging (MRI) or computed tomography (CT) can be used. Those two medical imaging modalities provide detailed structural information with a much better spatial resolution and sampling than emission tomography can provide. If the high resolution anatomical image is spatially aligned with a preliminary reconstruction of the emission data, and if the anatomical information can be extracted from the structural data, it is possible to compute the volumetric contributions of the different tissue structures to the corresponding voxels in the emission image. The knowledge that certain structures will give only partial contributions to voxels in the emission image can be used to estimate the amount of tracer activity that was averaged out by the PVE. Moreover, if the spatial resolution properties of the system are known, they can be taken into account when attempting to correct for the spill-over effect.

The spatial alignment of the functional and structural images and the ability to extract anatomical information from MRI or CT are two crucial steps for any PVC method. In fact, literature shows that the design and the evaluation of PVC

techniques has been influenced for a large part by the development of state-of-the-art image registration and segmentation algorithms. It is not the aim of this work to look deeper into image registration and segmentation methods. We will use methods that are available and for which it has been shown that they perform well for brain imaging.

Literature shows in general two methodological approaches for performing PVC in emission tomography. The first approach, which is also the oldest one, consists of using the anatomical information *after* the emission data have been reconstructed. Hence, this approach is a *post-processing* method. The second approach consists of using the anatomical information *during* the image reconstruction procedure. For this approach, statistical based image reconstruction, of which the Bayesian approach has been discussed in §2.4.3, is mostly used because it exhibits the necessary flexibility for including information during the reconstruction procedure.

3.3.2 Post-Processing Methods

Herscovitch *et al.* [1986], who initiated the search for an appropriate brain atrophy correction method for emission tomography, developed a post-processing method that corrects *global* PET data, averaged over several tomographic slices, for the influence of cerebral atrophy. The method makes use of CT measurements from which the CSF volumes of the ventricles and sulci (V^{vs}) and the total intracranial volume (V^{ic}) are extracted. The global PET measurements of CBF and cerebral metabolic rate for oxygen ($CMRO_2$) are then corrected for the influence of metabolically inactive CSF spaces by dividing the measured values by $1 - (V^{vs}/V^{ic})$. Videen *et al.* [1988] illustrated an improvement of this method using 2-D computer simulations in which the correction for metabolic inactive spaces involves *regional* PET data. The method requires aligned CT or MRI slices from which two tissue types have been extracted: *brain tissue* and *non-brain tissue*. A *brain tissue map* is created (δ^B) in which brain tissue voxels, i.e. GM and WM, are given the value 1 and non-brain tissue voxels, i.e. CSF and other, are given the value 0. Subsequently, the brain tissue map is convolved with the two-dimensional Gaussian PSF of the PET system, denoted h , to yield a spatial resolution corrected tissue map. The correction λ^{corr} of the observed PET data λ^{obs} can then be written as

$$\lambda^{\text{corr}} = \frac{\lambda^{\text{obs}}}{\delta^B \otimes h}. \quad (3.1)$$

Meltzer *et al.* [1990] extend the method to the correction of brain PET in three dimensions and makes use of MRI data. The application of MRI for atrophy correction in PET offers several advantages over CT. Improved sulci delineation and high contrast between brain and CSF when using T2-weighted pulse sequences permits greater accuracy in quantitative measurements. Moreover, the beam hardening artifact in CT is surpassed. Meltzer *et al.* [1990] reports that MRI allows further distinction between GM and WM, which could be useful in the correction for changes in the relative amounts of these tissues.

So far, the technique aims at a correction for the spill-over effect between CSF and brain tissue. It does not correct for the spill-over effect between GM and WM. Moreover, the fractional tissue contributions are ignored in these methods. A voxel is either brain tissue, or not. Hence, a considerable amount of information that is needed to correct for the partial volume effect, is neglected. The focus of these methods lies more on the spill-over than on the partial volume correction efforts.

Müller-Gärtner *et al.* [1992] extend the method of Meltzer *et al.* [1990] and describe a method which addresses the problem of PVE in the GM region. The method is based on the assumption that the *observed* reconstruction λ^{obs} is the convolution of the *actual* radioactivity distribution λ^{act} and the PSF h of the imaging system,

$$\lambda^{\text{obs}} = \lambda^{\text{act}} \otimes h. \quad (3.2)$$

The method considers the set of tissue types $\mathcal{T} = \{G, W, C\}$, i.e. GM, WM, and CSF, respectively. Each tissue type can be considered as a set of voxels. The MR data, from which the anatomical information is derived, is aligned with the emission data and *tissue images* are extracted. The tissue images δ_j^t are defined by $\delta_j^t = 1$, if voxel j is classified as belonging to tissue type $t \in \mathcal{T}$, and $\delta_j^t = 0$ otherwise. The actual radioactivity distribution in every voxel j is thought of being the sum of the individual tissue distributions,

$$\lambda_j^{\text{act}} = \lambda_j^G \delta_j^G + \lambda_j^W \delta_j^W + \lambda_j^C \delta_j^C, \quad (3.3)$$

where λ_j^G , λ_j^W , and λ_j^C , are the tissue activity concentrations in GM, WM, and CSF. Furthermore, the activity concentration within WM and CSF is assumed to be constant throughout the region, such that λ_j^W and λ_j^C in (3.3) are replaced by their mean values. These are measured in reference regions $W_{\text{ref}} \subset W$ and $C_{\text{ref}} \subset C$, respectively, in the observed reconstruction, and

$$\bar{\lambda}^W = \frac{\sum_j \lambda_j^{\text{obs}} \delta_j^{W_{\text{ref}}}}{\sum_j \delta_j^{W_{\text{ref}}}}, \quad \bar{\lambda}^C = \frac{\sum_j \lambda_j^{\text{obs}} \delta_j^{C_{\text{ref}}}}{\sum_j \delta_j^{C_{\text{ref}}}}. \quad (3.4)$$

Then, equation (3.2) becomes

$$\lambda^{\text{obs}} = (\lambda^G \delta^G) \otimes h + \bar{\lambda}^W (\delta^W \otimes h) + \bar{\lambda}^C (\delta^C \otimes h). \quad (3.5)$$

Under the condition that we can make the following approximation for the GM contribution

$$(\lambda^G \delta^G) \otimes h \approx \lambda^G (\delta^G \otimes h), \quad (3.6)$$

we can derive the following expression for the PVC of GM voxels $j \in G$,

$$\lambda_j^G = \left[\frac{\lambda^{\text{obs}} - \bar{\lambda}^W (\delta^W \otimes h) - \bar{\lambda}^C (\delta^C \otimes h)}{\delta^G \otimes h} \right]_j. \quad (3.7)$$

The approximation made in (3.6) is an equality when $\lambda^G = \bar{\lambda}^G$, or when h is a Dirac delta function. In reality, however, this is never the case.

Labbé *et al.* [1996] makes the assumption that all CSF contributions can be neglected for [¹⁸F]-FDG. From that assumption, $\bar{\lambda}^C$ is set to zero from the beginning by which (3.7) contains only GM and WM. The CSF component is removed from the PVC method. Itti *et al.* [1997] proposes a method in which the observed reconstruction is written as a spatially weighted average of the tracer concentration from an *active* compartment λ^{act} and an *inactive* compartment λ^{inact} . While previous methods used binary tissue images, a continuous range between zero and unity may now be used to characterize the contribution of a certain compartment. f^{act} and f^{inact} are the tissue contributions of the active and the inactive compartments, respectively. The observed reconstruction is then

$$\lambda^{\text{obs}} = \frac{(\lambda^{\text{act}} f^{\text{act}}) \otimes h + (\lambda^{\text{inact}} f^{\text{inact}}) \otimes h}{(f^{\text{act}} + f^{\text{inact}}) \otimes h}. \quad (3.8)$$

Using a similar approximation as in equation (3.6),

$$(\lambda^{\text{act}} f^{\text{act}}) \otimes h \approx \lambda^{\text{act}} (f^{\text{act}} \otimes h), \quad (3.9)$$

and with the assumption that the inactive compartment has no tracer uptake, i.e. $\lambda^{\text{inact}} = 0$, the PVC method of Itti *et al.* [1997] becomes

$$\lambda^{\text{act}} = \frac{(f^{\text{act}} + f^{\text{inact}}) \otimes h}{f^{\text{act}} \otimes h} \lambda^{\text{obs}}. \quad (3.10)$$

Another type of post-processing PVC technique was proposed by Rousset *et al.* [1998]. In their method, the geometric interaction between the observed reconstruction and the actual radioactive tracer distribution is characterized. Similar to Müller-Gärtner *et al.* [1992], the method starts from the assumption that the observed reconstruction is the convolution of the actual distribution λ^{act} and the PSF of the system (3.2) and the actual distribution is assumed to be the linear sum of T different tissue compartments,

$$\lambda^{\text{act}} = \sum_{t=1}^T \lambda^{\text{act},t} \delta^t, \quad (3.11)$$

and $\delta_j^t = 1$ if j belongs to tissue compartment t (cfr. 3.3). However, in this method, each tissue compartment is considered to have a uniform radioactive tracer distribution throughout the compartment, or $\lambda_j^{\text{act},t} \approx \bar{\lambda}^{\text{act},t} \delta_j^t$, such that

$$\lambda^{\text{obs}} = \sum_{t=1}^T \bar{\lambda}^{\text{act},t} (\delta^t \otimes h). \quad (3.12)$$

Then, in each compartment t' , the observed mean radioactive tracer distribution is equal to

$$\bar{\lambda}^{\text{obs},t'} = \frac{1}{\sum_l \delta_l^{t'}} \sum_j \delta_j^{t'} \lambda_j^{\text{obs}} \quad (3.13)$$

$$= \frac{1}{\sum_l \delta_l^{t'}} \sum_j \delta_j^{t'} \sum_{t=1}^T \bar{\lambda}^{\text{act},t} (\delta^t \otimes h)_j. \quad (3.14)$$

Equation (3.14) can then be written as

$$\bar{\lambda}^{\text{obs},t'} = \sum_{t=1}^T \omega_{t,t'} \bar{\lambda}^{\text{act},t}, \quad \text{and} \quad \omega_{t,t'} = \frac{1}{\sum_l \delta_l^{t'}} \sum_j \delta_j^{t'} (\delta^t \otimes h)_j, \quad (3.15)$$

which is a system of linear equations $\bar{\Lambda}^{\text{obs}} = \Omega \bar{\Lambda}^{\text{act}}$. The elements of $\Omega = \{\omega_{t,t'}\}$ express the spill-over of activity from tissue compartment t into tissue compartment t' . Ω is called the geometric transfer matrix (GTM). The actual tracer distribution mean value in each tissue compartment $\bar{\lambda}^{\text{act},t}$ is then found by solving the system of linear equations $\bar{\Lambda}^{\text{act}} = \Omega^{-1} \bar{\Lambda}^{\text{obs}}$. Rousset *et al.* [1998] finally proposes a theoretically more refined GTM in which the acquisition and reconstruction procedure of the imaging system are incorporated. Instead of using the convolution with the PSF of the system, the elements of the GTM are implemented as

$$\omega_{t,t'} = \frac{1}{\sum_l \delta_l^{t'}} \sum_j \delta_j^{t'} (\text{FBP}(\mathcal{P} \delta^t))_j, \quad (3.16)$$

where \mathcal{P} models the acquisition step, implemented as a projection operation, and FBP expresses the reconstruction step, implemented as the filtered back-projection operation. Frouin *et al.* [2002] compared the methods based on equation (3.15) and based on equation (3.16), and found not much difference.

Of all post-processing PVC methods presented so far, not one considers an appropriate noise model for the observed image data. A more general framework for PVC, in which both correlated and uncorrelated noise components are used, was recently proposed by Aston *et al.* [2002]. The general PVE, i.e. the combination of spill-over effect and partial tissue contribution, is modeled as

$$\lambda^{\text{obs}} = h \otimes \left[\left(\sum_r \sum_t \delta^r f^t \lambda_r^t \right) + \eta_c \right] + \eta_u, \quad (3.17)$$

where λ^{obs} is the observed reconstruction, η_c and η_u are the correlated and uncorrelated noise components, respectively, δ^r is the binary image vector for the selection of the anatomical regions, f^t is the tissue fraction vector, h accounts for the PSF of the system, and λ_r^t is the vector denoting the true tissue activity concentration in the different classified regions. Actually, equation (3.17) is formulated using matrix operations, rearranged to a linear equation of the form $ax = b + \epsilon$, and solved using weighted least-squares estimation.

3.3.3 Statistical Techniques

Accurate quantification of emission tomography data requires accurate modeling of the acquisition procedure. The statistical framework, which forms the foundation of many iterative reconstruction techniques for emission tomography, can very efficiently accommodate for this requirement (cfr. §2.4.3). The theory exhibits the necessary flexibility to model the acquisition procedure accurately, such that optimal

correction measures for the spill-over effect and other image degrading effects can be pursued. Furthermore, the objective function, which is optimized by the algorithm, can be adjusted in such way that it contains an additional regularization or penalization component. This component can then be used for the implementation of a PVC method. The structural information, which is required for performing PVC, can then be used during the image estimation step, as opposed to post-processing PVC methods.

Many research groups have explored various ways for the incorporation of structural information in the statistical reconstruction framework for emission tomography. With the introduction of the MAP reconstruction algorithm in emission tomography (cfr. §2.4.3), it soon became clear that two main objectives could be pursued. These two are (a) local regularization, for which e.g. Gibbs-Markov priors can be used, and (b) global regularization, for which e.g. Gaussian priors can be used. Both approaches have been investigated concerning the extension towards anatomy based regularization. Some groups have used combinations of both techniques, while others devised complete new ones.

An anatomy based spatially-variant penalized-likelihood method was proposed by Fessler *et al.* [1992]. In their method, a modified Gibbs-Markov prior, given by

$$M(\Lambda) \propto - \sum_j \sum_{k \in \mathcal{N}_j} \omega_{jk} (\lambda_j - \lambda_k)^2, \quad (3.18)$$

is used in MAP reconstruction of emission data. The prior weights ω_{jk} , which are held fixed for the duration of the estimation procedure, control the influence of the quadratic penalty function and depend on whether a tissue boundary is present in, or between, two neighboring voxels j and k . If a tissue boundary occurs, the prior weight is lowered and the penalty term tolerates the occurrence for an edge. In the other case, the penalty function favors small intensity differences for neighboring voxels, which gives smooth solutions. Optimization of the posterior function is achieved by means of the generalized EM method [Hebert and Leahy, 1989].

As shown in §2.4.3, the local smoothness properties of Gibbs-Markov priors provide a natural solution against image degrading effects on a local scale. Moreover, the prior is easily modified for the incorporation of additional, in this case structural, information provided by another imaging modality. In practice, however, the anatomical information will be imperfect due to e.g. noise in the MR data. Fortunately, the Gibbs-Markov prior lends itself naturally to an approach in which the prior weights ω_{jk} are *blurred* or *dilated* with a kernel whose width corresponds to the uncertainty of the structural information at the particular location. Although this approach is not necessarily the optimal choice for accommodating imperfect anatomical information, it yields reasonable results [Fessler *et al.*, 1992].

Instead of using anatomical information which is held fixed for the whole duration of the image estimation procedure, Gindi *et al.* [1993] propose the inclusion of a coupling term between anatomy and function in the MAP reconstruction of emission data. The coupling term influences the creation of image discontinuities in the vicinity of significant anatomical boundaries. In some cases, anatomical edges

may be completely missing or inappropriate edges may occur [Geman and Geman, 1984].

Ouyang *et al.* [1994] design a weighted line site approach which considers the joint probability distribution of the anatomical and the emission data. By that, the reconstruction of the emission data is more protected against possible discrepancies between the anatomical and the functional data, which could lead to image artifacts. Where there are inconsistencies, the reconstruction is performed with the emission data only.

The clinical feasibility of performing anatomy based reconstruction for whole-body PET-CT was investigated by Comtat *et al.* [2002]. The authors proposed a reconstruction method which offers a solution for mismatches between the anatomical and functional data. The method assumes that, for a set of tissue types \mathcal{T} , and based on the anatomical information contained in aligned CT data, binary tissue images δ_j^t can be constructed, where $\delta_j^t = 1$ if j is classified as belonging to tissue type $t \in \mathcal{T}$, and $\delta_j^t = 0$ otherwise. The uncertainty of the anatomical information is modeled by convolving the binary tissue images using a Gaussian smoothing kernel h with the width of the kernel corresponding to the accuracy of the anatomical and functional image alignment. This approach is similar to that proposed by Fessler *et al.* [1992]. The emission data are then reconstructed using a penalized weighted least-squares objective function (PWLS) [Fessler, 1994],

$$\Psi(\Lambda) = \sum_i \frac{\left(\sum_j c_{ij} \lambda_j - q_i \right)^2}{\sigma_i^2} + \beta \sum_j \sum_{k \in \mathcal{N}_j} \frac{\omega_{jk}}{d_{jk}} (\lambda_j - \lambda_k)^2, \quad (3.19)$$

where σ_i are the estimated standard deviations of the projection data, β is the weight of the penalty term, d_{jk} is the Euclidean distance between voxels j and k , and ω_{jk} are the penalty weights between neighboring voxels depending on the blurred anatomical labels,

$$\omega_{jk} = \sum_{t \in \mathcal{T}} (\delta^t \otimes h)_j (\delta^t \otimes h)_k. \quad (3.20)$$

The authors prefer the PWLS algorithm because the effect of all correction steps on the projection data (Fourier rebinning, attenuation, scatter, random detections, detector efficiencies, ...) are included in the standard deviation σ . The algorithm has also fast convergence properties with 3-D PET emission data. The anatomy based PWLS reconstruction is found by minimizing Ψ using a coordinate-descent algorithm,

$$\hat{\Lambda} = \arg \min_{\Lambda \geq 0} \Psi(\Lambda). \quad (3.21)$$

Lipinski *et al.* [1997] compare the local regularization approach, using a Gibbs-Markov prior, with the global regularization approach, using a Gaussian prior, for the incorporation of anatomical information in MAP reconstruction of PET projection data. For a set of tissue types \mathcal{T} , binary tissue images δ^t are extracted

from aligned MR data. For the local regularizing MAP algorithm, the log-prior is given by

$$M = - \sum_j \sum_{k \in \mathcal{N}_j} \frac{\omega_{jk}}{d_{jk}} \ln (\cosh |\lambda_j - \lambda_k|). \quad (3.22)$$

Only neighboring voxels belonging to the same tissue type are included, such that the local prior weights are defined as

$$\omega_{jk} = \sum_{t \in \mathcal{T}} \delta_j^t \delta_k^t. \quad (3.23)$$

Optimization of the log-posterior is achieved by the OSL reconstruction algorithm (2.63). In contrast to Gibbs-Markov priors, applying a Gaussian prior requires prior knowledge about the mean and standard deviation of the assumed underlying tracer activity distribution. To solve this problem, the algorithm is preceded by calculating the average activity for each tissue using a ML-EM reconstruction algorithm. This approach was previously suggested by [Carson \[1986\]](#) for the reconstruction of regions-of-interest. The average tissue activity for tissue t is then computed by

$$m_t^{n+1} = m_t^n \sum_{i=0}^{I-1} \frac{\tilde{c}_{it} q_i}{\sum_{t \in \mathcal{T}} \tilde{c}_{it} m_t^n}, \quad (3.24)$$

where $\tilde{c}_{it} = \sum_j \delta_j^t c_{ij}$ is the sensitivity of detector i for activity in the region occupied by tissue type t . It is assumed that $\sum_i \tilde{c}_{it} = 1$, for all $t \in \mathcal{T}$. For the global regularizing MAP algorithm, the log-prior is then given by

$$M = - \sum_j \frac{(\lambda_j - \mu_j)^2}{2\sigma_j^2}, \quad (3.25)$$

where $\mu_j = \sum_{t \in \mathcal{T}} \delta_j^t m_t$, and where σ_j is the standard deviation of the assumed underlying Gaussian tracer distribution. Optimization of the log-posterior is achieved by the following iterative algorithm, which was derived by [Levitian and Herman \[1987\]](#),

$$\lambda_j^{n+1} = \frac{1}{2} (\mu_j - \sigma_j^2) + \frac{1}{2} \sqrt{(\mu_j - \sigma_j^2)^2 + 4\sigma_j^2 \lambda_j^n \sum_i \frac{c_{ij} q_i}{\sum_{j'} c_{ij'} \lambda_{j'}^n}}. \quad (3.26)$$

It is assumed that $\sum_i c_{ij} = 1$, for all j . [Lipinski *et al.* \[1997\]](#) conclude that the local regularization approach proves to be more stable in the case of incomplete anatomical information. Small hypo- or hyperintensity regions, which have no anatomical counterpart, are better delineated than with the ML-EM algorithm. Shifted anatomical information results in a limited error of the reconstruction when the Gibbs-Markov prior is used.

Thus far, the incorporation of anatomical information has been based on binary tissue classification. Although in some methods the anatomical information

was blurred to handle the uncertainty of the structural information, for the Gibbs-Markov and Gaussian prior, tissue boundaries are assumed to occur *between* voxels. In Geman and Geman [1984], this is called the *line-site* approach, by which the authors refer to the Markov random field lattice. Although this approach yields already reasonable results, it is in theory insufficient to correct for the complete PVE. A substantial correction for PVE requires information about the partial activity contribution of each tissue to a certain voxel.

For that reason, Sastry and Carson [1997] base their method on a *tissue composition model*. They introduce *auxiliary* variables λ_{jt} which represent the activity level of tissue type t at voxel j . If j would be composed entirely of tissue type t , then the total activity would be λ_j . If the voxel is a composition of different tissue types, then the total activity is a sum over all activity levels λ_{jt} which are weighted by the corresponding tissue fractions f_j^t , or

$$\lambda_j = \sum_{t \in T} f_j^t \lambda_{jt}. \quad (3.27)$$

The authors derive a MAP reconstruction algorithm for the estimation of the auxiliary tissue type activities λ_{jt} . They consider two prior functions. For the first prior function, the activity level of each tissue type is assumed to be close to the global mean value. As such, a global constraint is imposed using a Gaussian prior, given by

$$M_G = - \sum_j \sum_{t \in T} \frac{(\lambda_{jt} - \mu_t)^2}{2\sigma_t^2}. \quad (3.28)$$

For the second prior function, it is assumed that, in addition to the global constraint, the activity within each tissue type is correlated and varies smoothly. This local constraint, which is modeled as a Gibbs-Markov prior, is then added to the global constraint, and the second prior is $M_{GS} = M_G + M_S$, where

$$M_S = - \frac{1}{N} \sum_j \sum_{t \in T} \sum_{k \in \mathcal{N}_j} \frac{(\lambda_{jt} - \lambda_{kt})^2}{2\varsigma_{jt}^2}, \quad (3.29)$$

and N is the number of neighbors in \mathcal{N}_j . The tissue means in equation (3.28) are computed from the current tissue activity estimates λ_{jt}^n ,

$$\mu_t = \frac{\sum_j f_j^t \lambda_{jt}^n}{\sum_j f_j^t}. \quad (3.30)$$

In equation (3.28), the standard deviation σ_t controls the strength of the global constraint and is taken proportional to the global tissue mean activity of the current estimate, or $\sigma_t \propto \mu_t$. In equation (3.29), the standard deviation ς_{jt} controls the strength of the local constraint and is taken proportional to the local tissue mean activity of the current tissue activity estimate, or $\varsigma_{jt} \propto \eta_{jt}$, where

$$\eta_{jt} = \frac{1}{N} \sum_{k \in \mathcal{N}_j} \lambda_{kt}^n. \quad (3.31)$$

The MAP estimates of λ_{jt} for using the first prior function M_G , and with the EM algorithm of Levitan and Herman [1987], are

$$\begin{aligned}\lambda_{jt}^{n+1} = & \frac{1}{2} \left(\mu_t - \sigma_t^2 \sum_i c_{ij} f_j^t \right) \\ & + \frac{1}{2} \sqrt{\left(\mu_t - \sigma_t^2 \sum_i c_{ij} f_j^t \right)^2 + 4\sigma_t^2 \lambda_{jt}^n \sum_i \frac{c_{ij} f_j^t q_i}{\sum_{j',t} c_{ij'} f_{j'}^t \lambda_{j't}^n}}\end{aligned}\quad (3.32)$$

When using the second prior function M_{GS} , the estimates are

$$\begin{aligned}\lambda_{jt}^{n+1} = & \frac{1}{2} \left(\Gamma_{jt} - \Omega_{jt}^2 \sum_i c_{ij} f_j^t \right) \\ & + \frac{1}{2} \sqrt{\left(\Gamma_{jt} - \Omega_{jt}^2 \sum_i c_{ij} f_j^t \right)^2 + 4\Omega_{jt}^2 \lambda_{jt}^n \sum_i \frac{c_{ij} f_j^t q_i}{\sum_{j',t} c_{ij'} f_{j'}^t \lambda_{j't}^n}}\end{aligned}\quad (3.33)$$

where

$$\Gamma_{jt} = \left(\frac{\mu_t}{\sigma_t^2} + \frac{\eta_{jt}}{\varsigma_{jt}} \right) \Omega_{jt}^2 \quad \text{and} \quad \Omega_{jt}^2 = \left(\frac{1}{\sigma_t^2} + \frac{1}{\varsigma_{jt}^2} \right)^{-1}. \quad (3.34)$$

Note that in (3.26) the tissue means μ_j are constant during iterations. As a result, the EM algorithm for MAP optimization with a Gaussian prior is exact [Levitin and Herman, 1987]. In (3.32) and (3.33), the tissue means μ_t and Γ_{jt} , respectively, are updated for each iteration. This results in algorithms that are only approximately EM.

Some groups have explored the use of objective functions, other than the Poisson likelihood, for the incorporation of structural information in emission tomography. Ardekani *et al.* [1996] present a method which is based on the *cross-entropy* or *Kullback-Leiber distance*. In general, the cross-entropy term S , which is given by

$$S(U, V) = \sum_i \left[u_i \ln \left(\frac{u_i}{v_i} \right) - (u_i - v_i) \right], \quad (3.35)$$

measures the dissimilarity between $U = \{u_i\}$ and $V = \{v_i\}$. By making use of the notational conventions in §2.4.3, we can write the cross-entropy between the measured emission data Q , and the projection of the current image estimate $\mathcal{P}\Lambda$, as

$$S(Q, \mathcal{P}\Lambda) = \sum_i \left[q_i \ln q_i - q_i \ln \left(\sum_j c_{ij} \lambda_j \right) - q_i + \sum_j c_{ij} \lambda_j \right]. \quad (3.36)$$

This formulation of the objective function is closely related to the log-likelihood $L(Q|\Lambda)$, as can be seen in combination with equation (2.47),

$$S(Q, \mathcal{P}\Lambda) = -L(Q|\Lambda) + \sum_{i=0}^{I-1} \left[q_i \ln q_i - q_i - \ln(q_i!) \right]. \quad (3.37)$$

Hence, maximizing the logarithm of the likelihood $L(Q|\Lambda)$ is equivalent to minimizing the cross-entropy $S(Q, \mathcal{P}\Lambda)$. The anatomy based reconstruction method which is presented by [Ardekani et al. \[1996\]](#) consists of minimizing a weighted sum of two cross-entropy terms. The first term is equal to equation (3.37), while the second term is the cross-entropy which measures the dissimilarity between the image estimate and a prior image model $\Theta = \{\theta_j \mid j = 0, \dots, J-1\}$. The anatomical information, which is derived from aligned MR data, is encoded in the prior image model. The voxel-by-voxel update formula which they obtain, is given by

$$\lambda_j^{n+1} = \frac{\lambda_j^n}{\sum_i c_{ij}} \left[\sum_i \frac{c_{ij} q_i}{\sum_{j'} c_{ij'} \lambda_{j'}^n} - \beta \ln \left(\frac{\lambda_j^n}{\theta_j} \right) \right]. \quad (3.38)$$

If the second term between square brackets in equation (3.38) becomes larger than the first term, i.e. when the weight β of the prior image model is large, the positivity constraint for Λ is violated. The alternative update function, derived from the Kuhn-Tucker conditions, is then

$$\lambda_j^{n+1} = \theta_j \exp \left[-\frac{1}{\beta} \left(\sum_i c_{ij} - \sum_i \frac{c_{ij} q_i}{\sum_{j'} c_{ij'} \lambda_{j'}^n} \right) \right] \quad (3.39)$$

Then, equations (3.38) and (3.39) form the hybrid minimum cross-entropy (MXE) reconstruction algorithm. The anatomical information is then incorporated in Θ using adaptive smoothing of the previous image estimate Λ^n ,

$$\theta_j = \frac{1}{N_j} \sum_{k \in \mathcal{N}_j} \frac{\omega_{jk}}{d_{jk}} \lambda_k^n \quad \text{with} \quad N_j = \sum_{k \in \mathcal{N}_j} \frac{\omega_{jk}}{d_{jk}}, \quad (3.40)$$

and where ω_{jk} are based on a gradient inverse weighted smoothing method

$$\omega_{jk} = \begin{cases} 1 & \iff \forall t \in \mathcal{T} : f_j^t = f_k^t, \\ \left[\sum_{t \in \mathcal{T}} (f_j^t - f_k^t)^2 \right]^{-1/2} & \iff \text{otherwise.} \end{cases} \quad (3.41)$$

This MXE algorithm was extended by [Som et al. \[1998\]](#) through the inclusion of a Gaussian smoothing kernel in the ω_{jk} of equation (3.41).

[Bowsher et al. \[1996\]](#) include an image segmentation model into their Bayesian reconstruction method and, while doing so, make use of high-resolution anatomical information. The presented method assumes that the tracer distribution can be approximated by a set of nearly uniform emission volumes or regions. The regions are distinguished from one another by their mean intensity and by their spatial separation. Neither the number of regions nor the region classification of individual voxels are assumed to be known a priori. Both are estimated as part of the image restoration or reconstruction. The disadvantage of the method lies in the the uniformity assumption within each region. Recently, [Bowsher et al. \[2003\]](#) proposed an emission tomography reconstruction framework which also includes parameters for the alignment of emission tomography data with MRI or CT. The method assumes uniform tracer activity within each region of a segmented MRI or CT image.

A Levenberg-Marquardt estimation procedure is used for joint optimization of the alignment parameters and the regional tracer activities. Again, the disadvantage of the methods lies in the uniformity assumption.

The correlation between spatially aligned anatomical and functional image sets of the same subject can be studied by means of the *joint histogram* of the intensity values of both imaging modalities. This approach in combination with basic concepts from information theory has shown to be very successful for the spatial registration of image data provided by different medical imaging modalities [Maes *et al.*, 1997]. Using a similar approach, Rangarajan *et al.* [2000] developed a Bayesian *joint mixture* framework for the incorporation of anatomical image intensity and region segmentation information into the reconstruction of emission data. The joint mixture framework is used to model the joint probability density function between anatomical and functional image data. In addition, segmentation images of the anatomical data are used to constrain the joint mixture model, and a prior on the joint mixture occupation probability is used to express the tight coupling between anatomy and function. The MAP estimation of the projection data then acquires the interpretation of including *mutual information* maximization between the anatomical and functional information. The objective function is a linear combination of the Poisson log-likelihood and the joint mixture log-prior. Parameters of the joint mixture prior are estimated from the projection and segmentation data. Then, the proposed reconstruction algorithm is a clever integration of an EM algorithm for the mixture decomposition, inside an EM algorithm for the log-likelihood of the emission data. Optimization of the log-posterior is obtained using an alternating descent algorithm.

3.3.4 Discussion

Literature shows two methodological approaches for performing PVC in emission tomography. The most important difference between those two is the stage at which the correction for the PVE is done, i.e. *during* or *after* reconstruction of the projection data. In §3.1 and §3.2, we have shown that contributions to the PVE are made at different stages of the imaging procedure. Against many image degrading effects generated by the acquisition hard- and software, little can be done once the data have been acquired. Although, there are exceptions, like e.g. resolution recovery and scatter correction techniques, which have been devised to compensate for the effect as much as possible. What is left for improvement are the contributions to the PVE that are made during the reconstruction procedure. For optimal PVC performance, a reconstruction strategy which gives minimal contributions to the PVE should be used.

In most cases, post-processing techniques make use of analytical reconstruction methods that make no effort in minimizing the contributions to the PVE. The statistical reconstruction framework maintains better solutions to achieve that goal. Resolution recovery and edge-preserved noise suppression, which are two essential components for performing PVC, can be modeled during the reconstruction procedure, and can thereby compensate for the PVE. In the next section, we propose an

anatomy based MAP reconstruction algorithm for PVC of emission tomography of the brain of epilepsy patients.

3.4 Anatomy Based MAP Reconstruction

We present an anatomy based MAP reconstruction algorithm, called A-MAP, which is designed to correct for the PVE during the reconstruction of emission tomography data of the brain using segmented MRI data. In a first step, we give an explicit formulation and derivation of the reconstruction algorithm.

3.4.1 Assumptions

The main purpose of white matter (WM) is to ensure connections between GM nerve cells. The metabolic activity of WM is known to be lower and much more uniform than that of GM [Huang *et al.*, 1980; Turkheimer *et al.*, 1994]. We will assume that the WM activity contribution in the reconstruction is based on a uniform distribution. One of the main tasks of the cerebrospinal fluid (CSF) is to protect the brain and play the role of buffer. Radiopharmaca, like e.g. ^{18}F -FDG and $^{99\text{m}}\text{Tc}$ -ECD, are not expected to enter the CSF when they are injected into a vein. For that reason, the basic assumption will be that during the acquisition period no emission data is expected to be originating from within the CSF. In practice however, we will assume that the CSF activity distribution is expected to be uniform with a zero mean value.

The identification of GM, WM and CSF is obtained from high-resolution anatomical MRI data of the brain. Current brain segmentation algorithms can very accurately determine the three tissue classes, i.e. GM, WM, and CSF [Van Leemput *et al.*, 1999]. The remaining unlabeled image voxels are grouped in an additional tissue class that is labeled with the name *other*. In most segmentation algorithms, the procedure returns the probability that a voxel belongs to a certain tissue class. That approach is generally called a *fuzzy tissue classification*. For each voxel, we will assume that the probability for a tissue class approximates the underlying tissue composition. In practice, high-resolution anatomical information is aligned (cfr. next paragraph) and down-sampled to the PET or SPECT sampling grid. One can reasonably assume that the aligned tissue probabilities approximate the underlying tissue composition and can be interpreted as a tissue fraction [Sastry and Carson, 1997]. The set of segmentation images is then denoted $\mathcal{F} = \{f_j^G, f_j^W, f_j^C, f_j^O\}$, with G for GM, W for WM, C for CSF, and O for the class *other*, and represents the a priori knowledge which will be incorporated in the reconstruction algorithm. Each voxel in these segmentation images contains a value between 0 and 1, which represents the tissue fraction for that particular voxel. Note that

$$\forall j : f_j^G + f_j^W + f_j^C + f_j^O = 1. \quad (3.42)$$

As mentioned before, differences in geometric alignment and image sampling are typical for images of the same patient using two different imaging modalities.

However, using a state-of-the-art image registration algorithm, it is possible to compute the affine transformation matrix \mathcal{T} that is required to align the MRI data with the emission tomography data [Maes *et al.*, 1997]. Of course, this action requires a preliminary reconstruction of the emission data. Because the human brain is a rather rigid structure, registration algorithms perform very well and are accurate. Therefore, we will neglect registration errors in the derivation of the algorithm.

3.4.2 Derivation of A-MAP

Consider a radioactive tracer distribution $\Lambda = \{\lambda_j \mid j = 0, \dots, J-1\}$ inside the brain of a subject that is located inside the FOV of an emission tomograph. In case of a PET scanner, q_i gamma ray pairs, and in case of a SPECT scanner, q_i photons are measured at line of response i . If λ_j represents the amount of activity in voxel j , and c_{ij} is the probability that photons emitted in voxel j are detected in detector (pair) i , then $E(q_i) = \sum_j c_{ij} \lambda_j$ represents the expected amount of photons, or photon pairs. The system matrix of detection probabilities $\{c_{ij}\}$ contains the mathematical description of the projection operation with the associated physical effects that take place in between emission and detection of photons. These effects include gamma ray attenuation and detector resolution modeling. We will ignore the contribution of scatter and, in case of PET, of random detections in the subsequent theoretical framework of this derivation. Since we assume that the measurements are samples from a Poisson distribution, the logarithm of the likelihood of measuring q_i , when $E(q_i)$ is expected, is given by equation (2.47). The Bayesian MAP estimation of reconstruction Λ is found by computing (2.62), in which L is the logarithm of the likelihood of measuring $Q = \{q_i\}$ given Λ , and M is the logarithm of the prior function that is used to impose additional constraints on the solution.

Each voxel of the radioactive tracer distribution can be thought of as a source containing a certain amount of tracer activity λ_j which is equal to the total amount of fractional activities of the contributing tissues. This *tissue composition model* of the tracer distribution can be written as

$$\forall j : \lambda_j = f_j^G \lambda_j^G + f_j^W \lambda_j^W + f_j^C \lambda_j^C + f_j^O \lambda_j^O. \quad (3.43)$$

The measured emission data, however, provides only sufficient information to estimate for each voxel the sum of all fractional activities. This means that there is not enough information to solve the reconstruction problem for each parameter of the composition model. Because of that, we are forced to introduce additional knowledge based on the above stated assumptions, make an approximation of the composition model, and reduce the number of unknown parameters.

We propose a MAP based reconstruction algorithm that is designed to perform PVC within a certain tissue of interest. For the presurgical evaluation of epilepsy patients, and presumably also for a number of other applications which are not investigated in this dissertation, this tissue of interest is the GM. In order to perform PVC, regularization is introduced within a number of tissue classes. Because

some voxels contain more than one tissue type, a method is needed to restrict the regularization to a single tissue class within a voxel. For that purpose, we introduce the following classification scheme.

We define a number of subsets of voxel space $\mathbb{J} = \{j \mid j = 0, \dots, J-1\}$. The subsets are based on the anatomical information that is included in the spatially aligned segmentation images. The first subset \mathbb{B} corresponds to voxels that are belonging to the brain, i.e. the subset of *brain* voxels. The second subset, complementary to \mathbb{B} , is denoted \mathbb{O} and represents the class *other*. These subsets are defined by

$$\mathbb{B} = \{j \in \mathbb{J} \mid f_j^G + f_j^W + f_j^C > \varepsilon\}, \quad (3.44)$$

$$\mathbb{O} = \mathbb{J} \setminus \mathbb{B}. \quad (3.45)$$

The threshold parameter ε controls the inclusion of voxels that are segmented into either GM, WM, or CSF. The value of this parameter should be very small, $0 < \varepsilon \ll 1$, such that all voxels containing at least some fraction of one of the three tissue types are included in \mathbb{B} . Subset \mathbb{G} is defined as the set of voxels in which the GM tissue fraction exceeds the value of the predefined segmentation threshold parameter ε , i.e. the subset of voxels containing at least some *gray matter*. The complementary part of \mathbb{G} in \mathbb{B} , is denoted \mathbb{N} , and named the subset of *non-gray matter* voxels. These subsets are defined by

$$\mathbb{G} = \{j \in \mathbb{J} \mid f_j^G > \varepsilon\}, \quad (3.46)$$

$$\mathbb{N} = \mathbb{B} \setminus \mathbb{G}. \quad (3.47)$$

For reasons that will become clear later, we want that voxels composed of mainly WM are included in subset \mathbb{W} , and voxels composed of mainly CSF are included in subset \mathbb{C} , i.e. the subset of *white matter* and *cerebrospinal fluid* voxels,

$$\mathbb{W} = \{j \in \mathbb{N} \mid f_j^W > (1 - \varepsilon)\}, \quad (3.48)$$

$$\mathbb{C} = \{j \in \mathbb{N} \mid f_j^C > (1 - \varepsilon)\}. \quad (3.49)$$

The set of remaining voxels within \mathbb{N} , i.e. those voxels that contain a mixture of WM and CSF, are included in subset \mathbb{R} , which is defined as

$$\mathbb{R} = \mathbb{N} \setminus (\mathbb{W} \cup \mathbb{C}). \quad (3.50)$$

An example of this classification scheme using simulated MRI data is shown in Fig. 3.3.

For the presurgical evaluation of epilepsy patients, but also in a number of other applications, it is very reasonable to assume that the uptake of tracer activity inside the WM and CSF are well modeled by means of a narrow Gaussian activity distribution with a position independent mean value. Moreover, in many cases the CSF activity is expected to approximate zero. For voxels containing GM, we will assume that the activities of WM and CSF are exactly equal to the mean of their distribution. In addition, we will assume that GM is surrounded by WM and CSF only, such that $f_j^O \approx 0$ for all voxels $j \in \mathbb{G}$. With these assumptions, the GM

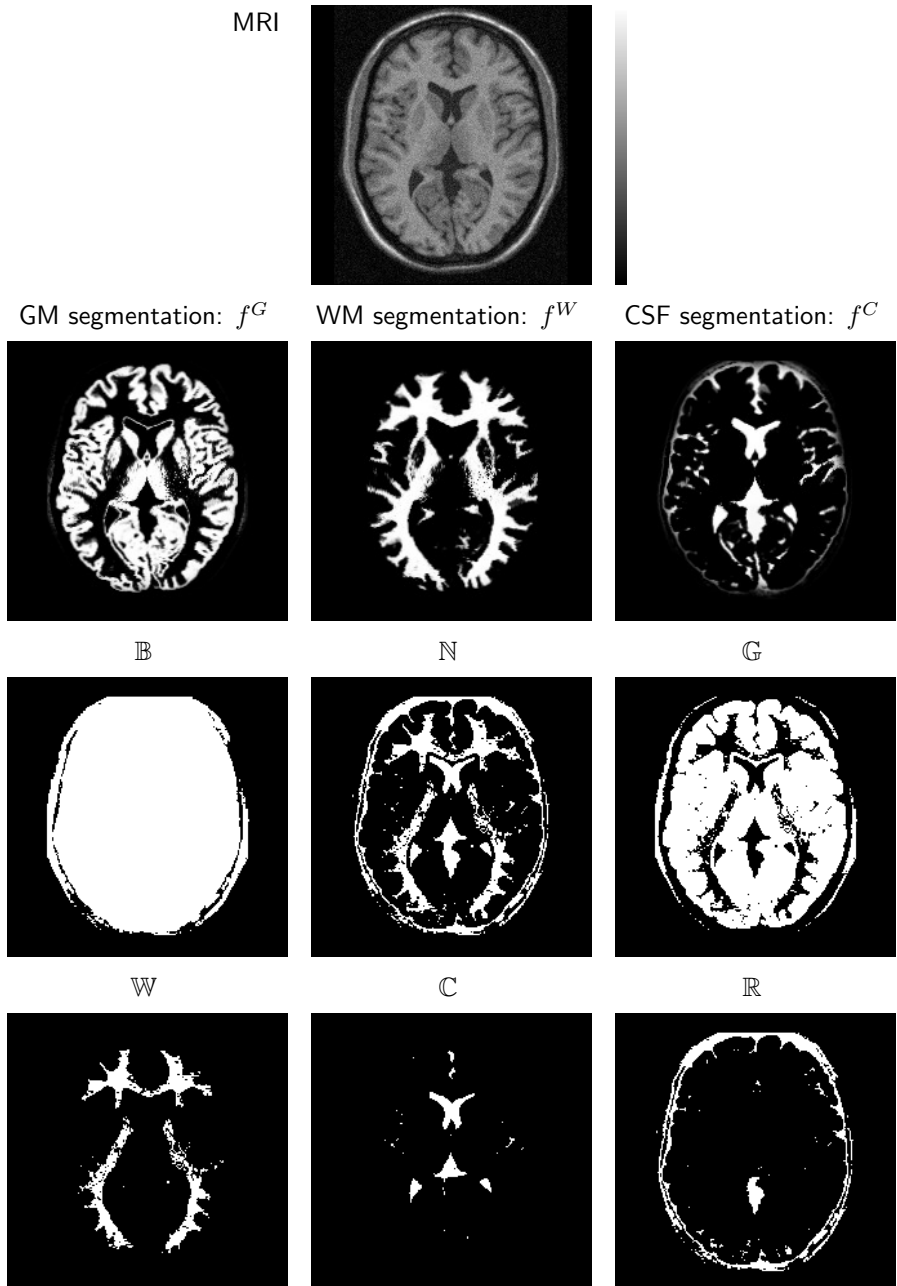


Figure 3.3: These images illustrate the use of subsets in A-MAP. This example is based on simulated MRI of a normal brain using a T1-weighted pulse sequence and a noise level of 7% [Collins *et al.*, 2002]. The GM, WM, and CSF segmentations were obtained by SPM99, and subsets B, N, G, W, C, and R were obtained by using equation (3.44)–(3.50). Voxels belonging to the subset are in white.

activity can be computed from the total activity of the voxel. Then, for all $j \in \mathbb{G}$, equation (3.43) is approximated by

$$\forall j \in \mathbb{G} : \lambda_j \approx f_j^G \lambda_j^G + f_j^W \bar{\lambda}^W + f_j^C \bar{\lambda}^C \quad (3.51)$$

with

$$\bar{\lambda}^W = \frac{1}{n_{\mathbb{W}}} \sum_{l \in \mathbb{W}} f_l^W \lambda_l, \quad n_{\mathbb{W}} = \sum_{l \in \mathbb{W}} f_l^W, \quad (3.52)$$

$$\bar{\lambda}^C = \frac{1}{n_{\mathbb{C}}} \sum_{l \in \mathbb{C}} f_l^C \lambda_l, \quad n_{\mathbb{C}} = \sum_{l \in \mathbb{C}} f_l^C. \quad (3.53)$$

This means that we have replaced the WM and CSF contribution in \mathbb{G} with $\bar{\lambda}^W$, i.e. the mean activity in the “white matter” region \mathbb{W} , and $\bar{\lambda}^C$, i.e. the mean activity in “CSF” region \mathbb{C} , respectively.

Instead of estimating $\Lambda = \{\lambda_j \mid j \in \mathbb{J}\}$, we introduce a new set of variables Λ^* , which is defined as

$$\Lambda^* = \{\lambda_j^* \mid j \in \mathbb{J}\} \triangleq \{\lambda_j^G \mid j \in \mathbb{G}\} \cup \{\lambda_j \mid j \in \mathbb{J} \setminus \mathbb{G}\}, \quad (3.54)$$

and can be considered as a parameter transformation of the set of original variables,

$$\forall j \in \mathbb{J} \setminus \mathbb{G} : \lambda_j \longrightarrow \lambda_j \quad (3.55)$$

$$\forall j \in \mathbb{G} : \lambda_j \longrightarrow \lambda_j^G = \frac{\lambda_j - f_j^W \bar{\lambda}^W - f_j^C \bar{\lambda}^C}{f_j^G}. \quad (3.56)$$

This transformation allows us to estimate only the GM activity contribution, even in those voxels containing a mixture of GM and other tissues. Using the approximation made in equation (3.51), the expectation of the measurement becomes

$$E(q_i) = \sum_{j \in \mathbb{J}} c_{ij} \lambda_j \quad (3.57)$$

$$\approx \sum_{j \in \mathbb{J} \setminus \mathbb{G}} c_{ij} \lambda_j + \sum_{j \in \mathbb{G}} c_{ij} \left(f_j^G \lambda_j^G + \frac{f_j^W}{n_{\mathbb{W}}} \sum_{l \in \mathbb{W}} f_l^W \lambda_l + \frac{f_j^C}{n_{\mathbb{C}}} \sum_{l \in \mathbb{C}} f_l^C \lambda_l \right) \quad (3.58)$$

$$\begin{aligned} &= \sum_{j \in \mathbb{J} \setminus \mathbb{G}} c_{ij} \lambda_j + \sum_{j \in \mathbb{G}} c_{ij} f_j^G \lambda_j^G + \frac{1}{n_{\mathbb{W}}} \left(\sum_{k \in \mathbb{G}} c_{ik} f_k^W \right) \left(\sum_{j \in \mathbb{W}} f_j^W \lambda_j \right) \\ &\quad + \frac{1}{n_{\mathbb{C}}} \left(\sum_{k \in \mathbb{G}} c_{ik} f_k^C \right) \left(\sum_{j \in \mathbb{C}} f_j^C \lambda_j \right). \end{aligned} \quad (3.59)$$

For notational convenience, we define

$$\delta_l^{\mathbb{X}} \triangleq \begin{cases} 1 & \iff l \in \mathbb{X}, \\ 0 & \iff l \notin \mathbb{X}. \end{cases} \quad (3.60)$$

Thereby, it is possible to rewrite equation (3.59) in the form

$$\begin{aligned} E(q_i) \approx & \sum_{j \in \mathbb{J} \setminus \mathbb{G}} \left[c_{ij} + \delta_j^{\mathbb{W}} \frac{f_j^W}{n_{\mathbb{W}}} \sum_{k \in \mathbb{G}} c_{ik} f_k^W + \delta_j^{\mathbb{C}} \frac{f_j^C}{n_{\mathbb{C}}} \sum_{k \in \mathbb{G}} c_{ik} f_k^C \right] \lambda_j \\ & + \sum_{j \in \mathbb{G}} c_{ij} f_j^G \lambda_j^G. \end{aligned} \quad (3.61)$$

If we introduce a new system matrix c_{ij}^* , the expectation of the measurement can be written as $E(q_i) = \sum_j c_{ij} \lambda_j \approx \sum_j c_{ij}^* \lambda_j^*$. Because $\delta_j^{\mathbb{J} \setminus \mathbb{G}} = 1 - \delta_j^{\mathbb{G}}$, we have

$$c_{ij}^* = \left[1 + \delta_j^{\mathbb{G}} (f_j^G - 1) \right] c_{ij} + \delta_j^{\mathbb{W}} \frac{f_j^W}{n_{\mathbb{W}}} \sum_{k \in \mathbb{G}} c_{ik} f_k^W + \delta_j^{\mathbb{C}} \frac{f_j^C}{n_{\mathbb{C}}} \sum_{k \in \mathbb{G}} c_{ik} f_k^C, \quad (3.62)$$

$$\lambda_j^* = \delta_j^{\mathbb{G}} \lambda_j^G + (1 - \delta_j^{\mathbb{G}}) \lambda_j. \quad (3.63)$$

Hence, the parameter transformation has led to the derivation of a new system matrix which depends on the original system matrix and the anatomical information contained by the segmentation images. The most probable tracer distribution for Λ^* is then given by the maximum-likelihood estimator (2.48) in which λ_j and c_{ij} are replaced by λ_j^* and c_{ij}^* , respectively.

Subsequently, the ML approach is extended to a MAP based reconstruction algorithm by imposing two additional constraints. These two are *global* and *local* smoothness within certain tissue classes of Λ^* . Voxels inside \mathbb{W} are composed of mainly WM. Because we assume that the WM tracer activity approximates a uniform activity distribution, prior knowledge is imposed in \mathbb{W} using a Gaussian prior $M^{\mathbb{W}}$, as described in (2.67). The mean WM activity contribution in \mathbb{W} is used as the mean of the Gaussian distribution function, i.e. $\mu = \bar{\lambda}^W$. Similarly, a Gaussian prior $M^{\mathbb{C}}$ is used for voxels in \mathbb{C} . Since it is assumed that the mean CSF activity contribution approximates zero, we include an additional constraint by setting the mean of the Gaussian distribution to zero. For voxels in \mathbb{R} , i.e. those voxels containing a mixture of WM and CSF, a Gaussian prior $M^{\mathbb{R}}$ is used in which the mean of the distribution is set to $f_j^W \bar{\lambda}^W$. The propagation of noise in \mathbb{G} is suppressed by means of a Gibbs smoothing prior $M^{\mathbb{G}}$, as described in (2.66). This prior is designed to penalize differences between neighboring λ_j^G , which means that local smoothness is imposed.

Then, the logarithm of the prior is equal to

$$M = M^{\mathbb{W}} + M^{\mathbb{C}} + M^{\mathbb{R}} + M^{\mathbb{G}}, \quad (3.64)$$

in which

$$M^{\mathbb{W}} = -\beta_{\mathbb{W}} \sum_{j \in \mathbb{W}} (\lambda_j - \bar{\lambda}^W)^2, \quad (3.65)$$

$$M^{\mathbb{C}} = -\beta_{\mathbb{C}} \sum_{j \in \mathbb{C}} \lambda_j^2, \quad (3.66)$$

$$M^{\mathbb{R}} = -\beta_{\mathbb{R}} \sum_{j \in \mathbb{R}} (\lambda_j - f_j^W \bar{\lambda}^W)^2, \quad (3.67)$$

$$M^{\mathbb{G}} = -\beta_{\mathbb{G}} \sum_{j \in \mathbb{G}} \sum_{k \in \mathcal{N}_j^{\mathbb{G}}} \frac{1}{d_{jk}} \Phi(\lambda_j^G, \lambda_k^G), \quad (3.68)$$

where $\beta_{\mathbb{X}}$ is the weight of the prior term with each tissue class \mathbb{X} , $\mathcal{N}_j^{\mathbb{G}} = \mathcal{N}_j \cap \mathbb{G}$, \mathcal{N}_j the neighborhood of voxel j , with $j \notin \mathcal{N}_j$, d_{jk} the Euclidean distance between voxel j and k , and Φ the local prior weight function.

The choice for Φ in (3.68) is based on the following rationale. Since the normal GM activity distribution is not uniformly distributed for most of the tracers, like e.g. ^{99m}Tc -ECD and ^{18}F -FDG, but more locally varying throughout the entire brain, the amount of penalty should not be based on the absolute, but rather on the relative difference of the GM activity of neighboring voxels. Moreover, the prior penalization term should become tolerant for differences that are large enough to be real. It has been shown that these properties are elegantly combined in the *relative difference prior* function [Nuyts *et al.*, 2002], in which Φ is given by

$$\Phi(x_j, x_k) = \frac{(x_j - x_k)^2}{x_j + x_k + \gamma|x_j - x_k|}, \quad (3.69)$$

where γ is a parameter controlling the point from which the prior function becomes tolerant. Penalization is quadratic for small and linear for large differences. The factor $2/\gamma$ is related to an *intermediate* relative difference value.

In Appendix A.1, we show that the logarithm of the prior M is concave if $M^{\mathbb{G}}$ is concave. The latter is true for Φ given by (3.69) [Nuyts *et al.*, 2002]. Since we assumed that the likelihood describes the Poisson nature of the emission data, the logarithm of the likelihood is concave under reasonable conditions [Shepp and Vardi, 1982]. Adding the concave logarithms of the likelihood and the prior gives a concave logarithm of the posterior. Consequently, the posterior has no multiple local maxima.

A heuristic gradient ascent form of the expectation maximization approach, as shown in (2.64), is used for the optimization of the MAP estimator of Λ^* . After Λ^* has been estimated, we have to perform the inverse parameter transformation of equations (3.55) and (3.56). Thereby, Λ^* is transformed back to the original image variables Λ , i.e. for all $j \in \mathbb{J}$,

$$\lambda_j = (1 - \delta_j^{\mathbb{G}}) \lambda_j^* + \delta_j^{\mathbb{G}} \left(f_j^G \lambda_j^* + \frac{f_j^W}{n_{\mathbb{W}}} \sum_{k \in \mathbb{W}} f_k^W \lambda_k^* + \frac{f_j^C}{n_{\mathbb{C}}} \sum_{k \in \mathbb{C}} f_k^C \lambda_k^* \right). \quad (3.70)$$

Henceforth, this iterative reconstruction algorithm is called Anatomy based MAP (A-MAP). The A-MAP algorithm is summarized by means of a pseudo-code in Fig. A.1 on p. 129.

3.4.3 Proof-of-Principle: A-MAP and PVC

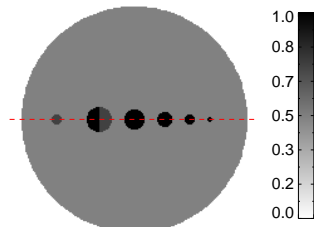
The A-MAP reconstruction algorithm corrects for the PVE. We illustrate this property using a simple 2-D software phantom which can be seen in Fig. 3.4(a). The image dimensions of the phantom are 200×200 voxels. In the center of the image, a uniform disc with a radius of 90 voxels and an intensity of 0.5 is inserted. An artificial tissue classification is used. The large disc is considered as “WM”. Along the equator of the uniform disc, and going from left to right, six smaller discs with a radius of 4, 10, 8, 6, 4, and 2 voxels, respectively, are added. The first and the last four of these smaller discs are considered to be totally composed of “GM”. The intensity in the first disc is set to 0.75 and the intensity of the last four are set to 1. For the second disc, the left half of the disc is composed of “GM” and has an intensity of 1. The right half of the disc is a composition of 50 % “GM” and 50 % “WM” tissue, and the intensity is set to 0.75. A PET acquisition procedure is simulated by projecting the phantom over 120 equidistant angles. The detector resolution effect is simulated by smoothing the projections along the detector surface using a 1-D Gaussian kernel with a FWHM of 5 voxel lengths. For this *proof-of-principle* experiment, we ignore the effect of attenuation and the contribution of noise and scatter.

The projection data are reconstructed using the A-MAP and the ML-EM reconstruction algorithms. Fuzzy tissue segmentation images for “GM” and “WM” are simulated by smoothing the exact anatomical information, derived from the phantom data, using a 2-D Gaussian kernel with an isotropic FWHM of 1.5 voxel lengths. The contribution of “CSF” is ignored. The segmentation threshold parameter for the A-MAP algorithm is set to $\varepsilon = 0.01$, the weights of the Gaussian priors are $\beta_W = 10$, $\beta_R = \beta_C = 0$, and the weight of the Gibbs smoothing prior is $\beta_G = 10$. In both reconstruction algorithms, the blurring due to finite resolution has been included in the projector and back-projector pair (2.33). An iteration scheme with a decreasing number of ordered subsets, consisting of (iterations \times subsets): 5×30 , 5×24 , 5×20 , 5×15 , 5×12 , 5×10 , 5×8 , 5×6 , 5×4 , 5×3 , 5×2 , 5×1 , is used. This scheme is approximately equivalent to 675 regular iterations. The ML-EM reconstructions are post-smoothed using a 2-D Gaussian kernel with an isotropic FWHM of 5 voxel lengths. Along the equator, line profiles are computed.

Fig. 3.4(a) shows the phantom image used for illustrating that A-MAP performs PVC. Fig. 3.4(b) shows the ML-EM reconstruction post-smoothed with a Gaussian kernel with an isotropic width of 5 voxels lengths. Fig. 3.4(c) shows the A-MAP reconstruction. A line profile of the phantom image through the higher intensity regions is shown in Fig. 3.4(d). In Fig. 3.4(e), the corresponding line profile through the GM tissue segmentation image is shown. A line profile through the ML-EM reconstruction without post-smoothing and for post-smoothed ML-EM reconstruction using a FWHM of 5 voxel lengths are shown in Fig. 3.4(d). A line profile through the A-MAP reconstruction is shown in Fig. 3.4(e). The mean and standard deviation of the recovery values within the GM regions are shown in the table in Fig. 3.4.

Although the projection data for this proof-of-principle experiment do not con-

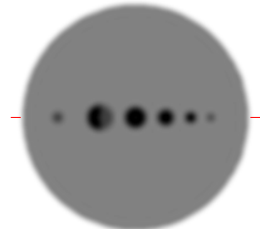
(a) Phantom image



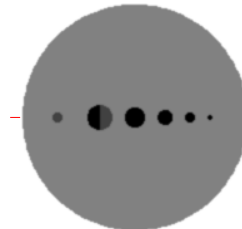
Recovery
“GM” region

	Recovery
	“GM” region
ML-EM-0	0.95 ± 0.11
ML-EM-5	0.90 ± 0.10
A-MAP	0.98 ± 0.05

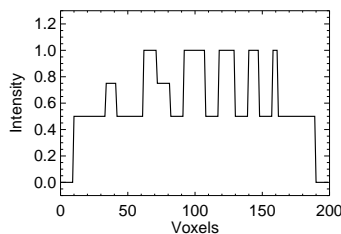
(b) ML-EM-5



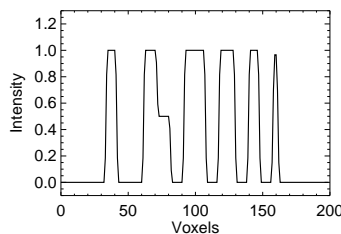
(c) A-MAP



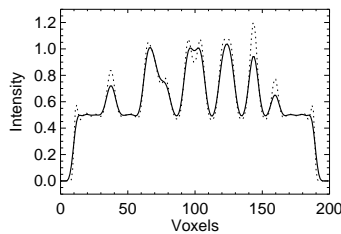
(d) Phantom



(e) “GM” segmentation



(f) ML-EM-0 and ML-EM-5



(g) A-MAP

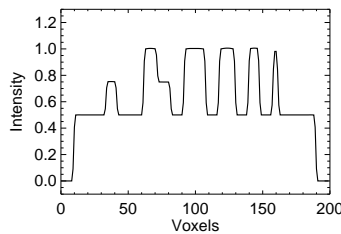


Figure 3.4: The 2-D phantom image which is used for illustrating the PVE is shown in (a). Image (b) shows the post-smoothed ML-EM reconstruction using 5 voxels FWHM. Image (c) shows the A-MAP reconstruction. Plot (d) shows the line profile through the phantom image along the equator. Plot (e) shows the line profile through the *fuzzy* segmentation image of “GM” tissue. Plot (f) shows the line profile through the ML-EM reconstruction without post-smoothing, i.e. ML-EM-0 (dotted line), and post-smoothed ML-EM using 5 voxels FWHM, i.e. ML-EM-5 (solid line). Plot (g) shows the line profile through the A-MAP reconstruction. The table shows the mean and standard deviation of the recovery values within the “GM” region.

tain Poisson noise, we still show the post-smoothed ML-EM reconstruction because the image and line profile illustrates the effect of noise suppression when using post-smoothing. The line profile shows very clearly a decrease of the intensity of the discs with a radius of 2 and 4 voxels, which is below the FWHM of the post-smoothing kernel. For the A-MAP reconstruction, which performs noise suppression by means of anatomical priors in WM and GM, the reduction of the intensity in these discs is negligible.

3.5 Discussion

We designed an iterative reconstruction algorithm, which has been dedicated to the detection of hypo-metabolic regions in FDG-PET and hyper-perfusion regions in ECD-SPECT data of the brain of epilepsy patients. In view of an improved detection capability of regions with a changed intensity, prior knowledge has been included in the reconstruction process. This prior knowledge is partly based on information derived from aligned MRI data, and partly on information about the underlying pathology. No anatomical information about the presence, location, or extent, of possible candidate epileptogenic regions is used during the reconstruction procedure. This approach is often referred to as being a case of *missing labels*. Using the anatomical information, we established a correction scheme for the PVE. The recovery of the resolution due to the PSF of the imaging system, which is included in the system matrix, is used to account as much as possible for the spill-over effect. It should be clear that, if a reconstruction algorithm aims at performing sufficient PVC, it should at least include a projection model that accounts for the resolution effect. Equations (A.31) and (A.32) in the appendix, show how the parameter transformation is reflected in an adjusted projection and back-projection operator. The correction for the PVE of WM and CSF in the GM region is shown in the second and third term of the new derived system matrix (3.62). The finite resolution and the attenuation effect are contained by the original system matrix, i.e. without the anatomical information. Gaussian and Gibbs-Markov priors are additionally used to suppress the propagation of noise (3.65–3.68). The prior functions allow us to smooth within the anatomical regions, and not over the boundaries that separate the regions. At the same time, the prior functions suppress the occurrence of Gibbs effects.

With the A-MAP reconstruction algorithm, we have included anatomical information during the reconstruction process as opposed to post-processing methods. Aston *et al.* [2002] developed a more general mathematical framework for PVC after the reconstruction process, in which explicit assumptions about the noise model are used. Although the approach is new and promising, their method considers PVC for a limited number of tissue regions and tissue types.

In the derivation of the A-MAP reconstruction method, we use the concept of a *tissue composition model*, which was also proposed by [Sastry and Carson, 1997]. In their method, that concept was used in combination with two regularization functions. The first function, which is a Gaussian prior, was used to impose a

Gaussian distribution to the fractional activity of each tissue. The second function, which adds a Gibbs prior to the first, was used to additionally smooth the fractional activities of identical neighboring tissues. In our method, we use a Gaussian prior to meet the approximately uniform activity assumptions for the WM tissue and the CSF. For the GM tissue, this type of regularization cannot be used, because normal GM glucose metabolism is locally varying throughout the brain. Moreover, the purpose of our method is to improve the detection of regions in which an increase of the GM perfusion or a decrease of the GM metabolism can be expected. Because the tracer uptake in GM is not expected to be uniform, we do not wish to use an a priori assumed Gaussian tracer activity distribution. Instead, we apply a Gibbs-Markov prior that tends to preserve strong edges. Because of partial volume effects, straightforward application of this prior would result in smoothing over the boundaries between GM and WM. This was avoided by using the approximation shown in equation (3.51), and the transformation shown in equations (3.55) and (3.56): in voxels containing a mixture of WM and GM tissue, the effect of the prior is restricted to the GM contribution. In that way, smoothing over tissue mixtures is avoided, as opposed to other techniques where noise suppression is applied to the total voxel activity [Ardekani *et al.*, 1996; Bowsher *et al.*, 1996; Comtat *et al.*, 2002; Fessler *et al.*, 1992; Lipinski *et al.*, 1997]. Note that a similar approximation of the tissue composition model was proposed by Müller-Gärtner *et al.* [1992] for their post-processing PVC method.

In clinical practice, occasionally spurious metabolic activity outside the brain can be seen in FDG-PET. We can reasonably assume that the activity will be enclosed in the subset \mathbb{O} , where the A-MAP reconstruction treats the activity distribution as unconstrained ML-EM.

Note that the iterative optimization method of the MAP based reconstruction algorithm (2.64) was not altered in the derivation of our algorithm. In fact, one could easily use other optimization schemes. The major change in A-MAP was made by the use of a parameter transformation.

We assume that, using the proposed reconstruction algorithm, the physicians will be able to differentiate more easily between real hypo-metabolic and hyper-perfused regions, and regions with a changed intensity due to the PVE. For that reason, we expect an improvement in the detection of subtle hypo-metabolic and hyper-perfused regions, whereas larger regions should already be visible using the current existing reconstruction techniques. This assumption will be tested in the next chapter.

It is clear that the detection performance obtained with A-MAP depends on the accuracy of the anatomical information. However, the current MR acquisition sequences perform well in practice and the image quality provides good contrast-to-noise ratio for the most important brain tissues (GM, WM, and CSF). Then, current state-of-the-art image segmentation and registration algorithms may also perform very well [Hill *et al.*, 2001; Maes *et al.*, 1997; Thurfjell *et al.*, 2000; Van Leemput *et al.*, 1999]. Although it was not the purpose to investigate the optimal choice for the threshold parameter ε in equations (3.44), (3.46), (3.48), and (3.49), we found that the chosen value showed good results when performing some preliminary tests.

The PVE as function of structure size and intensity was illustrated using a simple 2-D software phantom simulation (Fig. 3.4). Inclusion of the finite resolution into the projector and back-projector of an iterative reconstruction algorithm leads to the compensation for the spill-over effect, i.e. resolution recovery. However, perfect compensation for the blurring is impossible, and the ML-EM reconstruction algorithm may produce under- and overshoot artifacts, as one can see in Fig. 3.4(b) and Fig. 3.4(f) [Snyder *et al.*, 1987]. These artifacts disappear with post-smoothing, which is also required to suppress the noise. Unfortunately, post-smoothing leads to an underestimation of the true intensity value for the smaller structures inside the phantom. This bias effect is also seen in the mean recovery value within the GM region for the post-smoothed ML-EM reconstruction. In A-MAP, the compensation for the blurring problem is stabilized using anatomy based smoothing. The over- and undershoot artifacts are strongly reduced, which results in superior resolution recovery. Moreover, the mean recovery value within the GM region is much closer to the true value, and the spread around the mean is much lower than when using ML-EM.

In §3.3, we showed that there are a variety of emission tomography reconstruction techniques in which anatomical information can be incorporated either during or after the reconstruction procedure. Recently, we have compared the noise characteristics of A-MAP with that of post-processed ML for the incorporation of anatomical information, and with post-smoothed ML without the use of anatomical information [Nuyts *et al.*, 2003, 2005]. It was assumed that limited but exact anatomical information was available, and voxels were belonging entirely to a single class, which means that PVE were not considered. Post-processed ML was treated as an optimization problem, which not only allowed us to make a reasonable comparison with A-MAP, but also made it possible to take the noise covariance between neighboring voxels in the ML image into account. The objective function for post-processing of the ML reconstruction was set to the form $\Upsilon(X|\Lambda) + M$, with $\Upsilon(X|\Lambda)$ the logarithm of the probability for obtaining the ML reconstruction X , given that the true tracer distribution is Λ , and M an anatomy based prior function, which in this study was identical to that used for A-MAP. An approximate expression was derived for $\Upsilon(X|\Lambda)$ by investigating the characteristics of the ML algorithm at the maximum of the likelihood, as proposed by Fessler [1996]. To study the mean and variance, a second order Taylor series expansion of $L(Q|\Lambda)$ was computed at $\Lambda = X$. In matrix notation, this gives

$$L(Q|\Lambda) \simeq L(Q|X) - \frac{1}{2}(\Lambda - X)'F(\Lambda - X), \quad (3.71)$$

where F is the Fisher information matrix, which is defined as

$$F_{jk} = \sum_i \frac{c_{ij}c_{ik}}{\tilde{q}_i} \quad (3.72)$$

and where \tilde{q}_i denotes the expectation of q_i . Then, equation (3.71) approximates the likelihood $L(Q|\Lambda)$ as the logarithm of a multivariate Gaussian with mean X and covariance matrix F^{-1} , for a given measurement Q and the ML reconstruction X .

Consequently,

$$\Upsilon(X|\Lambda) \simeq -(\Lambda - X)'F(\Lambda - X) \quad (3.73)$$

$$= -(F^{1/2}\Lambda - F^{1/2}X)'(F^{1/2}\Lambda - F^{1/2}X) \quad (3.74)$$

ensures that the post-processing method takes into account the noise propagation from the raw data into the ML reconstruction. Actually, $F^{1/2}$ acts as a prewhitening filter which decorrelates the noise in the image X . Strong covariances between neighboring voxels imply that neighboring voxels carry significant information about one another, and the spread of that information is described by the Fisher information matrix. Optimal prewhitening ensures that all information about a particular voxel is used when the final value of that voxel is computed. Because $F^{1/2}$ is a shift variant filter which is difficult to implement, a number of practical approximations were implemented for subsequent evaluation using simulation experiments. In addition, post-processing without prewhitening was performed.

The theoretical analysis was verified with simulation experiments which included PET studies with attenuation and position independent detector blurring. The resulting images were analyzed with bias-noise curves, and the detection performance of small lesions was studied with the non-prewhitening observer [Barrett *et al.*, 1993] and a channelized Hotelling observer [Gifford *et al.*, 2000a]. *Straightforward* post-processing of the ML reconstruction, i.e. without prewhitening, showed inferior performance compared to both A-MAP and post-smoothed ML-EM. However, if the prewhitening step was added to the post-processing method, the results were comparable to both A-MAP and post-smoothed ML-EM. Unfortunately, the prewhitening procedure involves the application of a shift variant filter which makes the implementation much more complicated than that of A-MAP.

3.6 Conclusion

We can conclude that the use of anatomical information combined with prior information about the underlying pathology is very promising for the reconstruction of subtle hypo-metabolic and hyper-perfusion regions in the brain of epilepsy patients. The A-MAP reconstruction algorithm is extensively evaluated in the next chapter.

Chapter 4

Evaluation of the A-MAP Reconstruction Algorithm

“The final test of a theory is its capacity to solve the problems which originated it.”

GEORGE BERNARD DANTZIG
(1914–2005)

This chapter is mainly based on K. Baete *et al.*, “Evaluation of anatomy based reconstruction for partial volume correction in brain FDG-PET,” *NeuroImage*, vol. 23, no. 1, pp. 305–317, Sep. 2004.

4.1 Introduction

In section §3.4, we developed a new anatomy based reconstruction algorithm for PVC during the reconstruction of emission tomography data of the brain, called A-MAP. We presented the mathematical derivation of the reconstruction algorithm and demonstrated our proof-of-principle using a simple 2-D software phantom simulation experiment. In this chapter, we focus on the evaluation of the reconstruction algorithm.

The evaluation of A-MAP is done in different steps. In a first step, we investigate the use of perfect and imperfect anatomical information using 2-D software phantom simulation experiments. In 2-D, simulations run much faster which allows us to investigate features using many simulation experiments. In a second step, 3-D software phantom simulation experiments are used to investigate the influence of smoothing within GM, the effect of small misalignments between the anatomy

and the emission data, and the effect of local segmentation errors in the anatomical information. In a third step, a human observer study was performed to assess the detection performance with A-MAP. In a final step, a patient study was reconstructed to assess and illustrate the applicability of A-MAP in clinical practice. For all of these experiments, A-MAP is evaluated using simulated or measured PET data. The application of A-MAP to SPECT data is given in Chapter 6.

4.2 Materials and Methods

4.2.1 2-D Phantom Simulation Experiments

We studied the performance of A-MAP for the detection of hypo-metabolic regions using two Monte-Carlo simulation experiments. Because of the complexity of the shape of the human brain, we constructed a clinically realistic brain phantom. This phantom image was based on the 3-D digital brain phantom provided by the *Brain-Web* database [Collins *et al.*, 1998, 2002]. To speed up simulations, experiments were performed on a 2-D trans-axial slice of the digital phantom with plane coordinates $z = 8$ mm in the stereo-tactical Talairach framework [Talairach and Tournoux, 1988]. The digital phantom was used to make a baseline FDG-PET tracer distribution representing the glucose metabolism of a normal human brain. The GM, WM and CSF tissues were identified by means of the discrete anatomical model [Collins *et al.*, 1998]. In that model, each voxel has been classified as either GM, WM, CSF, or other. The binary tissue maps of GM, WM and CSF were smoothed using a two-dimensional isotropic Gaussian kernel with 2 mm FWHM to simulate the output of (most) segmentation algorithms. Thereby, we obtain fractional values which we consider to be tissue fractions. The baseline phantom was constructed by setting the activity to a clinically realistic number of 25 counts per voxel (cpv) in the GM region, 6.25 cpv in the WM region and 0 cpv in the CSF. Image dimensions are 217×217 voxels with an isotropic voxel size of 1 mm. We call this image the *baseline phantom*. In a duplicate of the baseline phantom, we selected 5 GM regions with a varying extent. The activity in these regions was decreased as in hypo-metabolic regions. We call this image the *hypo-metabolic phantom*. The extent E in mm^2 , the proportional decrease of activity Δ of the regions, as well as the long and short axis in mm of the ellipses that were used for the construction of the hypo-metabolic regions are listed in Table 4.1.

A PET acquisition procedure was simulated by projection of the baseline and the hypo-metabolic phantom over 144 angles using a uniform attenuation image derived from the contour of the digital brain phantom and with linear attenuation coefficient $\mu = 0.095 \text{ cm}^{-1}$ [Hubbell and Seltzer, 2004]. To account for the finite resolution effect of the detector, both sets of projection data were smoothed along the detector grid using a 1-D Gaussian kernel with 5 mm FWHM. These two sets of projection data were considered to be the noiseless PET measurements of the baseline and the hypo-metabolic phantoms. Of each projection data set, a number of Poisson noise realizations were computed for use in the following two simulation experiments.

4.2.1.1 Use of Perfect and Imperfect Anatomical Information

In a first experiment, we studied the performance of A-MAP for the detection of hypo-metabolic regions using the same anatomical information during reconstruction as for the construction of the phantoms. This reflects an ideal situation which enables us to study the optimal performance of using anatomical information.

In a second experiment, we studied the performance of the reconstruction algorithm for the detection of hypo-metabolic regions when using noisy and imperfect anatomical information during reconstruction. For each noise realization of the emission data, we constructed imperfect anatomical information. Because segmentation errors have a very complex behavior, we approximated the concept of imperfect anatomical information by assuming that segmentation errors occur at the tissue edges. We determined the inter-tissue interfaces of the binary tissue maps and within the two-voxel thick edges we arbitrarily redistributed clustered parts of the anatomical information. Thereafter, the redistributed binary tissue maps were smoothed, as in the first experiment, using a 2-D isotropic Gaussian kernel with 2 mm FWHM to obtain fuzzy segmentations with the corresponding tissue fractions $\{f^G, f^W, f^C, f^O\}$. In the experiment, different anatomical labels with segmentation errors were generated. The probability of error was the same for all tissue classes.

The following reconstruction parameter settings were used in both experiments. The threshold parameter is set to $\varepsilon = 0.01$. In that way, \mathbb{G} contains all voxels with at least 1 % GM, \mathbb{W} contains voxels with more than 99 % WM, and \mathbb{C} contains voxels with more than 99 % CSF. The global weight of the smoothing prior is $\beta_g = 8$. The global weights of the Gaussian priors and their widths are $\beta_W = \beta_C = \beta_R = 10/18$. For the relative difference prior, given by equation (3.69), we assumed that a relative difference of 5 % was an intermediate value. Hence, parameter γ is set to 40. All parameters were obtained by means of a pilot experiment.

In each of the two experiments, the performance of the A-MAP reconstruction algorithm was compared with post-smoothed ML-EM and MAP-EM. In this evaluation process, we used the post-smoothed ML-EM reconstruction algorithm as the current standard. ML-EM was implemented as described in (2.59), including resolution recovery (2.33). The reconstructed image was post-smoothed using a 2-D isotropic Gaussian blurring kernel. The FWHM of this kernel was varied between 3 mm and 15 mm. We used MAP-EM as an indicator for the non-anatomy based use of prior information. The MAP-EM reconstruction algorithm was implemented as described in (2.64), with

$$M = -\beta_g \sum_j \sum_{k \in \mathcal{N}_j} \frac{1}{d_{jk}} \Phi(\lambda_j, \lambda_k), \quad (4.1)$$

where Φ is replaced by the relative difference prior function, given by equation (3.69), and \mathcal{N}_j is a 3×3 neighborhood. Ordered subsets [Hudson and Larkin, 1994] were used in all three reconstruction algorithms. We used an iteration scheme with a decreasing number of subsets, consisting of (subsets \times iterations): 36 \times 5, 24 \times 5, 18 \times 5, 16 \times 5, 12 \times 5, 9 \times 5, 8 \times 5, 6 \times 5, 4 \times 5, 2 \times 5, 1 \times 10. This iteration scheme is almost equivalent to 685 regular iterations.

4.2.1.2 Evaluation measures

For notational convenience, we use the following definitions: B^{nl} and H^{nl} for the reconstructions of the noiseless PET projection data of the baseline and the hypo-metabolic phantom, respectively; $B^{(r)}$ and $H^{(r)}$ for the reconstructions of noise realization r of the PET projection data of the baseline and hypo-metabolic phantom, respectively; and B^{true} and H^{true} for the “true” baseline and hypo-metabolic phantom, respectively.

The performance of each reconstruction algorithm was measured using a variety of metrics. We used the simplest paradigm for the detection, i.e. the *signal known exactly, background known exactly* or SKE/BKE task [Barrett *et al.*, 1993]. The detection performance of hypo-metabolic regions was quantified using a non-prewhitening numerical computer observer [Wagner and Brown, 1985]. This computer observer was chosen for reasons of its tractability and not because it is presumed to mimic human observer performance. In each experiment, for each reconstruction algorithm, and for each noise realization r , we measured the following response function

$$s(I^{(r)}) = \sum_{j \in R} (B_j^{\text{nl}} - H_j^{\text{nl}}) \cdot I_j^{(r)}, \quad (4.2)$$

with I either B or H , and R being a region-of-interest (ROI) [Barrett *et al.*, 1993]. The signal-to-noise ratio (SNR) for R was computed using

$$\text{SNR} = \sqrt{2 \frac{[\bar{s}(B) - \bar{s}(H)]^2}{\sigma_s^2(B) + \sigma_s^2(H)}}, \quad (4.3)$$

with $\bar{s}(I)$ the mean and $\sigma_s^2(I)$ the variance of $s(I^{(r)})$ over all noise realizations. Bias and variance measurements were performed. The bias image b was calculated using

$$b(I) = \bar{I} - I^{\text{true}}, \quad (4.4)$$

with \bar{I} the mean of $I^{(r)}$ over all noise realizations, and I either B or H . The root mean squared (rms) bias $\tilde{b}(I)$ in ROI R was computed using

$$\tilde{b}(I) = \sqrt{\frac{1}{n_R} \sum_{j \in R} b_j^2(I)}, \quad (4.5)$$

with n_R the number of voxels in R . The variance image $\sigma^2(I)$ was calculated using

$$\sigma^2(I) = \frac{1}{P-1} \sum_{r=1}^P \left(I^{(r)} - \bar{I} \right)^2, \quad (4.6)$$

with P the number of noise realizations. The rms standard deviation was computed using

$$\tilde{\sigma}(I) = \sqrt{\frac{1}{n_R} \sum_{j \in R} \sigma_j^2(I)}. \quad (4.7)$$

4.2.2 3-D Phantom Simulation Experiments

We constructed a clinically realistic 3-D software phantom for subsequent Monte-Carlo simulation experiments. The construction of the phantom was based on 30 consecutive axial slices of the digital software phantom provided by the *BrainWeb* database. The software phantom dimensions are $218 \times 218 \times 30$ voxels with an isotropic voxel size of 1 mm. GM, WM, and CSF were identified by the discrete anatomical model [Collins *et al.*, 1998]. A baseline FDG-PET tracer distribution, representing the glucose metabolism of a normal human brain, was constructed. Tracer activity uptake was set to 12.5 counts/mm³ in GM, 3.125 counts/mm³ in WM, and no uptake in CSF. In a duplicate of the baseline phantom, called the hypometabolic phantom, tracer activity uptake in four 3-D regions within GM was decreased by 25 %.

The PET data acquisition process of a clinical PET scanner was simulated by projecting the baseline and the hypometabolic phantoms over 144 angles using a uniform attenuation image derived from the contour of the digital BrainWeb phantom. The linear attenuation coefficient was set to 0.095 cm⁻¹. The projections were smoothed along the detector grid using a 2-D Gaussian kernel with 5 mm FWHM, thereby accounting for the detector resolution effect of a clinical PET scanner. The smoothed projections were resampled to a realistic sampling frequency of 2×2 mm² detector elements, and Poisson noise realizations were computed for each sinogram.

The projection data were reconstructed using the ML-EM reconstruction algorithm for further comparison with the A-MAP reconstructions. During the reconstruction procedure, we included correction for the attenuation and finite resolution effect. An iteration scheme with a decreasing number of ordered subsets was used, which was consisting of (subsets \times iterations): 36 \times 6, 24 \times 6, 18 \times 6, 16 \times 6, 12 \times 6, 9 \times 6, 8 \times 6, 6 \times 6, 4 \times 6, 3 \times 6, 2 \times 6, 1 \times 6. This scheme is approximately equivalent to 834 regular iterations. ML-EM reconstructions were post-smoothed using a 3-D Gaussian kernel with an isotropic FWHM varying from 4 to 8 mm.

In the following three simulation experiments, we study the influence of the strength of anatomy based smoothing in GM, the influence of misaligned MR data, and the effect of local segmentation errors. The construction of the anatomical information is given in the description of each experiment. Unless stated otherwise, we use the following parameter settings for the A-MAP reconstruction algorithm in each simulation experiment. The segmentation threshold parameter was set to $\varepsilon = 0.01$, the weights of the Gaussian priors were $\beta_W = \beta_C = \beta_R = 0.4$, and the weight of the Gibbs smoothing prior was $\beta_G = 10$. For the relative difference prior, we used $\gamma = 40$. Correction for the attenuation and finite resolution effect, as well as making use of an iteration scheme, was identical to that of the ML-EM reconstruction algorithm.

4.2.2.1 Influence of Anatomical Prior Weight

A-MAP has been based on the assumption that changes of the cerebral glucose metabolism, due to lesions, should occur only in GM. Actually, no anatomical information about the presence, location, or extent of possible lesions is used during the reconstruction procedure. Consequently, a strong smoothing prior within GM could reduce the visibility of lesions. For that reason, we investigated the influence of smoothing within GM, i.e. the strength of the anatomical prior weight, and compared that to the influence of post-smoothing in ML-EM using 3-D simulated FDG-PET data.

The projection data were reconstructed using A-MAP. For that purpose, ML-EM reconstructions post-smoothed with 4 mm FWHM were used as the initial image for the iterative reconstruction procedure of A-MAP. The anatomical information was based on fuzzy tissue classification data of the GM, WM, and CSF, provided by the BrainWeb database [Collins *et al.*, 1998]. The fuzzy tissue classification data was resampled to the PET grid. Dimensions are $109 \times 109 \times 15$ voxels and an isotropic voxel size of 2 mm. The emission phantom data and the corresponding anatomical information are by design perfectly aligned. A-MAP reconstructions were performed using $\beta_{\text{G}} = 5$, $\beta_{\text{G}} = 10$, and $\beta_{\text{G}} = 15$, denoted A-MAP-1, A-MAP-2, and A-MAP-3, respectively.

4.2.2.2 Effect of Small Misalignments

Differences in geometrical alignment are typical for images of the same patient using two different imaging modalities. Using state-of-the-art image registration algorithms, it is possible to compute the affine transformation that is needed to align the MR with the PET data. The influence of errors in the alignment of the anatomical information was assessed.

Usually, registration errors are small for rigid MRI-PET or MRI-SPECT registration [Meyer *et al.*, 1997; Yokoi *et al.*, 2004]. We limited this experiment to: (a) a trans-axial shift of the “fuzzy” tissue classification data over 1 mm to the right, and (b) an axial rotation around the center axis over 1° . We considered the size of these errors realistic for current state-of-the-art registration algorithms. The anatomical information was resampled to the PET grid using linear interpolation after applying the transformation.

4.2.2.3 Effect of Segmentation Errors

It is clear that the performance of A-MAP depends on the accuracy of the anatomical information. For that purpose, we assessed the influence of small segmentation errors. To speed up the Monte-Carlo simulations, we used a smaller 3-D brain software phantom, i.e. a subset of the digital BrainWeb phantom in the surroundings of the middle frontal gyrus. The phantom dimensions were $68 \times 68 \times 26$ voxels with an isotropic voxel size of 1 mm. GM and WM tissue and CSF were identified in the corresponding discrete anatomical model. For all slices, the phantom tissue

information outside an inscribed circle was put to zero in order to avoid truncated projection data. The binary tissue segmentation images were smoothed using a 3-D isotropic Gaussian kernel with 1.5 mm FWHM to simulate the output of fuzzy segmentation algorithms. A baseline FDG-PET tracer distribution, representing the glucose metabolism of a normal brain, was constructed.

The PET data acquisition procedure used in previous experiments was applied. Poisson noise realizations of the projection data were computed and reconstructed using the ML-EM algorithm. The reconstructions were corrected for attenuation and resolution effect, and the ML-EM iteration scheme defined in §4.2.2 was used. The ML reconstructions were post-smoothed using a 3-D isotropic Gaussian kernel with a FWHM varying from 4 to 8 mm.

Three types of segmentation errors, often observed in segmentation images of clinical MR data, were semi-automatically constructed using standard morphological dilation and erosion operations. In the discrete tissue segmentations of GM, WM, and CSF, we simulated: (a) the “closing” of a sulcus, (b) the “thinning” of a gyrus, and (c) the “thickening” of a gyrus. The modified binary tissue maps were smoothed using a 3-D isotropic Gaussian kernel with 1.5 mm FWHM, to simulate fuzzy segmentations, and resampled to the PET grid using linear interpolation, consisting of $34 \times 34 \times 13$ voxels and an isotropic voxel size of 2 mm. The A-MAP reconstructions were performed using the non-modified and the modified GM, WM and CSF fuzzy tissue classifications.

4.2.2.4 Evaluation Measures

The performance of each reconstruction algorithm was measured using a number of metrics. For notational convenience, we use the same definitions as described in the first paragraph of §4.2.1.2.

Again, a non-prewhitening numerical computer observer was used for the quantification of the detection of the induced hypometabolic regions [Wagner and Brown, 1985]. For each reconstruction algorithm, and for each reconstruction of noise realization r of the projection data, we computed $s(I^{(r)})$, for I either B or H , using equation (4.2). The signal-to-noise ratio (SNR) in ROI R was computed using equation (4.3).

We measured the PVC performance of each reconstruction algorithm by computing the recovery of activity in every reconstructed voxel. The recovery value ρ was calculated as the ratio of the reconstructed activity divided by the true activity. We computed the mean μ_ρ and the standard deviation $\tilde{\sigma}_\rho$ of the recovery values within ROIs for the reconstructions based on the baseline and the hypometabolic phantom data, using

$$\mu_\rho(I) = \frac{1}{n_R} \sum_{j \in R} \left(\frac{1}{P} \sum_{r=1}^P \frac{I_j^{(r)}}{I_j^{\text{true}}} \right) \quad (4.8)$$

$$\tilde{\sigma}_\rho(I) = \sqrt{\frac{1}{n_R} \sum_{j \in R} \left[\frac{1}{P} \sum_{r=1}^P \left(\frac{I_j^{(r)} - \bar{I}_j}{I_j^{\text{true}}} \right)^2 \right]} \quad (4.9)$$

for $I = B$ and for $I = H$, where \bar{I}_j is the mean of $I_j^{(r)}$ over the reconstructions of all noise realizations r of the projection data, P is the number of noise realizations, and n_R is the number of voxels in ROI R . Additionally, we measured the distribution of the recovery values within GM.

4.2.3 Human Observer Study

A human observer study was designed to assess the performance of detecting hypometabolic regions using the A-MAP versus the ML-EM reconstruction algorithm. Six nuclear medicine physicians and residents-in-training were asked to localize regions with a reduced metabolism in 2-D simulated FDG-PET images of the brain. In order to make the observations as realistic as possible, but on the other hand not too time consuming, we constructed a 2-D realistic software phantom based on a single trans-axial slice of the digital BrainWeb phantom. Dimensions are 218×218 voxels with an isotropic voxel size of 1 mm. GM, WM and CSF tissues were identified using the discrete anatomical model. A baseline FDG-PET tracer distribution representing the glucose metabolism of a normal brain was constructed. Throughout the 2-D phantom, we delineated 25 regions which were restricted to the GM tissue (Fig. 4.16). The mean size of the regions was 3.7 cm^2 ($\sigma = 0.4 \text{ cm}^2$). For each of these regions, we constructed 20 hypometabolic phantoms in which the region had a proportional metabolic reduction value ranging from 5 % to 100 % in steps of 5 %, defined as the contrast level. All phantoms were resampled to a realistic PET sampling grid of 109×109 voxels and an isotropic voxel size of 2 mm using linear interpolation. The baseline tracer activity was set to 12.5 counts/mm³ in the GM tissue, 3.125 counts/mm³ in the WM and zero uptake in the CSF. The PET data acquisition procedure used in the previous experiments was applied. It was left to the observing nuclear medicine physician or resident-in-training to control the amount of post-smoothing required for further inspection of the ML-EM reconstructed images.

A clinically realistic high-resolution noisy MR image, corresponding to the digital BrainWeb phantom, was generated using the BrainWeb MR simulator [Collins *et al.*, 2002]. The noise level was 7 %. The noisy MR image was segmented into GM, WM and CSF tissues using the Statistical Parametric Mapping (SPM99) software package [SPM99]. By definition, the MR image and the emission phantom, based on the digital BrainWeb phantom, are perfectly aligned. The fuzzy tissue segmentation images were resampled to the PET grid and used in an A-MAP reconstruction of all simulated PET projection data of the baseline and hypometabolic phantoms.

An interactive user interface computer program was written for the human observers in order to evaluate the performance of detecting and localizing induced hypometabolic regions. The user interface was based on in-house developed medical image viewing software, implemented in IDL 5.1 (Research Systems, Inc.), which

is also used in the daily clinical environment. Physicians were invited to carry out two separate observing sessions, one for the A-MAP reconstructions and one for the ML-EM reconstructions. In a learning session for the observers, the program started with presenting the reconstructed images of noise realizations of the baseline phantom projection data. Observers were asked to get acquainted with the image quality, the influence of noise, and they were asked to tune the display settings. After the learning session, the program presented the reconstructed images of the hypometabolic phantom data in order of decreasing contrast of the hypometabolic regions. The program selected for each of the 20 contrast levels randomly 10 of the 25 hypometabolic reconstructed images belonging to that specific contrast level. Throughout the session, physicians were able to adjust the width of a 2-D Gaussian smoothing kernel applied during the image displaying, as well as using a variety of color lookup tables, scale parameters, cursor settings, and zoom factors.

The task of the observer was then to specify the most likely position of the hypometabolic region using a mouse click in the image field. The location and distance between true lesion barycenter and observer localization was measured and stored for further analysis. We defined a hit-range h as the radius of an imaginary sphere surrounding the true lesion barycenter. If the indicated position by the observer was within the imaginary sphere, the localization was considered to be correct. After every 10 images, the observer received feedback about the number of correct localizations for a hit-range of $h = 5$ mm. Display of the images was accompanied by the MR image from which the anatomical data was derived. This image served as additional anatomical information during the observation of both ML-EM and A-MAP reconstructed images. The cursor was linked between the images. Both the reconstructed image Λ , see equation (3.70), as well as the intermediate reconstructed image Λ^* , see equation (3.63), were shown when the user interface was used for observing A-MAP reconstructions. It was briefly explained in advance to the observers what the A-MAP images represented, and how they were created. During the observation session, physicians were able to consult a printout of the phantom image with small dots indicating the 25 possible location sites of the hypometabolic regions. One half of the physicians was asked to complete first the observation of the ML-EM reconstructions, and after that start with the observation of the A-MAP reconstructions. The other half was asked to follow the opposite order. For each reconstruction algorithm, we measured the score $S(h, \mathcal{O}, \mathcal{C})$, defined as the percentage of correct localizations, as function of the hit-range h , the observer \mathcal{O} , and the contrast level \mathcal{C} of the induced hypometabolic region. We calculated (a) the overall score, defined as the mean score over all contrast levels and for $h = 5$ mm, or

$$\text{overall score}(\mathcal{O}) = \frac{1}{n_C} \sum_{\mathcal{C}} S(h = 5, \mathcal{O}, \mathcal{C}) \quad (4.10)$$

where n_C is the number of contrast levels, (b) the average score, defined as the mean score over all observers for $h = 5$ mm, or

$$\text{average score}(\mathcal{C}) = \frac{1}{n_{\mathcal{O}}} \sum_{\mathcal{O}} S(h = 5, \mathcal{O}, \mathcal{C}) \quad (4.11)$$

where $n_{\mathcal{O}}$ is the number of observers, and (c) the average overall score, defined as the mean score over all contrast levels and observers, or

$$\text{average overall score}(h) = \frac{1}{n_{\mathcal{C}} \cdot n_{\mathcal{O}}} \sum_{\mathcal{C}} \sum_{\mathcal{O}} S(h, \mathcal{O}, \mathcal{C}) \quad (4.12)$$

4.2.4 Patient Study

We performed a patient study to illustrate the applicability of A-MAP in clinical practice. We selected FDG-PET and T1-weighted MR data of a female patient with well-documented epilepsy of age 41. She developed refractory temporal lobe epilepsy at age 18. Before she entered the presurgical evaluation procedure in our hospital, she suffered each month from about 20 complex partial seizures, for which no etiology was established. Two separate video combined electro-encephalography (video-EEG) sessions during and between seizures showed very clear left temporal epileptogenic EEG patterns. The patient underwent left temporal lobe resection, including the amygdala, but not the hippocampus. The patient has been free of seizures since surgery during a follow-up period of 2 years.

Presurgical FDG-PET acquisitions were performed on a CTI-Siemens ECAT EXACT HR+ scanner [Brix *et al.*, 1997]. The patient received a catheter inserted into the left brachial vein for tracer administration, and was positioned on the scanner bed. The head was immobilized and centered in the field-of-view. EEG monitoring was installed and recorded throughout the acquisition process to confirm the interictal condition of the patient. A transmission scan of 10 min, using $^{68}\text{Ge}/^{68}\text{Ga}$ rod sources, was acquired in 2-D mode to correct for gamma-ray attenuation. Thereafter, 150 MBq FDG was injected intravenously, and a 3-D mode emission scan of 30 min was started at 30 min post-injection.

The transmission scan was reconstructed using a maximum-a-posteriori reconstruction algorithm [Nuyts *et al.*, 1999b]. Randoms correction of the 3-D emission scan was performed on-line using a delayed time window. The reconstructed attenuation image was used to apply a scatter correction method to the 3-D emission data [Watson, 2000], followed by the Fourier Rebinning (FORE) algorithm [Defrise, 1995]. The obtained 2-D projection data were reconstructed using ML [Shepp and Vardi, 1982]. The dimensions of the reconstructed image are $110 \times 110 \times 63$ voxels with an in-plane pixel size of $2.25 \times 2.25 \text{ mm}^2$ and a plane separation of 2.425 mm. The ordered subsets technique was used [Hudson and Larkin, 1994]. An iteration scheme with a decreasing number of subsets and an increasing number of iterations was used, consisting of (subsets \times iterations): $36 \times 5, 24 \times 5, 18 \times 5, 16 \times 6, 12 \times 6, 9 \times 7, 8 \times 7, 6 \times 8, 4 \times 8, 3 \times 9, 2 \times 9, 1 \times 10$. This scheme is approximately equivalent to 812 regular iterations. We included correction for attenuation and a finite resolution of 5 mm FWHM [Brix *et al.*, 1997] during the reconstruction process.

Four T1-weighted MR acquisitions of the patient were obtained consecutively on a Siemens 1.5 Tesla MAGNETOM Vision scanner using the Magnetization Prepared Rapid Gradient Echo (3-D MPRAGE) sequence [Mugler and Brookman, 1990]. The following parameter settings were used: repetition time TR = 10 msec, echo time

$TE = 4$ msec, flip angle = 12° , inversion time = 300 msec, 256×256 matrix size, 160 sagittal slices, and 1 mm isotropic voxel size. All 4 MR images were spatially aligned using a mutual information based image registration algorithm [Maes *et al.*, 1997], and the mean MR image was computed. The MRI data were visually examined by an expert radiologist. The MRI data were reported to show no abnormalities.

Segmentation of the GM, WM and CSF tissues was performed using the Statistical Parametric Mapping (SPM2) software package [SPM2]. The affine transformation was computed to align the MR image with the post-smoothed ML reconstruction of the PET data. Then, the same transformation was used to align the segmentation images of the MRI data with the ML reconstruction. The anatomical information was resampled to the PET grid using linear interpolation. The ML reconstruction, post-smoothed using a Gaussian kernel with 5 mm FWHM, was used as the initial image for the A-MAP iterative reconstruction. We used the same iteration scheme, attenuation correction and resolution recovery, as for the ML reconstruction.

4.3 Results

4.3.1 2-D Phantom Simulation Experiments

4.3.1.1 Perfect Anatomical Information

The outline of the 2-D uniform attenuation image that was used in the 2-D phantom simulation experiments is shown in Fig. 4.1(a). For visualization purposes, a composition of the binary tissue maps of GM, WM and CSF was constructed and is also shown in Fig. 4.1(a). In that image, CSF is indicated in black, GM in dark gray and WM in light gray. The baseline phantom, constructed from the binary tissue maps, is shown in Fig. 4.2(a). This image acted as the baseline *ground truth* image.

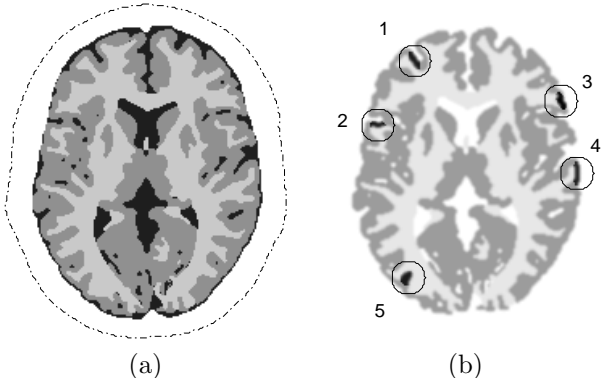
The construction of the phantom data, the implementation of the ML-EM, MAP-EM, and A-MAP reconstruction algorithms, as well as the simulation experiments were developed and performed on a Sun450 Model-4300 workstation (SUN Microsystems, Inc.) using the software package IDL 5.1 (Research Systems, Inc.).

A-MAP, using the exact anatomical information, ML-EM and MAP-EM reconstructed images of the noiseless PET emission data of the baseline are shown in Fig. 4.2(b-d). The noiseless projection data of the baseline phantom contained 8.6 Mcounts. For this experiment, we computed $P = 700$ Poisson noise realizations of the noiseless PET projection data of the baseline and the hypo-metabolic phantom. The subtraction images of the reconstructions of a single baseline and hypo-metabolic noise realization are shown in Fig. 4.3(a, c, and d). The SNR results for each reconstruction algorithm and for different ROI are shown in Table 4.2. The SNR values were scaled with respect to the SNR of the MAP-EM algorithm for comparison. Bias images $b(B)$ are displayed in Fig. 4.4(a, c, and d). For reasons of dynamic range, variance images were converted to standard deviation images and

Table 4.1: The extent E in mm^2 and the proportional decrease Δ of activity for the hypo-metabolic regions used in the design of the hypo-metabolic phantom. The last column shows the long and short axis in mm of the ellipses that were used for the construction of the hypo-metabolic regions. The GM activity was decreased within these ellipses. An isotropic voxel size of 1 mm was used.

Region number	E (mm^2)	Δ (%)	Ellipse long – short axis (mm)
1	43	20	12 – 6
2	28	22	10 – 5
3	42	24	12 – 5.3
4	44	20	15 – 6
5	45	20	9 – 9

Figure 4.1: The composition of the binary tissue maps is shown in (a): CSF is indicated in black, GM in dark gray, and WM in light gray. The outline of the uniform attenuation image is shown by the dash-dotted line. Within the outline the linear attenuation coefficient was set to 0.095 cm^{-1} . The locations of the hypo-metabolic regions are visualized in (b). The circles around each hypo-metabolic region i correspond to the regions-of-interest R_i .



displayed in Fig. 4.5(a, c, and d). The rms bias and rms standard deviation results in different ROIs of the reconstructions of the hypo-metabolic phantom data are shown in Fig. 4.6. For all reconstruction algorithms, a ROI equal to all voxels in the brain was used. The rms bias and rms standard deviation was also calculated within circular ROIs around each hypo-metabolic region, as shown in Fig. 4.1(b). Finally, line profiles were computed through hypo-metabolic region number 1 of the mean reconstructed images \bar{B} and \bar{H} . The difference between these line profiles for each algorithm are shown in Fig. 4.7.

4.3.1.2 Imperfect Anatomical Information

For this experiment, we computed $P = 400$ Poisson noise realizations of the noiseless PET emission data of the baseline and the hypo-metabolic phantom. Four hundred different imperfect anatomical label maps were computed. Using these maps, A-MAP reconstructions of the noisy emission data of the baseline and the

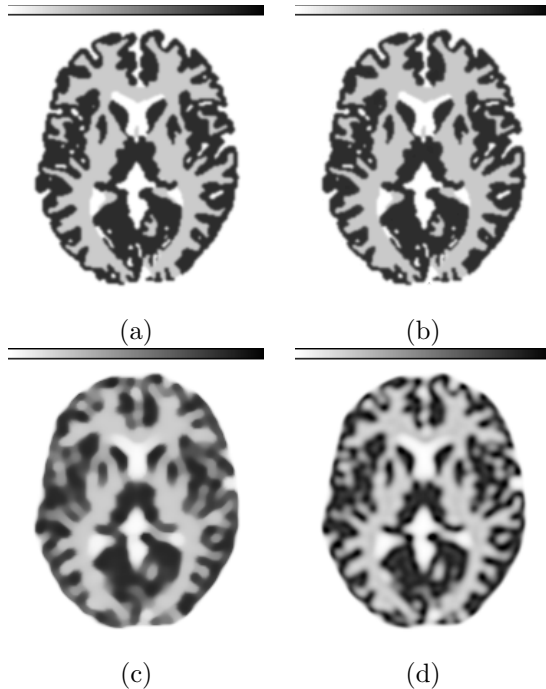


Figure 4.2: The baseline *ground truth* phantom image is shown in (a). The remaining figures show the reconstructed images of the noiseless baseline phantom emission data. The A-MAP reconstruction is shown in (b), MAP-EM is shown in (c), and the ML-EM reconstruction, without post-smoothing, is shown in (d). All images are scaled to the same intensity range, i.e. white corresponds to zero activity and black corresponds to an activity of 30 counts per voxel (cpv).

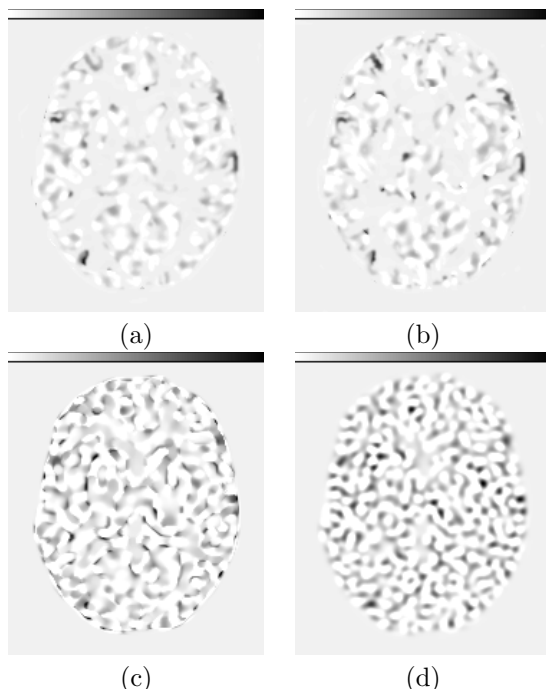


Figure 4.3: The subtraction images of the reconstructions of a baseline and a hypo-metabolic noise realization, or $B^{(r)} - H^{(r)}$, are shown for: (a) the A-MAP algorithm using perfect anatomical information, (b) the A-MAP algorithm using imperfect anatomical information, (c) the MAP-EM algorithm, and (d) the post-smoothed ML-EM algorithm using a two-dimensional isotropic Gaussian kernel with 4 mm FWHM. All images are scaled to the same intensity range, i.e. white corresponds to -0.5 cpv and black corresponds to 8 cpv.

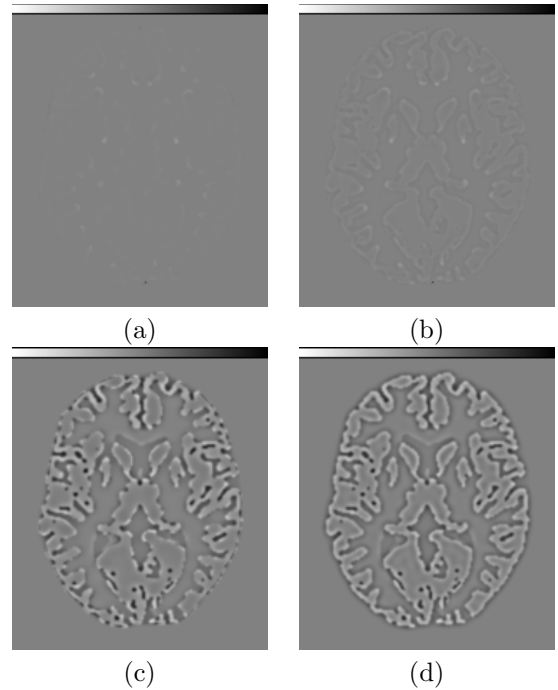


Figure 4.4: The bias images $b(B)$ of the reconstruction experiments, when using: (a) the A-MAP algorithm using perfect anatomical information, (b) the A-MAP algorithm using imperfect anatomical information, (c) the MAP-EM algorithm, and (d) the post-smoothed ML-EM algorithm using a two-dimensional isotropic Gaussian kernel with 4 mm FWHM. All images are the result from simulations where Poisson noise was used, except in the case of (b), where simulations included both Poisson noise and noise from MRI segmentations. All images are scaled to the same intensity range, i.e. white corresponds to -20 counts per voxel (cpv) and black corresponds to $+20$ cpv.

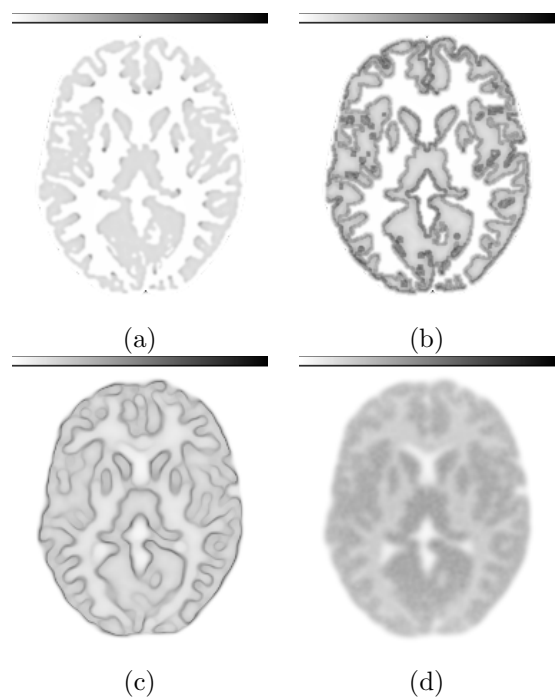


Figure 4.5: The standard deviation images $\sigma(B)$ of the reconstruction experiments, when using: (a) the A-MAP algorithm with perfect anatomical information, (b) the A-MAP algorithm with noisy and imperfect anatomical information, (c) the MAP-EM algorithm, and (d) the post-smoothed ML-EM algorithm using a two-dimensional isotropic Gaussian kernel with 4 mm FWHM. All images are the result from simulations where Poisson noise was used, except in the case of (b), where simulations included both Poisson noise and noise from MRI segmentations. All images are scaled to the same intensity range, i.e. white corresponds to zero and black corresponds to 5 cpv.

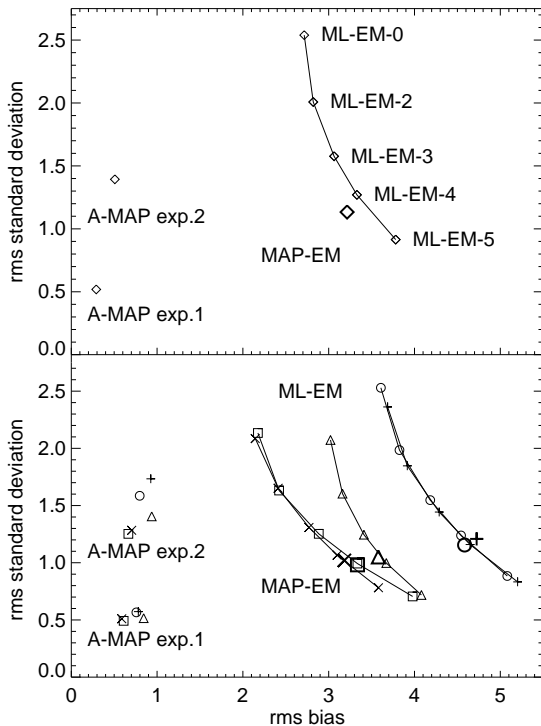


Figure 4.6: The root mean squared (rms) bias \bar{b} and the rms standard deviation $\tilde{\sigma}$ are shown for the reconstructions based on the hypo-metabolic phantom data. In the upper plot, diamond shaped data points (\diamond) show the results for a ROI equal to all voxels in the brain. In the lower plot, rms bias and rms standard deviation are shown for circular ROIs around hypo-metabolic region 1 (+), 2 (\circ), 3 (\triangle), 4 (\square), and 5 (\times). Poisson noise was used in all simulations. For A-MAP using imperfect anatomical information, simulations included both Poisson noise and noise from MRI segmentations. ML-EM- X means post-smoothed ML-EM using a two-dimensional isotropic Gaussian kernel with X mm FWHM. For MAP-EM, symbols are thicker and larger. For ML-EM, symbols belonging to the same ROI are connected by a solid line.

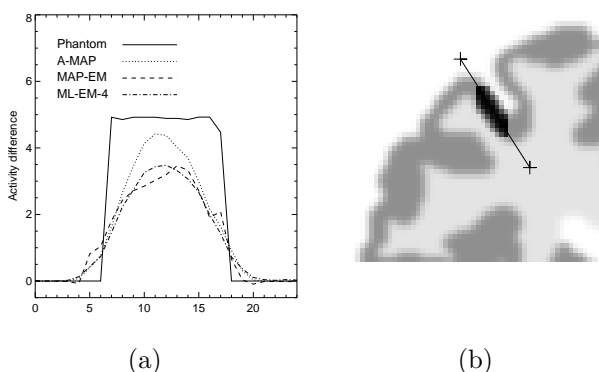


Figure 4.7: Plot (a) shows the activity profile of $\bar{B} - \bar{H}$ through hypo-metabolic region number 1 for A-MAP, MAP-EM and post-smoothed ML-EM using a two-dimensional isotropic Gaussian kernel with 4 mm FWHM. Figure (b) shows the location of the line profile in an enlarged view of the upper-left corner of the image that indicates the location of the hypo-metabolic regions.

hypo-metabolic phantom were performed, and figures-of-merit were calculated. The SNR results for each reconstruction algorithm and for different ROI are shown in Table 4.2. For comparison, SNR values were scaled with respect to the SNR of MAP-EM. The subtraction image of the reconstruction of a baseline and a hypo-metabolic noise realization are shown in Fig. 4.3(b). The bias image $b(B)$ of A-MAP is shown in Fig. 4.4(b). The standard deviation image of A-MAP is shown in Fig. 4.5(b). The root mean squared (rms) bias and rms standard deviation results in different ROIs of A-MAP reconstructions of the hypo-metabolic phantom data are shown in Fig. 4.6.

4.3.2 3-D Phantom Simulation Experiments

The location and the extent of the induced hypometabolic regions used in the phantom data are shown in Fig. 4.8. The simulated noiseless PET emission data of the 3-D baseline phantom contained 117 Mcounts. We computed 100 Poisson noise realizations of the PET projection data of the baseline and 100 of the hypometabolic phantom.

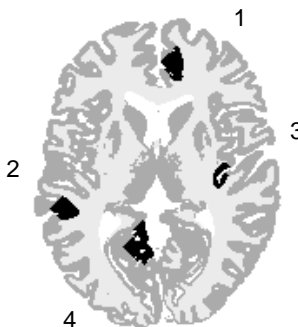
4.3.2.1 Influence of Anatomical Prior Weight

Fig. 4.9 shows the mean recovery value (4.8) results plotted against the standard deviation of the recovery values (4.9) for the ML reconstructions and for the A-MAP reconstructions using $\beta_G = 5.0, 10.0$, and 15.0 . The upper panel of Fig. 4.9 shows the results for the simulations based on the baseline phantom data, and computed within an overall 3-D ROI, defined by the GM and WM tissues in the phantom data for the 5 most central planes. The lower panel of Fig. 4.9 shows the results for the simulations based on the hypometabolic phantom data, and computed within four 3-D ROI around the corresponding hypometabolic regions.

A-MAP shows an overall improved mean recovery compared to post-smoothed ML for the reconstructions of the baseline phantom data. A similar improvement is seen in the mean recovery values in the ROIs around the hypometabolic regions of the reconstructions of the hypometabolic phantom data. Although the results depend on the ROI that was used, as can be seen in the lower panel of Fig. 4.9, the above pattern is the same for each ROI. ML-EM without post-smoothing, but including detector resolution recovery, shows comparable mean recovery values as A-MAP, but with a high standard deviation of these values.

The SNR results for post-smoothed ML and A-MAP for different ROI are shown in Table 4.3. The SNR of post-smoothed ML increases with increasing FWHM in the range from 0 to 8 mm. On the other hand, in all ROI, the SNR is almost unchanged for A-MAP when the prior weight is varied between $\beta_G = 5.0$ and 15.0 .

Fig. 4.10 shows the distribution of the recovery values within GM for ML-EM without post-smoothing, a post-smoothed ML-EM reconstruction using a Gaussian kernel with 5 mm FWHM, and an A-MAP reconstruction using $\beta_G = 10.0$, of a single noise realization of the baseline projection data. The mean and the standard



Region number	Size (cm ³)
1	1.5
2	1.2
3	0.8
4	1.7

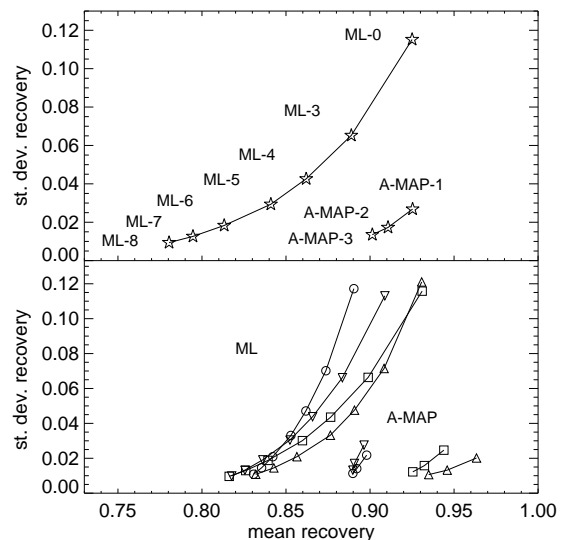
Figure 4.8: The central plane of the 3-D hypometabolic phantom that was used in the 3-D phantom simulation experiments. The locations of the hypometabolic regions are visualized in black. The size of the regions are given.

Table 4.2: Results of the signal-to-noise ratio (SNR) for both experiments and for different regions-of-interest (ROI): \mathbb{J} , i.e. the whole image, and R_i , a circular ROI with a ten voxel wide radius centered at the hypo-metabolic region i . SNR results of A-MAP and ML-EM were relatively scaled with respect to the SNR of MAP-EM. ML-EM- X means post-smoothed ML-EM using a two-dimensional isotropic Gaussian kernel with X mm FWHM.

A-MAP using perfect anatomical information $P = 700$ noise realizations						
Algorithm	SNR					
	\mathbb{J}	R_1	R_2	R_3	R_4	R_5
A-MAP	1.24	1.26	1.17	1.29	1.22	1.31
MAP-EM	1.00	1.00	1.00	1.00	1.00	1.00
ML-EM-0	0.77	0.74	0.76	0.80	0.74	0.77
ML-EM-4	1.01	0.97	0.98	1.06	1.05	1.02
ML-EM-8	1.25	1.26	1.22	1.23	1.20	1.30
ML-EM-12	1.24	1.28	1.18	1.25	1.18	1.30
ML-EM-15	1.20	1.27	1.13	1.23	1.17	1.27

A-MAP using imperfect anatomical information $P = 400$ noise realizations						
Algorithm	SNR					
	\mathbb{J}	R_1	R_2	R_3	R_4	R_5
A-MAP	0.98	0.86	0.86	1.15	0.98	1.09
MAP-EM	1.00	1.00	1.00	1.00	1.00	1.00
ML-EM-0	0.77	0.75	0.76	0.79	0.75	0.79
ML-EM-4	1.01	0.97	0.99	1.05	1.05	1.02
ML-EM-8	1.23	1.25	1.22	1.22	1.22	1.24
ML-EM-12	1.23	1.28	1.16	1.23	1.20	1.24
ML-EM-15	1.20	1.27	1.11	1.22	1.18	1.23

Figure 4.9: The plots show the results of the mean and the standard deviation of the recovery values for post-smoothed ML, and for A-MAP using different values for the GM prior weight (A-MAP-1, 2, and 3). ML- X means post-smoothed ML using a 3-D isotropic Gaussian kernel with X mm FWHM. Star shaped symbols in the upper panel show the results for the baseline phantom data, computed in an overall 3-D region-of-interest (ROI). The lower panel shows the results for the hypometabolic phantom data, computed within 3-D ROI around hypometabolic region 1 (∇), 2 (\square), 3 (\circ), and 4 (\triangle). For ML and A-MAP, symbols belonging to the same ROI are connected by a solid line.



deviation of the recovery values are: 0.89 ± 0.15 for A-MAP, 0.90 ± 0.24 for ML-EM without post-smooth, and 0.77 ± 0.13 for post-smoothed ML-EM using 5 mm FWHM.

4.3.2.2 Effect of Small Misalignments

The mean and standard deviation of the recovery values for A-MAP using misaligned anatomical information are shown in Fig. 4.11. Results for post-smoothed ML-EM and A-MAP using perfectly aligned anatomical information were added for comparison.

The use of shifted anatomical information in the A-MAP reconstructions shows

Figure 4.10: The distribution of recovery values ρ within GM for ML-EM without post-smoothing (ML-0, thin solid line), post-smoothed ML-EM using 5 mm FWHM (ML-5, dotted line), and A-MAP ($\beta_G = 10.0$, thick solid line), of a single noise realization of the baseline phantom projection data.

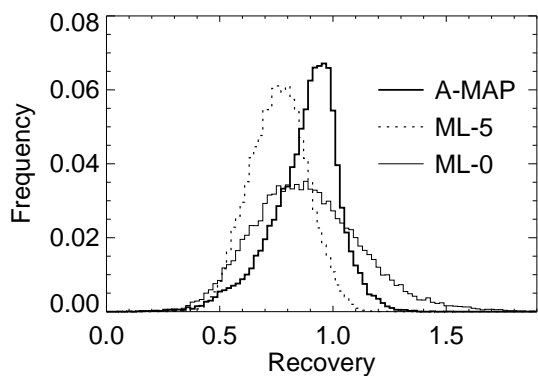


Table 4.3: Signal-to-noise ratio (SNR) of the 3-D phantom simulation experiments, in four 3-D ROIs around the hypometabolic regions. ML-EM- X means post-smoothed ML-EM using a 3-D Gaussian kernel with X mm FWHM.

Algorithm	ROI-1	ROI-2	ROI-3	ROI-4
ML-EM-0	24.6	22.4	14.7	25.5
ML-EM-4	38.0	31.5	21.1	39.5
ML-EM-5	41.6	33.4	23.0	42.6
ML-EM-6	45.5	35.4	25.2	45.3
ML-EM-7	47.7	36.6	26.6	46.6
ML-EM-8	48.9	37.5	27.4	47.2
A-MAP-1	42.3	37.6	23.9	40.8
A-MAP-2	44.9	37.8	23.5	41.0
A-MAP-3	45.4	36.9	23.2	41.2
A-MAP-2 (1 mm shift)	45.9	38.9	23.3	41.7
A-MAP-2 (1° rotation)	45.7	38.2	23.8	42.3

a reduction of the mean recovery value in the overall ROI and in the ROI around the hypometabolic regions, but has little effect on the standard deviation of the recovery. The use of rotated anatomical information shows a similar pattern. The SNR results for A-MAP using misaligned anatomical information are shown in Table 4.3. The results of the SNR in all ROI are comparable with the SNR for A-MAP using perfectly aligned anatomical information.

Fig. 4.12 shows the distribution of recovery values within GM, as defined by the baseline phantom, for ML-EM without post-smoothing, post-smoothed ML-EM using a Gaussian kernel with 5 mm FWHM, and A-MAP using shifted anatomical information, of a single noise realization of the baseline projection data. The mean and the standard deviation of the recovery values are 0.84 ± 0.23 for A-MAP using shifted anatomical information. The results for ML-EM are identical to those obtained in previous experiments (see §4.3.2.1).

4.3.2.3 Effect of Segmentation Errors

The simulated GM fuzzy tissue segmentation images, including the segmentation errors, are shown in Fig. 4.13. The noiseless projection data of the smaller 3-D phantom contained 12 Mcounts. Hundred Poisson noise realizations of the projection data were computed. The mean and standard deviation of the recovery values for assessing the influence of local segmentation errors within the anatomical information are shown in Fig. 4.14.

The influence of segmentation errors in A-MAP shows a small reduction of the mean recovery value in the overall ROI. A similar reduction is observed in the ROI around the modification sites. However, the mean recovery values are still better than those obtained by post-smoothed ML-EM.

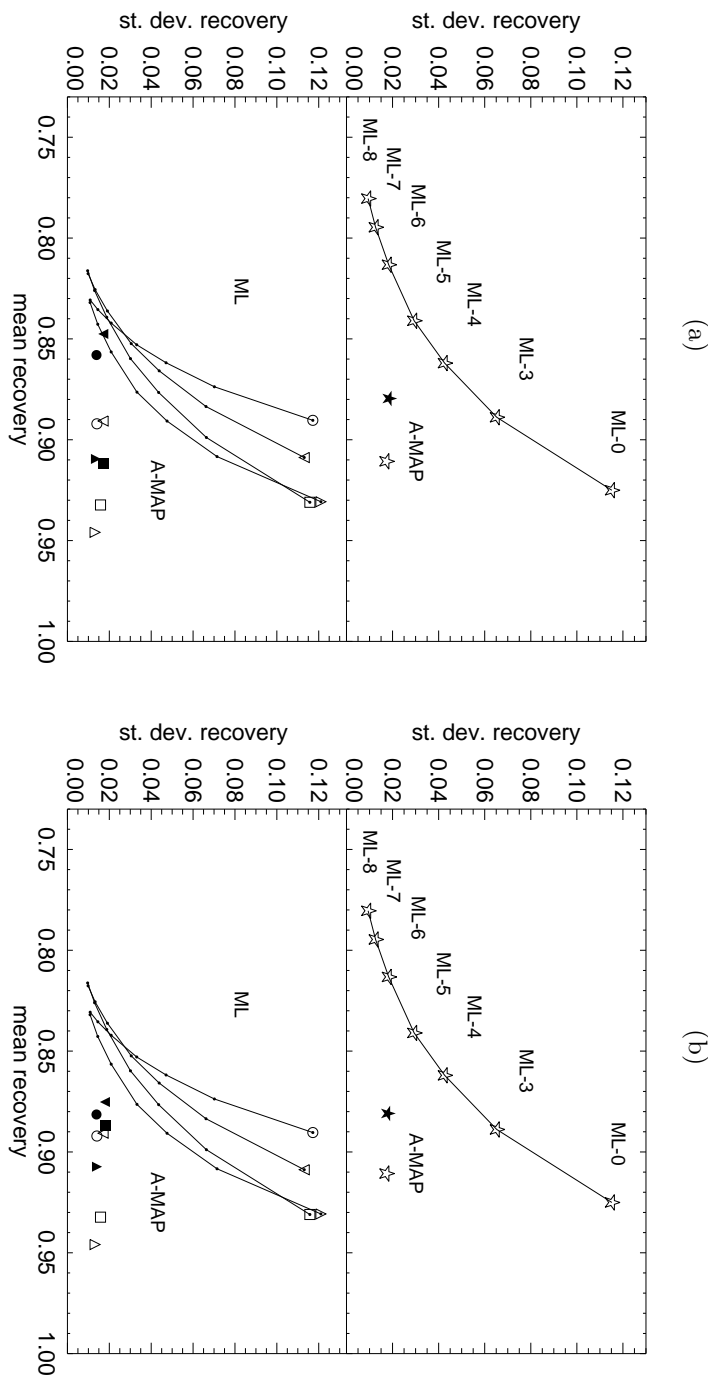


Figure 4.11: The plots show the results of the mean and the standard deviation of the recovery values for post-smoothed ML-EM and for A-MAP when using perfectly aligned anatomical information (open symbols) and intentionally misaligned anatomical information (filled symbols). Panel (a) shows the results for shifting the anatomy over 1 mm, and panel (b) for rotating the anatomy over 1° . Same conventions as in Fig. 4.9.

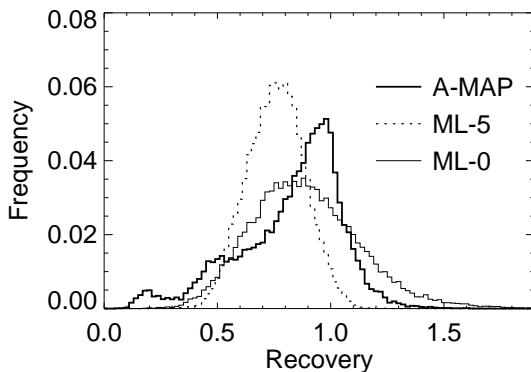


Figure 4.12: The distribution of recovery values within GM for ML-EM without post-smoothing (ML-0, thin solid line), post-smoothed ML-EM using 5 mm FWHM (ML-5, dotted line), and A-MAP using shifted anatomical information (thick solid line), of a single noise realization of the baseline phantom projection data.

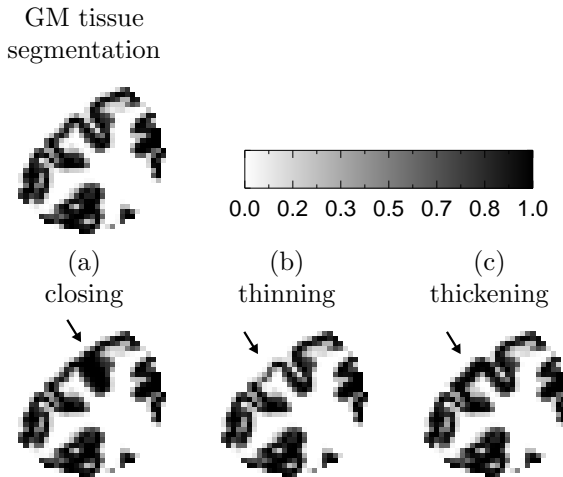


Figure 4.13: The GM fuzzy tissue segmentation data used for the construction of the emission data in the experiment assessing the effect of segmentation errors, is shown in the upper-left. The three types of simulated segmentation errors are: (a) the closing of a sulcus, (b) the thinning, and (c) the thickening of a gyrus. Only the central planes of the 3-D data are shown.

Fig. 4.15 shows the recovery values within GM for A-MAP using exact and modified anatomical information, and for post-smoothed ML-EM, using a single Gaussian kernel with 5 mm FWHM, of a noise realization of the projection data.

4.3.3 Human Observer Study

The user interfaces of the interactive computer program are shown in Fig. 4.18. The user interface was developed using IDL 5.1 (Research Systems, Inc.). The results of the human observer study are shown in Fig. 4.17. The A-MAP and ML average overall score, i.e. the average score over all contrast levels and observers, as function of the hit-range h , are shown in Fig. 4.17(a). Both curves level off at a hit-range of about 5 mm. The A-MAP and ML average score, i.e. the average score over all observers for $h = 5$ mm, and as function of the contrast level of the hypometabolic regions, are shown in Fig. 4.17(b). Since there were 25 possible locations for the

Figure 4.14: The plots show the results of the mean and the standard deviation of the recovery values for post-smoothed ML-EM and for A-MAP using modified anatomical information. The upper panel shows the results computed in an overall 3-D ROI. The lower panel shows the results computed within 3 different 3-D ROI around the sites of the corresponding induced segmentation errors. The filled symbols indicate the use of the modified anatomical information: (\blacktriangledown) for the *closing* of a sulcus, (\blacksquare) for the *thinning* of a gyrus, and (\bullet) for the *thickening* of a gyrus. Same conventions as in Fig. 4.9.

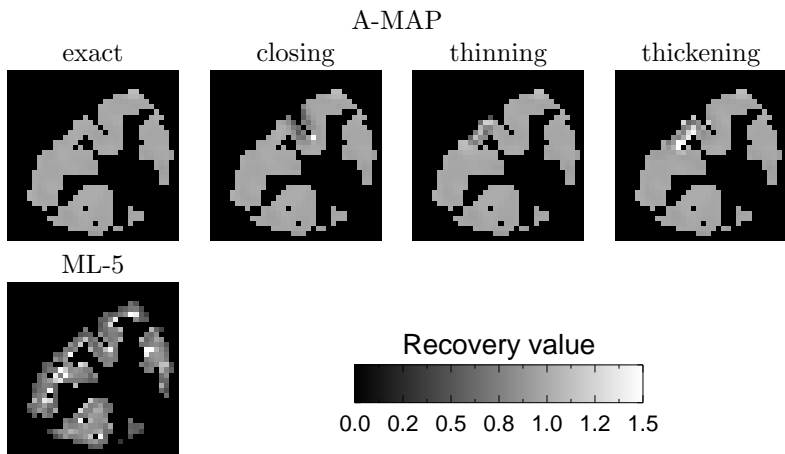
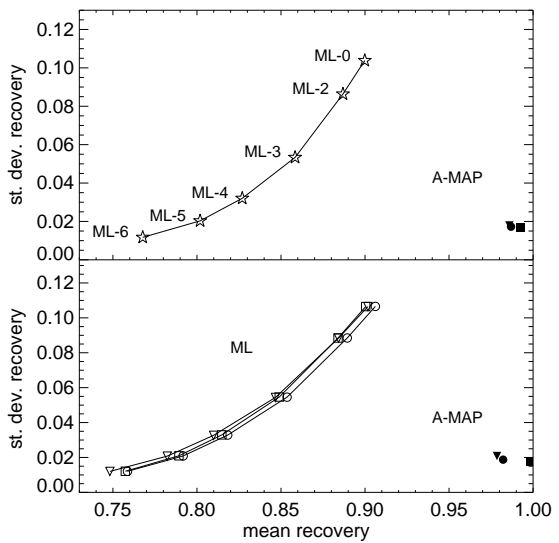


Figure 4.15: The images show the recovery values within GM for the central plane of the A-MAP reconstruction, using exact and modified anatomical information, and the post-smoothed ML reconstruction, using a Gaussian kernel with 5 mm FWHM, of a single noise realization of the projection data.

hypometabolic region, the probability of obtaining 2 or more correct answers by chance alone is 0.058. Fig. 4.17(c) shows the overall score, i.e. the average score over all contrast levels, for $h = 5$ mm, for each observer, and for using ML and A-MAP. For all observers, there is a systematic improvement of detection performance using the A-MAP algorithm. The ML algorithm shows a much larger variance than A-MAP. A Paired *t*-Test of the overall score data of ML (average overall score for $h = 5$ mm is 68.4 %) versus A-MAP (average overall score for $h = 5$ mm is 81.8 %) showed a significantly higher average overall score value for A-MAP ($p < 0.004$).

4.3.4 Patient Study

The results of the patient study are shown in Fig. 4.19. A coronal slice through the temporal lobe was selected for display, shown in panel A of Fig. 4.19. The A-MAP reconstruction image is shown for voxels j where $f_j^G + f_j^W + f_j^C > \varepsilon$, i.e. voxels belonging to the brain. The PET images show clearly a left temporal hypometabolism, which is concordant with the findings of the presurgical video-EEG registrations. We computed a line profile through the right and left temporal lobes of the post-smoothed ML and A-MAP reconstructed images. The line profile is shown in panel B of Fig. 4.19, and indicated in the coronal views.

4.4 Discussion

4.4.1 2-D Phantom Simulation Experiments

With the first 2-D software phantom simulation experiment, we compared the performance of post-smoothed ML-EM and regular MAP-EM with that of A-MAP using perfect anatomical information. For ML-EM a bias-noise curve was generated by varying the width of the post-smoothing kernel (Fig. 4.6). The MAP-EM result is very close to that of the ML-EM curve. This seems in agreement with the results obtained by Nuyts and Fessler [2003], and Stayman and Fessler [2004], who observed very similar noise characteristics for MAP-EM, or penalized likelihood, and post-smoothed ML-EM at matched resolution. These results also show that the post-smoothed ML-EM images using 4 mm FWHM have a good bias-noise trade-off. For that reason, we showed the results of ML-EM using 4 mm FWHM for comparison with A-MAP in Fig. 4.3, Fig. 4.4, and Fig. 4.5. The result of A-MAP yields a point at the left of this curve, implying that A-MAP produces lower bias at matched noise levels. The probability of error was the same for all tissue classes. It follows that the effect of these segmentation errors is seen as an increase in variance, while it has a negligible effect on bias. By varying the parameters of the prior, a bias-noise curve could be produced for A-MAP as well. The optimal point along that curve will depend on the application, and may well be very different for such tasks as visual inspection and quantitative analysis.

Table 4.2 reports the SNR results for lesion detection by means of a non-prewhitening numerical observer. A-MAP yielded SNR values close to the best

values obtained with post-smoothed ML-EM. This is in agreement with [Nuyts *et al.*, 2003], where we found no significant differences between the optimal SNR of A-MAP and the optimal SNR of post-smoothed ML-EM for simulation experiments using a simplified Shepp-Logan phantom.

With the second experiment, we illustrate the performance of A-MAP in a more challenging situation, i.e. when using imperfect anatomical information. In general, a whole variety of effects can contribute to the concept of imperfect anatomical information, e.g. registration errors, segmentation errors, randoms, scatter, patient movement during the acquisition procedure, . . . Since the joint influence of all of these effects on the errors is probably very complex, we have been focusing to segmentation errors for this study. That is, we assumed that errors introduced by poor segmentation of the MR image would lead to imperfect anatomical information.

The results of this experiment show an overall slight reduction of the SNR for A-MAP, compared to MAP-EM. Only hypo-metabolic regions 3 and 5 give better SNR results when using A-MAP (Table 4.2). The rms bias of A-MAP is lower than MAP-EM and post-smoothed ML-EM. The more pronounced increase of the rms standard deviation compared to the rms bias between the first and the second experiment for the A-MAP algorithm, as can be seen in Fig. 4.6, was in fact expected due to the specific design of the simulation experiment. Four hundred different imperfect anatomical label maps were used. As a result, the effect of anatomical errors shows up in our analysis as an increase in variance (Fig. 4.5). Because these errors are random in all directions with the same probabilities, there is no effect on the bias. This is confirmed by Fig. 4.4. Note that in clinical applications possible segmentation errors may lead to an increase of bias. The slight reduction of the SNR results of A-MAP compared to MAP-EM in this experiment can be attributed to the template based approach of the SNR computation. The size of the hypo-metabolic regions in the reconstructed image will vary together with the variation in the anatomical information. Inevitably, this influences the value of the signal response function, as it is computed using equation (4.2).

4.4.2 3-D Phantom Simulation Experiments

Using the 3-D BrainWeb software phantom, we measured and compared the recovery values of A-MAP and post-smoothed ML-EM. We measured how far the reconstruction was deviating from the true solution using mean recovery values, and how stable that solution was under the influence of noise using the standard deviation of recovery values. The results showed an overall improved recovery of the activity using A-MAP, as compared to ML-EM. A-MAP showed to be robust for variation of the weight of smoothing prior in the GM region. Within the hypometabolic regions, we observed similar recovery characteristics, indicating that the recovery improvement for A-MAP was not critically depending on the amount of smoothing within GM, at least for the range tested in the simulation experiments.

We have demonstrated the partial volume correction properties of A-MAP and post-smoothed ML using GM recovery values. The distribution of the recovery values for the reconstruction of a noise realization showed a clear underestimation



Figure 4.16: Composition image of the GM (gray), WM (light gray), and 25 induced hypometabolic lesions (black), which is used for the construction of the 2-D software phantom of the human observer study (§4.2.3).

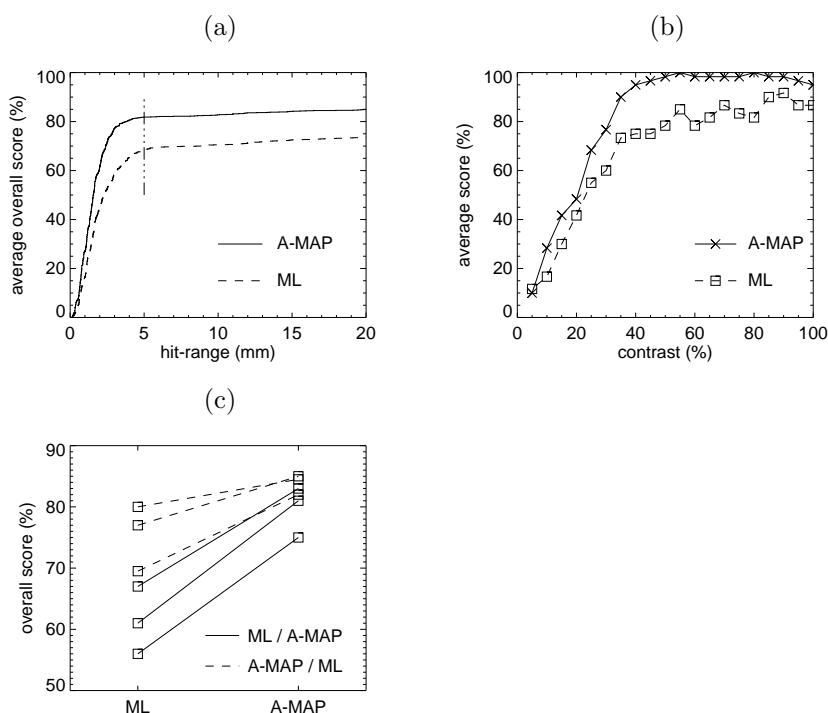


Figure 4.17: Results of the human observer study. Panel (a) shows the total score, i.e. over all contrast levels, for the mean observer as function of the distance between the true lesion location and the location indicated by the observer, for A-MAP (solid line) and ML (dashed line). Panel (b) shows the score for the mean observer as function of the contrast level of the hypometabolic regions, for A-MAP (solid line) and ML (dashed line). Panel (c) shows the total score, i.e. over all contrast levels, for each observer, and for ML and A-MAP. In (c), the solid lines are for the observers who started with the observation of the ML reconstructions, the dashed lines are for those who started with the A-MAP reconstructions.

of the GM activity for post-smoothed ML, whereas the use of A-MAP improved the GM recovery values. The ML reconstruction without post-smoothing showed less underestimation of the GM activity, but an increased spread of the recovery values (Fig. 4.10).

4.4.3 Registration and Segmentation Errors

Two important steps in the A-MAP procedure are the registration between an initial PET image and the MR image, and the segmentation of the MRI data. For small registration errors, we observed a reduction of the mean recovery values at a comparable level of standard deviation. The influence of segmentation errors was more limited. The use of shifted anatomical information introduced local underestimations of the GM activity. This can be seen in the left tail of the distribution of the recovery values, which is more extended towards lower values (Fig. 4.12).

We measured lesion detection performance using the SNR measure, reflecting the performance of a computer observer. With the simulation experiments, we observed that the SNR results for A-MAP were lower than the optimal SNR results for post-smoothed ML (Table 4.3). For ML, the optimal results corresponded to large FWHM of the post-smoothing kernel. With an increased weight of the prior, this effect might be similar for A-MAP. In the human observer study, we observed that the detection was improved using A-MAP, as opposed to post-smoothed ML. These results reflect the differences between computer observers and human observers for lesion detection.

4.4.4 Detection of Hypometabolic Regions

We hypothesized that physicians would demonstrate an improved detection of real hypometabolic regions, as opposed to regions with a decreased intensity due to PVE, using the A-MAP reconstruction algorithm. To test this hypothesis, we investigated the performance of visually detecting hypometabolic regions in A-MAP reconstructions compared to post-smoothed ML reconstructions by means of a human observer study.

Human observers were asked to specify the most likely position of the hypometabolic region, knowing that there was only one lesion in the image. This approach is also known as a multiple alternative forced choice experiment [Burgess, 1995]. As opposed to receiver operating characteristic analysis (ROC), or localizing ROC analysis [Gifford *et al.*, 2000b], our method avoids the use of a confidence rating or an explicit threshold which makes the procedure easier for the observers [Nuyts *et al.*, 1999b].

If available, MRI data are often used in clinical practice for the examination of FDG-PET. We included the MR image in the user interface during the observations of both A-MAP and post-smoothed ML to make sure that differences found between the two methods could not be attributed to the fact whether the MRI was present or not.

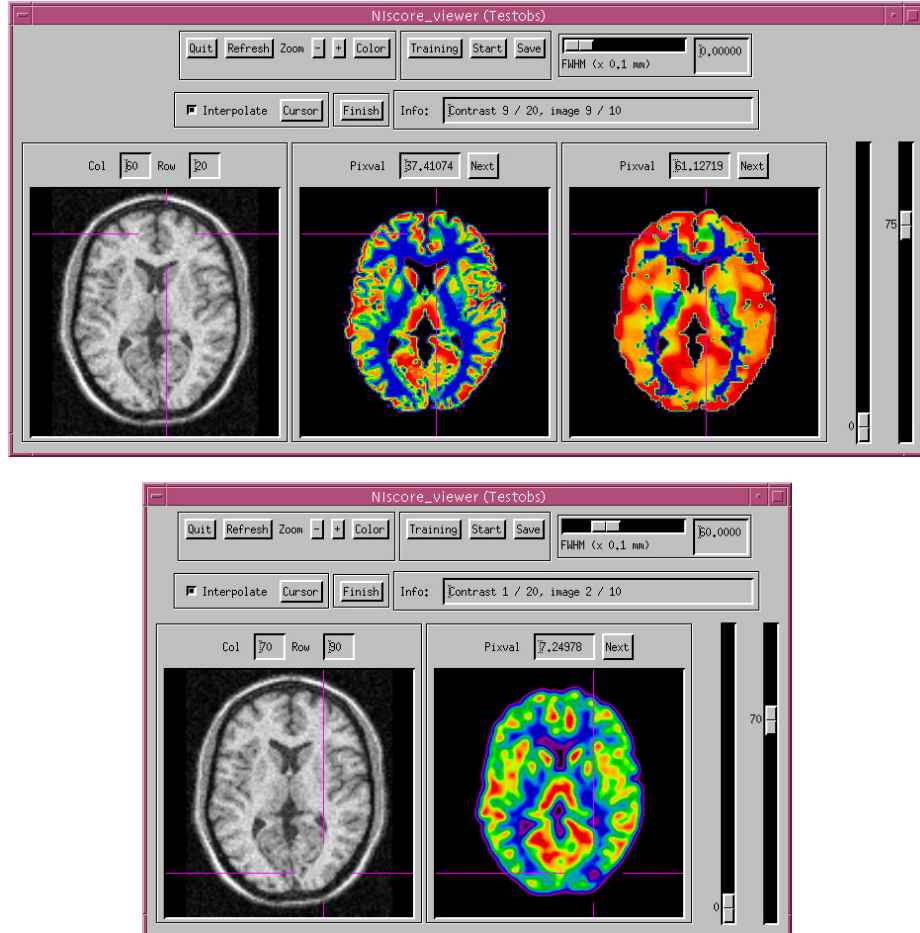


Figure 4.18: The A-MAP (top) and ML (bottom) user interfaces of the interactive computer program which was used for the human observer study (§4.2.3). For A-MAP, the interface shows the MR image, the A-MAP reconstruction Λ , and the intermediate A-MAP estimate of the GM fractional activity Λ^* . For ML, the program shows the MR image and the ML reconstruction. The interface allows for on-the-fly post-smoothing, selection and adjustment of color lookup tables, scale parameters, cursor settings, and zoom factors.

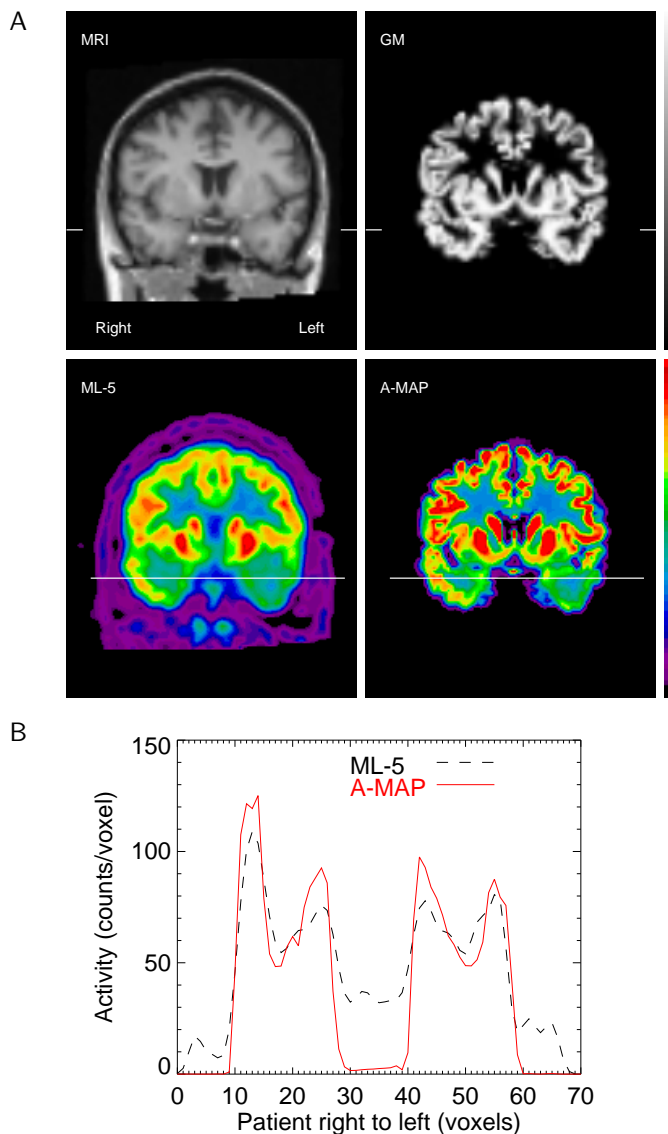


Figure 4.19: Panel A shows coronal views of the mean MRI, the GM segmentation, the post-smoothed ML reconstruction using an isotropic Gaussian with 5 mm FWHM, and the A-MAP reconstruction. A-MAP is only shown for brain voxels, i.e. with a GM, WM, or CSF tissue fraction value exceeding ε . Panel B shows the activity distribution along a line profile through the temporal lobes for ML and A-MAP. A-MAP displays a better recovery of the intensity without destroying the hypo-intensity due to the pathology in the left temporal lobe. The line profile is indicated in the coronal views.

The average overall score as function of the hit-range level off at about 5 mm for both A-MAP and ML, as shown in Fig. 4.17(a). This means that from that distance on, the score is not critically depending on the distance between true lesion barycenter and the observer indicated position. The average score of the observers for A-MAP as function of contrast, going from 100 % to about 80 %, shows a small initial increase in Fig. 4.17(b). This is probably a residual learning effect. This effect was not observed for post-smoothed ML, because physicians are more used to observe that kind of images.

The overall score for A-MAP was for each observer higher than that for ML, indicating a benefit of using the A-MAP reconstruction method for the detection of hypometabolic regions in FDG-PET images. Furthermore, the ML algorithm showed a larger variance for the overall score than A-MAP. This could suggest that the experience of the observer is more important for ML than for A-MAP.

One half of the observers were asked to begin with the observation of the ML-EM reconstructions, and proceed thereafter with the A-MAP reconstructions. The other half was asked to follow the opposite order. These two observer groups show a different performance behavior, which can be seen in Fig. 4.17(c). We attribute this difference to a learning effect that occurred during the course of the experiment. It seems that the observers who started with the A-MAP reconstructions acquired a better lesion detection performance with the A-MAP reconstructions, and used that knowledge for the observation of the ML-EM images. However, we did not verify the significance of this effect.

4.4.5 Clinical Application

The patient study was used to illustrate the feasibility of the A-MAP reconstruction method applied to measured FDG-PET projection data. Interestingly, the A-MAP algorithm also provides an estimate of the GM activity distribution λ^G inside GM region G . Further evaluation should reveal whether this information improves the diagnostic use of FDG-PET data for a range of different pathologies (e.g. epilepsy, dementia, movement disorders), and if the approach is applicable to other tracers. The A-MAP reconstruction, shown in Fig. 4.19, was restricted to the brain voxels only. Outside the brain, the A-MAP reconstruction algorithm is equivalent to an unconstrained ML algorithm, in which noise was not suppressed.

4.5 Conclusion

We can conclude that partial volume correction during the reconstruction process leads to a more accurate detection of hypometabolic regions in FDG-PET of the brain. The A-MAP reconstruction algorithm shows to be robust for small registration and segmentation errors. Finally, we demonstrated the applicability of A-MAP on real patient data.

Excess Height and Cluster Extent in Subtraction SPECT

This chapter is mainly based on K. Baete *et al.*, “Use of excess height and cluster extent in subtraction SPECT,” *IEEE Transactions on Nuclear Science*, vol. 49, no. 5, pp. 2332-2337, Oct. 2002.

5.1 Introduction

SPECT of the cerebral blood perfusion is a useful technique that is used during the presurgical evaluation of patients with refractory partial epilepsy [O’Brien *et al.*, 2000, 1998b, 1999; Spanaki *et al.*, 1999; Véra *et al.*, 1999]. The epileptogenic region shows an increased blood perfusion during an epileptic seizure, and in about half of the cases, the interictal blood perfusion is decreased in that region [Berkovic and Newton, 1997]. Consequently, visual side-by-side examination of SPECT perfusion images during, i.e. ictal, and in between seizures, i.e. interictal, could reveal one or more epileptogenic regions. However, visual side-by-side analysis is very subjective and some subtle but significant differences may not be appreciated by visual analysis alone. Besides, it has been shown that the localization of these epileptogenic regions can be improved when images are analyzed on a more quantitative basis [Devous *et al.*, 1998]. Image post-processing techniques and quantitative analysis methods could make it possible to enhance the detection of real differences between perfusion SPECT images of the brain.

Subtraction SPECT was proposed to partially solve the detection problem of differences in functional images of the human brain [Zubal *et al.*, 1995]. Instead of doing visual analysis through side-by-side comparison, it was proposed to spatially align both data sets, correct for differences due to the amount of injected activity or physical decay of the tracer, and compute differences on a voxel-by-voxel basis.

The more evolved *subtraction ictal SPECT co-registered to MRI* or SISCOM technique led to further increase of the diagnostic yield, and made it possible to examine functional and anatomical correlation in much more detail [O'Brien *et al.*, 1998a, 2000, 1998b, 1999]. In the SISCOM technique, the subtraction image of an ictal and an interictal SPECT is normalized and cut-off at a predefined intensity threshold. Thereby, only the largest perfusion differences are retained and visualized on top of, or fused with, co-registered MRI data of the same individual. The technique assumes that voxels exceeding the threshold are likely to belong to regions with epileptogenic or other physiological changes. Remark that the technique does not allow for the differentiation between pathological or other, maybe normal, physiological changes. Unfortunately, noise in the measured projection data can also lead to supra threshold differences, which makes the use of the subtraction SPECT technique more difficult.

The use of quantitative post-processing methods should make it possible to improve the diagnostic value of subtraction SPECT in clinical practice. For that purpose, a probabilistic discrimination between differences induced by noise on the one hand, and differences induced by physiological or pathological events on the other hand, should be made. Many functional imaging research groups, specialized in studying the neurophysiological behavior of the human brain, make use of a similar approach. For that purpose, a specialized software analysis program, called Statistical Parametric Mapping (SPM), was developed [SPM99]. SPM demands statistical modeling of the problem, i.e. a certain paradigm has to be evaluated against the image data. Although SPM is an excellent and powerful technique, it has some disadvantages for the analysis of subtraction SPECT data [Acton and Friston, 1998; Brinkmann *et al.*, 2000]. In subtraction SPECT or SISCOM, the number of scans per study is much too small, as opposed to typical SPM studies. This results in conservative inferences and an increased amount of false negative predictions. Moreover, when the statistical image is being constructed, the technique does not incorporate features of image processing, like e.g. the acquisition, reconstruction and post-processing. Altering one of these steps could generate subtraction images with other characteristics, thereby influencing the significance of the observed differences.

With the disadvantages of the theoretical model in mind, supra threshold difference tests have been explored using a simulation based approach [Poline and Mazoyer, 1993; Roland *et al.*, 1993]. In those studies, simulation experiments attempted to mimic real null statistic images using smoothed white noise Gaussian random fields with the variance of the noise and the FWHM of the smoothing kernel chosen to match that of real SPECT difference images. However, these approaches did not incorporate any properties of the acquisition procedure, the reconstruction method, or the characteristic features of the image processing.

In this chapter, we investigate an approach similar to that of SPM for characterizing the results of statistical image analysis. The significance of differences in a subtraction image is analyzed and expressed at the *voxel-level* and at the *cluster-level*. A *cluster* is defined as a group of supra threshold voxels that are connected. Two cluster parameters are defined: (a) the *excess height*, and (b) the *cluster extent*. The excess height of a cluster is defined as the largest difference shown by

voxels belonging to that cluster. The cluster extent is the number of voxels inside the cluster. In this study, which is based on a Monte Carlo approach, we propose an empirical method that assigns a probability for the excess height and cluster extent to every observed cluster of voxels in a subtraction image which is cut-off at a certain intensity threshold. The probability is assigned under the null hypothesis of no real perfusion change. The construction of the method is based on the standard epilepsy imaging protocol which is used in our department, but it can be used for other protocols as well. Of course, this method is then only valid for data processed with the same protocol. However, the advantage of our approach lies in the fact that characteristic features of the acquisition, reconstruction and image processing are incorporated in the method.

In a first instance, we investigate the reproducibility of this method by means of simulated Poisson noise realizations of measured projection data. We assume that the construction of noise realizations is the same as doing repeated measurements without the occurrence of physiological or physical changes. Also, we neglect the contribution of image registration errors. Actually, we rely on the fact that registration algorithms perform well in practice [Hill *et al.*, 2001; Maes *et al.*, 1997; Thurfjell *et al.*, 2000].

Secondly, physicians observing subtraction SPECT data in detail are naturally attracted by clusters that are very intense, i.e. having a large excess height. However, also more subtle differences might be detected if the size of the cluster is taken into account. Therefore, the empirical method was used to investigate if *the cluster extent is an important parameter, besides excess height, for the characterization of significant differences*. We tested this hypothesis using 3-D software phantom simulations in a number of experiments.

5.2 Materials and Methods

5.2.1 Distribution of Cluster Extent and Excess Height

We determined the distribution of the excess height and the extent of clusters, observed in the subtraction analysis of simulated perfusion images with no perfusion change.

An experienced nuclear medicine physician examined the reconstructed images of patients who received perfusion SPECT of the brain using ^{99m}Tc -ethyl cysteinate dimer (ECD). The first 10 patients showing a normal brain perfusion pattern were selected. All SPECT data were acquired with a triple-head gamma-camera (Triad, Trionix) equipped with LEUHR parallel hole collimators. Data were acquired using a 128×64 projection matrix with $2.54 \times 2.54 \text{ mm}^2$ voxels, obtained in step-and-shoot mode at 3° intervals over 360° , 15 seconds per projection, and using a manually defined non-circular orbit. The energy window was centered at 140 keV with a 20 % width. This acquisition protocol resembles the clinical standard epilepsy procedure at our department at the time of data collection.

Three hundred pseudo-random Poisson noise realizations were derived from the projection data of every individual. Each noise realization was reconstructed according to our standard clinical reconstruction procedure for brain SPECT. For that procedure, the projections are filtered in frequency space using a 2-D Butterworth filter with cut-off frequency 0.154 cyc/voxel and order 5, see equation (2.21). Thereafter, the projection data are reconstructed using FBP and with the ramp filter, see equation (2.18). Attenuation correction is performed using Chang's second order correction method, shown in equation (2.23), and using a linear attenuation coefficient of 0.12 cm^{-1} . For each individual, the reconstructed images were randomly divided into 150 pairs.

Subtraction SPECT Technique

Subtraction SPECT was applied to each image pair. For every reconstruction Λ^r , a subtraction mask image δ^r was defined to identify cerebral voxels,

$$\forall j : \delta_j^r = \begin{cases} 1 & \iff \lambda_j^r > 0.2 \max(\Lambda^r), \\ 0 & \iff \text{otherwise.} \end{cases} \quad (5.1)$$

Each reconstruction was normalized by the mean cerebral voxel intensity to account for the amount of injected tracer activity and the radioactive decay between the injection of the tracer and the acquisition of the data,

$$\tilde{\lambda}_j^r = \frac{\lambda_j^r}{\mu_{\Lambda^r}}, \quad \text{where} \quad \mu_{\Lambda^r} = \frac{\sum_k \delta_k^r \lambda_k^r}{\sum_k \delta_k^r}. \quad (5.2)$$

For each pair of images Λ^1 and Λ^2 , a subtraction image was computed by

$$\Delta_j = \delta_j^1 \delta_j^2 \left(\tilde{\lambda}_j^1 - \tilde{\lambda}_j^2 \right). \quad (5.3)$$

Subsequently, this subtraction image was convolved using a 3-D Gaussian smoothing kernel with an arbitrary chosen isotropic FWHM of 5 times the voxel size, i.e. with FWHM = 12.7 mm. The smoothed difference images were transformed to a standard z -score,

$$z_j = \delta_j^1 \delta_j^2 \left(\frac{\Delta_j - \mu_\Delta}{\sigma_\Delta} \right), \quad (5.4)$$

where μ_Δ and σ_Δ are the mean and the standard deviation of Δ_j for which $\delta_j^1 \delta_j^2 = 1$. Supra-threshold subtraction images were obtained by applying a threshold at $z \geq 2$. Supra-threshold clusters were defined by means of an 18-connectivity scheme [Worsley *et al.*, 1992]. The excess height as well as the extent of the observed clusters were measured.

For each individual, a cumulative distribution function (CDF) was computed for the measured cluster extent and excess height. Kolmogorov-Smirnov statistical comparison analysis was applied to the CDF curves to assess the inter-individual differences. Finally, data of all ten individuals were combined and a general mean CDF was computed for each parameter.

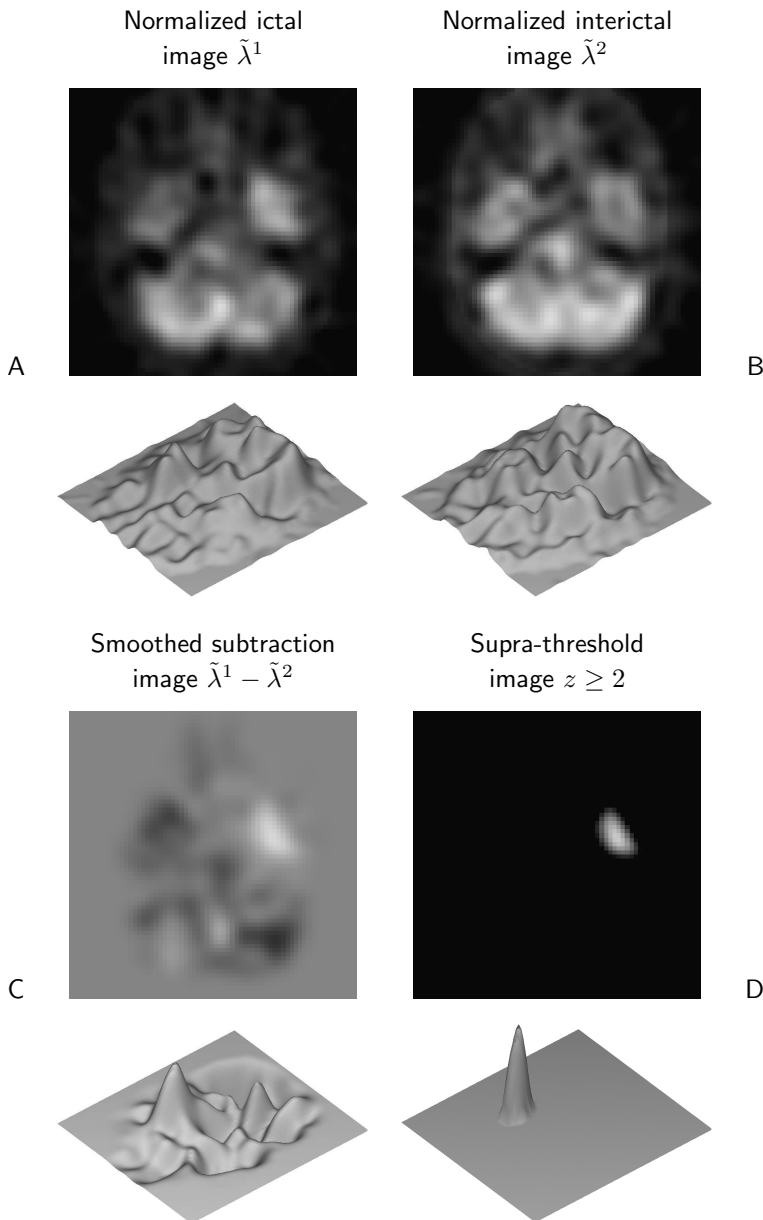


Figure 5.1: These ^{99m}Tc -ECD SPECT trans-axial slices of a patient with temporal lobe epilepsy illustrate the subtraction SPECT technique. Image A shows an ictal, and image B an interictal slice through the temporal lobes. The images have been normalized to the mean cerebral activity. Image C shows the smoothed subtraction image. Image D shows the supra-threshold image $z \geq 2$, where z has been computed using equation (5.4). One can clearly observe an ictal hyper-perfusion in one of the temporal lobes. A surface plot is shown below each image. Images and plots are scaled to their own minimum and maximum intensity.

5.2.2 Simulation Experiments

We studied the performance of the parameters excess height and cluster extent for the detection of induced clusters with two software phantom simulation experiments.

A 3-D software phantom, based on clinical brain MRI data, was constructed. Four T1-weighted MPRAGE images of the brain of an individual were acquired in one acquisition session. All images were co-registered and the average MR image was segmented using the SPM99 software package [SPM99]. The GM segmentation image was spatially registered to a ^{99m}Tc -ECD brain SPECT scan of the same individual, resampled to the sampling grid of the SPECT image, and converted to a binary image, i.e. only ones or zeros. Image registration was done using multi-modality image registration by maximization of mutual information (MIRIT) [Maes *et al.*, 1997]. The intensity of the binary GM image was scaled such that a clinical realistic count level was obtained when projecting the image with the incorporation of attenuation. The attenuation image was derived from the contour of the head in the MRI data. This image was used as the *baseline phantom*.

An *activation phantom* was made by adding a cluster, acting as a hyper-perfused region, to the baseline phantom. In the temporal pole of the segmentation map, which is a region that is frequently found to be involved in epilepsy, we fixed the central point of a sphere with an adjustable radius. The intensity of voxels common to the binary GM image and the sphere were proportionally increased. The induced cluster was restricted to the GM and deviated from a spherical shape when growing beyond the GM boundary. The activation phantom was characterized by the effective size, expressed by the number of voxels, and the proportional intensity increase of the hyper-perfused region. The effective cluster size was varied from 300 up to 1100 voxels in steps of 100 voxels. The proportional increase of intensity was varied from 4 to 12 percent in steps of 1 percent. We name this the *sample space*.

The acquisition process was simulated by projection of the baseline and activation phantom using the same uniform attenuation mask. For every combination of proportional increased intensity and size of the induced cluster, 50 pseudo-random Poisson noise realizations were computed for the projection data of both phantoms. Noise realizations of the projections were reconstructed with the standard clinical procedure, as described above, and every pair was normalized, subtracted and a threshold of $z = 2$ was applied. Each subtraction image was analyzed regarding the number of clusters, their extent, excess height and spatial location in the brain. In every subtraction image, the cluster, if existing, corresponding to the induced cluster in the activation phantom, was identified. This cluster was named the *retrieved cluster* (RC).

Extreme differences in size or height are easily perceived. In a first experiment, we measured the sensitivity of detecting the induced cluster in the subtraction image of a baseline and activation phantom, when looking at either the supra threshold cluster with the largest extent or the highest intensity. For every induced cluster in the activation phantom, with a given size and proportional increase of intensity, the fraction of subtraction images over 50 noise realizations that satisfied this criterion were measured. In that way, we quantify the detection capability of an induced

cluster based on the extreme values of the measurable parameters excess height or cluster extent.

In a second experiment, we analyzed the specificity and the sensitivity of each parameter for the classification of clusters. We computed cumulative distribution functions (CDF) of the measured parameter values in the subtraction of images without any signal present. For that purpose, 550 pairs of noise realizations of the projection data of the baseline phantom were analyzed.

The CDF curves were used to assign a probability for the parameters excess height and cluster extent to each observed cluster in the phantom simulation experiment. For every random variable X , which can be either the excess height or the cluster extent, $\text{CDF}(x) = 1 - \text{Prob}(X > x)$. This means that for an observed cluster with value x , the probability of observing a cluster with a value exceeding x equals $1 - \text{CDF}(x)$, under the condition of only noise. For the phantom simulation experiment, we have chosen different critical probability thresholds $0 \ll p_c < 1$ for the CDF. Clusters with a CDF value for the parameter excess height, respectively cluster extent, above p_c were considered to be significant for the excess height, respectively cluster extent.

For several values of p_c and for each parameter, the specificity and sensitivity of detecting the induced hyper-perfusion region were calculated. The fraction of subtraction images, in which the RC was significant, was computed. This represents the true positive fraction (TPF) or sensitivity when using the corresponding threshold p_c . The fraction of subtraction images in which a cluster, except the RC, was found to be significant was also computed. This represents the false positive fraction (FPF) or one minus the specificity. TPF and FPF were calculated for different sizes and heights of the induced cluster and for different probability thresholds p_c . For each parameter, the mean TPF was computed over all applied sizes and excess heights of the induced cluster, i.e. all samples in our sample space. Similarly, the mean FPF was computed. To compare the performance of the parameters cluster extent and excess height, an ROC curve was constructed based on the mean TPF and mean FPF for different probability thresholds.

5.3 Results

5.3.1 Cumulative Distribution Functions

The cumulative distribution function curves of the measured excess height and extent of observed clusters in subtraction images of 10 individuals are shown in Fig. 5.2. These curves show that noise in the projection data can induce considerably large differences in size and height in a subtraction image. A Kolmogorov-Smirnov statistical comparison test was performed to assess the inter-individual robustness. For the test, we used the data sets of the individuals with the most remote CDF curves seen in Fig. 5.2. The test showed $p > 0.10$ for both excess height and cluster extent. This means that the distribution function of both parameters are not significantly different between individuals.

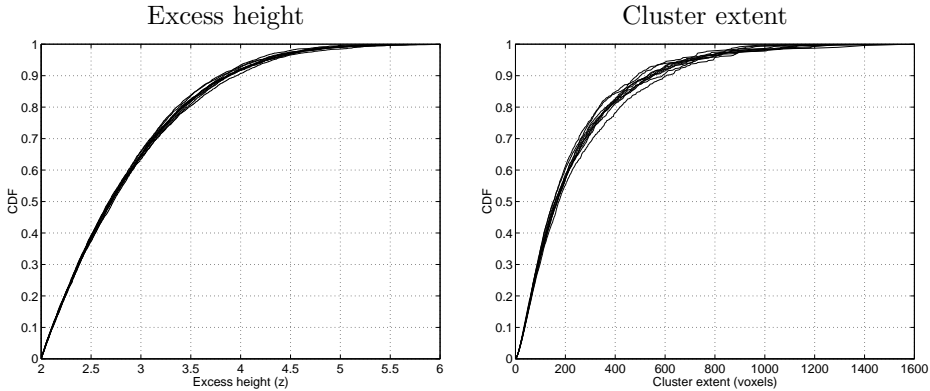


Figure 5.2: Each curve represents the empirical cumulative distribution function (CDF) of the excess height (*left*) and cluster extent (*right*) of clusters found in 150 thresholded subtraction images. These images are subtractions of reconstructed noise realizations of the projection data of an individual. Ten individuals were included in this study.

5.3.2 Simulation Experiments

We analyzed 81 samples with different size and proportional increase of intensity of the induced cluster. For each sample, the fraction of subtraction images in which the true retrieved cluster was the cluster with the highest intensity, respectively the largest extent, were computed. Results are shown in Fig. 5.3.

In the second phantom simulation experiment, the critical probability threshold p_c was first set to 0.95 and the true and false positive fraction of subtraction images for all samples based on excess height and cluster extent were computed. The results are shown in Fig. 5.4. The mean values of the TPF and FPF over all samples in the sample space are:

$p_c = 0.95$	Excess height	Cluster extent
mean TPF	0.70	0.40
mean FPF	0.33	0.02

Thereafter, the probability threshold p_c was varied between 0.100 and 0.998 and the mean TPF and mean FPF of all subtraction images were computed. The ROC-curve containing the results is shown in Fig. 5.5. The area under the ROC-curve (AUC) based on the excess height is 0.74. The AUC based on the cluster extent is 0.83. Statistical comparison of both ROC curves was performed using the ROC-analysis software package ROCKIT 0.9b [Herman *et al.*, 1998; Metz *et al.*, 1998]. The test showed a significant difference ($p < 0.0001$) between both curves.

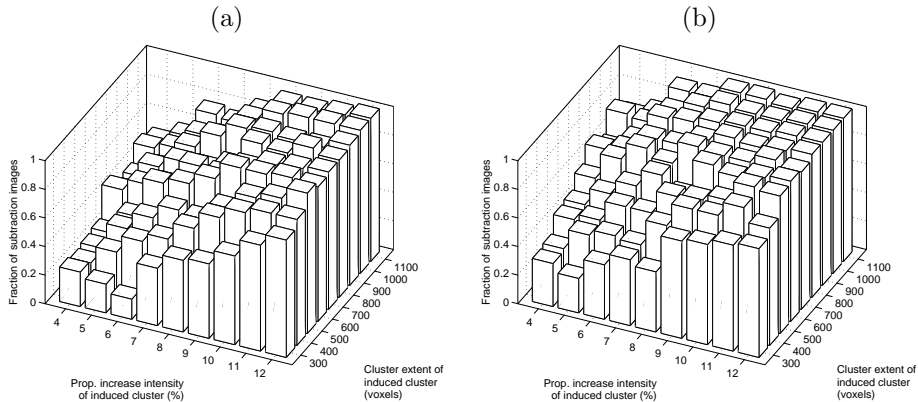


Figure 5.3: Each bar represents the fraction of subtraction images in which the retrieved cluster (RC) was the observed cluster with the highest excess (a), respectively the largest extent (b).

5.4 Discussion

The subtraction SPECT technique which we use, has been based on the method proposed by O'Brien *et al.* [1998a]. The method has been dedicated to the presurgical evaluation of epilepsy patients. One could question whether the construction of the brain masks, and applying a threshold of $z \geq 2$ for obtaining supra-threshold clusters, were optimal for the task of detecting real perfusion changes. However, the implementation of the subtraction method was reported by O'Brien *et al.* [1998a], it has been validated [O'Brien *et al.*, 2000, 1998b, 1999], and it is used for the clinical analysis of epilepsy patients at our department.

We have described the construction of empirical CDF curves for the parameters excess height and cluster extent of observed clusters in subtraction images (Fig. 5.2). Conceptually, the Monte Carlo approach and the construction of the CDF curves is straightforward. Unlike previous studies [Poline and Mazoyer, 1993; Roland *et al.*, 1993], our simulations are based on measured projection data. Even though there is a known considerable inter-individual variation between brain perfusion SPECT images, the method proved to be robust for a data set of 10 normal individuals. In practice, this Monte Carlo approach requires substantial computer time. Mainly for that reason few empirical approaches have been attempted before [Holmes, 1994]. However, the CDF curves have to be computed only once for a given acquisition and reconstruction procedure.

The first experiment of the phantom simulation study investigated the detection performance of the parameters excess height and extent using a specific criterion, viz. the largest parameter values. It showed (see Fig. 5.3) that a better detection of the induced cluster could be achieved when looking at the largest cluster rather than at the cluster with the greatest excess height in the subtraction image. The mean sensitivity over the sample space based on extent is about 11% higher compared

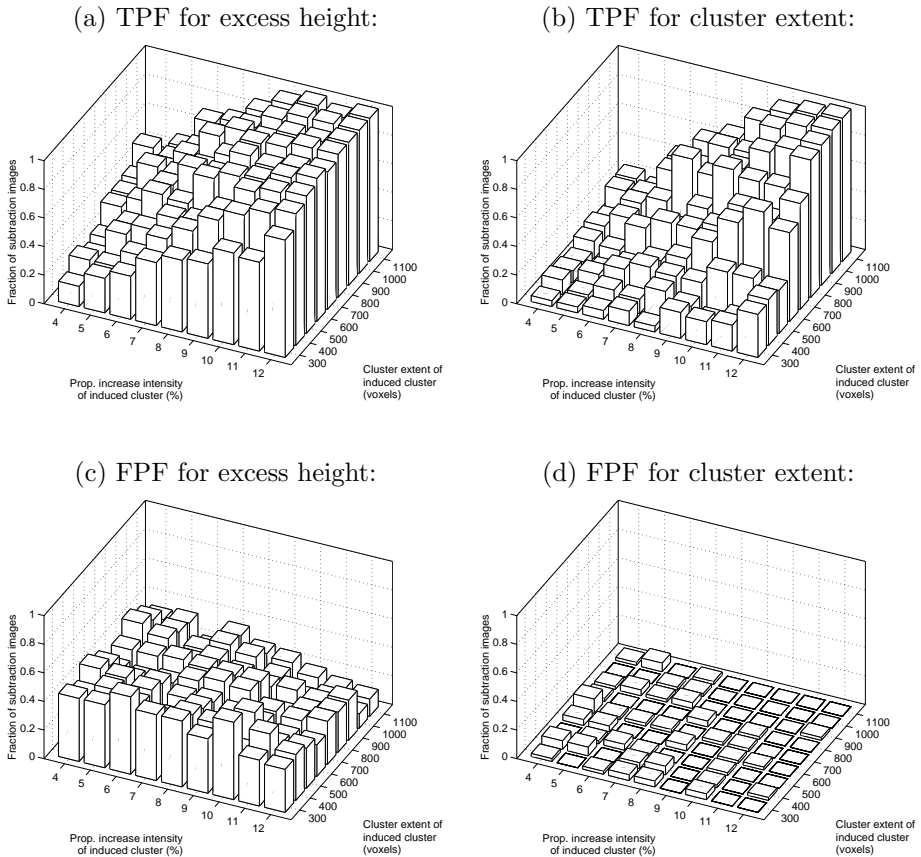


Figure 5.4: For different samples in size and height of the induced cluster, the true positive fraction (TPF) for excess height (a) and cluster extent (b), and the false positive fraction (FPF) for excess height (c) and cluster extent (d) is calculated. The critical probability threshold p_c was set to 0.95.

to the mean value based on excess height. For less intense induced clusters, the increase of mean sensitivity based on extent can even reach 25 % higher compared to excess height. This proves what has been assumed before, viz. close congregation of voxels have more significance than high intensity values [O'Brien *et al.*, 1998a].

In the second experiment of the phantom simulation, we chose initially a 0.95 probability threshold for excess height and cluster extent. Inferences based on this significance level are commonly used in statistical analysis. The computed TPF and FPF of subtraction images for different samples in the sample space at this significance level are shown in Fig. 5.4(a)–(d). Striking is the FPF bar chart of excess height, which shows an overall high amount of false positives at the 0.95 significance level, compared to the FPF bar chart of cluster extent. The difference between both bar charts could be caused by different behavior of the detection parameter at the

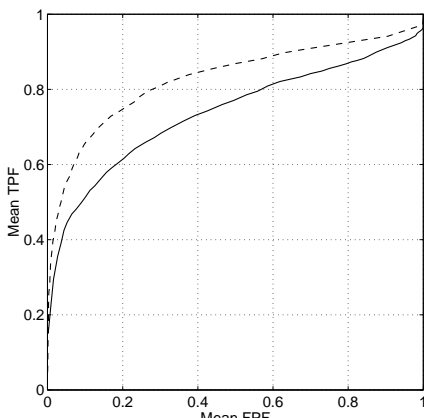


Figure 5.5: ROC-curves based on different probability thresholds p_c for the parameters excess height (solid line) and cluster extent (dashed line). Results are determined on the mean TPF and FPF values over all samples.

chosen significance level. Therefore, the critical probability threshold p_c was varied to assess the difference in overall performance between excess height and extent. We chose to construct the ROC curves based on the mean TPF and mean FPF over the sample space. The ROC curve (Fig. 5.5) of extent showed a much better characterization of clusters and was proven to be significantly different from that of excess height. This shows that the accuracy of extent in the detection of an induced hyper-perfusion in a subtraction image is better than that of excess height. The area under the ROC curve of the cluster extent is about 12 % higher compared to that of the excess height. Besides the analysis over the whole sample space, we divided the sample space in subregions and computed ROC curves using the mean TPF and mean FPF over the subregion. For every subregion, the area under the ROC curve for the cluster extent was always greater than that for the excess height. Based on a visual assessment study, others found similar results for the sensitivity and specificity of subtraction SPECT when cluster extent was used as a criterion [Spanaki *et al.*, 1999].

One could question the choice of the sample space we made in this experiment. However, the sample space was chosen in such a way that detection of the induced cluster was visually not obvious. Detection of induced hyper-perfused regions with larger values for proportional increase and size seemed to be of no problem. This has been examined visually with several activation phantoms and their corresponding subtraction images.

One should consider that large differences between, e.g. ictal and interictal images, can influence the histogram of the subtraction image and hence the generation of supra threshold clusters. This will contribute to a lower FPF of the remaining observed clusters. However, in such cases these differences are obvious in a visual analysis. In the case of more moderate differences this effect is less prominent.

Further analysis of our method in clinical practice is required to evaluate its value in the characterization of supra threshold clusters in subtraction SPECT images.

5.5 Conclusion

We presented a method for the construction of CDF curves for the parameters excess height and cluster extent of supra-threshold clusters in the subtraction analysis of perfusion SPECT images of the brain. The method showed to be robust and is easy to implement. Using the CDF curves, probabilities can be attained to each observed supra-threshold cluster. These cluster probabilities can provide some help for physicians in the interpretation of SPECT perfusion changes. Furthermore, we showed that the cluster extent, besides excess height, is an important parameter for the characterization of supra-threshold clusters.

Noise Suppression and Partial Volume Correction in Subtraction SPECT

6.1 Introduction

In chapter 5, we investigated the behavior of the measured excess height and cluster extent of supra-threshold clusters in subtraction images of simulated SPECT perfusion data of the brain. The acquisition and reconstruction procedures simulated in that study were designed to be comparable to the ones that are used for the presurgical evaluation of epilepsy patients at our department. We have not changed these settings during our investigation. However, it is reasonable to assume that, if the imaging protocol should be changed, e.g. if a different reconstruction method should be applied, or if the amount of noise suppression should be altered, this would change the behavior of the excess height and the extent of supra-threshold clusters. For that reason, we focus in the following study on the role of the reconstruction and noise suppression technique.

6.2 Materials and Methods

In a first experiment, we investigate the effect of using different reconstruction methods and post-smoothing kernels on the behavior of excess height and cluster extent of supra-threshold clusters in the subtraction analysis of simulated brain perfusion SPECT data in which no signal change was present (data was different only for the presence of noise in the projections). In a second experiment, we assess the performance of finding an artificially induced hyper-perfused region using a

variety of reconstruction methods and noise suppression techniques.

6.2.1 Simulation Experiments

A clinically realistic 3-D software phantom was constructed. The phantom was based on 135 consecutive axial slices of the digital software phantom, provided by the BrainWeb database [Collins *et al.*, 2002]. The phantom measures $218 \times 218 \times 134$ voxels and has an isotropic voxel size of 1 mm. GM, WM, and CSF were identified by means of a discrete anatomical model [Collins *et al.*, 1998]. From the GM and WM tissues, a high-resolution baseline ^{99m}Tc -ECD tracer distribution was constructed such that the blood perfusion of a normal human brain could be simulated. Tracer activity uptake was set to 100 counts/cm³ within GM and 25 counts/cm³ within WM. These values relate well to realistic clinical projection data, when taking into account the effect of uniform attenuation and Poisson noise¹. This phantom is further referred to as the *baseline phantom*. In a duplicate of the baseline phantom, the tracer uptake in a 3-D region within GM, more specifically located in the *insula*, was increased by 15 %. The size of the region is 7.938 cm³, which corresponds to a cluster of 487 voxels in the SPECT image sampling space (cfr. infra). This phantom, which is shown in Fig. 6.5, is further referred to as the *hyper-perfusion phantom*. A uniform attenuation image was constructed in which all tissues of the discrete anatomical model were given a linear attenuation coefficient of 0.15 cm⁻¹ [Hubbell and Seltzer, 2004].

The SPECT data acquisition procedure of a clinical SPECT scanner (Triad, Trionix), used for the presurgical evaluation of epilepsy patients at our department, was simulated by projecting the baseline and hyper-perfusion phantom data at high-resolution, i.e. using $1 \times 1 \text{ mm}^2$ detector elements. Projections were performed over 360 degrees, with a step angle of 3°, using the uniform attenuation image, taking into account the distance dependent resolution characteristics of a parallel hole collimator, and completing a circular orbit with radius 20 cm. To make the simulations of the distance dependent resolution effect of the collimator more realistic, we measured the FWHM of the PSF of a thin line source, filled with ^{99m}Tc , at a number of distances from the surface of one of the LEUHR collimators on the SPECT scanner. The results of the measurements are shown in Fig. 6.1. The following resolution model, equivalent to equation (2.7), was fitted using the method of least-squares to the measured FWHM for each distance d ,

$$\text{FWHM}^2(d) = \text{FWHM}_{\text{intr}}^2 + [\alpha(d + d_0)]^2. \quad (6.1)$$

This model takes into account the thickness² of the collimator d_0 , which was 50 mm. The results of the fit are $\text{FWHM}_{\text{intr}} = 3.47 \text{ mm}$ and $\alpha = 0.04$, and these values were

¹This was assessed using the projection data of interictal ^{99m}Tc -ECD scans of two epilepsy patients, scanned at our department.

²The collimator hole length is 34.9 mm for a LEUHR collimator of the Triad scanner, and the collimator is not in direct contact with the crystal. Source: user manual of the Triad XLT scanner, Trionix, Twinsburg, Ohio, USA.

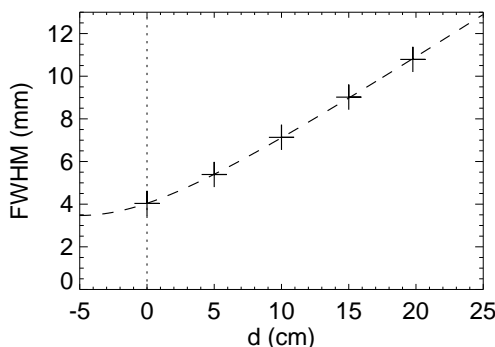


Figure 6.1: The plot shows the measured FWHM of the PSF of a thin line source at a number of distances d from the surface of a LEUHR collimator on a Triad XLT SPECT scanner (Trionix, Twinsburg, Ohio, USA). The measurements are shown by the + -signs, the model given by equation (6.1) which was fitted to the measurements is shown by the dashed line.

used for the construction, as well as for the reconstruction of the projection data. The fit model is also shown in Fig. 6.1.

The high-resolution projection data are resampled to a more realistic detector sampling frequency of $2.54 \times 2.54 \text{ mm}^2$, using linear interpolation. One hundred random Poisson noise realizations were computed for the projection data of the hyper-perfusion phantom, and 200 for the projection data of the baseline phantom. All noise realizations were reconstructed using each of the following three reconstruction methods:

1. the FBP reconstruction method, preceded by applying 2-D *Butterworth* low-pass filtering of the projection data, cfr. equation (2.21). Filter characteristics are: order $n = 5$, and a cut-off frequency of $\nu_0 = 0.154 \text{ cyc}/\text{voxel}$. Attenuation correction was performed using Chang's second order correction method (2.23). This reconstruction method has been validated for clinical brain perfusion SPECT imaging at our department. We refer to this method by the name CBP.
2. the ML-EM reconstruction method, including attenuation correction, and correction for the distance dependent resolution effect, i.e. the Gaussian diffusion method as explained in §2.4.2.
3. the A-MAP reconstruction method, including attenuation correction, and correction for the distance dependent resolution effect, i.e. the Gaussian diffusion method as explained in §2.4.2.

For the ML-EM and the A-MAP algorithm, an iteration scheme with a decreasing number of ordered subsets was used, consisting of (subsets \times iterations): 30×10 , 20×10 , 10×10 , 1×10 . The scheme is approximately equivalent to 610 regular iterations. The CBP and ML-EM reconstructions were post-smoothed using a Gaussian kernel with the FWHM ranging from 0 to 50 mm in steps of 10 mm. For A-MAP, noise suppression is handled by the Gibbs smoothing prior (3.68). Three different regularization weights were used for the Gibbs smoothing prior within GM. The prior weight was set to $\beta_G = 10, 50$, and 100 .

6.2.2 Subtraction and Cluster Analysis

For each reconstruction method and each noise suppression strategy, 100 reconstructions of the baseline and 100 of the hyper-perfusion data were randomly selected, and 100 image pairs were formed. These pairs give rise to a set of *signal present* subtraction images. The 200 reconstructions of the baseline data were used to make 100 image pairs. These pairs give rise to *signal absent* subtraction images.

Subtraction analysis was performed according to the procedure described in §5.2.1. However, two different subtraction mask images were used. The first subtraction mask was designed to select all voxels belonging to the brain, as defined in equation (3.44),

$$\forall j : \delta_j^B = \begin{cases} 1 & \iff f_j^G + f_j^W + f_j^C > 0.01, \\ 0 & \iff \text{otherwise}, \end{cases} \quad (6.2)$$

and is called the *brain-mask*. The second subtraction mask selects all voxels with at least 50 % GM,

$$\forall j : \delta_j^G = \begin{cases} 1 & \iff f_j^G > 0.5, \\ 0 & \iff \text{otherwise}, \end{cases} \quad (6.3)$$

and is called the *GM-mask*. For each subtraction image and for both subtraction masks, supra-threshold clusters were computed. For every cluster the following set of parameters were computed:

- the cluster extent, i.e. the number of supra-threshold voxels,
- the excess height, i.e. the maximum z -value within the cluster,
- the coordinates of all local maxima within the cluster, and
- the fraction of the volume of each cluster overlapping with the true hyper-perfusion region.

Cumulative distribution functions (CDF) were computed for the cluster extent and the excess height of the clusters observed in the signal absent subtraction images. The CDF curves were used to assign a probability for cluster extent and excess height to the clusters observed in the signal present subtraction images. A critical probability threshold $0 \ll p_c < 1$ was defined such that clusters with a probability exceeding p_c were considered to be significant for cluster extent or excess height.

For each subtraction image, the supra-threshold clusters, if existing and overlapping with the true hyper-perfusion region, were identified and given the name *retrieved cluster* (RC). For several values of p_c and for each parameter, both the specificity and sensitivity of detecting the induced hyper-perfusion region were calculated. The fraction of signal present subtraction images, in which at least one of the RC's were significant, was computed. This fraction represents the *sensitivity* or TPF for the corresponding parameter and probability threshold p_c . The fraction of signal absent subtraction images, in which at least one of the RC's were significant, was computed. This fraction represents one minus the specificity or FPF for the corresponding parameter and probability threshold p_c . To compare the detection

performance of cluster extent and excess height for each of the reconstruction methods, noise suppression strategies, and image masks, we constructed ROC curves by means of the TPF and FPF for the whole range of probability thresholds. The *area under the ROC-curve* (AUC) was computed and used as a measure of detection performance.

The fraction of signal present subtraction images, in which a RC was equal to the cluster with the largest extent or the highest excess height, was computed. This fraction represents the sensitivity of detecting the induced hyper-perfusion region when looking only to the cluster with the largest extent or the highest intensity, respectively. This quantifies the detection capability of an induced cluster based on the extreme values of the cluster extent and excess height.

6.3 Results

6.3.1 Cumulative Distribution Functions

The CDF of the measured excess height and extent of supra-threshold clusters, observed in 100 signal absent subtraction images, and reconstructed using CBP, ML-EM, and A-MAP, are shown in Fig. 6.2. SPECT subtraction was performed using a subtraction mask for the brain and for GM. Within each plot, multiple CDF curves represent different strengths of the noise suppression method. For CBP and ML-EM, this means using different widths of the post-smoothing kernel. For A-MAP, this means using a varying weight of the Gibbs smoothing prior within the GM tissue region.

6.3.2 Cluster Analysis

For a more practical implementation of the simulation experiment, and because the CDF is a monotonic function, we have chosen to use a critical excess height and critical cluster extent instead of a critical probability threshold p_c for the construction of ROC curves. Clusters exceeding the critical excess height, or critical cluster extent, were then considered to be significant for either excess height, or cluster extent, respectively. The critical excess height was varied between $z = 2$ and $z = 6$ in steps of 0.005, and between $z = 6$ and $z = 20$ in steps of 0.01. The critical cluster extent was varied between 2 and 2000 voxels in steps of 1 voxel, between 2000 and 20000 voxels in steps of 10 voxels, and between 20000 and 30000 voxels in steps of 100 voxels.

The AUC was computed for every ROC curve constructed by the TPF and FPF at different levels of the critical excess height and the critical cluster extent. Detection performance, expressed by the AUC, for the excess height and cluster extent in signal present subtraction images of CBP, ML-EM, and A-MAP reconstructions, when using different noise suppression strategies, and for the brain and GM subtraction masks, are shown in Fig. 6.3. The fraction of subtraction images in which the retrieved cluster (RC) was found to be equal to the cluster with the highest

intensity, respectively the largest extent, were computed. These results are shown in Fig. 6.4.

As an illustration of the performance of the different reconstruction algorithms, the results of a noise realization are shown in Fig. 6.5. The supra-threshold subtraction image of a simulated hyper-perfusion and baseline SPECT reconstruction, using one of the reconstruction algorithms, is shown on top of the baseline reconstruction. There is no post-smoothing applied for the CBP reconstructions. The ML-EM reconstructions have been post-smoothed using a Gaussian kernel with a FWHM of 10 mm. For this illustration, the A-MAP reconstructions were post-smoothed using a Gaussian kernel with a FWHM of 3.81 mm, i.e. 1.5 times the length of the pixel.

6.4 Discussion

We investigated the influence of the reconstruction and noise suppression method on the excess height and cluster extent of supra-threshold clusters in subtraction images of simulated SPECT perfusion data. To make the experiments realistic, simulations were based on a 3-D high-resolution brain software phantom, and the simulated acquisition procedure was based on that of a clinical SPECT scanner, which is used for the presurgical evaluation of epilepsy patients at our department.

We computed empirical CDF curves for the excess height and extent of supra-threshold clusters in subtraction SPECT data with no perfusion change, when using CBP, ML-EM, and A-MAP, with a variety of noise suppression settings, and using a brain and GM subtraction mask. This procedure is similar to what has been described in §5.2.1. The CDF curves, shown in Fig. 6.2, demonstrate that noise in the projection data can induce supra-threshold clusters with a considerable large extent and excess height. Moreover, the shape and range over which the CDF curves evolve, shows strong variation between reconstruction methods and strengths of the applied noise suppression technique. This means that visual or quantitative assessment of differences between SPECT images can be difficult when the data have been reconstructed using different reconstruction or noise suppression techniques. A similar problem can occur when different acquisition methods have been used.

The CDF of the excess height for CBP shows no change for different widths of the Gaussian post-smoothing kernel. We attribute this effect to the underlying FBP algorithm, which provides an un-weighted least-squares solution to the reconstruction problem (cfr. 2.22). If two reconstructed images only differ by their noise content, which can be approximated by a Gaussian distribution, and if both images have been normalized and subtracted, then the subtraction image is also Gaussian distributed. Moreover, if the subtraction image is subsequently post-smoothed using a Gaussian kernel, and normalized to a z -score, then the distribution of the intensity of the z -score image is normal. Indeed, we observe that the CDF of the excess height for CBP follows the CDF of a truncated normal distribution above 2 standard deviations.

For the ML-EM reconstruction method, increased post-smoothing results in a

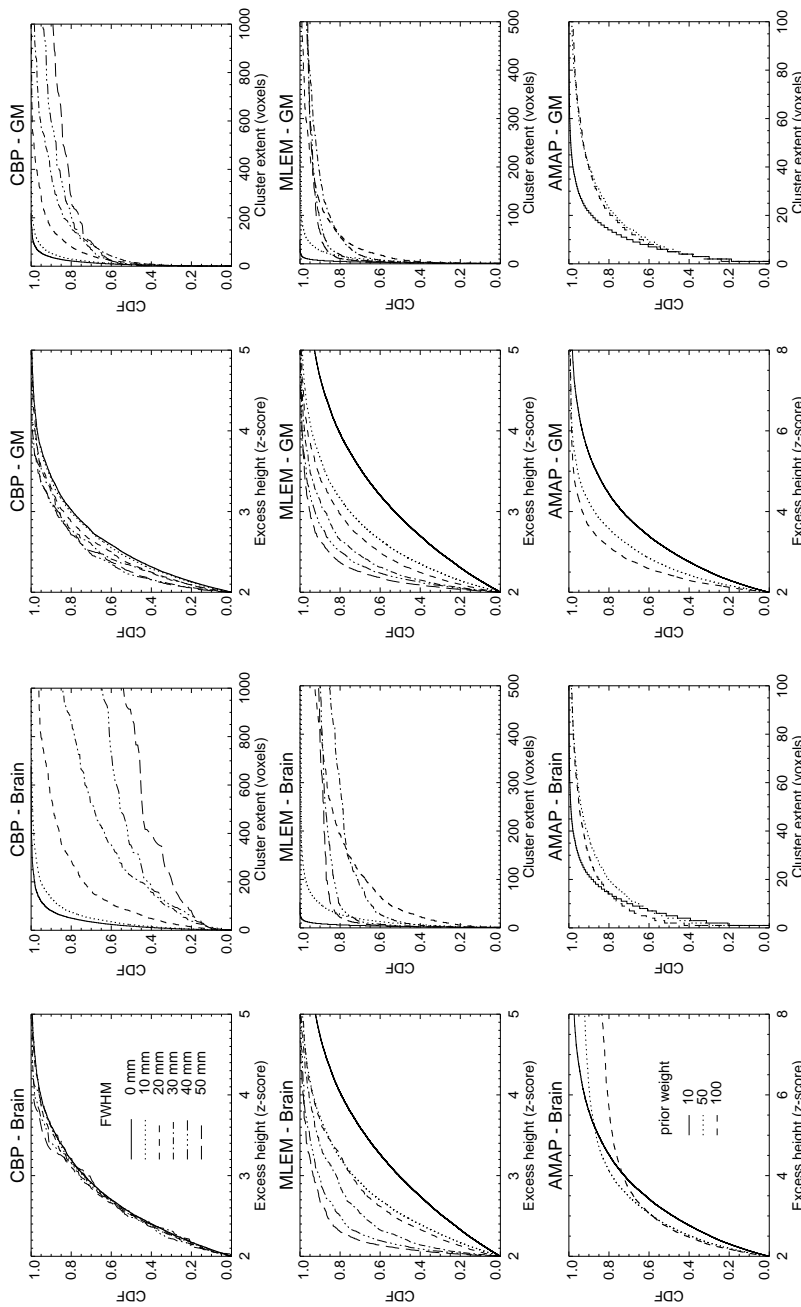


Figure 6.2: Each curve represents the empirical CDF of the excess height (columns 1 and 3) and cluster extent (columns 2 and 4) of supra-threshold clusters found in 100 subtraction images of CBP (first row), ML-EM (second row), and A-MAP (third row) reconstructions of signal-absent noise realizations of the projection data of a brain software phantom. Multiple curves within each plot represent the different noise suppression strengths that were used for each reconstruction method. Subtractions were performed for all voxels belonging to the brain (columns 1 and 2) and for all voxels with at least 50 % GM (columns 3 and 4).

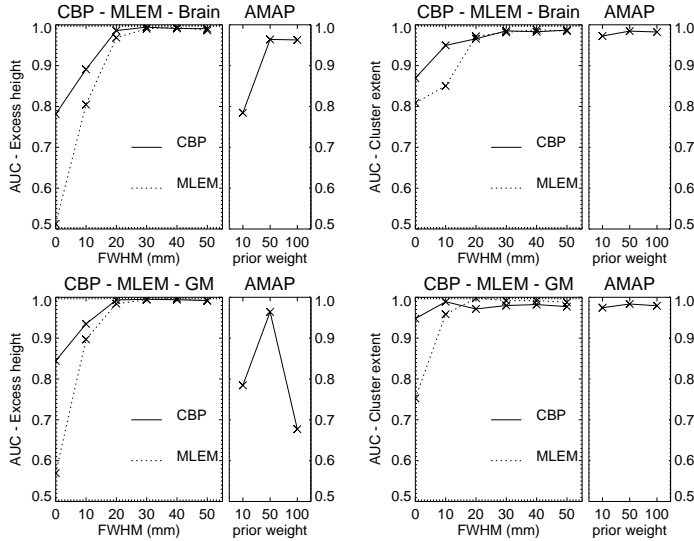


Figure 6.3: Each curve represents the AUC for the excess height (first column) and cluster extent (second column) when using CBP, ML-EM, and A-MAP with different smoothing kernels and prior weights. Subtractions for this detection experiment were performed for all voxels belonging to the brain (first row) and for all voxels with at least 50 % GM (second row).

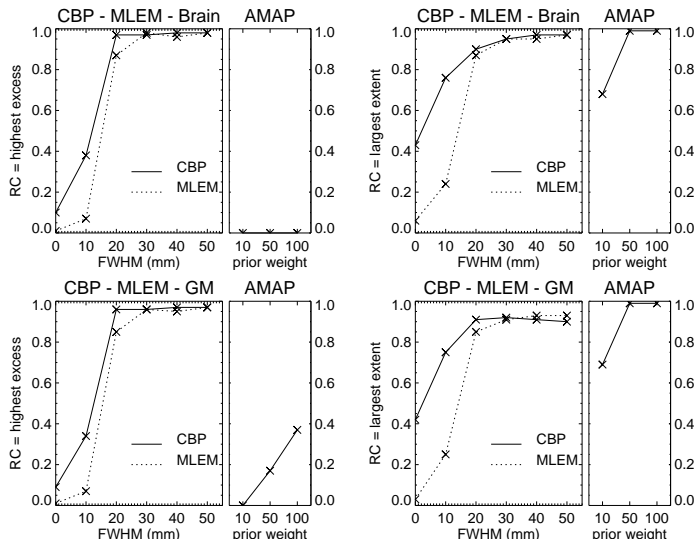


Figure 6.4: Each curve represents the fraction of subtraction images in which the retrieved cluster (RC) was the observed cluster with the highest excess (first column) and the largest extent (second column). Subtractions were performed for all voxels belonging to the brain (first row) and for all voxels with at least 50 % GM (second row).

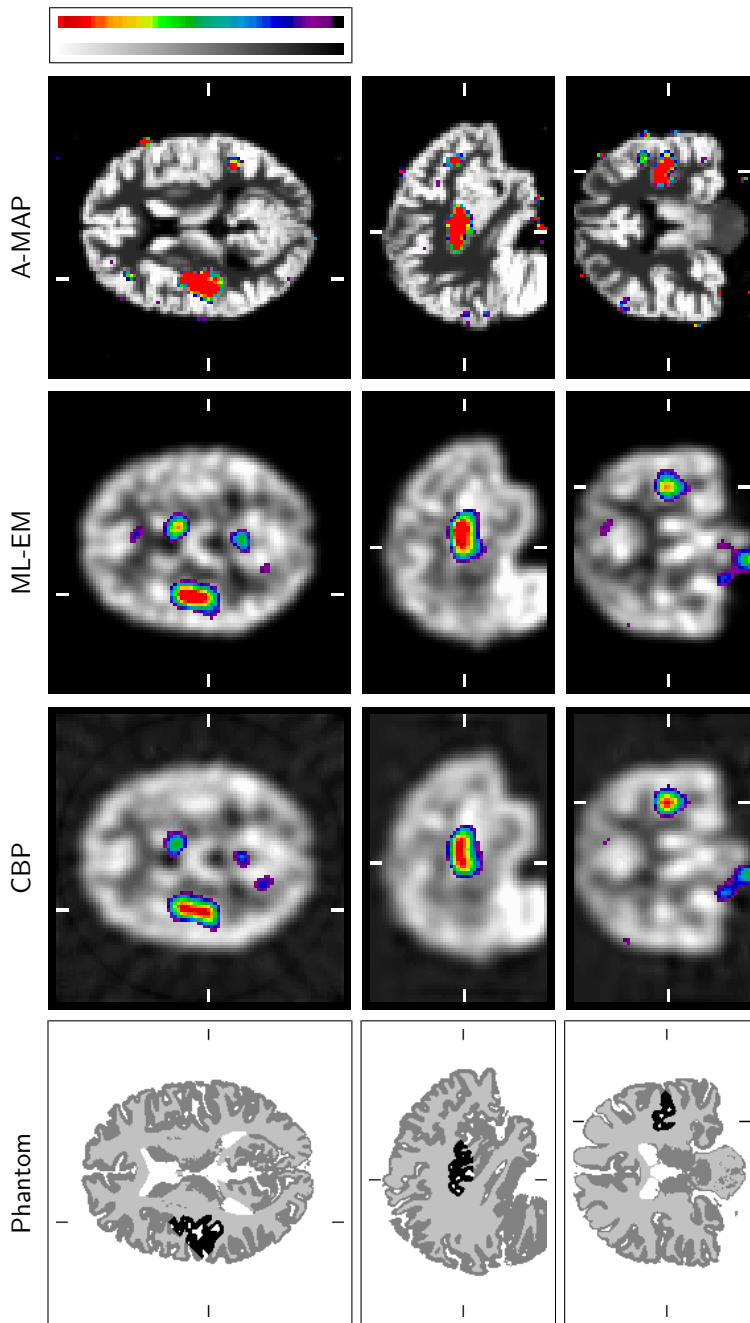


Figure 6.5: The first column shows a composition image of the hyper-perfusion phantom. For reasons of visualization, the ratio of intensities between GM, WM, and the hyper-perfused region are different to those used in the simulation experiments. The other columns show the supra-threshold subtraction of the hyper-perfusion and baseline SPECT reconstructions of one of the noise realizations on top of the baseline SPECT reconstruction, for CBP without post-smoothing (*second column*), ML-EM post-smoothed using a Gaussian kernel with 10 mm FWHM (*third column*), and A-MAP (*fourth column*). The first row shows trans-axial, the second row coronal, and the third row sagittal views through the region of induced hyper-perfusion.

gradual reduction of the excess height of supra-threshold clusters. Hence, increased post-smoothing seems to narrow the distribution of the subtraction image for ML-EM, as opposed to CBP. For A-MAP, the excess height shows a similar effect when the subtraction is being performed for the GM mask. When the brain mask is used, an increase of the prior weight leads to clusters with very high excess heights. We attribute this effect to isolated or very small clusters of voxels that are not connected to the large group of voxels in subset \mathbb{G} , i.e. the subset of voxels containing at least some GM (cfr. 3.46). The presence of these isolated or very small clusters of voxels in the GM segmentation image is not expected, because of the morphological shape of the human brain. Actually, this effect is due to a combination of noise in the MR data, and misclassifications by the segmentation algorithm. As a result, the neighborhood of the Gibbs-Markov prior in the A-MAP reconstruction method is almost unable to “see” these voxels, by which they are practically left to be unconstrained. These voxels can then give rise to high intensity values in the reconstructed image with large estimation errors. Eventually, these voxels may induce large differences in the subtraction images for A-MAP, which can be seen by the shape of the CDF curves for the excess height.

The CDF of the cluster extent for CBP shows that supra-threshold clusters have gradually larger extents when the width of the post-smoothing kernel is increased. The CDF of CBP for the excess height and for the cluster extent are comparable to the results which were obtained in previous experiments (§5.3.1). The ML-EM reconstruction method shows a more complex pattern for the CDF of the cluster extent. For moderate post-smoothing, the effect on the CDF curve is similar to that of CBP. However, when excessive post-smoothing is applied, the distribution becomes more and more dominated by a larger fraction of clusters with rather small cluster extents, and a smaller fraction of clusters with large cluster extents. For A-MAP, the CDF of the cluster extent remains practically unchanged when the prior weight is varied. Furthermore, it seems that the measured extent of clusters are in general much smaller for using the A-MAP reconstruction method, than for ML-EM or CBP. We attribute this effect to the combination of resolution recovery, noise suppression by means of multiple priors, and the partial volume correction framework of the A-MAP algorithm.

We assessed the detection performance of each reconstruction method and noise suppression technique using ROC analysis. The ROC curves were converted to AUC values such that different reconstruction methods could be compared. The results that were obtained for CBP and ML-EM show that the detection performance is improved, for the excess height, as well as for the cluster extent, when Gaussian post-smoothing is being applied. Moreover, the detection performance continues to improve when the width of the post-smoothing kernel is increased. However, between 20 and 30 mm FWHM, the AUC reaches optimal performance levels. It has been shown that the highest signal-to-noise ratio is achieved by *matched filter* smoothing, however at the expense of a reduction in resolution [Tanaka and Iinuma, 1970]. Indeed, the volume of the induced hyper-perfusion lesion equals 7.938 cm^3 , which is approximately equivalent to a sphere with a diameter of 24.75 mm. Additional simulation experiments and ROC analysis have shown that the detection

performance drops for kernel widths above 60 mm FWHM.

The AUC values for simulations without post-smoothing are systematically higher for CBP than for ML-EM. The reason for this effect is that the CBP reconstruction method includes Butterworth low-pass filtering of the projection data. The pre-processing of the projections make that the CBP reconstructions are smoother than the reconstructions obtained by the ML-EM method. The difference in detection performance between CBP and ML-EM disappears gradually when post-smoothing is being applied. This is because the smoothness of the reconstructions become more and more dependent on the post-smoothing kernel, as opposed to the initial smoothness imposed by the reconstruction method. The cluster extent shows a better detection performance than the excess height for CBP and ML-EM when the kernel width is below 20 mm FWHM. For CBP, this confirms the results which were obtained in §5.3.2. In that study, the mean AUC for excess height was 0.74, and for cluster extent 0.83. In this study, we obtain AUC values of 0.78 for excess height and 0.87 for cluster extent, when no post-smoothing is applied.

A-MAP shows a lower detection performance for the excess height than for the cluster extent. Again, we attribute this effect to the presence of isolated or very small clusters of voxels that are not connected to the large group of voxels in subset \mathbb{G} . These practically unconstrained voxels give rise to large differences in the subtraction image, which shows a reduction of the detection performance for the parameter excess height. On the other hand, the results for the detection performance of A-MAP based on the cluster extent, are comparable to the optimal values for the detection performance obtained by CBP and ML-EM. Although increased post-smoothing, performed after CBP or ML-EM, gives improved detection performance, it has the disadvantage that the localization power is gradually being decreased. A-MAP does not have that problem, as can be seen in Fig. 6.5.

The curves showing the fraction of subtraction images in which the RC is the cluster with the highest excess or the largest extent for CBP and ML-EM follow a behavior which is quite similar to that of the AUC. The fractions of subtraction images grow when Gaussian post-smoothing is being applied, and reach a maximum for kernel widths between 20 and 30 mm FWHM. These results are similar to those obtained for the AUC, and they are in agreement with the matched filter theorem [Tanaka and Iinuma, 1970]. Additional simulation experiments have also shown that the fractions drop for kernel widths above 50 mm FWHM.

A-MAP shows a different behavior than CBP or ML-EM. Due to the presence of isolated or small clusters of voxels which produce large differences, the fraction of images in which the cluster with the highest excess equals the RC is zero for using the brain subtraction mask. For using the GM subtraction mask, the fraction grows when the weight of the prior is increased. On the other hand, the observed cluster with the largest extent equals the RC in almost all images when the prior weight exceeds 50 and for using the brain as well as the GM subtraction mask. The results of this experiment, and those of the CDF curves for A-MAP, show that the algorithm produces in general much smaller clusters of which the smallest ones are more unconstrained.

Further analysis of this method in clinical practice is required to evaluate its

value for the detection and characterization of epileptogenic regions in subtraction SPECT.

6.5 Conclusion

In this simulation study, we have shown that the subtraction analysis of ictal and interictal SPECT perfusion data can be formulated in a probabilistic framework. Furthermore, the use of strong post-smoothing improves the accuracy and performance of the technique for using CBP or ML-EM. When high-resolution MRI is available, anatomy based reconstruction of SPECT data can lead to similar results without the need for post-smoothing and loss of localization power.

General Conclusion

"If we want to solve a problem that we have never solved before, we must leave the door to the unknown ajar."

RICHARD P. FEYNMAN
(1918–1988)

7.1 Main Contributions

The work performed within the scope of this dissertation has yielded some contributions to the field of medical imaging. These contributions involve the improvement of emission tomography techniques for the presurgical evaluation of patients with refractory partial epilepsy. The primary aim of this work has been to reduce the influence of image degrading effects on the detection of epileptogenic regions in ECD-SPECT and FDG-PET data. We have been focusing on the correction of the partial volume effect in PET and SPECT, and on the influence of noise, the noise suppression technique, and the reconstruction method in the subtraction analysis of SPECT data.

We investigated the origin and influence of the partial volume effect (PVE) in PET and SPECT, and we studied its consequences for clinical decision making. A broad range of partial volume correction (PVC) techniques, which were found in scientific literature, have been analyzed. We reviewed post-processing and statistical based PVC techniques. Although a whole variety of PVC methods have been proposed, we developed a new method which we abbreviated as A-MAP [Baete *et al.*, 2004a,b]. In contrast to other PVC methods, A-MAP has been designed to perform PVC of the GM tissue during statistical reconstruction of the projection data. The algorithm makes use of segmented MRI data and includes specific assumptions about the pathology which allows for the use of more a priori knowledge

during the reconstruction, as opposed to other PVC methods. The assumptions on which A-MAP has been based, as well as the mathematical derivation of the iterative reconstruction algorithm were presented. Furthermore, we proved that the objective function which is optimized by the algorithm has no multiple local maxima. We illustrated the PVC properties of the reconstruction algorithm by means of a proof-of-principle simulation experiment.

We performed extensive evaluation of the new reconstruction algorithm [Baete *et al.*, 2004a]. We used a number of 2-D and 3-D software phantom based simulation experiments to assess its performance. For that purpose, a realistic 3-D brain software phantom was constructed from which segmented MRI, PET, and SPECT data was derived. We investigated the use of perfect and imperfect anatomical information provided by the segmented MRI data using 2-D based simulations. Imperfect anatomical information decreased the detection performance of the algorithm. Using 3-D based simulation experiments, we looked at the influence of the anatomical prior weight, the effect of small misalignments between the anatomical information and the emission tomography data, and the effect of local segmentation errors. A-MAP showed to be robust for variation of the anatomical prior weight, small misalignments, and local segmentation errors. We have used figures-of-merit, such as the signal-to-noise ratio, bias, and variance, to assess the performance of A-MAP. We designed a human observer study, which involved the contribution of multiple nuclear medicine physicians and residents-in-training of our department. We assessed the performance of detecting hypometabolic regions in simulated FDG-PET data when using A-MAP and the ML-EM reconstruction algorithm. The overall detection score for A-MAP was for each human observer higher than that of ML, indicating a benefit of using A-MAP for the detection of hypo-metabolic regions in FDG-PET data. Finally, we used FDG-PET and MRI data of a patient with refractory partial epilepsy to illustrate the applicability of A-MAP in clinical practice.

We studied the influence of noise on the subtraction analysis of simulated ictal and interictal ECD-SPECT data. We proposed a method for statistical based characterization of supra-threshold clusters in subtraction SPECT [Baete *et al.*, 2002]. Supra-threshold clusters are characterized by their excess height or extent. We analyzed the behavior of the excess height and extent of the clusters under the influence of noise only and used these results to assign a probability under the null hypothesis of no real physiological change to each observed cluster in subtraction SPECT images. The reproducibility of the approach was assessed by means of 3-D software phantom simulation experiments. The size and intensity of an induced hyperperfused region was varied and multiple simulation experiments were performed. For different probability thresholds, sensitivity and specificity for the detection of this induced region was measured. ROC analysis showed a better detection performance when based on the cluster extent. We concluded that the cluster extent is an important parameter for the characterization of significant supra-threshold clusters in subtraction SPECT images.

Finally, we studied the influence of noise suppression and the use of different reconstruction methods on the characterization of supra-threshold clusters in sub-

traction SPECT image. We analyzed the behavior of excess height and extent of clusters under the influence of noise. The empirical method for the assignment of a probability under the null hypothesis of no real physiological change was then used for the detection of an induced region of hyper-perfusion. For different probability thresholds, sensitivity and specificity was measured for all noise suppression techniques and reconstruction methods. ROC analysis showed that strong post-smoothing improves the detection performance when using the CBP and ML-EM reconstruction methods. The difference between the detection performance of the excess height and the cluster extent disappeared when using larger widths of the post-smoothing kernel. The use of A-MAP showed similar results for the cluster extent, but without the need for post-smoothing. This might improve the presurgical localization accuracy of epileptogenic regions.

7.2 Suggestions for Future Research

Clinical Evaluation

In this dissertation, we have been working primarily with realistic software phantom simulation experiments for the evaluation of new techniques, because the ground truth is seldom known in patient studies. The next step is to evaluate the new techniques more thoroughly in a clinical setting. However, the evaluation and clinical validation of medical imaging and image reconstruction techniques is inherently difficult, and can sometimes be unconvincing to the medical imaging community. There is a clear need for guidelines how to evaluate reconstruction techniques and other image processing issues in PET and SPECT [Zaidi and Montandon, 2006].

Nevertheless, physicians are currently evaluating the usefulness of A-MAP in a clinical setting using a retrospective study. We selected FDG-PET projection data of well documented patients with refractory partial epilepsy and for which concordant results have been obtained. The projection data have been reconstructed using ML-EM and A-MAP. A nuclear medicine physician and a neurologist have been asked to perform independent inspection of the reconstructed data and report all abnormalities by means of a region based approach. For that purpose, the reconstructed images have been aligned with a template. Although we do not have a real golden standard, we will try to compare the techniques and investigate whether the observed abnormalities are consistent with the pathology. Especially the effect on the clinical decision making is important.

With the development of A-MAP, we obtained a PVC technique for the GM activity distribution in emission tomography data of the human brain. An interesting side-effect of A-MAP is the estimation of the GM fractional activity distribution for voxels which are classified as containing at least some GM tissue (cfr. §3.4.2 and Fig. A.1 on p. 129). In this work, we have not investigated the usefulness of this information. However, we expect that this additional knowledge might help for the inspection of regions containing a mixture of GM and WM.

For A-MAP, we imposed assumptions on the activity distribution within WM.

If A-MAP should be used for other neurological applications in PET or SPECT, a problem might occur regarding the uniformity assumption of the WM activity distribution. Further clinical evaluation should reveal what the implications are when this assumption is being violated.

Multi-modal Imaging and Signal Processing

During the course of this dissertation, some important improvements have been made in MRI and EEG. These imaging and signal processing modalities are essential for the general evaluation of patients with refractory epilepsy.

Srivastava *et al.* [2005] developed a methodology for the automatic detection of focal cortical dysplasia by means of an improved segmentation strategy which reduces misrepresentations of tissue segmentations. An increasing number of studies show that focal cortical dysplasia are related to epileptogenic lesions in many cases of refractory partial epilepsy. Further understanding of focal cortical dysplasia is required and needs more investigation of the correlation between functional imaging and pathological analysis of surgically resected cortical samples [Palmini *et al.*, 2004]. We also believe that further improvements to the segmentation of MRI data may have a beneficial effect on the performance of A-MAP [Srivastava *et al.*, 2001].

De Clercq *et al.* [2005] developed a new technique for the removal of scalp EEG artifacts, caused by sources other than the brain, which might obscure the epileptiform activity within the EEG recording. This technique may allow to detect seizure onset much earlier than other methods, and obtain a better localization of the epileptogenic region. The combination and integration of the results obtained by these new imaging and signal processing techniques may shed new light on the understanding of epileptic seizures. Therefore, it is important that each of the different techniques are optimized and that methods for integration of the information are developed.

Extensions of A-MAP

A-MAP may be extended to brain imaging protocols in which tracer molecules other than ^{18}F -FDG or $^{99\text{m}}\text{Tc}$ -ECD are used, or to other pathologies. However, for each application, it will be required that the assumptions underlying A-MAP are validated. Further investigation has to show the potential usefulness of A-MAP in these conditions.

Another important and useful extension may be the application of A-MAP to measured projection data of dynamic acquisition protocols. Dynamic studies are mostly used for quantitative assessment of the kinetic behavior of an administered tracer molecule. Of interest to the investigators are the uptake and exchange of the tracer molecule during the course of time into different compartments. Dynamic studies are an example of measuring in extreme conditions. The count levels in the projection data are low due to the short duration of the acquisition frames, by which image noise levels are high. Straightforward noise suppression, such as image

post-smoothing, is avoided because it may destroy the quantitative accuracy of the measurement. However, also in this situation the measurements are influenced by the PVE. There are different approaches for application of PVC techniques in kinetic modeling. One is to perform PVC after kinetic modeling of the data, or before. We believe that the data should be corrected before the model is applied and A-MAP is obviously the method of choice.

In recent years, the imaging of small laboratory animals using dedicated equipment, like e.g. micro-PET and micro-SPECT, has shown to be a valuable tool for fundamental biomedical research. This new emerging research field, often referred to as *molecular imaging*, aims at the pre-clinical analysis of, and search for, new drugs and tracer molecules, imaging of enzymes, receptors, and the expression of genes *in vivo*. In some applications, quantitative analysis may be important, and even though the spatial resolution of the imaging equipment may be sufficient, there may be a need for PVC of the obtained images. Simultaneous to this work, Dirk Bequé developed a technique for the calibration of the sensitivity and acquisition geometry of high-resolution pinhole micro-SPECT [Bequé *et al.*, 2003, 2005]. Application of A-MAP could represent a suitable regularization of the under-determined problem of pinhole and multi-pinhole image reconstruction. We anticipate that the use of A-MAP yields a significant improvement of image quality in these applications.

In a number of applications, state-of-the-art medical imaging may require that the anatomical and functional images of the subject are available and spatially aligned for visual inspection. In clinical oncology, for example, simultaneous inspection of CT and PET images may be required for an optimal assessment of the condition of the patient. For that purpose, multi-modal image registration techniques have been developed to align the images. In recent years, however, a more practical solution has appeared with the development of a combined PET/CT scanner [Townsend and Beyer, 2002]. For certain PET/CT applications in which PVC might be needed for a specific organ, we believe that A-MAP might be useful. Again, further investigation should assess its applicability.

However, anatomy and function in PET/CT are not acquired simultaneously, but consecutively. In some studies, the reconstructed images of the two modalities are not always fully aligned and image registration techniques are therefore still being required. A similar technological evolution of multi-modal imaging is taking place between MRI and PET. Some research groups have successfully investigated the compatibility of PET acquisition hardware inside the magnetic field of an MRI device [Shao *et al.*, 1997; Slates *et al.*, 1999]. We expect that, within a few years, true simultaneous MRI and PET will be commercially available. It is likely that many potential clinical applications for combined MRI and PET will soon appear [Marsden *et al.*, 2002]. A-MAP may already be one of these applications.

Subtraction Technique

The SPECT subtraction method, which we described in Chapter 5, supplies information about the extent, excess height, location, and the cluster and excess height probability for each of the observed clusters in a SISCOM analysis. This approach

may be useful as a supplemental tool for the evaluation of SISCOM data. Physicians may choose to use a certain probability threshold to retain only significant clusters, and ignore those attributed to noise. Preferably, this approach should be evaluated using a large number of SPECT studies. Retrospective analysis may compare the results obtained by SISCOM with the post-surgical outcome. In that analysis, it may be useful to compare the geometry of the surgically resected region with the outline of the epileptogenic cluster obtained by SISCOM, and correlate the results with patient outcome.

The subtraction technique may also be used to compare images of a patient in two conditions, when using the same imaging modality and acquisition protocol. For example, cerebral perfusion imaging with and without administering of the drug acetazolamide (Diamox®) is a commonly used test for the vascular reserve in patients suffering stroke, transient ischemic attacks, or arteriovenous malformations. Patients showing positive reaction to the drug have a better prognosis for intracranial bypass surgery.

The normalization of emission tomography images prior to subtraction is crucial because the global tracer activity in the brain is not necessarily equal during acquisition. How to perform the normalization step remains to be a subtle issue, because the developed methods are difficult to validate, and the underlying epileptic pathology is largely unknown and unpredictable [Boussion *et al.*, 2002; Vandecan, 2004]. In this work, we have been using a heuristic method for the construction of the reference region which is used to determine the mean activity (cfr. 5.2). More research is however needed on this topic. Segmented MRI data might be used to e.g. use WM as a region for normalization, especially in combination with an A-MAP reconstruction of the SPECT/PET data.

A.1 Proof of Concavity

We prove that M , which is the logarithm of the prior defined in equation (3.64), is concave if the term $M^{\mathbb{G}}$, which is defined in equation (3.68), is concave.

A function M is concave if and only if the Hessian, i.e. the matrix of second derivatives of M , is negative semi-definite, or

$$\sum_{k,l \in \mathbb{J}} x_k x_l \frac{\partial^2 M}{\partial \lambda_k \partial \lambda_l} \Big|_{\vec{x}} \leq 0 \quad (\text{A.1})$$

for all $\vec{x} = \{x_j \mid j \in \mathbb{J}\}$.

Since the sum of concave functions is concave, it is sufficient to prove that $M^{\mathbb{W}}$, $M^{\mathbb{C}}$ and $M^{\mathbb{R}}$, defined in equations (3.65), (3.66), and (3.67), respectively, are concave. It is clear that $M^{\mathbb{C}}$ is a concave function. Then, it remains to be shown that $M^{\mathbb{W}}$ and $M^{\mathbb{R}}$ are concave. We proof this for $M = M^{\mathbb{W}}$, given by

$$M = -\beta_{\mathbb{W}} \sum_{j \in \mathbb{J}} \left(\delta_j^{\mathbb{W}} \lambda_j - \frac{\sum_r \delta_r^{\mathbb{W}} f_r \lambda_r}{\sum_s \delta_s^{\mathbb{W}} f_s} \right)^2. \quad (\text{A.2})$$

Without loss of generality, we can assume that $\beta_{\mathbb{W}} = 1$.

Proof. The first derivatives of M are

$$\frac{\partial M_j}{\partial \lambda_k} = \delta_j^{\mathbb{W}} \delta_k^{\mathbb{W}} \frac{f_k}{n_{\mathbb{W}}} \left(\lambda_j - \frac{1}{n_{\mathbb{W}}} \sum_r \delta_r^{\mathbb{W}} f_r \lambda_r \right) \iff j \neq k \quad (\text{A.3})$$

$$\frac{\partial M_k}{\partial \lambda_k} = -\delta_k^{\mathbb{W}} \left(1 - \frac{\delta_k^{\mathbb{W}} f_k}{n_{\mathbb{W}}} \right) \left(\lambda_k - \frac{1}{n_{\mathbb{W}}} \sum_r \delta_r^{\mathbb{W}} f_r \lambda_r \right) \quad (\text{A.4})$$

with $n_{\mathbb{W}} = \sum_s \delta_s^{\mathbb{W}} f_s$. The second derivatives of M are

$$\frac{\partial M_j^2}{\partial \lambda_k \partial \lambda_l} = -\delta_j^{\mathbb{W}} \delta_k^{\mathbb{W}} \delta_l^{\mathbb{W}} \frac{f_k f_l}{n_{\mathbb{W}}^2}, \quad \iff \quad j \neq k, j \neq l, k \neq l \quad (\text{A.5})$$

$$\frac{\partial M_j^2}{\partial \lambda_k^2} = -\delta_j^{\mathbb{W}} \left(\frac{\delta_k^{\mathbb{W}} f_k}{n_{\mathbb{W}}} \right)^2, \quad \iff \quad j \neq k \quad (\text{A.6})$$

$$\frac{\partial M_k^2}{\partial \lambda_k \partial \lambda_l} = \delta_k^{\mathbb{W}} \delta_l^{\mathbb{W}} \frac{f_l}{n_{\mathbb{W}}} \left(1 - \frac{\delta_k^{\mathbb{W}} f_k}{n_{\mathbb{W}}} \right), \quad \iff \quad k \neq l \quad (\text{A.7})$$

$$\frac{\partial M_k^2}{\partial \lambda_k^2} = -\delta_k^{\mathbb{W}} \left(1 - \frac{\delta_k^{\mathbb{W}} f_k}{n_{\mathbb{W}}} \right)^2. \quad (\text{A.8})$$

Equation (A.1) is equivalent to

$$\sum_k x_k^2 \frac{\partial^2 M}{\partial \lambda_k^2} + \sum_{\substack{k,l \\ k \neq l}} x_k x_l \frac{\partial^2 M}{\partial \lambda_k \partial \lambda_l} \leq 0. \quad (\text{A.9})$$

The first term of this equation can be written as

$$\sum_k x_k^2 \frac{\partial^2 M}{\partial \lambda_k^2} \quad (\text{A.10})$$

$$= \sum_k x_k^2 \frac{\partial^2 M_k}{\partial \lambda_k^2} + \sum_{\substack{k,j \\ k \neq j}} x_k^2 \frac{\partial^2 M_j}{\partial \lambda_k^2} \quad (\text{A.11})$$

$$= - \sum_k x_k^2 \delta_k^{\mathbb{W}} \left(1 - \frac{f_k}{n_{\mathbb{W}}} \right)^2 - \sum_{\substack{k,j \\ k \neq j}} x_k^2 \delta_k^{\mathbb{W}} \delta_j^{\mathbb{W}} \left(\frac{f_k}{n_{\mathbb{W}}} \right)^2 \quad (\text{A.12})$$

$$= - \sum_k x_k^2 \delta_k^{\mathbb{W}} \left(1 - \frac{f_k}{n_{\mathbb{W}}} \right)^2 - \sum_k x_k^2 \delta_k^{\mathbb{W}} \left(\frac{f_k}{n_{\mathbb{W}}} \right)^2 \sum_{\substack{j \\ j \neq k}} \delta_j^{\mathbb{W}} \quad (\text{A.13})$$

$$= - \sum_k x_k^2 \delta_k^{\mathbb{W}} \left(1 - \frac{f_k}{n_{\mathbb{W}}} \right)^2 - (N-1) \sum_k x_k^2 \delta_k^{\mathbb{W}} \left(\frac{f_k}{n_{\mathbb{W}}} \right)^2 \quad (\text{A.14})$$

$$= - \sum_k x_k^2 \delta_k^{\mathbb{W}} \left(1 - 2 \frac{f_k}{n_{\mathbb{W}}} + N \frac{f_k^2}{n_{\mathbb{W}}^2} \right) \quad (\text{A.15})$$

with $N = \sum_j \delta_j^{\mathbb{W}}$. The second term of (A.9) can be written as

$$\sum_{\substack{k,l \\ k \neq l}} x_k x_l \frac{\partial^2 M}{\partial \lambda_k \partial \lambda_l} = \quad (\text{A.16})$$

$$= \sum_{\substack{k,l \\ k \neq l}} x_k x_l \frac{\partial^2 M_k}{\partial \lambda_k \partial \lambda_l} + \sum_{\substack{k,l \\ k \neq l}} x_k x_l \frac{\partial^2 M_l}{\partial \lambda_k \partial \lambda_l} + \sum_{\substack{k,l,j \\ k \neq l \\ j \neq k \\ j \neq l}} x_k x_l \frac{\partial^2 M_j}{\partial \lambda_k \partial \lambda_l} \quad (\text{A.17})$$

$$= \sum_{\substack{k,l \\ k \neq l}} x_k x_l \delta_{k,l}^{\mathbb{W}} \frac{f_l}{n_{\mathbb{W}}} \left(1 - \frac{f_k}{n_{\mathbb{W}}} \right) + \sum_{\substack{k,l \\ k \neq l}} x_k x_l \delta_{k,l}^{\mathbb{W}} \frac{f_k}{n_{\mathbb{W}}} \left(1 - \frac{f_l}{n_{\mathbb{W}}} \right) \\ - \sum_{\substack{k,l,j \\ k \neq l \\ j \neq k \\ j \neq l}} x_k x_l \delta_{k,l,j}^{\mathbb{W}} \frac{f_k f_l}{n_{\mathbb{W}}^2} \quad (\text{A.18})$$

$$= \sum_{\substack{k,l \\ k \neq l}} x_k x_l \delta_{k,l}^{\mathbb{W}} \left\{ \frac{f_l}{n_{\mathbb{W}}} \left(1 - \frac{f_k}{n_{\mathbb{W}}} \right) + \frac{f_k}{n_{\mathbb{W}}} \left(1 - \frac{f_l}{n_{\mathbb{W}}} \right) \right\} \\ - \sum_{\substack{k,l \\ k \neq l}} x_k x_l \delta_{k,l}^{\mathbb{W}} \frac{f_k f_l}{n_{\mathbb{W}}^2} \sum_{\substack{j \\ j \neq k \\ j \neq l}} \delta_j^{\mathbb{W}} \quad (\text{A.19})$$

$$= \sum_{\substack{k,l \\ k \neq l}} \frac{x_k x_l \delta_{k,l}^{\mathbb{W}}}{n_{\mathbb{W}}} \left[\left(f_k + f_l - 2 \frac{f_k f_l}{n_{\mathbb{W}}} \right) - (N-2) \frac{f_k f_l}{n_{\mathbb{W}}} \right] \quad (\text{A.20})$$

$$= \sum_{\substack{k,l \\ k \neq l}} \frac{x_k x_l \delta_{k,l}^{\mathbb{W}}}{n_{\mathbb{W}}} \left(f_k + f_l - N \frac{f_k f_l}{n_{\mathbb{W}}} \right) \quad (\text{A.21})$$

with $\delta_{k,l}^{\mathbb{W}} = \delta_k^{\mathbb{W}} \delta_l^{\mathbb{W}}$. Then, equation (A.9) can be written as

$$- \sum_k x_k^2 \delta_k^{\mathbb{W}} \left(1 - 2 \frac{f_k}{n_{\mathbb{W}}} + N \frac{f_k^2}{n_{\mathbb{W}}^2} \right) + \sum_{\substack{k,l \\ k \neq l}} \frac{x_k x_l \delta_{k,l}^{\mathbb{W}}}{n_{\mathbb{W}}} \left(f_k + f_l - N \frac{f_k f_l}{n_{\mathbb{W}}} \right) \leq 0 \quad (\text{A.22})$$

which is equivalent to

$$- \sum_k x_k^2 \delta_k^{\mathbb{W}} + \sum_{k,l} \frac{x_k x_l \delta_{k,l}^{\mathbb{W}}}{n_{\mathbb{W}}} \left(f_k + f_l - N \frac{f_k f_l}{n_{\mathbb{W}}} \right) \leq 0 \quad (\text{A.23})$$

The inequality that still has to be proven is

$$\frac{2}{n_{\mathbb{W}}} \left(\sum_k x_k \delta_k^{\mathbb{W}} \right) \left(\sum_k x_k f_k \delta_k^{\mathbb{W}} \right) \leq \sum_k x_k^2 \delta_k^{\mathbb{W}} + \frac{N}{n_{\mathbb{W}}^2} \left(\sum_k x_k f_k \delta_k^{\mathbb{W}} \right)^2 \quad (\text{A.24})$$

Consider

$$\left(\frac{1}{\sqrt{N}} \sum_k x_k \delta_k^{\mathbb{W}} - \frac{\sqrt{N}}{n_W} \sum_k x_k f_k \delta_k^{\mathbb{W}} \right)^2 \geq 0 \quad (\text{A.25})$$

from which the following inequality can be extracted

$$\frac{2}{n_W} \left(\sum_k x_k \delta_k^{\mathbb{W}} \right) \left(\sum_k x_k f_k \delta_k^{\mathbb{W}} \right) \leq \frac{1}{N} \left(\sum_k x_k \delta_k^{\mathbb{W}} \right)^2 + \frac{N}{n_W^2} \left(\sum_k x_k f_k \delta_k^{\mathbb{W}} \right)^2 \quad (\text{A.26})$$

Also, consider the following inequality

$$0 \leq \sum_{k,l} (x_k \delta_k^{\mathbb{W}} - x_l \delta_l^{\mathbb{W}})^2 \quad (\text{A.27})$$

$$2 \sum_{k,l} x_k x_l \delta_{k,l}^{\mathbb{W}} \leq \sum_{k,l} x_k^2 \delta_k^{\mathbb{W}} + \sum_{k,l} x_l^2 \delta_l^{\mathbb{W}} \quad (\text{A.28})$$

$$2 \left(\sum_k x_k \delta_k^{\mathbb{W}} \right)^2 \leq 2N \sum_k x_k^2 \delta_k^{\mathbb{W}} \quad (\text{A.29})$$

$$\frac{1}{N} \left(\sum_k x_k \delta_k^{\mathbb{W}} \right)^2 \leq \sum_k x_k^2 \delta_k^{\mathbb{W}} \quad (\text{A.30})$$

Then, combining (A.26) and (A.30) proves (A.24). The proof for the concavity of $M = M^{\mathbb{R}}$ is similar. Hence, the logarithm of the prior M in (3.64) is concave if $M^{\mathbb{G}}$ is concave. ■

A.2 Implementation of the A-MAP Reconstruction Algorithm

The implementation of the A-MAP reconstruction algorithm is summarized by means of pseudo-code in Fig. A.1. The projection based on system matrix c_{ij}^* is implemented as

$$\begin{aligned} \sum_{j \in \mathbb{J}} c_{ij}^* \lambda_j^* &= \underbrace{\sum_{j \in \mathbb{J}} (1 - \delta_j^{\mathbb{G}}) c_{ij} \lambda_j}_{\text{sinogram}} + \underbrace{\left(\frac{1}{n_W} \sum_{j \in \mathbb{J}} \delta_j^{\mathbb{W}} f_j^W \lambda_j \right)}_{\text{weight}} \cdot \underbrace{\left(\sum_{j \in \mathbb{J}} \delta_j^{\mathbb{G}} c_{ij} f_j^W \right)}_{\text{sinogram}} \\ &\quad + \underbrace{\left(\frac{1}{n_C} \sum_{j \in \mathbb{J}} \delta_j^{\mathbb{C}} f_j^C \lambda_j \right)}_{\text{weight}} \cdot \underbrace{\left(\sum_{j \in \mathbb{J}} \delta_j^{\mathbb{G}} c_{ij} f_j^C \right)}_{\text{sinogram}} + \underbrace{\sum_{j \in \mathbb{J}} \delta_j^{\mathbb{G}} c_{ij} f_j^G \lambda_j^G}_{\text{sinogram}} \end{aligned} \quad (\text{A.31})$$

A-MAP reconstruction algorithm	
Initialization of Λ^* : $\lambda_j^* \leftarrow 1$	
Pre-computation of c_{ij}^* using equation (3.62)	
Iterative loop:	
for n : 1 → number of iterations do begin	
$\mathcal{P}_i \leftarrow \sum_j c_{ij}^* \lambda_j^*$ (projection)	
$\mathcal{B}_j \leftarrow \sum_i c_{ij}^* \left(\frac{q_i}{\mathcal{P}_i} - 1 \right)$ (back-projection)	
$\lambda_j^* \leftarrow \lambda_j^* + \lambda_j^* \frac{\mathcal{B}_j + \frac{\partial M}{\partial \lambda_j} \Big _{\Lambda^*}}{\sum_i c_{ij}^* - \lambda_j^* \frac{\partial^2 M}{\partial \lambda_j^2} \Big _{\Lambda^*}}$ (update)	
endfor	
Transformation to Λ using equation (3.70):	
$\lambda_j \leftarrow (1 - \delta_j^G) \lambda_j^* + \delta_j^G \left(f_j^G \lambda_j^* + \frac{f_j^W}{n_W} \sum_{k \in W} f_k^W \lambda_k^* + \frac{f_j^C}{n_C} \sum_{k \in C} f_k^C \lambda_k^* \right)$	

Figure A.1: Pseudo-code of the implementation of A-MAP. For the description of the variables see §3.4.2.

and the back-projection of a sinogram x_i is implemented as

$$\begin{aligned} \sum_i c_{ij}^* x_i &= \underbrace{\left(1 - \delta_j^G \right) \left(\sum_i c_{ij} x_i \right)}_{\text{image}} + \underbrace{\left(\frac{1}{n_W} \sum_i \left[\sum_{k \in J} \delta_k^G c_{ik} f_k^W \right] x_i \right)}_{\text{weight}} \cdot \underbrace{\left(\delta_j^W f_j^W \right)}_{\text{image}} \\ &+ \underbrace{\left(\frac{1}{n_C} \sum_i \left[\sum_{k \in J} \delta_k^G c_{ik} f_k^C \right] x_i \right)}_{\text{weight}} \cdot \underbrace{\left(\delta_j^C f_j^C \right)}_{\text{image}} + \underbrace{\delta_j^G f_j^G \left(\sum_i c_{ij} x_i \right)}_{\text{image}}. \quad (\text{A.32}) \end{aligned}$$

References

- P. D. Acton and K. J. Friston. Statistical parametric mapping in functional neuroimaging: beyond PET and fMRI activation studies. *Eur. J. Nucl. Med.*, 25:663–667, 1998.
- L.-E. Adam, J. Zaers, H. Ostertag, H. Trojan, M. E. Bellemann, and G. Brix. Performance evaluation of the whole-body PET scanner ECAT EXACT HR+ following the IEC standard. *IEEE Trans. Nucl. Sci.*, 44(3):1172–1179, 1997.
- S. Alenius, U. Ruotsalainen, and J. Astola. Using local median as the location of the prior distribution in iterative emission tomography image reconstruction. *IEEE Trans. Nucl. Sci.*, 45(6):3097–3104, 1998.
- B. A. Ardekani, M. Braun, B. F. Hutton, I. Kanno, and H. Iida. Minimum cross-entropy reconstruction of PET images using prior anatomical information. *Phys. Med. Bio.*, 41:2497–2517, 1996.
- J. A. Aston, V. J. Cunningham, M.-C. Asselin, A. Hammers, A. C. Evans, and R. N. Gunn. Positron emission tomography partial volume correction: estimation and algorithms. *J. Cereb. Blood Flow Metab.*, 22(8):1019–1034, 2002.
- K. Baete, J. Nuyts, K. Van Laere, W. Van Paesschen, S. Ceyssens, L. D. Ceuninck, O. Gheysens, A. Kelles, J. Vandenevryden, P. Suetens, and P. Dupont. Evaluation of anatomy based reconstruction for partial volume correction in brain FDG-PET. *NeuroImage*, 23(1):305–317, 2004a.
- K. Baete, J. Nuyts, W. Van Paesschen, A. Maes, S. Ghoorun, P. Suetens, and P. Dupont. Use of excess height and cluster extent in subtraction SPECT. *IEEE Trans. Nucl. Sci.*, 49(5):2332–2337, 2002.
- K. Baete, J. Nuyts, W. Van Paesschen, P. Suetens, and P. Dupont. Anatomical-based FDG-PET reconstruction for the detection of hypo-metabolic regions in epilepsy. *IEEE Trans. Med. Imag.*, 23(4):510–519, 2004b.
- P. Bailey and F. Bremer. A sensory cortical representation of the vagus nerve: with a note on the effects of low blood pressure on the cortical electrogram. *J. Neurophysiol.*, 1(5):405–412, 1938.
- H. H. Barrett, J. Yao, J. P. Rolland, and K. J. Myers. Model observers for assessment of image quality. *Proc. Natl. Acad. Sci. USA*, 90(21):9758–9765, 1993.
- D. Bequé, J. Nuyts, G. Bormans, P. Suetens, and P. Dupont. Characterization of acquisition geometry of pinhole SPECT. *IEEE Trans. Med. Imag.*, 22(5):599–612, 2003.

- D. Bequé, J. Nuyts, P. Suetens, and G. Bormans. Optimization of geometrical calibration in pinhole SPECT. *IEEE Trans. Med. Imag.*, 24(2):180–190, 2005.
- S. F. Berkovic and M. R. Newton. *Epilepsy: a comprehensive textbook*, chapter Single photon emission computed tomography, pages 969–975. Lippincott-Raven Publ., Philadelphia, 1997.
- S. F. Berkovic and I. E. Scheffer. Genetics of the epilepsies. *Epilepsia*, 42(Suppl. 5):16–23, 2001.
- N. Boussion, C. Houzard, K. Ostrowsky, P. Ryvlin, F. Mauguière, and L. Cinotti. Automated detection of local normalization areas for ictal-interictal subtraction brain SPECT. *J. Nucl. Med.*, 43(11):1419–1425, 2002.
- J. E. Bowsher, D. M. DeLong, T. G. Turkington, and R. J. Jaszczak. Aligning emission tomography and MRI images by optimizing the emission-tomography image reconstruction objective function. In *Conference Record of the Nuclear Science Symposium and Medical Imaging Conference*, volume 4, pages 2562–2565, Portland, USA, 2003.
- J. E. Bowsher, V. E. Johnson, T. G. Turkington, R. J. Jaszczak, C. E. Floyd, and R. E. Coleman. Bayesian reconstruction and use of anatomical a priori information for emission tomography. *IEEE Trans. Med. Imag.*, 15(5):673–686, 1996.
- B. H. Brinkmann, T. J. O'Brien, D. B. Webster, B. P. Mullan, P. D. Robins, and R. A. Robb. Voxel significance mapping using local image variances in subtraction ictal SPET. *Nucl. Med. Commun.*, 21:545–551, 2000.
- G. Brix, J. Zaers, L. E. Adam, M. E. Bellemann, H. Ostertag, H. Trojan, U. Haberkorn, J. Doll, F. Oberdorfer, and W. J. Lorenz. Performance evaluation of a whole-body PET scanner using the NEMA protocol. *J. Nucl. Med.*, 38(10):1614–1623, 1997.
- M. J. Brodie, H. M. de Boer, and S. I. Johannessen. European white paper on epilepsy. Definition of epilepsy. *Epilepsia*, 44(Suppl. 6):15–16, 2003a.
- M. J. Brodie, H. M. de Boer, and S. I. Johannessen. European white paper on epilepsy. Refractory epilepsy. *Epilepsia*, 44(Suppl. 6):81–82, 2003b.
- P. P. Bruyant, J. Sau, and J.-J. Mallet. Streak artifact reduction in filtered backprojection using a level line-based interpolation method. *J. Nucl. Med.*, 41(11):1913–1919, 2000.
- A. E. Burgess. Comparison of receiver operating characteristic and forced choice observer performance measurement methods. *Med. Phys.*, 22(5):643–655, 1995.
- R. E. Carson. A maximum likelihood method for region-of-interest evaluation in emission tomography. *J. Comp. Assist. Tomogr.*, 10(4):654–663, 1986.
- G. D. Cascino. Advances in neuroimaging: surgical localization. *Epilepsia*, 42(1):3–12, 2001.
- R. Casse, C. C. Rowe, M. Newton, S. U. Berlangieri, and A. M. Scott. Positron emission tomography and epilepsy. *Mol. Imag. Biol.*, 4(5):338–351, 2002.
- B. S. Chang and D. H. Lowenstein. Epilepsy. *N. Engl. J. Med.*, 349(13):1257–1266, 2003.
- L.-T. Chang. A method for attenuation correction in radionuclide computed tomography. *IEEE Trans. Nucl. Sci.*, NS-25(1):638–643, 1978.
- D. L. Collins, A. P. Zijdenbos, V. Kollokian, J. G. Sled, N. J. Kabani, C. J. Holmes, and A. C. Evans. Design and construction of a realistic digital brain phantom. *IEEE Trans. Med. Imag.*, 17(3):463–468, 1998.

- D. L. Collins, A. P. Zijdenbos, V. Kollokian, J. G. Sled, N. J. Kabani, C. J. Holmes, and A. C. Evans. Brainweb: simulated brain database. [Online] Available: <http://www.bic.mni.mcgill.ca/brainweb/>, 2002.
- C. Comtat, P. E. Kinahan, J. A. Fessler, T. Beyer, D. W. Townsend, M. Defrise, and C. Michel. Clinically feasible reconstruction of 3D whole-body PET/CT data using blurred anatomical labels. *Phys. Med. Biol.*, 47:1–20, 2002.
- W. De Clercq, A. Vergult, B. Vanrumste, J. Van Hees, A. Palmini, W. Van Paesschen, and S. Van Huffel. A new muscle artifact removal technique to improve the interpretation of the ictal scalp electroencephalogram. In *Proc. of the 2005 IEEE Engineering in Medicine and Biology 27th Annual Conference (IEEE-EMB)*, pages 1136–1139, Shanghai, China, 2005.
- M. Defrise. A factorization method for the 3D X-ray transform. *Inverse Problems*, 11(5):983–994, 1995.
- A. P. Dempster, N. M. Laird, and D. B. Rubin. Maximum likelihood from incomplete data via the EM algorithm. *J. Royal Statistical Society B*, 39(1):1–38, 1977.
- M. D. Devous, R. A. Thisted, G. F. Morgan, R. F. Leroy, and C. C. Rowe. SPECT brain imaging in epilepsy: a meta-analysis. *J. Nucl. Med.*, 39:285–293, 1998.
- J. S. Duncan. Imaging and epilepsy. *Brain*, 120(2):339–377, 1997.
- J. S. Duncan. Neuroimaging for epilepsy: quality and not just quantity is important. *J. Neurol. Neurosurg. Psychiatry*, 73(6):612–613, 2002.
- L. P. Ekström and R. B. Firestone. WWW Table of Radioactive Isotopes, version 2.1, january 2004. [Online] Available: <http://ie.lbl.gov/toi/index.asp>. Lawrence Berkeley National Laboratory, Berkeley, CA, USA, 2004.
- J. Engel, J., T. R. Henry, M. W. Risinger, J. C. Mazziotta, W. W. Sutherling, M. F. Levesque, and M. E. Phelps. Presurgical evaluation for partial epilepsy: relative contributions of chronic depth-electrode recordings versus FDG-PET and scalp-sphenoidal ictal EEG. *Neurology*, 40(11):1670–1677, 1990.
- J. Engel, Jr. Concepts of epilepsy. *Epilepsia*, 36(Suppl. 1):S23–S29, 1995.
- J. Engel, Jr. Classifications of the International League Against Epilepsy: Time for reappraisal. *Epilepsia*, 39(9):1014–1017, 1998.
- F. Fazio and D. Perani. Importance of partial-volume correction in brain PET studies. *J. Nucl. Med.*, 41(11):1849–1850, 2000.
- J. A. Fessler. Penalized weighted least-squares image reconstruction for positron emission tomography. *IEEE Trans. Med. Imag.*, 13(2):290–300, 1994.
- J. A. Fessler. Mean and variance of implicitly defined biased estimators (such as penalized maximum likelihood): applications to tomography. *IEEE Trans. Image Processing*, 5(3):493–506, 1996.
- J. A. Fessler. Statistical methods for image reconstruction. Short course notes of the 2004 NSS-MIC conference. [Online]. <http://www.eecs.umich.edu/~fessler/>, 2004.
- J. A. Fessler, N. H. Clinthorne, and W. L. Rogers. Regularized emission image reconstruction using imperfect side information. *IEEE Trans. Nucl. Sci.*, 39(5):1464–1471, 1992.

- B. Fischl and A. M. Dale. Measuring the thickness of the human cerebral cortex from magnetic resonance images. *Proc. Natl. Acad. Sci. USA*, 97(20):11050–11055, 2000.
- V. Frouin, C. Comtat, A. Reilhac, and M.-C. Grégoire. Correction of partial-volume effect for PET striatal imaging: fast implementation and study of robustness. *J. Nucl. Med.*, 43(12):1715–1726, 2002.
- S. Geman and D. Geman. Stochastic relaxation, Gibbs distributions, and the Bayesian restoration of images. *IEEE Trans. Pattern Anal. Machine Intell.*, PAMI-6(6):721–741, 1984.
- S. Geman and D. E. McClure. Bayesian image analysis: an application to single photon emission tomography. In *Proceedings of the Statistical Computing Section of the American Statistical Association*, pages 12–18, 1985.
- H. C. Gifford, M. A. King, D. J. de Vries, and E. J. Soares. Channelized Hotelling and human observer correlation for lesion detection in hepatic SPECT imaging. *J. Nucl. Med.*, 41(3):514–521, 2000a.
- H. C. Gifford, M. A. King, R. G. Wells, W. G. Hawkins, M. V. Narayanan, and P. H. Pretorius. LROC analysis of detector-response compensation in SPECT. *IEEE Trans. Med. Imag.*, 19(5):463–473, 2000b.
- G. Gindi, M. Lee, A. Rangarajan, and I. G. Zubal. Bayesian reconstruction of functional images using anatomical information as priors. *IEEE Trans. Med. Imag.*, 12(4):670–680, 1993.
- P. Green. Bayesian reconstructions from emission tomography data using a modified EM algorithm. *IEEE Trans. Med. Imag.*, 9(1):94–98, 1990.
- T. Hebert and R. Leahy. A generalized EM algorithm for 3-D bayesian reconstruction from poisson data using gibbs priors. *IEEE Trans. Med. Imag.*, 8(2):194–202, 1989.
- T. R. Henry. Functional neuroimaging with positron emission tomography. *Epilepsia*, 37(12):1141–1154, 1996.
- T. R. Henry. Therapeutic mechanisms of vagus nerve stimulation. *Neurology*, 59:S3–S14, 2002.
- B. A. Herman, J.-H. Shen, H. B. Kronman, and P.-L. Wang. ROCKIT 0.9b. [Online, 2001] Available: <http://www-radiology.uchicago.edu/krl>. Kurt Rossmann laboratories for radiologic image research, University of Chicago, Chicago, IL, USA, 1998.
- P. Herscovitch, A. P. Auchus, M. Gado, D. Chi, and M. E. Raichle. Correction of positron emission tomography data for cerebral atrophy. *J. Cereb. Blood Flow Metab.*, 6(1):120–124, 1986.
- D. L. Hill, P. G. Batchelor, M. Holden, and D. J. Hawkes. Medical image registration. *Phys. Med. Bio.*, 46:R1–R45, 2001.
- E. J. Hoffman, S.-C. Huang, and M. E. Phelps. Quantitation in positron emission computed tomography: 1. Effect of object size. *J. Comp. Assist. Tomogr.*, 3(3):299–308, 1979.
- E. J. Hoffman, S.-C. Huang, and M. E. Phelps. Quantitation in positron emission computed tomography: 3. Effect of sampling. *J. Comp. Assist. Tomogr.*, 4(6):819–826, 1980.
- A. P. Holmes. *Statistical issues in functional brain mapping*. PhD thesis, Glasgow University, Scotland, UK, 1994.

- S. C. Huang, M. E. Phelps, E. J. Hoffman, K. Sideris, C. J. Selin, and D. E. Kuhl. Noninvasive determination of local cerebral metabolic rate of glucose in man. *Am. J. Physiol.*, 238:E69–E82, 1980.
- J. H. Hubbell and S. M. Seltzer. Tables of X-Ray mass attenuation coefficients and mass energy-absorption coefficients (version 1.4). [Online] Available: <http://physics.nist.gov/xaamdi>. National Institute of Standards and Technology, Gaithersburg, MD, USA, 2004.
- H. M. Hudson and R. S. Larkin. Accelerated image reconstruction using ordered subsets of projection data. *IEEE Trans. Med. Imag.*, 13(4):601–609, 1994.
- T. Ichihara, K. Ogawa, N. Motomura, A. Kubo, and S. Hashimoto. Compton scatter compensation using the triple-energy window method for single- and dual-isotope SPECT. *J. Nucl. Med.*, 34(12):2216–2221, 1993.
- ILAE, 1981. Commission on Classification and Terminology of the International League Against Epilepsy. Proposal for revised clinical and electroencephalographic classification of epileptic seizures. *Epilepsia*, 22:489–501, 1981.
- ILAE, 1989. Commission on Classification and Terminology of the International League Against Epilepsy. Proposal for revised classification of epilepsies and epileptic syndromes. *Epilepsia*, 30:389–399, 1989.
- L. Itti, L. Chang, T. Ernst, and F. Mishkin. Improved 3D correction for partial volume effects in brain SPECT. *Hum. Brain Map.*, 5:379–388, 1997.
- J. H. Jackson. On epilepsy and epileptiform convulsions. In J. Taylor, editor, *Selected writings of John Hughlings Jackson*, page 253. Hodden and Stoughton, London, 1931.
- R. C. Knowlton. Multimodality imaging in partial epilepsies. *Curr. Opin. Neurol.*, 17(2):165–172, 2004.
- D. E. Kuhl, J. Engel, J. M. E. Phelps, and C. Selin. Epileptic patterns of local cerebral metabolism and perfusion in humans determined by emission computed tomography of 18FDG and 13NH3. *Ann. Neurol.*, 8(4):348–360, 1980.
- C. Labb  , J. C. Froment, A. Kennedy, J. Ashburner, and L. Cinotti. Positron emission tomography metabolic data corrected for cortical atrophy using magnetic resonance imaging. *Alzheimer Dis. Assoc. Disord.*, 10(3):141–170, 1996.
- K. Lange and R. E. Carson. EM reconstruction algorithms for emission and transmission tomography. *J. Comp. Tomogr.*, 8(2):306–316, 1984.
- D. S. Lee, J. S. Lee, K. W. Kang, M. J. Jang, S. K. Lee, J.-K. Chung, and M. C. Lee. Disparity of perfusion and glucose metabolism of epileptogenic zones in temporal lobe epilepsy demonstrated by SPM/SPAM analysis on ^{15}O water PET, [^{18}F]FDG-PET, and [$^{99\text{m}}\text{Tc}$]-HMPAO SPECT. *Epilepsia*, 42(12):1515–1522, 2001.
- E. Levitan and G. T. Herman. A maximum a posterior probability expectation maximization algorithm for image reconstruction in emission tomography. *J. Nucl. Med.*, 6:185–192, 1987.
- R. M. Lewitt. Reconstruction algorithms: transform methods. *Proc. IEEE*, 71(3):390–408, 1983.
- B. Lipinski, H. Herzog, E. Rota Kops, W. Oberschelp, and H. W. M  ller-G  rtner. Expectation maximization reconstruction of positron emission tomography images using anatomical magnetic resonance information. *IEEE Trans. Med. Imag.*, 16(2):129–136, 1997.

- F. Maes, A. Collignon, D. Vandermeulen, G. Marchal, and P. Suetens. Multimodality image registration by maximization of mutual information. *IEEE Trans. Med. Imag.*, 16(2):187–198, 1997.
- P. K. Marsden, D. Strul, S. F. Keevil, S. C. R. Williams, and D. Cash. Simultaneous PET and NMR. *Br. J. Radiol.*, 75:S53–S59, 2002.
- S. Matej and R. M. Lewitt. Image representation and tomographic reconstruction using spherically-symmetric volume elements. In *Proceedings of the 1992 IEEE Nuclear Science Symposium and Medical Imaging Conference*, volume 2, pages 1191–1193, Orlando, Florida, USA, 1992.
- A. W. McCarthy and M. I. Miller. Maximum likelihood SPECT in clinical computation times using mesh-connected parallel computers. *IEEE Trans. Med. Imag.*, 10(3):426–436, 1991.
- C. C. Meltzer, J. P. Leal, H. S. Mayberg, H. N. Wagner, Jr., and J. J. Frost. Correction of PET data for partial volume effects in human cerebral cortex by MR imaging. *J. Comput. Assist. Tomogr.*, 14(4):561–570, 1990.
- C. E. Metz, B. A. Herman, and C. A. Roe. Statistical comparison of two ROC-curve estimates obtained from partially-paired datasets. *Med. Decis. Making*, 18:110–121, 1998.
- C. R. Meyer, J. L. Boes, B. Kim, P. H. Bland, K. R. Zasadny, P. V. Kison, K. Koral, K. A. Frey, and R. L. Wahl. Demonstration of accuracy and clinical versatility of mutual information for automatic multimodality image fusion using affine and thin-plate spline warped geometric deformations. *Med. Image Anal.*, 1(3):195–206, 1997.
- J. P. Mugler and J. R. Brookman. Three-dimensional magnetization-prepared rapid gradient-echo imaging (3-D MPRAGE). *Magn. Reson. Med.*, 15(1):152–157, 1990.
- H. W. Müller-Gärtner, J. M. Links, J. L. Prince, R. Bryan, E. McVeigh, J. Leal, C. Davatzikos, and J. Frost. Measurement of radiotracer concentration in brain gray matter using positron emission tomography: MRI-based correction for partial volume effects. *J. Cereb. Blood Flow Metab.*, 12(4):571–583, 1992.
- E. Mumcuoglu, R. M. Leahy, and S. R. Cherry. Bayesian reconstruction of PET images: methodology and performance analysis. *Phys. Med. Bio.*, 41:1777–1807, 1996.
- E. Mumcuoglu, R. M. Leahy, S. R. Cherry, and Z. Zhou. Fast gradient-based methods for Bayesian reconstruction of transmission and emission PET images. *IEEE Trans. Med. Imag.*, 13(4):687–701, 1994.
- J. Nuysts, K. Baete, D. Bequé, and P. Dupont. Comparison between MAP and post-processed ML for incorporating anatomical knowledge in emission tomography. In *Conference Record of the Nuclear Science Symposium and Medical Imaging Conference*, volume 3, pages 2007–2011, Portland, USA, 2003.
- J. Nuysts, K. Baete, D. Bequé, and P. Dupont. Comparison between MAP and post-processed ML for incorporating anatomical knowledge in emission tomography. *IEEE Trans. Med. Imag.*, 24(5):667–675, 2005.
- J. Nuysts, D. Bequé, P. Dupont, and L. Mortelmans. A concave prior penalizing relative differences for maximum-a-posteriori reconstruction in emission tomography. *IEEE Trans. Nucl. Sci.*, 49(1):56–60, 2002.
- J. Nuysts, P. Dupont, S. Stroobants, R. Benninck, L. Mortelmans, and P. Suetens. Simultaneous maximum-a-posteriori reconstruction of attenuation and activity distributions from emission sinograms. *IEEE Trans. Med. Imag.*, 18(5):393–403, 1999a.

- J. Nuyts, P. Dupont, S. Stroobants, A. Maes, L. Mortelmans, and P. Suetens. Evaluation of maximum-likelihood based attenuation correction in positron emission tomography. *IEEE Trans. Nucl. Sci.*, 46(4):1136–1141, 1999b.
- J. Nuyts and J. A. Fessler. A penalized-likelihood image reconstruction method for emission tomography, compared to post-smoothed maximum-likelihood with matched spatial resolution. *IEEE Trans. Med. Imag.*, 22(9):1042–1052, 2003.
- T. J. O'Brien, M. K. O'Connor, B. P. Mullan, B. H. Brinkmann, D. Hanson, C. R. Jack, and E. L. So. Subtraction ictal SPET co-registered to MRI in partial epilepsy: description and technical validation of the method with phantom and patient studies. *Nucl. Med. Commun.*, 19:31–45, 1998a.
- T. J. O'Brien, E. L. So, B. P. Mullan, G. D. Cascino, M. F. Hauser, B. H. Brinkmann, F. W. Sharbrough, and F. B. Meyer. Subtraction peri-ictal SPECT is predictive of extratemporal epilepsy surgery outcome. *Neurology*, 55:1668–1677, 2000.
- T. J. O'Brien, E. L. So, B. P. Mullan, M. F. Hauser, B. H. Brinkmann, N. I. Bohnen, D. Hanson, G. D. Cascino, C. R. Jack, and F. W. Sharbrough. Subtraction ictal SPECT co-registered to MRI improves clinical usefulness of SPECT in localizing the surgical seizure focus. *Neurology*, 50:445–454, 1998b.
- T. J. O'Brien, E. L. So, B. P. Mullan, M. F. Hauser, B. H. Brinkmann, C. R. Jack, G. D. Cascino, F. B. Meyer, and F. W. Sharbrough. Subtraction SPECT co-registered to MRI improves postictal SPECT localization of seizure foci. *Neurology*, 52:137–146, 1999.
- X. Ouyang, W. H. Wong, V. E. Johnson, X. Hu, and C. Chen. Incorporation of correlated structural images in PET image reconstruction. *IEEE Trans. Med. Imag.*, 13(4):627–640, 1994.
- A. Palmini, I. Najm, G. Avanzini, T. Babb, R. Guerrini, N. Foldvary-Schaefer, G. Jackson, H. O. Luders, R. Prayson, R. Spreafico, and H. V. Vinters. Terminology and classification of the cortical dysplasias. *Neurology*, 62(6 Suppl. 3):S2–S8, 2004.
- M. Platt and M. R. Sperling. A comparison of surgical and medical costs for refractory epilepsy. *Epilepsia*, 43(Suppl. 4):25–31, 2002.
- J.-B. Poline and B. M. Mazoyer. Analysis of individual positron emission tomography activation maps by detection of high signal-to-noise-ratio pixel clusters. *J. Cereb. Blood Flow Metab.*, 13:425–437, 1993.
- J. Radon. Über die bestimmung von funktionen durch ihre integralwerte längs gewisser mannigfaltigkeiten. Berichte über die verhandlungen. *Sächsischen Akademie der Wissenschaft*, 69:262–277, 1917. Translation: *IEEE Trans. Med. Imag.*, 5(4):170–176, 1986.
- A. Rangarajan, I.-T. Hsiao, and G. Gindi. A Bayesian joint mixture framework for the integration of anatomical information in functional image reconstruction. *J. Math. Imag. Vision*, 12(3):119–217, 2000.
- P. E. Roland, B. Levin, R. Kawashima, and S. Åkerman. Three-dimensional analysis of clustered voxels in ^{15}O -butanol brain activation images. *Hum. Brain Map.*, 1:3–19, 1993.
- F. Rosenow and H. Lüders. Presurgical evaluation of epilepsy. *Brain*, 124(9):1683–1700, 2001.
- O. G. Rousset, Y. Ma, and A. C. Evans. Correction for partial volume effects in PET: principle and validation. *J. Nucl. Med.*, 39(5):904–911, 1998.

- T. M. Salmenpera and J. S. Duncan. Imaging in epilepsy. *J. Neurol. Neurosurg. Psychiatry*, 76(Suppl. 3):iii2–iii10, 2005.
- S. Sastry and R. E. Carson. Multimodality Bayesian algorithm for image reconstruction in positron emission tomography: a tissue composition model. *IEEE Trans. Med. Imag.*, 16(6):750–761, 1997.
- Y. Shao, S. R. Cherry, K. Farahani, K. Meadors, S. Siegel, R. W. Silverman, and P. K. Marsden. Simultaneous PET and MR imaging. *Phys. Med. Bio.*, 42(10):1965–1970, 1997.
- L. A. Shepp and Y. Vardi. Maximum likelihood reconstruction for emission tomography. *IEEE Trans. Med. Imag.*, 1(2):113–122, 1982.
- A. M. Siegel. Presurgical evaluation and surgical treatment of medically refractory epilepsy. *Neurosurg. Rev.*, 27(1):1–18, 2004.
- M. Signorini, E. Paulesu, K. Friston, D. Perani, A. Colleluori, G. Lucignani, F. Grassi, V. Bettinardi, R. S. J. Frackowiak, and F. Fazio. Rapid assessment of regional cerebral metabolic abnormalities in single subjects with quantitative and nonquantitative [¹⁸F]FDG PET: a clinical validation of statistical parametric mapping. *NeuroImage*, 9(1):63–80, 1999.
- R. B. Slates, K. Farahani, Y. Shao, P. K. Marsden, J. Taylor, P. E. Summers, S. Williams, J. Beech, and S. R. Cherry. A study of artefacts in simultaneous PET and MR imaging using a prototype MR compatible PET scanner. *Phys. Med. Bio.*, 44(8):2015–2027, 1999.
- D. L. Snyder, M. I. Miller, L. J. Thomas, and D. G. Politte. Noise and edge artifacts in maximum-likelihood reconstructions for emission tomography. *IEEE Trans. Med. Imag.*, MI-6(3):228–238, 1987.
- S. Som, B. F. Hutton, and M. Braun. Properties of minimum cross-entropy reconstruction of emission tomography with anatomically based prior. *IEEE Trans. Nucl. Sci.*, 45(6):3014–3021, 1998.
- M. V. Spanaki, S. S. Spencer, M. Corsi, J. MacMullan, J. Seibyl, and I. G. Zubal. Sensitivity and specificity of quantitative difference SPECT analysis in seizure localization. *J. Nucl. Med.*, 40:730–736, 1999.
- SPM2. Statistical parametric mapping. Wellcome department of imaging neuroscience, London, UK. [Online] Available: <http://www.fil.ion.ucl.ac.uk/spm>, 2003.
- SPM99. Statistical parametric mapping. Wellcome department of imaging neuroscience, London, UK. [Online] Available: <http://www.fil.ion.ucl.ac.uk/spm>, 1999.
- S. Srivastava, F. Maes, D. Vandermeulen, W. Van Paesschen, P. Dupont, and P. Suetens. Feature-based statistical analysis of structural MRI data for automatic detection of focal cortical dysplastic lesions. *NeuroImage*, 27(2):253–266, 2005.
- S. Srivastava, K. Van Leemput, F. Maes, D. Vandermeulen, and P. Suetens. Validation of nonlinear spatial filtering to improve tissue segmentation of MR brain images. In *MICCAI '01: Proceedings of the 4th International Conference on Medical Image Computing and Computer-Assisted Intervention*, pages 507–515, London, UK, 2001. Springer-Verlag.
- J. W. Stayman and J. A. Fessler. Compensation for nonuniform resolution using penalized-likelihood reconstruction in space-variant imaging systems. *IEEE Trans. Med. Imag.*, 23(3):269–284, 2004.

- J. Talairach and P. Tournoux. *Co-planar stereotaxic atlas of the human brain*. Thieme, New York, 1988.
- E. Tanaka and T. A. Iinuma. Approaches to optimal data processing in radioisotope imaging. *Phys. Med. Bio.*, 15(4):683–694, 1970.
- L. Thurfjell, Y. H. Lau, J. L. Andersson, and B. F. Hutton. Improved efficiency for MRI-SPET registration based on mutual information. *Eur. J. Nucl. Med.*, 27:847–856, 2000.
- D. W. Townsend and T. Beyer. A combined PET/CT scanner: the path to true image fusion. *Br J Radiol*, 75(90009):24S–30, 2002.
- F. Turkheimer, R. M. Moresco, G. Lucignani, L. Sokoloff, F. Fazio, and K. Schmidt. The use of spectral analysis to determine regional cerebral glucose utilization with positron emission tomography and [¹⁸F]fluorodeoxyglucose: theory, implementation, and optimization procedures. *J. Cereb. Blood Flow Metab.*, 14(3):406–422, 1994.
- P. Van Bogaert, N. Massager, P. Tugendhaft, D. Wikler, P. Damhaut, M. Levivier, J. Brotchi, and S. Goldman. Statistical parametric mapping of regional glucose metabolism in mesial temporal lobe epilepsy. *NeuroImage*, 12(2):129–138, 2000.
- K. Van Leemput, F. Maes, D. Vandermeulen, and P. Suetens. Automated model-based tissue classification of MR images of the brain. *IEEE Trans. Med. Imag.*, 18(10):897–908, 1999.
- W. Van Paesschen. Ictal SPECT. *Epilepsia*, 45(Suppl. 4):35–40, 2004.
- Y. Vandecan. Role of normalization and influence of smoothing in the subtraction analysis of ictal and interictal brain SPECT images in epilepsy. M.Sc. Thesis, Katholieke Universiteit Leuven, Leuven, Belgie, 2004.
- P. Véra, A. Kaminska, C. Cieuta, A. Hollo, J. L. Stiévenart, I. Gardin, D. Ville, J. F. Mangin, P. Plouin, O. Dulac, and C. Chiron. Use of subtraction ictal SPECT co-registered to MRI for optimizing the localization of seizure foci in children. *J. Nucl. Med.*, 40:786–792, 1999.
- T. O. Videen, J. S. Perlmutter, M. A. Mintun, and M. E. Raichle. Regional correction of positron emission tomography data for the effects of cerebral atrophy. *J. Cereb. Blood Flow Metab.*, 8(5):662–670, 1988.
- R. F. Wagner and D. G. Brown. Unified SNR analysis of medical imaging systems. *Phys. Med. Bio.*, 30(6):489–518, 1985.
- C. C. Watson. New, faster, image-based scatter correction for 3D PET. *IEEE Trans. Nucl. Sci.*, 47(4):1587–1594, 2000.
- G. L. Westbrook. *Principles of neural science*, chapter Seizures and epilepsy, pages 910–935. McGraw-Hill, New York, NY, 4th edition, 2000.
- WHO, 2005. Atlas: epilepsy care in the world. Technical report, World Health Organization, 2005.
- WHO, TRS-492. The medical uses of ionizing radiation and isotopes. Technical Report Series 492, World Health Organization, 1972.
- K. J. Worsley, A. C. Evans, S. Marrett, and P. Neelin. A three-dimensional statistical analysis for CBF activation studies in human brain. *J. Cereb. Blood Flow Metab.*, 12:900–918, 1992.

- T. Yokoi, T. Soma, H. Shinohara, and H. Matsuda. Accuracy and reproducability of co-registration techniques based on mutual information and normalized mutual information for MRI and SPECT brain images. *Ann. Nucl. Med.*, 18(8):659–667, 2004.
- H. Zaidi and M.-L. Montandon. The new challanges of brain PET imaging technology. *Curr. Med. Imag. Rev.*, 2(1):3–13, 2006.
- I. G. Zubal, S. S. Spencer, K. Imam, J. Seibyl, E. O. Smith, G. Wisniewski, and P. B. Hoffer. Difference images calculated from ictal and interictal technetium-99m-HMPAO SPECT scans of epilepsy. *J. Nucl. Med.*, 36:684–689, 1995.
- D. Zumsteg and H. G. Wieser. Presurgical evaluation: current role of invasive EEG. *Epilepsia*, 41(Suppl. 3):S55–S60, 2000.

Publications

International Journals

1. **K. Baete**, J. Nuyts, W. Van Paesschen, A. Maes, S. Ghoorun, P. Suetens, and P. Dupont, "Use of excess height and cluster extent in subtraction SPECT," *IEEE Transactions on Nuclear Science*, Vol. 49, No. 5, pp. 2332–2337, Oct. 2002.
2. **K. Baete**, J. Nuyts, W. Van Paesschen, P. Suetens, and P. Dupont, "Anatomical based FDG-PET reconstruction for the detection of hypo-metabolic regions in epilepsy," *IEEE Transactions on Medical Imaging*, Vol. 23, No. 4, pp. 510–519, Apr. 2004.
3. **K. Baete**, J. Nuyts, K. Van Laere, W. Van Paesschen, S. Ceyssens, L. De Ceuninck, O. Gheysens, A. Kelles, J. Vandeneijnden, P. Suetens, and P. Dupont, "Evaluation of anatomy based reconstruction for partial volume correction in brain FDG-PET," *NeuroImage*, Vol. 23, No. 1, pp. 305–317, Sep. 2004.
4. J. Nuyts, **K. Baete**, D. Bequé, and P. Dupont, "Comparison between MAP and post-processed ML for incorporating anatomical knowledge in emission tomography," *IEEE Transactions on Medical Imaging*, Vol. 24, No. 5, pp. 667–675, May 2005.
5. N. Nelissen, W. Van Paesschen, **K. Baete**, K. Van Laere, A. Palmini, H. Van Billoen, P. Dupont, "Correlations of interictal FDG-PET metabolism and ictal SPECT perfusion changes in human temporal lobe epilepsy with hippocampal sclerosis," *NeuroImage*, in press, 2006.
6. S. Ghoorun, **K. Baete**, J. Nuyts, W. Groenewald, P. Dupont, "The influence of attenuation correction and reconstruction techniques on the detection of hypo-perfused lesions in brain SPECT images," *Nucl. Med. Commun.*, in press, 2006.

International Conference Proceedings

1. **K. Baete**, J. Nuyts, D. Vandermeulen, A. Maes, W. Van Paesschen, and P. Dupont, "Excess height versus cluster extent in subtraction SPECT," *Proc. of 2001 IEEE Nuclear Science Symposium and Medical Imaging Conference*,

- Vol. 3, pp. 1424–1428, M5C-18, San Diego, California, USA, 4-10 Nov. 2001.
- 2. **K. Baete**, J. Nuyts, W. Van Paesschen, P. Suetens, and P. Dupont, “Anatomical based FDG-PET reconstruction for the detection of hypometabolic regions in epilepsy,” *Proc. of 2002 IEEE Nuclear Science Symposium and Medical Imaging Conference*, Vol. 3, pp. 1481–1485, M10-94, Norfolk, Virginia, USA, 13-16 Nov. 2002.
 - 3. **K. Baete**, J. Nuyts, W. Van Paesschen, P. Suetens, and P. Dupont, “Evaluation of an anatomical based MAP reconstruction algorithm for PET in epilepsy,” *Proc. of 2003 IEEE Nuclear Science Symposium and Medical Imaging Conference*, Vol. 3, pp. 2017–2021, M5-4, Portland, Oregon, USA, 22-25 Oct. 2003.
 - 4. J. Nuyts, **K. Baete**, D. Bequé, and P. Dupont, “Comparison between MAP and post-processed ML for incorporating anatomical knowledge in emission tomography,” *Proc. of 2003 IEEE Nuclear Science Symposium and Medical Imaging Conference*, Vol. 3, pp. 2007–2011, M5-2, Portland, Oregon, USA, 22-25 Oct. 2003.

National Abstracts and Proceedings

- 1. **K. Baete**, J. Nuyts, A. Maes, W. Van Paesschen, and P. Dupont, “Excess height vs. cluster extent in subtraction SPECT,” *Tijdschrift voor Nucleaire Geneeskunde*, 2001, Jg. 23, Nr. 4, Dec. 2001, pp. 165-166.

International Conference Abstract

- 1. P. Dupont, **K. Baete**, J. Nuyts, D. Vandermeulen, W. Van Paesschen, “Anatomical based reconstruction for positron emission tomography using [18F]fluoro-2-deoxy-D-glucose in epilepsy,” *BrainPET 2003*, Calgary, Alberta, Canada, 2003.
- 2. S. Ghoorun, **K. Baete**, J. Nuyts, W.A. Groenewald, and P. Dupont, “Influence of attenuation correction and reconstruction techniques on the detection of hypoperfused lesions in brain SPECT studies,” *EANM'04, Annual Congress of the European Association of Nuclear Medicine*, Helsinki, Finland, 2004.
- 3. S. Ghoorun, **K. Baete**, Y. Vandecan, R. Ambayi, J. Nuyts, W. Van Paesschen, and P. Dupont, “Influence of reconstruction and smoothing in the Subtraction Analysis of Ictal and Interictal Brain SPECT images in epilepsy,” *52th Annual meeting of the Society of Nuclear Medicine*, Toronto, Ontario, Canada, 2005.
- 4. **K. Baete**, Y. Vandecan, W. Van Paesschen, J. Nuyts, K. Van Laere, P. Suetens, and P. Dupont, “Anatomy based reconstruction for subtraction analysis of ictal and interictal perfusion SPECT,” *Human Brain Mapping*, Toronto, Ontario, Canada, 2005.
- 5. N. Nelissen, W. Van Paesschen, **K. Baete**, G. Van Driel, K. Van Laere,

- A. Palmini, H. Van Billoen, and P. Dupont, "FDG-PET and subtraction ictal-interictal SPECT correlations in patients with refractory mesial temporal lobe epilepsy associated with hippocampal sclerosis," *26th International Epilepsy Congress, ILAE*, Paris, France, 2005.
6. S. Ghoorun, **K. Baete**, Y. Vandecan, R. Ambayi, J. Nuyts, W. Van Paesschen, P. Dupont, "Influence of reconstruction and Gaussian smoothing on the subtraction analysis of ictal and interictal brain SPECT images," *27th International Symposium on Radioactive Isotopes in Clinical Medicine and Research*, Bad Gastein, Austria, 2006.

National Symposia and Scientific Meetings

1. T. De Potter, A. Maes, **K. Baete**, and L. Mortelmans, "Subtraction analysis of ECD-SPECT during and after global transient amnesia," *Symposium of the Belgian Society of Nuclear Medicine*, CR-7, Knokke, Belgium, 18-20 May 2001.
2. **K. Baete**, J. Nuyts, A. Maes, W. Van Paesschen, and P. Dupont, "Excess height vs. cluster extent in subtraction SPECT," *Scientific meeting of the Belgian Society of Nuclear Medicine*, Brugmann Hospital, Brussels, Belgium, 29 Sept. 2001.
3. **K. Baete**, J. Nuyts, W. Van Paesschen, K. Van Laere, and P. Dupont, "Anatomical based reconstruction for FDG-PET in epilepsy," *Symposium of the Belgian Society of Nuclear Medicine*, P-31, Knokke, Belgium, 23-25 May 2003.

Master Theses

1. **K. Baete**, "Periode analyse van foto-metrische waarnemingen van de β Cephei ster ν Eridani," Fac. Wetenschappen, Inst. voor sterrenkunde, K.U. Leuven, 1999.
2. **K. Baete**, en S. Boons, "Modellering van spatiale resolutie en correctie voor Compton scatter in SPECT," Fac. Toegepaste Wetenschappen en Fac. Geneeskunde, K.U.Leuven, 2000.

Curriculum Vitae

Kristof Baete was born in Brugge, Belgium, on May 19, 1976. He received a Master of Science degree in Physics from the Katholieke Universiteit Leuven in 1999. His master thesis, which was conducted at the Institute of Astronomy, involved the frequency determination of the variable and pulsating β -Cephei star ν Eridani. He completed the complementary studies in Biomedical and Clinical Engineering, and Medical Radiation Physics in 2000, and the advanced studies in Medical Radiation Physics in 2005. In 2000, he started working as a researcher for the faculty of Applied Sciences, department of Electrical Engineering (ESAT), center for Processing of Speech and Images (PSI), laboratory of Medical Image Computing (MIC). He worked at the division of Nuclear Medicine in the university hospital Gasthuisberg. His work has been supported by K.U.Leuven grants IDO-99/005 and OT-00/32. Since 2004, he is a Medical Physicist at the division of Nuclear Medicine.

Education

1. Doctoraatsopleiding Ingenieurswetenschappen, K.U.Leuven, 2000–2006.
2. Gediplomeerde in de Gespecialiseerde Studies Medische Stralingsphysica, K.U.Leuven, 2004–2005.
3. Gediplomeerde in de Aanvullende Studies Biomedische en Klinische Ingenieurstechnieken en Medische Fysica, optie Medische Stralingsphysica, K.U.Leuven, 1999–2000.
4. Licentiaat Natuurkunde, K.U.Leuven, 1997–1999.
5. Kandidaat Natuurkunde, K.U.Leuven Campus Kortrijk, 1995–1997.

Scientific Training

1. Short course “Task-Based Assessment of Image Quality”, by C.E. Metz and H.H. Barrett. IEEE NSS-MIC, November, 2002, Norfolk, VA.
2. Astronomical observation at the *Hochalpine Forschungsstation Jungfraujoch*, November, 1998, Switzerland.

